VOLUME 31 FEBRUARY 1953 NUMBER 2

# Canadian Journal of Physics

*Editor:* G. M. VOLKOFF

This supplementary issue
is dedicated to
PROFESSOR GRAY
in recognition of his contribution
to science

*Published by* THE NATIONAL RESEARCH COUNCIL
OTTAWA CANADA

# CANADIAN JOURNAL OF PHYSICS

(*Formerly Section A, Canadian Journal of Research*)

The CANADIAN JOURNAL OF PHYSICS is published bimonthly by the National Research Council of Canada under the authority of the Chairman of the Committee of the Privy Council on Scientific and Industrial Research. Matters of general policy are the responsibility of a joint Editorial Board consisting of members of the National Research Council of Canada and the Royal Society of Canada.

The National Research Council of Canada publishes also: *Canadian Journal of Botany, Canadian Journal of Chemistry, Canadian Journal of Medical Sciences, Canadian Journal of Technology, Canadian Journal of Zoology.*


---



---


**Manuscripts** should be addressed to:

DR. LÉO MARION,
Editor-in-Chief,
Canadian Journal of Physics,
National Research Council,
Ottawa, Canada.

Each manuscript should be typewritten, double-spaced, and the original and one extra copy submitted (see **Notice to Contributors** inside of back cover).

**Subscriptions, renewals, and orders for back numbers** should be addressed to:

Administrative Services,
National Research Council,
Ottawa, Canada.

Subscription rate: $3.00 a year; single numbers: 50 cents. Special rates can be obtained for subscriptions to more than one of the Journals published by the National Research Council

*From a portrait by Grant Macdonald*

J. A. Gray

*To*

PROFESSOR J. A. GRAY

this issue is dedicated by his friends and former students as a tribute on the occasion of his retirement as Chown Research Professor of Physics, Queen's University

## Professor Joseph Alexander Gray, O.B.E., F.R.S.

Joseph Alexander Gray was born in Australia on February 7, 1884. He received his early education at the State School and the University High School in Melbourne. He studied at Ormond College and at the University of Melbourne from which he graduated in 1907 with the degree of Bachelor of Science. His professors were T. R. Lyle, F.R.S., and E. F. J. Love in physics and J. H. Michell, F.R.S., and E. J. Nanson in mathematics. During his undergraduate career he won several scholarships and prizes and obtained first class final honours in mathematics and in physics in consecutive years. Rutherford's book *Radioactivity* chosen as one of his student prizes made a profound impression and determined his entry into the modern physics of radioactivity. In 1908 he went to England and worked for one year under the Honourable R. J. Strutt at the Imperial College of Science. The award of an Exhibition of 1851 Scholarship made possible a period of three years devoted to research in radioactivity with Rutherford at the University of Manchester. For this work he was awarded the degrees of Master of Science and Doctor of Science.

In 1912 Dr. Gray came to Canada and joined the staff of McGill University. During the First World War he served with the Canadian Army and with the Royal Engineers. He was mentioned in dispatches and appointed an Officer of the Order of the British Empire for his work on methods for evaluating wind and temperature corrections in sound ranging. In 1919 Dr. Gray returned to McGill University as Associate Professor of Physics. In 1924 he was appointed Chown Research Professor of Physics at Queen's University, a position that he has held with distinction until his retirement on October 1, 1952.

Professor Gray was elected a Fellow of the Royal Society of Canada in 1922 and a Fellow of the Royal Society of London in 1932. He was President of Section III of the Royal Society of Canada in 1939-1940 and has served as a member of the National Research Council (1942-1948) and as Chairman of the Selection Committee for Nuffield Fellowships in the Natural Sciences (1948-1952).

Professor Gray's scientific work has been on the properties of $\beta$-, $\gamma$- and X-rays. In Rutherford's laboratory he showed that X-rays are produced by $\beta$-rays and that $\beta$-rays (of radium E) have a range. The latter experiment may be said to be the origin of the absorption and range method, now so widely used by nuclear physicists and radiochemists. By ingenious absorption experiments he showed that both $\gamma$- and X-rays undergo a change in quality on being scattered. This result on change of wave length preceded by several years the quantum theory of scattering by free electrons. Dr. Gray's experiments on the absorption of the $\gamma$-rays of radium are well known. Some other investigations, perhaps not so well known, were on the angular distribution of X-rays scattered by gases and on the small angle scattering of X-rays by powders. Since that time, powerful techniques for the study of molecules and molecular groups have been derived from such experiments.

Efforts to obtain an accelerator for nuclear research at Queen's University were finally successful in 1950 when a 70-Mev. synchrotron was put into operation. Since then Professor Gray and his students have studied the spectrum of X-rays from the synchrotron and numerous nuclear reactions that are induced by these X-rays.

Professor Gray has always had a high regard for new experimental techniques. Mention must be made of the pioneer work in his laboratory in 1940 on the measurement of small ionization currents with a vibrating reed and an alternating current amplifier. Several years ago, when the nuclear emulsion technique was becoming established, he quickly assessed its power and adopted it. The laboratory is now excellently equipped for this type of work.

One of Professor Gray's important contributions to Canadian science has been his training of select research students. Of fifty graduate students who have worked in his laboratory, no less than ten have won the Exhibition of 1851 Scholarship. A number of these graduates now hold important positions in universities and atomic energy projects in Canada and the United States. He has always encouraged his students to maintain a sceptical attitude towards current scientific theories, has impressed upon them that the mere accumulation of data does not constitute experimental physics, and has emphasized the importance of expressing themselves clearly in writing.

At a Convocation on October 25, 1952, Queen's University conferred on Professor Gray the degree of Doctor of Laws. In conclusion, one can not do better than quote from Principal Mackintosh's citation:

". . . Joseph Alexander Gray, Fellow of the Royal Society of London, until a few weeks ago Chown Research Professor of Physics in this university, who has been one of that distinguished group of effective pioneers in the field of nuclear physics, and from whose laboratory has flowed a long and continuous line of first-class physicists, living evidence of the high standards of his scholarship and the scrupulous care of his selection".

B. W. Sargent

Canadian Journal of Physics

*Issued by* THE NATIONAL RESEARCH COUNCIL OF CANADA

VOLUME 31 FEBRUARY, 1953 NUMBER 2

# LONG DURATION ECHOES FROM AURORA, METEORS, AND IONOSPHERIC BACK-SCATTER[1]

BY D. W. R. MCKINLEY AND PETER M. MILLMAN

ABSTRACT

In the course of the Ottawa meteor program some unusual echoes have been detected on 33 Mc. Echoes from the aurora are discussed and correlated with visual observations. Two mechanisms of radio reflections from the aurora have been proposed but the data here presented are insufficient to favor one over the other. On Aug. 4, 1948, six extremely long duration meteor echoes were observed which may have been due to abnormal ionospheric conditions. From time to time since August, 1948, a weak semipermanent echo has been recorded, usually appearing at a range of about 80 km., and enduring up to an hour. It is suggested that this echo is due to back-scatter from the same sources in the lower *E*-region that are presumed to be responsible for long-range very high frequency propagation.

## INTRODUCTION

From time to time, during the combined meteor program (3) carried out by the Dominion Observatory and the National Research Council, radar echoes of unusual types have been observed. Some of these echoes have been correlated with the visual aurora; for a few hours on one occasion meteor echoes of abnormally long duration were obtained; and there are several records of a weak semipermanent echo at a range near 80 to 100 km. This last-mentioned phenomenon remained in some cases for over an hour and could rarely be correlated either with the aurora or with meteors. It should be pointed out that the main emphasis has always been on the meteor research, and that the observation of auroral and ionospheric scatter echoes could have been greatly facilitated by a different selection of observing periods and by designing the instrumentation to favor their detection.

The Ottawa radar station at lat. 45° N., long. 75° W., radiated pulses 20 $\mu$sec. long with a peak power of 200 to 400 kw., on a frequency of 33 Mc. The transmitting and receiving antennas were each half-wave dipoles mounted horizontally a quarter-wave above ground. The radiation pattern was therefore broad, falling off slowly from a maximum in the zenith, with very little energy being transmitted at elevation angles below 10 degrees.

A continuously-moving film camera photographed the echoes displayed as intensity-modulation on a cathode ray tube, thus producing a range–time record.

[1] *Manuscript received October 15, 1952.*

*Contribution from the Radio and Electrical Engineering Division, National Research Laboratories, and from the Dominion Observatory, Ottawa, Canada. Issued as N.R.C. No. 2885, and Contributions from the Dominion Observatory, Vol. 2, No. 12.*

Normally, the recorded sweep length was about 400 km., and the 20 km. calibration marks appeared as black lines. During some periods of auroral activity the sweep was increased to 650 km. and every 100 km. range mark was reversed to appear as a white line. In 1947 and 1948 the film speed was 1 in. per min. Since early 1949, records have been made at 4 in. per min. with the range scale limited to 260 km. to improve the resolution of the meteor echoes. Similar radar equipments, though with considerably lower power outputs, were in operation at Arnprior and Carleton Place on some occasions (4).

During the first two weeks of August, 1948, the three radar stations were operated 24 hr. a day. At night teams of visual observers were in action at all stations, and several batteries of direct cameras and spectrographs were in use. It may not be surprising therefore that much of the material of this paper was obtained in this period of sustained peak activity. The equipment was in operation for only a small fraction of the time on a year-round basis so that no general statistics of the frequency of occurrence of auroral or scatter echoes can be furnished.

## AURORAL ECHOES

A strong auroral echo was noted for the first time on the night of April 21/22, 1948. It appeared for about six minutes at the extreme range recorded, between 320 and 400 km. Visually a bright aurora was visible for a fair portion of the night.

A brilliant visual aurora was seen again on Aug. 7/8, 1948, and the auroral echoes appeared at $22^h\ 55^m$ E.S.T. when the maximum range of the display was altered from 400 km. to 650 km. From then on, and coincident with a fine visual display, the auroral echoes were present in various forms almost continuously for over six hours. They disappeared about 15 min. after sunrise but appeared again briefly at $07^h\ 30^m$ and sporadically in the period from $16^h$ to $22^h$ E.S.T. on Aug. 8. In spite of good visual aurora on the next two nights the echoes were not visible on the radar until $01^h\ 50^m$, Aug. 10, when they appeared almost continuously for three hours. A brief report of these observations was made at the Conference on Auroral Physics, July, 1951, at London, Ont.

In general the minimum range of the auroral echoes varied from 300 to 500 km. while the maximum was beyond the recorded limit of 650 km. A visual monitor oscilloscope with a 1000 km. sweep frequently showed auroral echoes out to the limit of its range. In a few cases the minimum range dropped below 300 km. and at $3^h\ 07^m$ and again at $3^h\ 31^m$, Aug. 8, weak auroral echoes were observed at an extreme minimum range of 110 km.

Several distinct categories of auroral echoes were recorded and, for convenience in reference, six types have been designated by Greek letters in a classification somewhat similar to that already suggested for the meteor echoes (3). These types are listed below and typical examples are illustrated in Fig. 1.

*Continuing echoes at one or more discrete ranges, giving the appearance of a number of parallel lines—*

$\alpha$ (alpha)—steady decrease in range
$\epsilon$ (epsilon)—approximately constant range
$\delta$ (delta)—steady increase in range

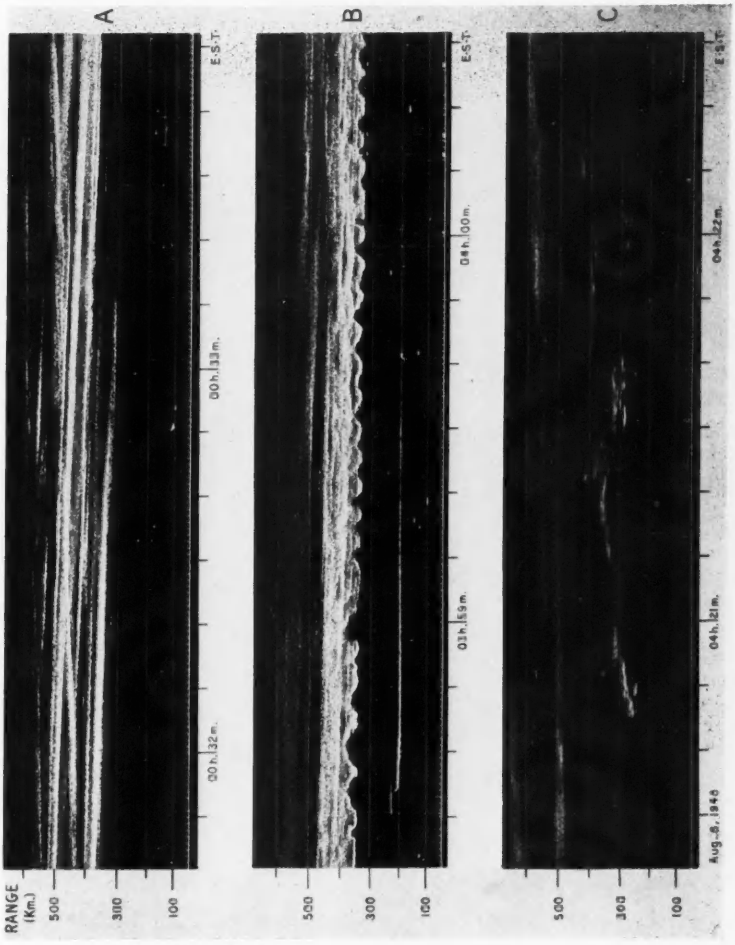


[Figure to be viewed broadside.]

Typical auroral echoes recorded at Ottawa, Aug. 8, 1948.

FIG. 1 (*A*). Radar echo type $\alpha$ with some type $\delta$. Visually a strong-rayed band was visible in the northwest at an elevation between 20 and 25 degrees.

FIG. 1 (*B*). Radar echo type $\sigma$ with some type $\alpha$. Morning twilight had masked most of the visual display by this time but a violet corona was still faintly visible between 15° and 20° south of the zenith.

FIG. 1 (*C*). Radar echo type $\kappa$ with a tendency to type $\nu$ at longer ranges. Daylight prevented visual observations.

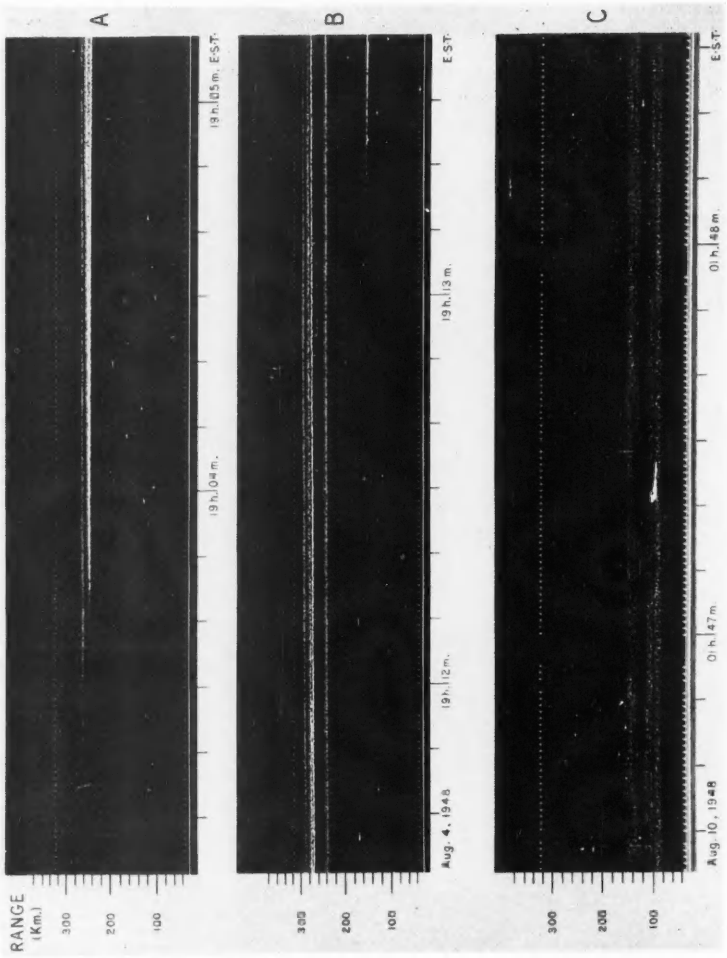


[Figure to be viewed broadside.]

FIG. 2 (*A*). Meteor echo No. 2 (see Table V). The *Ah*-characteristic, or "moving head" echo appears at $19^h\ 03^m\ 14^s$, and the various *e*-characteristic echoes appear from a few seconds to several minutes later.

FIG. 2 (*B*). Meteor echo No. 2, about eight minutes after Fig. 2 (*A*). Meteor echo No. 3, appears at $19^h\ 12^m\ 32^s$ at maximum range and decreases in range.

FIG. 2 (*C*). Ionospheric back-scatter echoes (see Table VI). As a rule the scatter echo has a minimum range between 80 and 90 km. and extends in range from 10 to 20 km. This unusual record shows the 80 km. echo extending over 30 to 40 km. in range, and a second echo, of shorter duration, appearing at 130 km. minimum range.

*Echoes giving the appearance of clumps or patches rather than parallel lines—*

$\kappa$ (kappa)—echo sharp and distinct

$\nu$ (nu)—echo diffuse and hazy

*Echoes with fairly sharp minimum ranges which vary by from 5 to 50 km. in a roughly periodic manner, giving a "scalloped" effect—*

$\sigma$ (sigma)

It is of interest to note the relative frequency with which the above echo types have appeared during the three main periods when auroral echoes were recorded. The percentage of the total period during which each echo type was visible has

TABLE I

FREQUENCY OF AURORAL ECHO TYPES

| Date 1948 | E.S.T. (hours) | Duration of period in minutes | Percentage of period during which echo type was visible | | | | | |
|---|---|---|---|---|---|---|---|---|
| | | | $\alpha$ | $\epsilon$ | $\delta$ | $\kappa$ | $\nu$ | $\sigma$ |
| Aug. 7/8 | 22.9 – 5.2 | 378 (night) | 48 | 3 | 18 | 4 | 7 | 4 |
| Aug. 8 | 16.0 – 21.8 | 348 (day) | 0 | 1 | 7 | 1 | 1 | 3 |
| Aug. 10 | 1.9 – 4.8 | 174 (night) | 47 | 0 | 20 | 1 | 1 | 3 |

been listed in Table I. Where more than one echo type was clearly evident at the same time, each type was counted in the tabulation. Because of the difficulty of accurately separating the various echo types, the results in Table I give a qualitative indication but should not be considered as significant quantitative data. It will be seen that type $\alpha$ was much the most frequent during the two night periods but did not appear at all in the day period. In the case of both the night periods type $\delta$ became relatively more frequent as the night advanced and as sunrise approached. Type $\sigma$ did not appear during the night periods before $2^h\ 45^m$ and was most frequent between $3^h$ and $4^h$.

Maximum range could not be recorded in most cases as it was beyond the display limit. Table II shows the mean minimum range for each echo type. Type $\delta$ tended to have a slightly greater minimum range than type $\alpha$. The most significant feature of Table II is the greater minimum ranges for the day period. In spite of this the mean minimum range for type $\alpha$ did not show signs of increasing as dawn approached.

TABLE II

MEAN MINIMUM RANGE OF AURORAL ECHO TYPES

| Date 1948 | E.S.T. (hours) | Mean minimum range (km.) | | | | | |
|---|---|---|---|---|---|---|---|
| | | $\alpha$ | $\epsilon$ | $\delta$ | $\kappa$ | $\nu$ | $\sigma$ |
| Aug. 7/8 | 22.9 – 5.2 | 410 | 450 | 440 | 380 | 460 | 380 |
| Aug. 8 | 16.0 – 21.8 | | 580 | 510 | 500 | 440 | 560 |
| Aug. 10 | 1.9 – 4.8 | 390 | | 420 | 400 | 450 | 350 |

It is probably unwise to attempt to draw any firm conclusions from Tables I and II because of the small quantity of observational data. However, since

auroral echoes of such detail and strength do not seem very common, it was thought advisable to put some of their characteristics on record.

The group of visual meteor observers included several experienced in auroral recording, and detailed plots and notes concerning the chief auroral formations were made throughout both night periods. Acknowledgments are due to Mr. J. M. Grant who was not only the most consistent auroral observer but who also coordinated and reduced all the visual auroral observations. On Aug. 7/8 the first visual auroral record was made at $22^h\ 26^m$ E.S.T., though probably some evidence of auroral activity was visible before this. Ray structure in the north increased in intensity and extended up to the zenith by $23^h$. At $23^h\ 10^m$ flaming aurora commenced and at $23^h\ 14^m$ a corona was visible and the general intensity of the display had still further increased. From this time till dawn rayed-bands, rays, flaming aurora, and a corona were general and were intermittently visible, in most cases with high intensity. The display extended to within 50° of the south horizon by $23^h\ 20^m$; to 30° from the south point at $23^h\ 32^m$; to 20° from the south point at $01^h\ 00^m$; and to within 10° of the south horizon at $01^h\ 50^m$. It then continued to cover most of the sky till daylight.

Astronomical twilight at Ottawa commenced at $02^h\ 53^m$ on Aug. 8 and sunrise was at $04^h\ 55^m$. Violet auroral rays were first noted at $03^h\ 17^m$ and were seen from then on as long as visual observations were possible. Dawn masked the last visible traces of the aurora at $4^h$ E.S.T. Störmer has shown that the blue and violet rays are those illuminated by the sun and that these have an average height considerably greater than the green rays lying in the earth's shadow (9, 10).

On the night of Aug. 9/10 the visual display was somewhat similar to that of Aug. 7/8 but developed more slowly and clouds seriously impaired visual observations after $01^h\ 30^m$ E.S.T. During the first half of the night auroral activity was confined chiefly to the north portion of the sky, with frequent appearance of pulsating zones, arcs, and rayed-bands. A corona appeared at $01^h\ 08^m$ and by $01^h\ 18^m$ the visual aurora extended to within 30° of the south horizon. It covered the whole sky by $01^h\ 25^m$ and for the next hour flaming aurora was visible in the gaps between clouds. The sky then became completely overcast.

Attempts to correlate the visual auroral forms with the radar echoes have not been very successful. One of the difficulties is the omnidirectional character of the radar transmission. For the night of Aug. 7/8 the altitudes and azimuths of the brighter portions of the visual aurora were computed and compared with the range and type of echo. No simple correlation could be detected. During most of the period of observation the aurora covered such a large fraction of the sky that it was impossible to tell which part of the display was causing the radar echoes. From $23^h\ 57^m$ to $00^h\ 17^m$ no auroral echo was visible within the range of the tube, and between $02^h\ 10^m$ and $02^h\ 34^m$ very little appeared. Yet during these two periods the visual aurora continued with no apparent decrease in intensity. When type $\alpha$ echo was present the brightest visual aurora was in general in or near the northwest quadrant of the sky. For the other echo types there was more of a tendency for the visual aurora to be in the north or south quadrants.

One possibly significant feature was the first appearance of the scalloped effect, type $\sigma$, at $02^h\ 48^m$ and the increase in frequency and intensity of this type until $04^h\ 02^m$. At the beginning of twilight at $02^h\ 53^m$ the top of the earth's shadow was just over 300 km. above the surface of the earth. At $03^h\ 17^m$, when the first violet rays were seen, the sun was illuminating the atmosphere down to a height of 200 km. over Ottawa. The first strong type $\sigma$ appeared at $03^h\ 18^m$ at a range of 380 km. Hence there seems to be some evidence that type $\sigma$ is connected with the violet colored sunlit rays. During the second night period, on Aug. 10, the only type $\sigma$ recorded occurred between $03^h\ 46^m$ and $03^h\ 52^m$ E.S.T.

Heights of the aurora were computed by combining the observed elevations of the brightest parts of the visual forms with the maximum and minimum ranges of the radar echoes recorded at the same time. Putting together all visual-radar heights computed gave the frequency distribution listed in Table III. These

TABLE III

FREQUENCY DISTRIBUTION OF VISUAL-RADAR AURORAL HEIGHTS

| Height (km.) | 70 | 80 | 90 | 100 | 110 | 120 | 130 | 140 | 150 | 160 | 170 | 180 |
|---|---|---|---|---|---|---|---|---|---|---|---|---|
| Frequency | 0 | 2 | 4 | 8 | 15 | 18 | 19 | 21 | 21 | 18 | 17 | 17 |
| Height (km.) | 190 | 200 | 210 | 220 | 230 | 240 | 250 | 260 | 270 | 280 | 290 | 300 |
| Frequency | 15 | 12 | 10 | 9 | 6 | 5 | 5 | 3 | 2 | 1 | 0 | 0 |

heights appear reasonable when compared with those determined by direct photographic triangulation (10). Separating the heights for various types of echoes, types $\alpha$ and $\kappa$ were lowest followed by type $\sigma$ then type $\epsilon$, and type $\delta$ was highest. Mean height for type $\alpha$ was 159 km., for type $\delta$ 183 km. This greater average height for type $\delta$ agrees with the fact that this type appeared more frequently during morning twilight and the daylight period. It should be noted that the frequency distribution of heights given in Table III is limited by the recorded radar range, e.g. 650 km., and lacks many points from the high end of the distribution. Auroral echoes frequently were seen on the monitor oscilloscope at ranges greater than 650 km.

Although, as noted above, lower powered radar stations were operated simultaneously at Arnprior and Carleton Place in addition to Ottawa, in general their range was not extended for auroral recording, and there was only one brief period, from $04^h\ 08^m$ to $04^h\ 39^m$ E.S.T., Aug. 8, when simultaneous auroral echoes could be measured at all three points. Radar triangulation of these echoes gave the results listed in Table IV. Unfortunately, the visual observations had just terminated when these echoes were recorded. The computed heights are typical for the lower ends of the sunlit auroral rays as measured by Störmer.

If the sloping echo lines of type $\alpha$ and type $\delta$ are assumed to indicate motions of approach and recession respectively then, by measuring the rate of change of range, it is possible to compute velocities in the line of sight. These represent minimum velocities of the auroral formations over the earth's surface. For the morning of Aug. 8, 28 measures of velocity gave absolute values ranging from

470 to 940 meters per sec. with a mean of 680 meters per sec. Velocities of recession averaged slightly higher than those of approach. These measures did not include the type $\epsilon$ echoes which were much less frequent and gave virtually no radial velocity.

TABLE IV

THREE-STATION TRIANGULATION OF AURORAL ECHOES, AUG. 8, 1948

| E.S.T. | Type | True height (km.) | Bearing from Ottawa | Elevation from Ottawa |
|---|---|---|---|---|
| $04^h\ 08^m\ 40^s$ | $\delta$ | 191 | 050° | 32° |
| $04^h\ 21^m\ 12^s$ | $\kappa$ | 192 | 028° | 34° |
| $04^h\ 21^m\ 20^s$ | $\kappa$ | 289 | 031° | 56° |
| $04^h\ 38^m\ 40^s$ | $\kappa$ | 201 | 350° | 32° |

Störmer has plotted the motion of auroral formations from his photographic triangulation. Taking random examples from his results for the years 1918 to 1921 (8), we find velocities ranging from 100 to 2000 meters per sec. commonly recorded, with a few cases outside this range. Aspinall and Hawkins give 23 radial velocity measures of the aurora in a paper describing their radar observations on 72 Mc. per sec. (1). All but five of these had absolute values under 1000 meters per sec. These authors conclude that the apparent radial velocities of the aurora observed by radar represent true motions of the auroral formations and this seems to be the most logical interpretation of the phenomenon.

However, the hypothesis advanced by Aspinall and Hawkins that the discrete types of auroral echoes are produced by perpendicular scattering from the long straight auroral rays does not seem to explain all cases of auroral echoes observed on 33 Mc. per sec. If the auroral rays lie along the magnetic lines of force then perpendicular scattering at Ottawa would result in ranges over 500 km. and would not explain the low-range echoes observed. This is particularly true in the case of the twilight echoes, a fair percentage of which probably arise from the sunlit rays with their bases well over 100 km. high. It seems likely that, as in the case of meteor echoes (3), auroral echoes on frequencies near 30 Mc. per sec. do not always arise from perpendicular or near-perpendicular scattering. It may be that the scattering pattern is broad enough to return appreciable energy at angles far from the perpendicular, which could account for the short-range observations. This would also explain the echoes received from aurora visible in the south. Currie and Forsyth have recently suggested an alternative mechanism where the echoing sources are presumed to be concentrated at the base of the rays and to be roughly spherical in shape with an omnidirectional scattering pattern. Each source is assumed to carry a localized absorbing region immediately below it which attenuates the echo signal when the source approaches the zenith. Qualitatively, both mechanisms yield similar scattering patterns. Our present observational data are insufficient to form any conclusions favoring the one hypothesis over the other.

On the night of Aug. 7/8, 1948, the general noise level on the display decreased about 6 db. when strong aurora was present. As the major part of the noise on

33 Mc. comes from galactic sources, rather than from terrestrial sources or from the first stage of the receiver, it seems probable that the aurora creates a general absorbing region which masks out part of the external noise. While this effect is in the right direction to support Currie and Forsyth, the magnitude of the observed absorption may be inadequate. Attenuation of the order of 50 db. or more would be needed to account for the observed reduction in auroral echo strength near the zenith.

## LONG-DURATION METEOR ECHOES

Most of the meteor echoes recorded by the Ottawa radar have durations shorter than one second. During a strong meteor shower the fraction of echoes longer than one second increases but rarely exceeds one-tenth to one-fifth of the total. The total hourly rates for all types of meteor echoes run from 150 to 2000 per hour, depending on the time of day and whether or not a strong shower is present. The number enduring for as long as five minutes is small and might average one every 24 hr. or longer. Even the brightest fireballs observed at Ottawa, some of them $-3$ to $-5$ visual magnitude, have failed to produce echoes lasting longer than six or seven minutes, although the intensity of these echoes was high. It is therefore of interest to note that in a two-hour period during the early evening of Aug. 4, 1948, six meteor echoes were observed with durations from nine minutes to over half an hour. None of these echoes was remarkably strong and only one had sufficient amplitude to appear on both the Arnprior and Carleton Place records as well. Unfortunately, since sunset occurred about midway in this period, visual meteor observations had not yet commenced.

TABLE V

LONG DURATION METEOR ECHOES OBSERVED AT OTTAWA
AUG. 4, 1948

| Meteor No. | Type[a] | E.S.T. | Duration | Initial range, km. | Final range, km. | Radial drift rate |
|---|---|---|---|---|---|---|
| 1 | *F* | $18^h\ 47^m.4$ | 15.6 min. | 235 | 270 | + 37 m./sec. |
| 2[b] | *Ahe7* | $19^h\ 3^m.2$ | 1.0 sec. (*Ah*) | 278 | 240 | − 40 km./sec. |
| | | | 18.5 min. (*e*) | 240 | 340 | + 90 m./sec. |
| 3 | *E3* | $19^h\ 12^m.5$ | 31.5 min. | > 400[c] | 240 | − 85 m./sec. |
| 4[d] | *F* | $19^h\ 30^m.9$ | 15.5 min. | 163 | 223 | + 64 m./sec. |
| 5 | *E3* | $19^h\ 45^m.7$ | 9.1 min. | 162 | 210 | + 88 m./sec. |
| 6 | *E2* | $20^h\ 18^m.8$ | 32.0 min. | 247 | > 400[c] | + 80 m./sec. |

[a] *For a glossary of echo types see Ref. (3).*
[b] *See Fig. 2 (A) and (B).*
[c] *Recorded range cut off at about 400 km., see Fig. 2 (B).*
[d] *This echo was triangulated. See text.*

In Table V some characteristics of these echoes are listed. The time of initial appearance of the echo is given, although only in the case of Meteor No. 2 is this time definitely known to coincide with the actual passage of the meteor. In the other cases the typical *E*- and *F*-type echo characteristics may have commenced several seconds or more after the passage of the meteor. Meteor echo No. 3 first appeared at the limit of recorded range and it is quite likely that it would have

been visible much sooner if the range limit had been extended. Similarly, the echo from Meteor No. 6 drifted off the record while still well above noise level. In each case the time, duration, and initial and final ranges apply to the *F*- or to the most prominent *E*-characteristic of the echo. Meteor No. 2 had in addition an *Ah*-characteristic, or an echo moving with the apparent velocity of the meteor, see Fig. 2(*A*).

The rates of radial range drift in the last column of Table V are relative to the Ottawa station. If one were to assume that the ionized cloud drifted in a straight line with constant velocity it would be possible to calculate this true drift velocity from the curvature of the echo record. However, the curvature is small and the observational errors large; furthermore the method would yield no information about the orientation of the velocity vector, i.e., the directions and magnitudes of the horizontal and vertical components.

Fortunately, Meteor No. 4 was also recorded at Arnprior and Carleton Place between $19^h\ 36^m$ and $19^h\ 44^m$, and, using the methods outlined in Reference (4), the $x$, $y$, and $z$ coordinates of the ionized cloud could be computed at selected times in this interval. The path of the drifting cloud appeared to be remarkably straight and at fairly constant height. The calculations yielded a value of $120 \pm 5$ meters per sec. for the true drift velocity in a direction from 75° east of true north. The mean height above sea level, after correction for the earth's curvature, was $117 \pm 2$ km.

There can be little doubt that these long-duration echoes are due to meteors and not to aurora or other causes. These echoes, except for the durations, are similar in every respect to thousands of well-authenticated meteor echoes in our records, and are markedly different from the auroral echoes. The appearance of the "moving head" or *Ah* echo in the case of Meteor No. 2 is fairly conclusive evidence. It is true that weak aurora was observed visually low in the north starting at $22^h\ 30^m$ but there was no sign of it at high angles, and our experience has been that a strong visual auroral display is required before the Ottawa radar can detect echoes from it. It may be a coincidence that the *Uhb* echo described in detail in a previous paper (4) occurred on the same night only an hour before this series of long-duration echoes. It may also be noted that on the following day solar radiation near 10 Å was detected on a rocket flight; this was considered to be unusual at the time this observation was reported (6).

Two hypotheses may be put forward to account for these phenomenal durations. First, the meteors themselves may have been extraordinary either in size or in physical composition. This seems unlikely as the mean echo strengths were average, and in fact many short-duration echoes occurring at the same time were of much stronger intensity. Second, conditions in the ionosphere during this period may have been abnormal. If we tentatively assume that all six of the long-duration echoes occurred at heights above 110 km., based on the measured height of No. 4, then it might be plausible to suggest that the abnormal conditions existed only above 110 km. The majority of meteor echoes occur below 110 km., with a mean about 95 km. (5). Hence, if we consider the ionosphere to have been

normal below 110 km., there is no difficulty in accounting for the numerous strong short-duration echoes which were observed at the same time.

## IONOSPHERIC BACK-SCATTER ECHO

The power of the Ottawa radar equipment was increased in July, 1948, to about 400 kw. peak, and shortly thereafter a faint semipermanent echo appeared occasionally on the records at a relatively constant range. The echo strength would grow slowly up to the receiver noise level or slightly higher at maximum, and then fade away, with durations varying from a few minutes to over an hour. The range was usually between 80 and 100 km., but at times it appeared at ranges up to 120 km., or more, and in one or two instances echoes appeared concurrently at two ranges. These observations have been informally reported previously (6, 7). An outstanding example of this type of echo is illustrated in Fig. 2 (*C*).

It is highly improbable that this echo can be a direct reflection from a ground target. A 10-ft. steel fence surrounds the Ottawa station and further attenuates the weak low-angle radiation from the half-wave dipole. No ground echoes have been seen on the meteor radar set beyond 15 km. No strong permanent echoes at 80–100 km. range have been detected during 12 years' experience in operating high-powered military radars at this station. These equipments operated on wave lengths varying from 3 meters to 1 cm., with high-gain rotating arrays beamed along the ground, and from tower heights up to 200 ft. The echo is even less likely to be due to very long-range ground or ionospheric scatter appearing on the second sweep, because a spark-wheel modulator was used which introduced a sweep-to-sweep jitter of as much as 50 $\mu$sec. Furthermore the spark-wheel was driven by a nonsynchronous induction motor so that the pulse recurrence frequency varied from 116 to 118 c.p.s. On the very few occasions that long-range ground scatter has been observed there has been no doubt of its character because the echo wanders aimlessly all over the display owing to the motor speed variation, and has a ragged edge caused by the spark-wheel jitter.

It was concluded that the constant-range echo was produced at or near vertical incidence from some source or sources in the ionosphere at heights of 80 to 100 km. Scatter from sporadic-*E* clouds was considered to be a possibility, but unfortunately the information available in 1948 from the Ottawa ionospheric station, which was operated by another agency, was too meager to afford any hope of correlation. At times the echo has appeared shortly after a large meteor echo has been recorded but the association was probably fortuitous in view of the large number of cases where very bright meteors have not been followed by the constant-range echo. Shower meteors of smaller sizes may contribute to the conditions causing the echo but this again is uncertain as it has been observed when no strong meteor showers have been present. The echo has in some instances been detected during a strong aurora, but often there has been no evidence of coincident aurora.

Table VI lists the times and durations of the more marked appearances of this echo, that is those occasions when the echo voltage reached at least one-half the

TABLE VI

OBSERVATIONS OF IONOSPHERIC BACK-SCATTER ECHOES

| Date | Time | Duration in minutes | Minimum range, km. | Echo width, km. | Maximum S/N ratio | Remarks |
|---|---|---|---|---|---|---|
| Aug. 9, 1948 | 04h 42m | 10 | 80 | 40 | 0.5 | |
| | 11h 59m | 76 | 80 | 15 | 1 | Double echo |
| | 12h 06m | 14 | 105 | 10 | 0.5 | |
| | 16h 42m | 20 | 80 | 20 | 0.5 | |
| Aug. 10, 1948 | 01h 06m | 48 | 80 | 40 | 1.5 | Double echo See Fig. 2(C) |
| | 01h 43m | 8 | 130 | 30 | 1 | |
| | 11h 46m | 18 | 80 | 15 | 0.5 | |
| | 14h 23m | 42 | 80 | 10 | 0.5 | |
| Aug. 11, 1948 | 02h 36m | 37 | 80 | 20 | 0.5 | |
| | 03h 57m | 50 | 80 | 20 | 1 | |
| | 12h 57m | 19 | 80 | 20 | 1 | |
| | 13h 26m | 24 | 80 | 15 | 0.5 | |
| | 14h 56m | 36 | 85 | 15 | 0.5 | |
| | 18h 18m | 32 | 80 | 10 | 0.5 | |
| Aug. 12, 1948 | 02h 38m | 24 | 80 | 15 | 1 | |
| | 06h 46m | 26 | 80 | 10 | 0.5 | |
| Aug. 13, 1948 | 12h 22m | 68 | 85 | 15 | 0.5 | |
| Oct. 21, 1948 | 01h 25m | 16 | 80 | 10 | 0.5 | |
| Dec. 10, 1948 | 15h 05m | 5 | 80 | 20 | 1 | |
| June 28, 1949 | 11h 42m | 28 | 90 | 10 | 1.5 | |
| | 12h 45m | 11 | 90 | 10 | 0.5 | |
| | 13h 25m | 18 | 85 | 15 | 0.5 | |

noise voltage on the display. Long-duration echoes with this signal-to-noise ratio are clearly discernible owing to the integrating characteristics of the film. These strong appearances were noted most frequently in the early afternoon hours, or the early morning hours. Many other periods have been noted when the echo was barely detectable and these have occurred at any time of the day or night.

It should be remarked that the echo was seen on the records infrequently and very weakly after the middle of 1949. Several reasons can be advanced to account for this. First, the performance of the transmitter slowly deteriorated in 1949 and 1950, until a check power measurement in 1950 showed that the peak power was down to about 100 kw. Second, in 1949 the film speed was increased to 4 in. per min. which lessened the effectiveness of the integration process. Third, the operating periods became shorter and less frequent until the radio work practically ceased in the early part of 1951. Fourth, solar activity was at a maximum in 1948 and has fallen off since. Obviously, if one were interested in pursuing the observations of this echo, the transmitter power and pulse length should be increased, receiver band width narrowed, vertical antenna gain increased, and recording conditions adjusted for maximum enhancement of the echo.

We have concluded that this semipermanent echo is caused by back-scatter from fine-structure discontinuities or turbulence in the lower ionosphere. Evi-

dence of fine-structure in the *E*-region was presented in a previous paper based on meteor observations (3). It seems highly probable that the sources responsible for this scatter echo are identical with those that are presumed to support the long-range very high frequency radio propagation reported by Bailey *et al.* (2). If so, the Ottawa observations in 1948 possibly constitute the first direct evidence of these sources.

## REFERENCES

1. ASPINALL, A. and HAWKINS, G. S. J. Brit. Astron. Assoc. 60: 130. 1950.
2. BAILEY, D. K., BATEMAN, R., BERKNER, L. V., BOOKER, H. G., MONTGOMERY, G. F., PURCELL, E. M., SALISBURY, W. W., and WIESNER, J. B. Phys. Rev. 86: 141. 1952.
3. McKINLEY, D. W. R. and MILLMAN, PETER M. Proc. Inst. Radio Engrs. 37: 364. 1949.
4. McKINLEY, D. W. R. and MILLMAN, PETER M. Can. J. Research, A, 27: 53. 1949.
5. MILLMAN, PETER M. and McKINLEY, D. W. R. Sky and Telescope, 8: 114. 1949.
6. Proceedings of the Conference on Ionospheric Physics. (July 1950). Geophysical Research Papers No. 11, p. 67, and No. 12, p. 24. 1952. Air Force Cambridge Research Centre.
7. Radio Progress During 1951. Proc. Inst. Radio Engrs. 40: 424. 1952.
8. STÖRMER, C. Geophysical Pubs. Oslo Academy. Vol. 4. No. 7. 1926.
9. STÖRMER, C. Nature, 142: 1034. 1938.
10. STÖRMER, C. Trans. Chalmers Univ. of Technol. Gothenburg, Sweden. No. 90. 1949.

# AN EXPERIMENTAL STUDY OF A DIVERGENT NUCLEAR REACTOR[1]

By J. G. Bayly

ABSTRACT

Experimental measurements of the relaxation times of a nuclear reactor were compared with the theoretical relaxation times in the range 1.6 to 186 sec. The work was done with the Chalk River Zero Energy Experimental Pile, ZEEP, in 1947, and showed that agreement within the experimental error could be obtained if the theoretical model used to represent the reactor was of the age-velocity type with a correction for the effect of the reflector.

## I. INTRODUCTION

A direct measurement of a reactor's dynamic response to a change in either the physical dimensions or the amount of neutron absorbing material in the reactor is of interest in the design of servomechanisms for controlling the pile power, and as a means of checking the accuracy of the nuclear constants involved and the theoretical formulae. The calculation of the theoretical dynamic response is simplified if the reactor shape is simple. Unfortunately the reactor available for these experiments, the Chalk River Zero Energy Experimental Pile (ZEEP), was not as geometrically simple as the model used for the calculations. The ZEEP, which has been described in the literature (9), differed from the mathematical model in that its cylindrical graphite reflector extended above and below the reacting core, and there was a bottom reflector consisting of the heavy water in the dished bottom on the tank and a graphite column below the tank. The effect of this bottom reflector could be taken into account only approximately.

When the amount of neutron absorbing material in a reactor is reduced, or the size of the reactor increased, the excess effective multiplication constant, $k_e$ (defined in the list of symbols), can be made positive, and after the initial transients have died out, the pile power increases exponentially with a period $T$. This period, which measures the reactor's dynamic response, may be measured experimentally, and may be calculated from the nuclear constants of the reactor. In these experiments, the effective multiplication constant was varied by changing the size of the reactor by adjusting the depth of the heavy water moderator.

The experimental data consisted in measurements of the period $T$ and of $\Delta h$, the difference between the maximum height of the moderator for which the reactor operates at a constant power level and the height of the moderator which made the reactor power diverge with the period $T$.

The calculated value of the period was found by first obtaining the excess effective multiplication constant $k_e$ from $\Delta h$, and finally using the theoretical relation between $k_e$ and $T$ to get the pile period $T$. Some details of these calculations are given in the next section.

[1] *Manuscript received September 23, 1952.*
*Contribution from the Chalk River Project, Atomic Energy of Canada, Ltd., Chalk River, Ontario. Issued as A.E.C.L. No. 25.*

## II. THEORETICAL RELATIONS

Since the theory of nuclear reactors is now readily available in the literature (2, 4, 10, 12), no derivations of the theoretical equations will be given here. The notation used is defined in the list of symbols.

The relation between $k_e$ and the height of the moderator may be calculated with an accuracy depending upon the mathematical model used to simulate the reactor.

As a result of the discrepancy between the experimental results and the theory available at the time, (1947), V. H. Rumsey, then of the Chalk River Laboratories, re-examined the theoretical relation between the height of the moderator and $k_e$. As shown by Rumsey (8), if the pile's graphite reflector is ignored and the neutrons are assumed to be all of one (thermal) velocity, the calculated relation will be in error by 25%. The two group model, in which the neutrons are classed as either "fast" or thermal, gives an error of 15%, while the age velocity model results in an error of about 10%. The inclusion by Rumsey of the effect of the reflector on the pile brought theory and experiment within about 3% of each other.

As applied to the ZEEP, the age velocity theory with reflector correction gives for the excess multiplication factor

$$k_e = (M^2 + 2K^2L^2L_s^2 + K^2L_s^4)\frac{\pi^2}{1.05}\left(\frac{1}{h_0^2} - \frac{1}{h^2}\right). \qquad \text{I}$$

This factor is also given as a function of $T$, the relaxation time of the reactor, by

$$k_e = \frac{\tau}{T} + c\sum_i \frac{\mu_i \tau_i}{T + \tau_i}. \qquad \text{II}$$

The nuclear constants are listed in Table I. The value of $\tau$ for the ZEEP was obtained by Gilbert and Fergusson (3). Published values of the intensities and

TABLE I

NUCLEAR CONSTANTS OF ZEEP

$M^2 = 237$ cm.$^2$ $\quad K^2 = 794 \times 10^{-6}$ cm.$^{-2}$
$L^2 = L_s^2 = 118.5$ cm.$^2$ $\quad h_0 = 147.5$ cm.
$\tau = 0.86 \times 10^{-3}$ sec. $\quad c = 8.044 \times 10^{-3}$
$\tau_m = 10$ sec.

| | $i$ | $\tau_i$, seconds | $\mu_i$ |
|---|---|---|---|
| Delayed neutron | 1 | 0.07 | 0.0317 |
| | 2 | 0.62 | 0.1078 |
| | 3 | 2.19 | 0.3065 |
| | 4 | 6.50 | 0.2705 |
| | 5 | 31.8 | 0.2113 |
| | 6 | 80.2 | 0.0323 |
| Delayed $\gamma$–$n$ reactions | 7 | 3.6 | 0.0258 |
| | 8 | 59.0 | 0.00808 |
| | 9 | 204. | 0.00277 |
| | 10 | 660. | 0.00133 |
| | 11 | 2340 | 0.000819 |
| | 12 | 8640 | 0.000923 |
| | 13 | 22680 | 0.0001275 |
| | 14 | 273600 | 0.0000407 |

mean lives for delayed neutrons (7) and photoneutrons (1, 5, 11) were used, with a correction for the gamma-ray absorption (75%) in the uranium rods. The effective height of the moderator in the reactor was found, by Johns and Sargent (6), to be 16.1 ± 0.5 cm. above the nominal level as indicated by a manometer. This correction has been applied in finding $k_e$ from equation I. The other ZEEP constants, $K^2$, $M^2$, $L^2$, and $L_s^2$, are also taken from the work of Johns and Sargent (6).

## III. TRANSIENTS

When the reactivity of a reactor is changed by changing the moderator level or a control rod position, the neutron flux density distribution must change in order to satisfy the new boundary conditions. This produces a redistribution transient which decays in the order of $4 \times 10^{-3}$ sec. Compared with the relaxation times used, this was negligibly small.

A second, and more serious transient results from the fact that the number of delayed neutrons, relative to the total neutron population, changes when $k_e$ changes. The delayed neutron transient, at a time $t$ after the pile starts to diverge, (8, 10) amounts to

$$\frac{k_e}{c} \exp -\left(\frac{c - k_e}{\tau} + \frac{k_e}{(c - k_e)\tau_m}\right)t$$

of the total neutron density.

Using the approximation $T = (c - k_e)\tau_m/k_e$, and substituting the numerical values of $c$, $\tau$, and $\tau_m$, the transient expression becomes

$$\frac{1}{1 + 0.1T} \exp -\left(\frac{9.3T}{T + 10} + \frac{1}{T}\right)t.$$

All measurements were taken at least $2T$ after the start of the pulse. Hence for $T > 2$ sec., and $t > 2T$, the transient was always $< 0.1\%$. Measurements in the range below 2 sec. were made after delays of more than $2T$ to keep the transient negligible. Thus for $T = 1.62$ sec. the delay used was 5.7 sec., so that the transient was less than 0.01%.

## IV. EXPERIMENTAL PROCEDURE

The level of the heavy water moderator was adjusted until the relaxation time was approximately 30 min. By varying the level in steps of 0.05 cm. and measuring the rate of change of the power, the critical level giving $k_e = 0$ was found by interpolation. Since the reactor had to be shut down in order to change the moderator level, each adjustment of the level took about an hour, making the accurate determination of the critical level very time consuming. For this reason the critical level was measured within ± 0.02 cm., the estimated uncertainty in reading the manometer, for only the fourth group of experiments, that in which the longest relaxation time (187 sec.) was used. For other experimental runs, the critical level was found to within ± 0.05 cm., and the correction discussed in Section V was applied.

After the critical level was determined, the reactor was shut down by a motor driven control rod and the height of the heavy water moderator was raised by

an amount $\Delta h$. The values of $\Delta h$ used are shown in Table II. To obtain reproducible results, it was necessary to keep the reactor in this condition for from 10 to 20 times the expected relaxation time.

TABLE II

| Group No. | $T$(exp.) (seconds) | $\Delta h$ (cm.) | $\Delta h$ (corr.) (cm.) | $k_e \times 10^3$ | $T$(calc.) (seconds) | $\frac{T(\text{calc.})}{T(\text{exp.})}$ |
|---|---|---|---|---|---|---|
| 1 | 8.12 | 2.33 | 2.25 | 3.48 | 7.92 | 0.975 |
| | 5.03 | 2.75 | 2.67 | 4.11 | 5.12 | 1.018 |
| | 4.50 | 2.90 | 2.82 | 4.33 | 4.49 | 0.998 |
| | 3.84 | 3.05 | 2.97 | 4.56 | 3.89 | 1.013 |
| 2 | 28.20 | 1.21 | 1.17 | 1.83 | 28.45 | 1.009 |
| | 14.57 | 1.73 | 1.69 | 2.63 | 14.40 | 0.988 |
| | 9.25 | 2.12 | 2.08 | 3.28 | 9.08 | 0.982 |
| | 6.68 | 2.42 | 2.38 | 3.67 | 6.79 | 1.016 |
| | 4.74 | 2.79 | 2.75 | 4.34 | 4.58 | 0.966 |
| | 3.58 | 3.07 | 3.03 | 4.65 | 3.66 | 1.022 |
| | 2.82 | 3.32 | 3.28 | 5.02 | 2.93 | 1.039 |
| | 2.48 | 3.47 | 3.43 | 5.24 | 2.59 | 1.044 |
| 3 | 6.41 | 2.44 | 2.45 | 3.78 | 6.41 | 1.000 |
| | 2.805 | 3.34 | 3.35 | 5.12 | 2.805 | 1.000 |
| | 2.233 | 3.61 | 3.62 | 5.52 | 2.216 | 0.992 |
| | 1.911 | 3.80 | 3.81 | 5.80 | 1.915 | 1.002 |
| | 5.85 | 2.55 | 2.56 | 3.95 | 5.75 | 0.983 |
| | 29.80 | 1.10 | 1.12 | 1.75 | 30.55 | 1.025 |
| 4 | 16.7 | 1.60 | 1.60 | 2.49 | 16.14 | 0.966 |
| | 30.5 | 1.075 | 1.075 | 1.68 | 32.25 | 1.057 |
| | 186.6 | 0.29 | 0.29 | 0.457 | 206.9 | 1.109 |
| 5 | 13.3 | 1.72 | 1.76 | 2.73 | 13.4 | 1.008 |
| | 5.86 | 2.52 | 2.56 | 3.95 | 5.76 | 0.983 |
| | 3.20 | 3.10 | 3.14 | 4.81 | 3.32 | 1.038 |
| | 2.375 | 3.47 | 3.51 | 5.36 | 2.41 | 1.015 |
| | 2.095 | 3.62 | 3.66 | 5.58 | 2.14 | 1.021 |
| | 1.99 | 3.70 | 3.74 | 5.69 | 2.02 | 1.015 |
| | 1.80 | 3.80 | 3.84 | 5.84 | 1.85 | 1.028 |
| | 1.62 | 3.91 | 3.95 | 6.00 | 1.69 | 1.043 |
| 6 | 82.4 | 0.567 | 0.567 | 0.892 | 86.2 | 1.046 |
| | 80.8 | 0.571 | 0.571 | 0.896 | 86.6 | 1.072 |
| | | | | | | Mean value 1.015 ± 0.031 |

When the control rod was removed, the multiplication constant became greater than unity and after the initial transients had died out, the power level ran exponentially, as:

$$W = W_0 \exp(t/T).$$

The time taken for the power to rise between two preselected values $W_1$ and $W_2$ was measured, and from this time and the ratio $W_2/W_1$ the experimental value $T$(exp.) of the relaxation time was found.

Since the range of values of $T$ was large, two methods of measurement were used. For the shorter relaxation times, two ionization chambers were used, one for each of the preselected power levels. When the output voltage from the more sensitive ionization chamber reached a preset level, an electronic gate circuit ad-

mitted pulses from a 500 c.p.s. oscillator to a scaling circuit. The other ionization chamber closed the gate when its output voltage reached the upper preset power level. This signal also operated a relay which reversed the electric motor sending the control rod back into the reactor, thus shutting it down. Since the oscillator frequency was constant to 0.05%, and the time between oscillator pulses was 0.002 sec., the time between the opening and closing of the gate was given by the scaler with an error of $\pm$ 0.05% $\pm$ 0.002 sec.

For measuring longer relaxation times, a galvanometer connected to a direct current amplifier and an ionization chamber were used. The galvanometer was used as a null instrument to indicate the difference between the amplifier output and an applied bucking voltage.

When the galvanometer passed through its null position, indicating that the power level was at $W_1$, a stop watch was started. The bucking voltage was increased to the value appropriate to $W_2$ and the galvanometer sensitivity was reduced in the ratio $W_2/W_1$. Thus the galvanometer passed through the null position corresponding to $W_2$ with the same velocity with which it passed the $W_1$ null position. In this way the effect of the mechanical lag of the meter was eliminated, and the stop watch, which had been stopped when the $W_2$ null was indicated, gave the time required.

The actual ratio of power levels, $W_2/W_1$, was measured in the following way. The reactor power was held constant at one of the levels, while a reading was taken on an electroscope of the intensity of the $\gamma$ radiation from the reactor. The same electroscope was used to measure the radiation produced when the reactor power was held at the other level. In each case the power had to be kept steady until the gamma-emitting fission products built up to their equilibrium concentration. The equilibrium condition was indicated by the consistency of the electroscope readings.

The lowest power level was chosen so that the delayed neutron transient (see Section III) was negligible. The highest level was determined by the safe biological tolerance. In general the ratio of power levels was approximately ten.

## V. ERRORS

The largest errors in the measurements were in the value of the critical height required to give $k_e = 0$. It was possible to apply a correction to the critical height by making use of the fact that an error in the critical height has a larger percentage effect on $\Delta h$ for the long relaxation times than it has for the short ones. Thus each set of points was corrected by adjusting the critical height for the set so that the point having the largest $T$ lay on the $\Delta h$ vs. $T$ curve for which the critical height error is least, i.e., the curve determined by experiment group No. 4.

When this correction was applied the uncertainty in $\Delta h$ was reduced from $\pm$ 0.05 cm. to $\pm$ 0.02 cm., the estimated probable error in reading the manometer. This introduces an uncertainty varying from 1.2% to 10% in $T$(calc.) for $T$ ranging from 1.6 to 186 sec.

The other sources of error were much less important. In the measurement of $T$(exp.), errors in the power ratio $W_2/W_1$ were estimated at 0.5%, and errors in the time $t$ for the power to rise from one level to the other were 0.2%. Since

$$T(\text{exp.}) = \frac{t}{\log_e(W_2/W_1)}$$

the error $dT(\text{exp.})/T(\text{exp.})$ produced by $d(W_2/W_1)/(W_2/W_1)$ was

$$\frac{dT(\text{exp.})}{T(\text{exp.})} = -\frac{1}{\log_e(W_2/W_1)} \times \frac{d(W_2/W_1)}{W_2/W_1}$$

The ratio $W_2/W_1$ was approximately 10, so that a 0.5% error in $W_2/W_1$ introduced an error of 0.22% in $T$(exp.). Combined with the similar error in $t$, the resulting probable error in $T$(exp.) was 0.3%.

## VI. RESULTS

In Table II, the experimental results are shown assembled into six groups. The members of any one group have their values of $\Delta h$ based on one measurement of the critical height, and a correction, discussed in Section V, is applied to all members of the group to give the values listed under $\Delta h$(corr.).

This table also gives the values of $k_e$, obtained from $\Delta h$(corr.) by means of equation I, and the theoretical relaxation time $T$(calc.) obtained from $k_e$ by means of equation II. The ratio of $T$(calc.) to $T$(exp.) is also shown. The average value of $T$(calc.)/$T$(exp.) is 1.015, and the r.m.s. value of the deviations from this average is 0.031.

The ratio is also shown plotted against $T$(exp.) in Fig. 1. The broken lines represent the errors predicted in Section V. The experimental results lie reasonably well within the probable errors except in the range $1.6 < T < 4$ sec., where the theoretical results exceed the experimental by about 2%. This error probably results from the approximations used in deriving equation I.

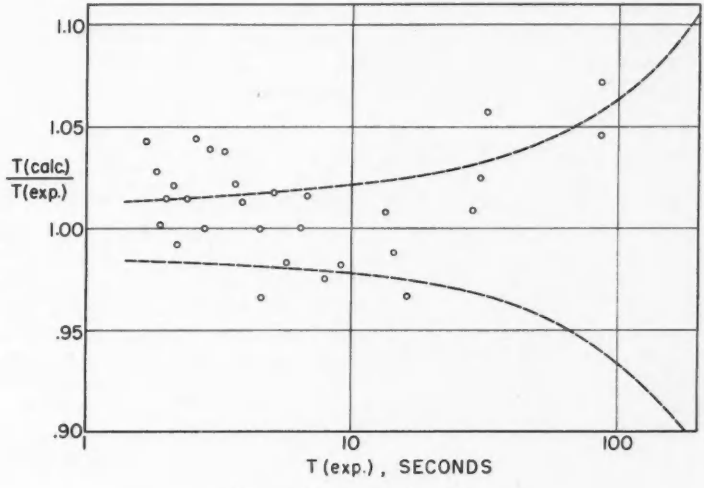


FIG. 1. Experimental results.

## VII. CONCLUSION

Agreement between the observed and theoretical dynamic response of a nuclear reactor may be expected only if the theory of the reactor is fairly complete. In the present case of a heavy water reactor with a graphite reflector, the age-velocity model for the slowing down of neutrons with a correction for the dynamic effect of the reflector was sufficient to give theoretical results in agreement with experiment.

## VIII. ACKNOWLEDGMENT

I should like to thank Dr. B. W. Sargent for several stimulating discussions and for making available some calculations of the excess multiplication constant as a function of the relaxation time.

## LIST OF SYMBOLS

$c$ the ratio of the number of delayed neutrons to the total neutron population when the reactor power has been steady for a time long compared with the greatest of the $\tau_i$.
$h$ the effective height of the core of the reactor.
$h_0$ the value of $h$ for which the reactor power remains constant.
$k_e$ the average number of fissions, minus one, produced by the neutrons from one fission.
$L$ the diffusion length of thermal neutrons.
$L_s$ the slowing down length for fast neutrons from fission.
$M^2$ the migration area of neutrons in a finite pile.
$T$ the relaxation time, or period, of the reactor.
$K^2$ the Laplacian of the reactor.
$\mu_i$ the intensity relative to $c$, of neutrons resulting from the decay of nuclei of type $i$.
$\tau$ the mean life of a neutron in the ZEEP.
$\tau_i$ the mean life of nuclei of type $i$.
$\tau_m$ the effective mean delay of all delayed neutrons.

## REFERENCES

1. BERNSTEIN, S., PRESTON, W. M., WOLFE, G., and SLATTERY, R. E. Phys. Rev. 71: 573. 1947.
2. FRIEDMAN, F. L. Science and engineering of nuclear power. Vol. 1. Addison-Wesley Press, Inc., Cambridge, Mass. 1949. p. 167.
3. GILBERT, C. W. and FERGUSSON, G. J. CRP-377, 1948.
4. HURWITZ, H. Nucleonics, 5: 61. July, 1949.
5. JOHNS, M. W. and SARGENT, B. W. CRP-416, 1949.
6. JOHNS, M. W. and SARGENT, B. W. CRP-355, 1947.
7. Plutonium Project Report. Revs. Modern Phys. 18: 513. 1946.
8. RUMSEY, V. H. CRT-372, 1948.
9. SARGENT, B. W. Science and engineering of nuclear power. Vol. 2, Addison-Wesley Press, Inc., Cambridge, Mass. 1949. p. 60.
10. SOODAK, H. and CAMPBELL, E. C. Elementary pile theory. AECD-2201. John Wiley & Sons, Inc., New York. 1948.
11. SPATZ, W. D. B., HUGHES, D. J., and CAHN, A. Phys. Rev. 72: 163. Abs. G4, 1947.
12. WIGNER, E. P. J. Applied Phys. 17: 857. 1946.

NOTE: Reports referred to in References 3, 5, 6, and 8 may be obtained from the Document Office, Atomic Energy of Canada Limited, Chalk River, Ontario.

# THE ANGULAR DISTRIBUTION OF GAMMA RAYS IN THE $C^{12}(p,p'\gamma)$ REACTION[1]

By H. E. Gove[2] and N. S. Wall


## ABSTRACT

Protons of 7.1 Mev. energy from the MIT cyclotron have been used to investigate the angular distribution of gamma rays from the $C^{12}(p,p'\gamma)$ reaction with respect to the incoming proton beam. These gamma rays result from transitions between the first excited state of $C^{12}$ at 4.45 Mev. and the ground state. The resulting distribution can be fitted by the expansion

$$I(\theta) = 1 - 0.31 \cos 4\theta$$

which is consistent with an assignment of two for the angular momentum of the first excited state of $C^{12}$.


## INTRODUCTION

Continuing the investigation of the first excited state of $C^{12}$ using 7.1 Mev. protons from the MIT cyclotron (9), the angular distribution of the 4.45 Mev. gamma ray (1) has been measured with respect to the incident beam. The measurement of the angular distribution of the inelastic protons (9) corresponding to this level contained both even and odd terms in the Legendre polynomial expansion as high as the sixth order. It was impossible to predict the spin of the excited state from these data since at least two states of opposite parity are involved in the compound nucleus. It should be remarked that the gamma distribution discussed here was taken with an incident proton energy about 200 kev. lower on the average than that for the inelastic proton distribution because a thicker target was employed.

Recent measurements (12) indicate that the angular momentum of the first excited state of $C^{12}$ is two with even parity, agreeing with the theoretical predictions of Haefner (10) based on the alpha-particle model of $C^{12}$ and with substantially all other even–even nuclei (8, 14).

The results of the present investigation are consistent with this value.

## APPARATUS

The gamma ray was detected with a sodium iodide scintillation counter employing an RCA 5819 photomultiplier and the counter arrangement is illustrated in Fig. 1. This is a slight modification of the scintillation spectrometer used for heavy charged particles (16).

The counter was mounted on one of the movable arms in the MIT scattering chamber (5). The associated electronics consisting of a preamplifier, linear amplifier, single channel analyzer, scaler, and stabilized high voltage supply have been previously described (16). The sodium iodide crystal which was cleaved from a

[1] *Manuscript received October 21, 1952.*
*Contribution from the Laboratory for Nuclear Science and Engineering, Massachusetts Institute of Technology, Cambridge, Massachusetts. This work has been supported in part by the joint program of the O.N.R. and the A.E.C.*
[2] *Now at Atomic Energy of Canada Limited, Physics Division, Chalk River, Ontario.*

larger piece was approximately a one-half inch cube. The target used was a 0.004 in. thick polyethylene sheet and it was bombarded with 7.1 Mev. protons from the MIT cyclotron.

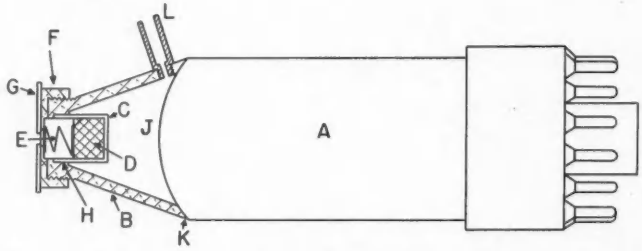


FIG. 1. Diagram of the sodium iodide gamma counter. The sodium iodide crystal (*D*) is held against the bottom of the glass container (*C*) by a dural leaf spring (*E*). The glass container is held to the aluminum reflector (*B*) by "Duco" cement (*H*) while the reflector itself is held to the tube (*A*) by "Ambroid" cement (*K*). The volume of the reflector is filled with DC-703 silicone oil (*J*) through a spout on the top (*L*). A lead diaphragm (*G*) is fastened to the aluminum end cap (*F*).

## EXPERIMENTAL PROCEDURE

The gamma-ray spectrum from the reaction $C^{12}(p,p')C^{12*} \rightarrow C^{12} + \gamma + 4.45$ Mev. is shown in Fig. 2. This was measured with a Los Alamos single channel analyzer (13) and was checked at several angles with no detectable differences in shape occurring. For all angles of the detector the target was fixed with its surface perpendicular to the incident proton beam.

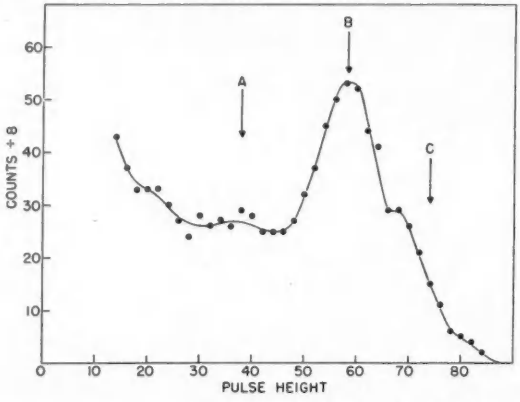


FIG. 2. The gamma-ray spectrum from the $C^{12}(p,p'\gamma)$ reaction. *B* indicates the pair production peak in which both annihilation quanta escape. *C* indicates the Compton edge and *A* shows the setting of the lower gate on the discriminator used for measuring angular distributions.

The spectrum is unusually simple since only one gamma ray is emitted from the target at this bombarding energy. The main peak *B* in Fig. 2 is the pair production peak of energy 3.43 Mev. in which both of the annihilation quanta

escape and the section of the spectrum designated as $C$ is the Compton edge. Between $B$ and $C$ is the region in which a peak of energy 3.94 Mev. corresponding to the escape of one of the annihilation quanta would occur. This, and the maximum energy of the Compton electrons, probably accounts for the bump on the side of the main pair peak. There is a slight indication of a peak corresponding to the full energy of 4.45 Mev. from the photoelectric effect and pair formation where both annihilation quanta are absorbed. This spectrum is similar to the one obtained by Bell and Jordon using a Po–Be source (2).

To measure the angular distribution the upper gate on the single channel analyzer was removed and the lower gate set below the pair peak at $A$ in Fig. 2. The analyzer then passes all pulses greater than the lower gate.

The counting time was determined by a double proportional counter monitor mounted on the lid of the scattering chamber which viewed the target at 30°. This monitor detected, principally, elastically scattered protons from the target and was set to count $2^{13}$ particles for each experimental point taken on the angular distribution. The average number of pulses counted above the lower gate during this monitor time was about five thousand. Fractions of a count on a scale of 128 were not recorded. From this, one would expect a standard deviation in the data of 3%.

Background was constant at all angles greater than 20° and had an average value of 4%. For angles smaller than 20° it rose rapidly owing to the proton beam striking parts of the detector. Because of this, the minimum angle at which the gamma-ray intensity could be measured was 17°.

The position of the beam on the target was measured by bombarding a piece of photographic film placed in the target holder. The resulting discoloration gave a clear indication of the spot size and position. The entry slit could be adjusted until the spot coincided with the center of rotation of the detector. The main intensity of the beam was confined to an area on the target $\frac{1}{8}$ in. wide and $\frac{3}{8}$ in. high. The solid angle of the detector was approximately $4 \times 10^{-2}$ steradians.

The zero angle position was determined in two ways. First, the proton counter was moved into the proton beam and the resulting gamma-ray intensity was measured as a function of angle near zero. For this purpose a lead disk $\frac{1}{32}$ in. thick was placed over the end cap of the detector as shown in Fig. 1. This disk had a $\frac{1}{8}$ in. diameter hole through its center. Protons striking the lead produced relatively few gamma rays but those passing through the hole struck the aluminum cap resulting in a large gamma-ray production. The resulting intensity distribution was a sharp peak with a width at half maximum of about five degrees. The zero angle could be determined to an accuracy of $\pm$ 0.5°. The second and perhaps more fundamental method of determining the zero angle position was to measure the gamma-ray distribution from the target on both sides of the beam. This also served to check the symmetry of the experimental arrangement. The results of both methods were in good agreement.

The gamma-ray intensity was measured every 4°.5 from 16°.7 to 151°.7 on one side of the beam and from 19°.4 to 82°.4 on the other. At each angle the background was checked by removing the target from the beam and counting

for the average time of the two runs at that angle. This assumed that the beam intensity remained constant and this could be checked by observing the beam current collected in a Faraday cup and measured with an RCA ultrasensitive microammeter.

## RESULTS

The resulting distribution is shown in Fig. 3. The solid circles represent points taken from 16°.7 to 151°.7 on one side of the proton beam and the crosses those taken from 19°.4 to 82°.4 on the other side. It appears that within the statistical fluctuations, the zero angle has been determined correctly and the distribution is symmetric about zero.

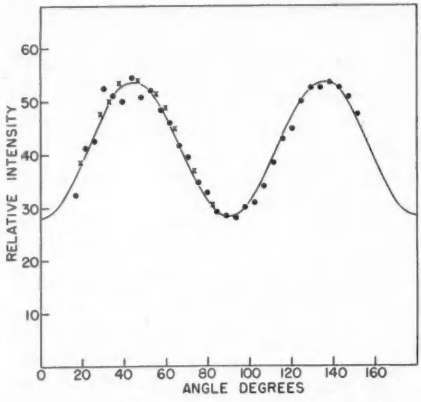


FIG. 3. The angular distribution of the gamma ray from the $C^{12}(p,p'\gamma)$ reaction with respect to the direction of the incident proton beam. The solid circles are experimental points measured on one side of the beam and the crosses those measured on the other side. The solid curve is proportional to $1 - 0.31 \cos 4\theta$.

Since the distribution is also symmetric about 90° it can be fitted by an expansion of even-order Legendre polynomials or even powers of the cosine. In fact it can be represented most simply by the expression

$$I(\theta) = 1 - 0.31 \cos 4\theta.$$

This is also equivalent to the expansions

$$I'(\theta) = 1 + 3.6 \cos^2\theta - 3.6 \cos^4\theta,$$

$$I''(\theta) = P_0 + 0.23\, P_2 - 0.56\, P_4.$$

The solid curve in Fig. 3 is a plot of these equations.

## DISCUSSION

General treatments of charged particle-induced gamma-ray angular distributions have been developed recently. In particular, the gamma–gamma angular correlation and the angular distribution of each gamma ray in the $(p,\gamma_1\gamma_2)$ process has been discussed by Biedenharn, Arfken, and Rose (3). A general treatment of the $(p,p'\gamma)$ process in which the angular distribution of the gamma

ray alone is observed has been developed by Hittmair (11). A review of angular correlations in nuclear reactions has been presented by Deutsch (7). Expressions for the angular distributions of pure multipole radiations are given by Blatt and Weisskopf (4) and Condon and Shortley (6).

It has been pointed out by Sharp (15) that the general expression for the angular distribution of the gamma ray in the $(p,p'\gamma)$ process obtained by Hittmair (11) contains only even powers of the cosine in cases where a single multipole radiation of even order is emitted, regardless of whether states of different parity are involved in the compound nucleus. As usual, the maximum power of the cosine which can occur is twice the multipole order or twice the angular momentum of the initial state in the gamma transition—whichever is smaller. The situation for the case in which states of different parity are involved in the compound nucleus and in which the multipole order of the gamma transition is odd is similar.

The radiative transition dealt with in this experiment is known to occur between a state of angular momentum $J$ and one of angular momentum zero, hence the only multipole order allowed is $J$. Since the angular distribution contains only even powers of the cosine with four the highest power, it is consistent with an angular momentum $J = 2$ for the first excited state of $C^{12}$ and excludes the possibility of $J = 1$.

## ACKNOWLEDGMENTS

It is a pleasure to acknowledge the advice and assistance of Mr. H. F. Stoddart and other members of the staff of the MIT cyclotron. The stimulating and instructive discussions with Dr. W. T. Sharp and Dr. L. G. Elliott of Atomic Energy of Canada, Ltd., were very helpful.

## REFERENCES

1. AJZENBERG, F. and LAURITSEN, T. Energy levels in light nuclei. To be published in Revs. Modern Phys.
2. BELL, P. R. and JORDON, W. H. Phys. Rev. 79: 392. 1950.
3. BIEDENHARN, L. C., ARFKEN, G. B., and ROSE, M. E. Phys. Rev. 83: 586. 1951.
4. BLATT, J. M. and WEISSKOPF, V. F. Theoretical nuclear physics. John Wiley & Sons, Inc., New York. 1952. Chapter XII.
5. BOYER, K., GOVE, H. E., HARVEY, J. A., DEUTSCH, M., and LIVINGSTON, M. S. Rev. Sci. Instruments, 22: 310. 1951.
6. CONDON, E. U. and SHORTLEY, G. H. The theory of atomic spectra. Cambridge University Press, London. 1951. Chapter IV.
7. DEUTSCH, M. Reports on Progress in Physics, 14: 196. 1951.
8. GOLDHABER, M. and SUNYAR, A. W. Phys. Rev. 83: 906. 1951.
9. GOVE, H. E. and STODDART, H. F. Phys. Rev. 86: 572. 1952.
10. HAEFNER, R. R. Revs. Modern Phys. 23: 228. 1951.
11. HITTMAIR, O. Phys. Rev. 87: 375. 1952.
12. HUBBARD, T. P., NELSON, E. B., and JACOBS, J. A. Phys. Rev. 87: 378. 1952.
13. JOHNSTONE, C. W. Los Alamos (Drawing No. 4r-26323).
14. SCHARFF-GOLDHABER, G. Phys. Rev. 87: 218A. 1952.
15. SHARP, W. T. Physics Division, Atomic Energy of Canada Ltd., Chalk River, Ont. Private communication.
16. STODDART, H. F. and GOVE, H. E. Phys. Rev. 87: 262. 1952.

# FRONTAL PRECIPITATION AND LIGHTNING OBSERVED BY RADAR[1]

By J. S. Marshall

ABSTRACT

A typical pattern (revealed by radar) of precipitation along a cold front includes both showers containing many nearly vertical cells, and continuous rain characterized by uniformity below the freezing level and the "bright band" of melting snow at that level. Observations in vertical section were made by scanning at angles of elevation up to 30°. At wave length 3 cm., observations of this sort reveal some of the snow above the bright band, and its trailing pattern. At 10.7 cm., little is seen of the snow, but transient echoes with duration of the order of one second are observed, attributable to lightning. These echoes have not been detected when scanning in the vertical at wave length 3.2 cm., although others have reported something of the sort at 3.2 cm. when different observing techniques were used. The transient echoes occur outside, but close to, regions of rain; most frequently about one mile from the top of a shower cell. It is probable, combining 3.2 cm. observations of snow on one occasion with 10.7 cm. observations of the transients on another occasion, that the transients occur in regions not only near rain, but at the same time in or near a region filled with snow.

## 1. THE PLAN VIEW

The most impressive precipitation patterns revealed by radar in the Ottawa–Montreal region tend to be those of cold-front passages. Figs. 1, 3, and 5 show

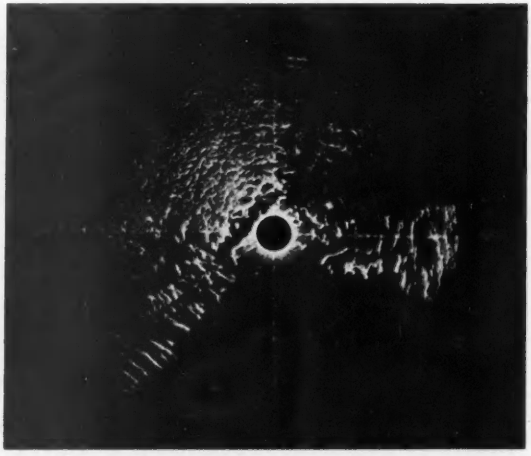

FIG. 1. Plan View (P.P.I.) obtained by holding the beam just above the horizon and rotating it about a vertical axis. A single revolution lasting 15 sec. has been photographed. The range-marking circles are at 20 and 40 miles. North is at the top of the picture.

the situation of July 5, 1948, as recorded by a height-finding radar* at Ottawa. It was noted at the time that the records contained transient echoes of special

[1] *Manuscript received October 15, 1952.*
*Contribution from the Macdonald Physics Laboratory, McGill University, Montreal, Que.*
**Radar specifications: wave length 10.7 cm., peak power 200 kw., pulse length 1 μsec., p.r.f. 300 sec.$^{-1}$, beam 8° horizontal × 1½° vertical, polarization horizontal.*

interest, but the reporting of these echoes was delayed in the hope of obtaining corroborative observations on 3.2 cm. equipment now in use at Montreal.

Fig. 1 is a photograph of the Plan Position Indicator taken at time 2017 E.S.T. Until about an hour before this time, the radar had shown only scattered air-mass showers or moderate thunderstorms. The synoptic situation was one of a warm front, broad and diffuse at the surface, lying quasi-stationary. Apparently at about 1900 hours the portion of the front near Ottawa began to move southward as a small cold front. The motion of the front as a cold front was indicated first by the radar pattern, and then following the thunderstorms by a drop in the temperature and dew point at Ottawa (between 2030 and 2130 E.S.T.). Estimated winds and temperatures over Ottawa at 2300 E.S.T. are shown in Fig. 2.

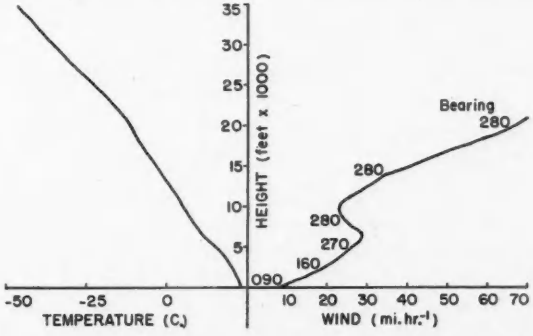


FIG. 2. Approximate temperatures and winds aloft at 2300 E.S.T., July 5, 1948.

The Plan Position indicator shows, as is typical of a cold-front passage, a line of shower activity extending from southwest to northeast. In advance of the frontal line of showers there is a cluster of intense showers, while behind the line is an extensive region of continuous rain. The cluster, and presumably the individual showers forming the line, moved out of the west at about 23 miles per hour, or with the velocity of the wind somewhere near the freezing level.

The pebbly character of the continuous-rain echo in Fig. 1 does not indicate a texture of this sort in the rain itself. It arises from the essential nature of radar echoes from a large number of incoherent sources or scatterers (the raindrops). The average signal intensity can be correlated fairly closely to the intensity of the precipitation, but the instantaneous value is a randomly varying quantity with a standard deviation about the mean value that is equal to the mean value. (Rain echo when the pulse length is $\tau$ is similar to resistor noise when the circuit band width is $1/\tau$.) The linear scale of the pebbling is determined by the distance along the picture to an independent signal. Radially, this distance is $\tau/2c$, where $\tau$ is the pulse length, and $c$ the velocity of light, or 0.093 miles in this case. Tangentially, it is $r\theta$, where $r$ is the range, and $\theta$ the beam width. The beam width in this case was 8°, and so the corresponding scale value is $r/7$, or 1.4 miles at 10 miles. Thus, at range 10 miles, there should be a factor of 15 between the scale of

the "continuous rain" pattern radially and tangentially. Apart from this anisotropy, which is readily discernible, the pattern in the region of continuous rain is very similar to that of the general gray background, which is due to assorted circuit noises.

This pebbled pattern inherent in radar echoes from precipitation can be smoothed out by averaging several independent data at each point, that is, by superimposing several consecutive scans of the areal display on a single photograph* (Fig. 6). The pebbled pattern is not observed to the same extent in the showery portions of the pattern. Most likely, this is because of the sharp edges of the shower pattern, the signal jumping suddenly at the edge of the shower from zero to a value well above saturation. It just might be, alternatively, that the more rapid shuffling of the raindrops by turbulence in the showers provides a larger number of independent data and thus reduces the pebbling or graininess. The shower echoes do suffer from another sort of distortion, however, owing to the properties of the circuits of the particular radar used. The circuits become blocked by sudden strong signals, so that every sudden rise to saturation is followed by a period of zero sensitivity when not even the normal gray of the background is recorded.

## 2. VERTICAL SECTIONS

Vertical sections through the region of precipitation are shown in Fig. 3. The radar scanned upward from the horizontal to elevation 30° in eight seconds, down to horizontal again in an equal time, and a time-exposure photograph was taken of each eight-second scan. In Fig. 3*a* the advance thunderstorm is shown on bearing 88° at time 1946 E.S.T. It rises to heights greater than 30,000 ft. The individual cells are very confused in this section, and tilted as much as 45° from the vertical. (Of this tilt, about 9° is due to distortion in the radar picture.) The line of shower activity, observed on bearing 200° at time 2034 E.S.T. in Fig. 3*b*, is approximately 25,000 ft. high. It is less intense, as indicated by the smaller regions of circuit blocking, and somewhat less confused.

A vertical section through the continuous precipitation (bearing 290°, time 2023 E.S.T., Fig. 3*c*) is entirely different. The intense horizontal band at height 10,000 ft. comes approximately at the zero-degree isotherm or freezing level, and is attributed to relatively intense echo from melting snow, while the continuum of echo from that height down to the ground is the somewhat less strong signal from rain, very nearly constant with height. (The weakening of the signal toward the ground at great range is attributable to a weakening of the radar beam by the screening effect of trees and so forth at low angles of elevation.) Again the pebbly pattern does not indicate any such pebbling in the distribution of rain in space.

The region above the bright band is presumably filled with snow that is not being detected by the radar. The signal from snow is known to be somewhat less than that from rain of the same intensity or rainfall-rate (3). There is also a possibility that the radar signal is weakened appreciably in passing through the

**A report has been prepared and will be published shortly giving a comprehensive theoretical treatment of this pebbling and of means of smoothing it.*

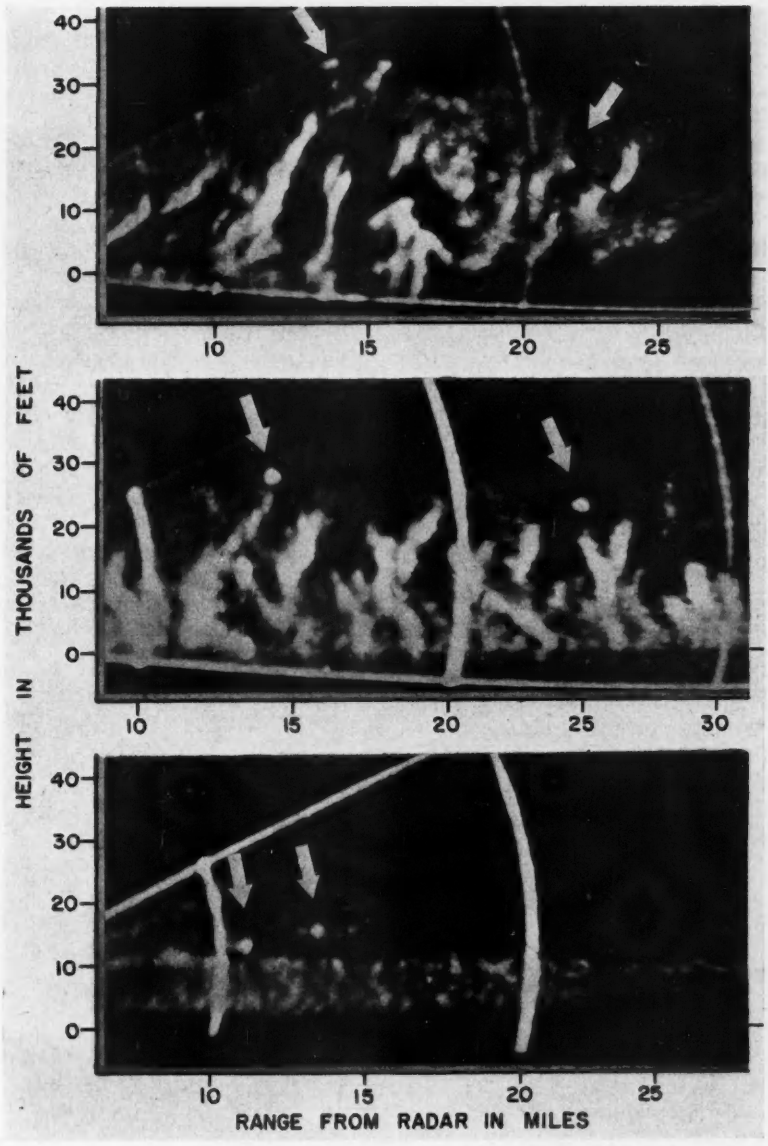


FIG. 3. Vertical sections of the precipitation pattern: (*a*) the "advance" thunderstorm, (*b*) the "frontal line" showers, (*c*) the continuous rain. Lightning echoes are indicated by arrows.

melting snow of the bright band, especially when the transit through that band is so oblique as to make the distance of that passage several times the thickness of the band.

## 3. LIGHTNING ECHOES

The observed pattern of a thunderstorm will change considerably in as little as a minute. On the day under discussion, the patterns were rather confused and more rapidly changing than usual. A study of the pictures revealed a transient form of echo, each echo or echo pair appearing on just one scan in all but one case, and therefore having a lifetime of less than eight seconds. Such echoes could hardly be attributed to precipitation even in this rapidly changing situation. In the presence of considerable electrical activity, it seems fair to attribute these echoes to regions of ionization or of heated air created suddenly by lightning.

The radar was equipped with two displays for use with vertical scanning, one recording height against range, and the other angle of elevation against range. Both displays were photographed and both sets of photographs contained the same transient echoes. Their appearance on the height/range display is shown in Fig. 3, where the sample pictures of the different sorts of rain echo were selected to include in each case a transient echo. In the sequences of shower pictures where these transient echoes were observed, there was approximately one transient per five pictures. In the case of continuous rain, transient echoes were very much less frequent.

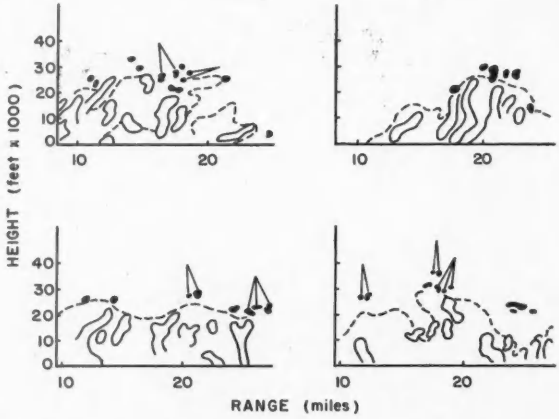


FIG. 4. All lightning pictures from a five-minute sequence are superimposed on a general sketch of the precipitation pattern during that sequence. Pairs and groups of three echoes that occurred simultaneously are indicated by joined straight lines. A broken line outlines the precipitation, while cells of dense precipitation are shown in outline. Change in the precipitation pattern during a five-minute sequence is considerable.

In Fig. 4, all transient echoes from each of four short sequences of pictures (sequences lasting five or six minutes) have been drawn in against a single pattern of the rain echoes fairly representative of the rain distribution for the duration

of that sequence. The most probable height of all 32 transient echoes is 30,000 ft. (temperature − 40°C.), while 75% of them come between 25,000 and 35,000 ft. (temperatures − 23°C. and − 49°C.).

In general, the height of the transient echo is related to the height of the neighboring precipitation echo. It is almost as likely to be to one side of a cell-top as directly above; and the average distance from cell-top to transient echo is about 4000 ft. "Cell-top" for the purpose is the cell-top observed by radar, and is thus the top or almost the top of a column of precipitation. This precipitation is presumably contained within a cumulo-nimbus cloud, and the water cloud may extend to greater heights than the precipitation. The radar does not reveal specifically whether the precipitation it records is rain, snow, or a mixture of both. While both rain and snow are reported by aircraft flying through thunderstorms at these heights, the nature of the radar cell-tops suggests that they are composed of rain or rain and hail, and surely not of snow alone. In the one case recorded on

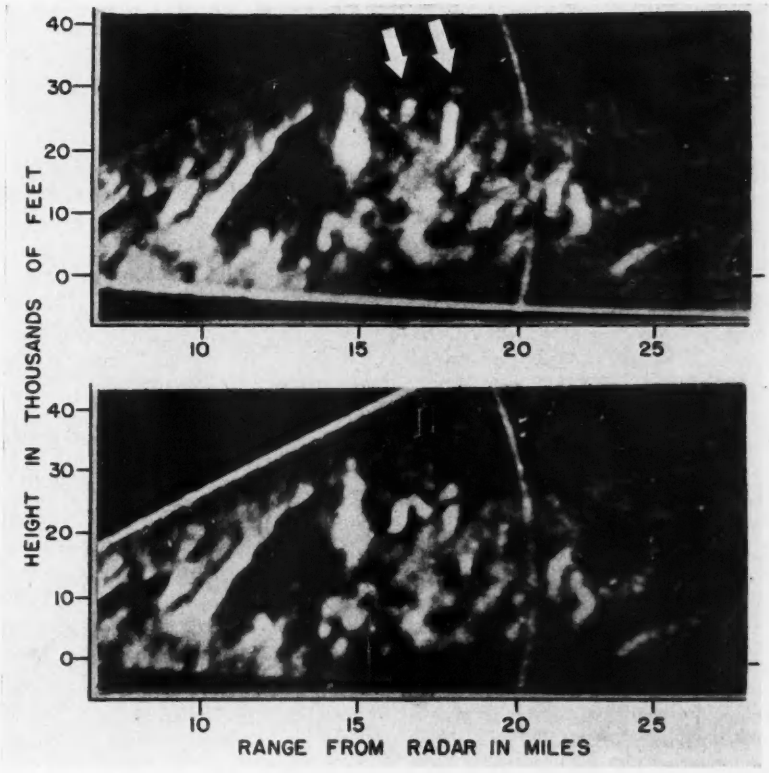


FIG. 5. Persistent or recurrent lightning echoes appear on these consecutive eight-second photographs, the two lightning "blobs" of the earlier member reappearing more intense and joined in the later member.

this day of transient echoes in a region of continuous precipitation (Fig. 3*c*) the components of the transient were above but within 5000 ft. of the bright band, i.e. were in a region of snow close to a region of melting snow and rain.

The one case of a transient echo persisting and developing from one picture to the next is shown in Fig. 5. In the first picture, two transient "blobs" can be seen which were not in the preceding picture taken eight seconds sooner. In the second picture, it seems to be these two blobs that are joined by a curved line of varying thickness. One picture was photographed scanning through decreasing elevation, the other through increasing elevation. The time separation at the particular elevation of these echoes is thus not exactly eight seconds, but is of that order (probably either 5 or 11). It seems more likely that the original echoing regions persisted, rather than appearing for a fraction of a second for the first picture and reappearing at just the right moment for the second picture. There is this indication, then, that echoes of this sort may persist for several seconds. The failure of any other of the echoes to be seen in successive pictures indicates more strongly that most of the echoes have a duration of less than five seconds.

Most of the transient echoes are strong enough to produce the "blocking" in the circuits described earlier. Their size as recorded suggests that they are larger than the resolution limits of either the radar pulse or the radar display, with an average linear dimension of roughly 2500 ft. and a ratio of maximum to minimum dimension seldom exceeding 2 to 1. This refers to a single echo. In the persistent case of Fig. 4, there were two such echoes which were subsequently joined. While this was the only persistent case, there were eight other cases of paired echoes, with separations between centers averaging about 4000 ft., or the same as the separation of cell-top to echo. Two cases with separations of 6000 and 9000 ft. involved more than two echoes, so that the separation between adjacent members never exceeded one mile.

## 4. OTHER REPORTS OF LIGHTNING ECHOES

Ligda (1) reports the observation of radar echoes from lightning by Sweeney and Peterson in 1945 and his own recording of them photographically and using a pulse integrator in 1949. Ligda observed such echoes on both 10.7 and 3.2 cm. wave lengths. To observe them, he directed the radar beam at the tops of storm cells. The extent of the lightning echoes in range was as small as one and one-half miles and on occasion as great as eight miles, with several different peaks in the latter case. The duration on an A-scope was comparable with the reaction time of the scope photographer, presumably of the order of 0.2 sec. On the "pulse integrator" records, where the averaging of 100 pulses gives enhanced discrimination against the random background of precipitation echo, the lightning echoes appear to increase rapidly in strength for a small fraction of a second to 10 times the amplitude of the background, then decay exponentially, returning to the level of the background in from one to five seconds. (This is the present writer's interpretation of the published record.)

Miles (4) reports observations in Southern Rhodesia at 10 cm. with a vertically-directed beam. He recorded intense echoes which occurred simultaneously with

lightning flashes. In the case that he has used to illustrate his brief advance note, the lightning echo extended from 26,600 to 28,500 ft. for a duration of 0.39 sec., while in the published photograph, the precipitation as recorded at wave length 10 cm. appears to extend to height 21,500 ft.

The echoes observed by Ligda, those by Miles, and those reported now seem to be all the same thing. Each of the three sets of observations taken by itself indicates strongly that the echoes are related to lightning, while Miles' report that the echoes are simultaneous with lightning flashes would seem conclusive on this point.

## 5. OBSERVATIONS AT WAVE LENGTH 3.2 CM.

The program of observations at Ottawa was terminated in 1948. Similar observations in vertical section have been made for the past four years in the Montreal region, using a wave length of 3.2 cm. It was expected that similar transient echoes would be observed, and that the faster scanning rate of twice a second would give a better indication of the duration of such echoes. Although similar weather situations have been observed, there has been no indication of any transient echo. On the other hand, the 3.2 cm. equipment with its somewhat greater sensitivity to precipitation has revealed the snow above the bright band in the echoes of continuous rain.

Fig. 6 shows a vertical section through frontal precipitation as observed on the 3.2 cm. equipment at 1930 E.S.T., August 3, 1951. The picture has been chosen

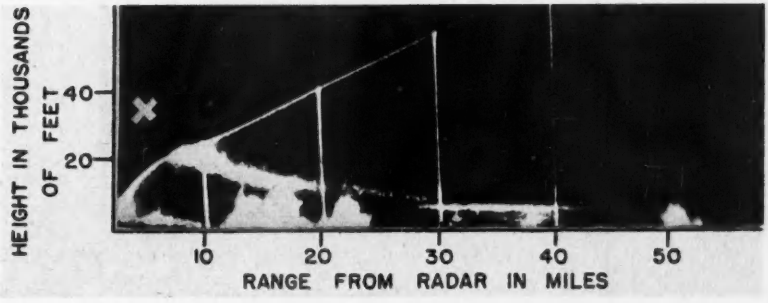


FIG. 6. Situation similar to that of Figs. 1 and 3 observed by 3 cm. radar located ahead of the front and looking back through the showers at the continuous rain beyond. The snow that melts to continuous rain can be seen to originate ahead of the showers (estimated position marked ×) and to trail back through the shower region before melting to rain.

to resemble the one that would have been obtained on July 5, 1948 by a radar sufficiently sensitive to detect the snow that melts to continuous rain in the bright band. Discussing it in that sense, as an approximation to the correct picture for July 5, 1948, the radar should be imagined as located east of the precipitation and looking to the west, so that east and west are at the left and right respectively of Fig. 6. Snow is being generated continuously at height greater than 20,000 ft., at range less than 10 miles from the radar. The "continuous generating cell" in which the snow forms is somewhere above the oblique upper edge of the radar

picture. The snow falls into less rapidly moving air and so trails behind the cell. The slope of the snow trail at any height is the ratio of the rate of descent of snow through air to the wind at that height relative to the wind at the height at which the snow was generated (2). The slope at the height of the freezing level may be as small as 1 in 20 or even 1 in 50. Most important to the present discussion, the snow generating cells tend to be high above the freezing level and 20 to 50 miles east of the region of the continuous rain for which they are responsible.

Cumulus clouds lying to the east of the region of continuous rain may be expected to rise into snow-filled air. Entrainment of the snow into the sides of the rising cloud could be the precipitation agent that converts the cumulus cloud to a shower. Differences in potential between the snow that has fallen from a greater height and cloud and rain that has come up from below may have something to do with the occurrence of the lightning around the cell-tops that is observed by the 10.7 cm. radar.

Since the showers that appear at ranges 10-24 miles in Fig. 6 scarcely reach the snow trail, it is not likely that they are seeded by it. There is a likelihood, though, that some electrical interaction is occurring between the shower tops and the snow trail, but that any echoes so created at wave length 3.2 cm. are too weak to be detected against the fairly intense background of echo from snow and rain.

The snow trails for the case of July 5, 1948, cannot be drawn in reliably because while the upper winds are known, the height at which the snow was generated is not. The pattern of snow trails may have been more diffuse than in Fig. 6. But almost certainly the region around the shower tops contains snow, either patterned in well defined streaks or distributed somewhat more generally.

The general problem of interaction between the obliquely falling snow of the continuous rain mechanism and the towering columns of water cloud and precipitation of the shower mechanism is probably a topic calling for further consideration. The two precipitation patterns move with winds at different levels, so that there should be in general a continually changing relationship between them.

## 6. CONCLUSIONS REGARDING LIGHTNING ECHOES

All the lightning echoes observed seem to be in regions free of precipitation of such intensity as to be detected by the 10 cm. radar. To judge by observations of similar situations by 3 cm. radar, they are all in snowfall regions. It is not clear, however, whether the snow is present as a continuum, or in streaks; thus it could be that the transient echoes come from clear-air gaps between shower precipitation and snow trails. All the lightning echoes associated with showers (or at least one member in the case of a pair) were within about one mile of the top of a column of intense rain or mixed precipitation. The one case associated with continuous rain was in snow and within 5000 ft. of the bright band of melting snow and rain at the freezing level. No such transient echoes have been observed on our 3 cm. equipment, which was more sensitive to precipitation than the 10 cm. equipment. In this connection, it should be noted that sensitivity to precipitation varies inversely as the fourth power of the wave length. It may be that similar transient echoes at 3 cm. were obscured by reflections from snow in the same

region. Similarly, of course, it could be that the 10 cm. pictures contain similar echoes at lower heights, but that these are obscured by the rain echoes. Since the transient echoes at 10 cm. are obviously intense, this does not seem very likely.

Lightning echoes on 3 cm. radar have been reported only by Ligda, using equipment of very high power. It seems probable that the echoes at 3 cm. are weak compared with those from moderate snow, while on 10 cm. they are strong compared with moderate rain. While sensitivity to precipitation is inversely proportional to the fourth power of the wave length, that to lightning would appear to increase more gradually with decreasing wave length, or possibly to decrease.

Regarding duration, the three sets of observations discussed seem to be in agreement as to the time being not less than 0.2 sec. There would be no conflict in any of them with the interpretation that we have placed on Ligda's "pulse integrator" record, of signals rising suddenly, then dying away gradually so that a small fraction of the peak echo strength persists even after several seconds.

## 7. ACKNOWLEDGMENTS

The observations of July 5, 1948, were part of a program conducted by the Defence Research Board's Radio Propagation Laboratory that summer. They were made on a height-finding radar built by the National Research Council and located at the Radio Field Station of the Council's Division of Radio and Electrical Engineering. The 3-cm. picture was obtained on August 3, 1951, at the McGill University Radar Weather Observatory, Montreal Airport, which is supported by grants (Grant No. 99, Project No. D 48-95-11-08) and loans of equipment from the Defence Research Board. Upper air and synoptic information, considerably in excess of that included here, was derived by R. H. Douglas and A. S. Dennis from Meteorological Division (Department of Transport) charts.

## REFERENCES

1. LIGDA, M. G. H. Bull. Am. Meteorol. Soc. 31: 279. 1950.
2. MARSHALL, J. S. J. Meteorol. 10: February. 1953.
3. MARSHALL, J. S. and GUNN, K. L. S. J. Meteorol. 9: 322. 1952.
4. MILES, V. G. Nature, 170: 365. 1952.

# THE DETECTION OF POLARIZED $\gamma$ RADIATION BY THE COMPTON PROCESS[1]

By N. R. Steenberg

ABSTRACT

The general relationship between the polarization vector describing partially polarized $\gamma$ radiation and the effects measurable by scattering experiments is presented. The results are applied to the radiation emitted by nuclei aligned at low temperatures and some experimental results are predicted.

## 1. INTRODUCTION

Interest in the question of polarized $\gamma$ radiation has arisen in connection with experiments on the alignment of nuclei at very low temperatures. Nuclei so aligned have been observed to emit $\gamma$ radiation anisotropically (2). Such radiation can be expected to be partially polarized. The degree of this polarization has been calculated by the author (6) and is given in terms of the components of a polarization vector, **P**, introduced by Fano (3). The purpose of this paper is to show, in general, how the components of **P** are related to effects which are measurable with polarization sensitive detectors. The results are then applied to two particular cases which are of experimental interest.

It is concluded that the experimental method used in (2) should produce a clearly observable effect due to plane polarization. The detection of circularly polarized $\gamma$ radiation is more difficult owing to the small fraction of the electrons in magnetized iron which are polarized (see (3) ). Furthermore a different method of nuclear alignment than that successfully used in (2) must be employed to obtain circularly polarized radiation. However if this method can produce a sufficient degree of alignment (temperatures of the order of 0.001° K.), an observable effect will be obtained.

Such experiments will yield information about the oriented nucleus and the radiation it emits not given by the angular distribution. The character (electric or magnetic) of the radiation is given by an observation of plane polarized radiation and the sign of the magnetic moment of the nucleus by an observation of the circularly polarized radiation.

## 2. THE SCATTERING OF POLARIZED $\gamma$ RADIATION

In (6) the degree of polarization of a beam of $\gamma$ quanta was expressed in terms of the components of the vector $\mathbf{P} = (p_1, p_2, p_3)$. $p_1$ and $p_2$ represent the degree of plane polarization and $p_3$ the degree of circular polarization. Assuming that the radiation is in a state of pure elliptical polarization, a right, orthogonal system of axes, $\xi\,\eta\,\zeta$, is introduced with the axis $\zeta$ in the direction of propagation and axes $\xi$ and $\eta$ along the axes of the ellipse. Then, if $I^{\xi}$ and $I^{\eta}$

[1] *Manuscript received October 15, 1952.*
*Contribution from the Clarendon Laboratory, Oxford, England.*

are the intensities of the components of the radiation plane polarized in the directions of axes $\xi$ and $\eta$,

$$[1] \qquad \begin{cases} p_1 = \dfrac{I^\xi - I^\eta}{I^\xi + I^\eta}, \\ p_2 = 0, \\ p_3 = \pm\, 2\,\dfrac{(I^\xi I^\eta)^{\frac{1}{2}}}{I^\xi + I^\eta}. \end{cases}$$

The + or − sign is taken depending on whether the radiation is right or left circularly polarized. If the polarization is not pure $\mathbf{P}^2 < 1$. If it is unpolarized $\mathbf{P}^2 = 0$.

Fano (3) shows that, in general, the fraction of the initial intensity transmitted by a polarization analyzer is $\frac{1}{2}(1 + \mathbf{P} \cdot \mathbf{Q})$ where $\mathbf{Q} = (q_1, q_2, q_3)$ is a vector depending only on the analyzer. For our purpose an improvement in notation is to define new vectors $\mathbf{V} = (1, p_1, p_2, p_3)$ and $\mathbf{W} = (1, q_1, q_2, q_3)$ so that the fraction transmitted is $\frac{1}{2}\,\mathbf{W} \cdot \mathbf{V}$.

In order to detect polarized $\gamma$ radiation some type of scattering process is required. To describe such a process Fano introduces a $4 \times 4$ matrix $\mathbf{T}$ to represent the scattering as follows: if $I_0 = I^\xi + I^\eta$ is the total intensity in quanta per sec. per cm.$^2$ incident on the scatterer and $I$ is the intensity in quanta per sec. per unit solid angle scattered into a solid angle $d\omega$ at an angle $\theta$ from the $\zeta$ axis and in a plane making an angle $\phi$ with the $\xi\,\zeta$ plane (see Fig. 1),

$$[2] \qquad \frac{I}{I_0} = \frac{d\sigma}{d\omega} = \tfrac{1}{2}\,\mathbf{W}\,\mathbf{T}(\theta, \phi)\,\mathbf{V}.$$

$d\sigma$ is the differential Compton cross section. $\mathbf{W}$ is a row vector, $\mathbf{V}$ a column vector, and matrix multiplication is implied. The matrix $\mathbf{T}$ given by Fano is restricted to scattering in the $\xi\,\zeta$ plane, $\phi = 0$. $\mathbf{T}(\theta, \phi)$ is related to $\mathbf{T}(\theta, 0)$ by a simple transformation (a rotation of the Poincaré sphere about the axis $\zeta$) such that $\mathbf{T}(\theta, \phi) = \mathbf{T}(\theta, 0)\,\mathbf{D}(\phi)$ where

$$[3] \qquad \mathbf{D}(\phi) = \begin{bmatrix} 1 & 0 & 0 & 0 \\ 0 & \cos 2\phi & \sin 2\phi & 0 \\ 0 & -\sin 2\phi & \cos 2\phi & 0 \\ 0 & 0 & 0 & 1 \end{bmatrix}.$$

If the scattered radiation is detected by a simple detector, insensitive to polarization, $\mathbf{W} = (2, 0, 0, 0)$, and if the incident radiation is unpolarized, $\mathbf{V} = (1, 0, 0, 0)$, equation 2 reduces to the familiar Klein–Nishina formula.

## 3. PLANE POLARIZATION

Consider a partially polarized beam of $\gamma$ quanta emitted at a source $O$ in Fig. 1, being scattered at $S$ and detected by simple counters at $a$ and $b$. The polarization is assumed to be elliptical with the axes of the ellipse along $\xi$ and $\eta$.

The measurable effect is the ratio, $\rho = (I_a - I_b)/(I_a + I_b)$. $I_a$ and $I_b$ are the scattered intensities at $a$ and $b$ and are proportional to the counting rates

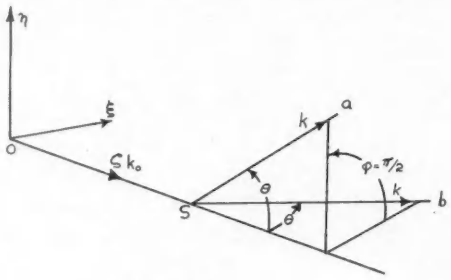


FIG. 1.

if equal efficiencies are assumed. What is desired is the relationship between $\rho$ and $p_1$. From equation 2, $I_a = I_0 \frac{1}{2}\mathbf{WT}(\theta, \pi/2)\,\mathbf{V}$ and $I_b = \frac{\gamma}{\epsilon} I_0 \frac{1}{2}\mathbf{WT}(\theta, 0)\,\mathbf{V}$. Thus

$$\rho = p_1 \frac{\sin^2\theta}{\left(\frac{k}{k_0} + \frac{k_0}{k} - \sin^2\theta\right)}. \qquad [4]$$

$k_0$ and $k$ are the momenta of the incident and scattered quantum in units of $mc$.

The factor $\sin^2\theta \Big/ \left(\frac{k}{k_0} + \frac{k_0}{k} - \sin^2\theta\right)$ represents the theoretical upper limit of resolution for such a device if infinitesimal source, scatterer, and counter are assumed. For practical purposes account must be taken of the finite size of these elements. Metzger and Deutsch (4) have investigated the resolution of such a device and express their results in terms of a figure of merit, $R$. If we replace $\sin^2\theta \Big/ \left(\frac{k}{k_0} + \frac{k_0}{k} - \sin^2\theta\right)$ by an experimental factor, $f$, it is related to $R$ thus, $f = (R - 1)/(R + 1)$.

## 4. CIRCULAR POLARIZATION

An experiment to detect circularly polarized annihilation radiation has been reported by Clay and Hereford (1). They measured, in effect, the relative intensities of Compton electrons knocked out of an iron foil magnetized parallel and antiparallel to the direction of propagation. Let $J$ be the intensity of electrons knocked out at $\theta = 0$, then $J$ is proportional to the intensity of $\gamma$ radiation scattered at $\theta = \pi$. The detector is assumed to record only electrons of energy $(k_0 - k) = 2k_0^2/(1 + 2k_0)$. Then if $J^+$ and $J^-$ refer to the field being parallel and antiparallel to the direction of propagation respectively and $\epsilon$ is the fraction of the electrons polarized, equation 2 gives

$$\frac{J^+ - J^-}{J^+ + J^-} = p_3\epsilon \frac{(k_0 + k)}{(1 + k_0 - k)}. \qquad [5]$$

The factor $\epsilon(k_0 + k)/(1 + k_0 - k) = \epsilon(2k_0 + 2k_0^2)/(1 + 2k_0 + 2k_0^2)$ is again seen to be the theoretic upper limit of resolution which will need correction to fit experimental conditions.

## 5. γ RADIATION FROM ALIGNED NUCLEI

Let us now consider γ radiation emitted by nuclei which have been aligned at low temperatures, that is, distributed unequally among the $2I + 1$ possible spin orientations with respect to the axis of alignment ($I$ = nuclear spin) Several methods of nuclear alignment are described by Simon, Rose, and Jauch (5). In (6) formulae were derived which gave the dependence of $p_1$ and $p_3$ on the degree of nuclear alignment and on the angle $\beta$ between the direction of emission and the axis of alignment. Two situations of interest were not considered in (6). These are nuclear alignment along two axes and emission of more than one observed γ ray.

For the technique (e.g. that described in (2)) which gives biaxial alignment, $p_3 = 0$ and we need only consider $p_1$. In this case half the nuclei are aligned along each of the two axes $z'$ and $z''$ of Fig. 2 separated by an angle $2\psi$. We choose the axis $z$ which bisects $z'$ and $z''$ as the polar axis. There are then three positions of interest at which $p_1$ could be measured, namely, $a$, in the equatorial plane perpendicular to the $z'\,z''$ plane, $b$, in the equatorial plane and in the $z'\,z''$ plane, and $c$, along the polar axis $z$.

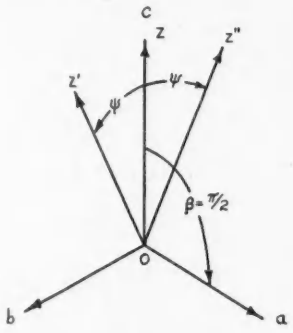


FIG. 2.

At $a$ it is not difficult to deduce that $p_1^a = p_1(\pi/2) \cos 2\psi$ where $p_1(\pi/2)$ is the value of $p_1$ for uniaxial alignment at $\beta = \pi/2$, at the same temperature.

In (6) $p_1$ is shown to be a polynomial in $\cos^2 \beta$, $p_1(\beta) = p_1(\cos^2 \beta)$. Thus at $b$, $p_1^b = p_1(\cos^2 (\psi \pm \pi/2))$. At both $a$ and $b$ the $\xi$ axis is taken to be in the equatorial plane.

At $c$ we define the $\xi$ axis to be in the $z'\,z''$ plane, whence $p_1^c = -p_1(\cos^2 \psi)$.

Also given in (6) is an approximate formula for $p_1$ which is valid for low degrees of (uniaxial) alignment, such that at any angle $\beta$, $p_1(\beta) = p_1^* \sin^2 \beta$, where $p_1^*$ is the value of $p_1(\pi/2)$ determined by the temperature, nuclear spin, and multipole order. The analogous formulae for biaxial alignment are,

$$[6] \qquad \begin{cases} p_1^a = & p_1^* \cos 2\psi, \\ p_1^b = & p_1^* \cos^2 \psi, \\ p_1^c = & -p_1^* \sin^2 \psi. \end{cases}$$

When the radiation consists of two constituents, $k_0$ and $k_0'$, the scattering of each must be described by a separate matrix $\mathbf{T}(k_0, \theta, \phi)$ and $\mathbf{T}(k_0', \theta, \phi)$. If $\delta$ and $\delta'$ are the counter efficiencies for the two scattered $\gamma$ rays the total scattered intensity is

$$[7] \qquad \delta I + \delta' I' = \tfrac{1}{2} \mathbf{W}[\delta I_0 \mathbf{T}(k_0) \mathbf{V} + \delta' I_0' \mathbf{T}(k_0') \mathbf{V}'] .$$

Equation 7 must be used in place of equation 2 to modify the results given above when both $\gamma$ rays are detected simultaneously.

If however $k_0 \simeq k_0'$, $I_0 = I_0'$, and $\mathbf{V} = \mathbf{V}'$ as in the example discussed below, both $\gamma$ rays are equivalent and equations 3 and 4 can be used as they stand. If $k_0$ and $k_0'$ are sufficiently different it should be possible to bias the detector so that either $\delta$ or $\delta'$ is zero.

## 6. APPLICATIONS AND DISCUSSION

The formulae derived above will now be applied to a practical example. Plane polarized $\gamma$ radiation can be produced by the experiment on $^{60}$Co described in (2). The method used gives biaxial alignment for which $\psi \simeq 38°$. The two $\gamma$ rays emitted by $^{60}$Co have very nearly the same energy, 1.12 and 1.33 Mev., thus $k_0 \simeq k_0' \simeq 2.4$. Furthermore $I_0 = I_0'$ and $\mathbf{V} = \mathbf{V}'$. The results of Metzger and Deutsch give at 1.22 Mev., $R = 1.7$; thus, for an instrument having the geometry they describe, $f = 0.26$.

In this case equations 4 are approximately true for $p_1{}^* = 0.1$ (the parameter describing the degree of alignment, $A/2kT = 0.19$). With this value of $p_1{}^*$, $\rho$ has the values 0.6%, 1.6%, and $-1.0\%$ at $a$, $b$, and $c$ respectively.

At saturation (i.e. $T = 0$, all nuclei have their spins fully aligned), $\rho$ has the values 6.3%, 11.6%, and $-6.2\%$ at $a$, $b$, and $c$ respectively.

Since the degree of nuclear alignment obtained in (2) was about 75% of saturation ($A/2kT \simeq 1.0$), we can conclude that this effect should be clearly observable despite the loss of definition due to the biaxial alignment. Evidently position $b$ is the most favorable.*

The most promising method of nuclear alignment which will yield circularly polarized $\gamma$ radiation is the R.-G. method described in (5).† Let us assume that $^{60}$Co has been aligned by this method in a typical salt which at a temperature of 0.05° K. should yield a value of $|p_3| = 0.2$ observed along the (single) axis of alignment. Then with $k_0 = 2.4$ and $\epsilon = 2.2/26$, (1), the maximum effect as given by equation 5 is $(J^+ - J^-)/(J^+ + J^-) = 0.016$ or 1.6%. A higher degree of alignment would be desirable in order to observe this effect decisively. At a temperature of 0.001° K., effectively at saturation, $|p_3| \simeq 1$ and the effect is about 8%.

[*Notes added in proof*]

* *This effect has now been observed: Bishop, G., Daniels, J., Goldschmidt, G., Halban, H., Kurti, N., and Robinson, F. N. H. Phys. Rev. 88: Dec. 15, 1952.*

† *This method, the Rose-Gorter method, i. e. hyperfine structure coupling combined with an external magnetic field, has now been used successfully to produce an anisotropy in the angular distribution of approximately 50%: Ambler, E., Grace, M. A., Halban, H., Johnson, C. E., and Kurti, N. (to be published). The author is indebted to these workers for permission to announce this result here.*

Another method has been suggested for detecting the circularly polarized radiation. This is by observing the difference in transmission through an iron absorber magnetized parallel and antiparallel with the direction of propagation. Such an experiment has been analyzed by the author and found to be less favorable than the observation of electrons scattered from a magnetized foil. The maximum effect in the situation described above is 0.6%.

It is evident that the loss of definition due to the necessity of scattering the radiation makes these effects more difficult to observe than the angular distribution. However plane polarized radiation should be measurable wherever an anisotropic angular distribution is obtained.

The observation of circular polarized radiation is rendered still more difficult by the small fraction of the electrons polarized by the magnetic field. In order to obtain a measurable effect nuclear alignment near saturation is required.

Some information concerning the radiation and the oriented nucleus can be obtained from the observation of these effects as was pointed out in (6). The character of the radiation is determined by the sign of $p_1$, $p_1 > 0$ or $p_1 < 0$ according as the radiation is electric or magnetic, and in the case of circularly polarized radiation the sign of $p_3$ determines the sign of the magnetic moment of the oriented nucleus.

## 7. ACKNOWLEDGMENTS

The author is indebted to the Royal Commission for the Exhibition of 1851 for an Overseas Scholarship and to Dr. J. A. Spiers for his advice and guidance.

## REFERENCES

1. CLAY, F. P. and HEREFORD, F. L. Phys. Rev. 85: 675. 1952.
2. DANIELS, J. M., GRACE, M. A., and ROBINSON, F. H. Nature, 168: 780. 1951.
3. FANO, U. J. Optical Soc. Am. 39: 859. 1949.
4. METZGER, F. and DEUTSCH, M. Phys. Rev. 78: 551. 1950.
5. SIMON, A., ROSE, M. E., and JAUCH, J. M. Phys. Rev. 84: 1155. 1951.
6. STEENBERG, N. R. Proc. Phys. Soc. (London), A, (to be published).

# CROSS SECTION FOR THE REACTION $Be^9(\gamma, p)Li^8$[1]

By R. N. H. Haslam, L. Katz, E. H. Crosby,[2]
R. G. Summers-Gill,[3] and A. G. W. Cameron[4]

ABSTRACT

The reaction $Be^9(\gamma, p)Li^8$ has been investigated by detecting the 0.88 sec. $Li^8$ $\beta$-activity, by the use of a cycling apparatus which allows intermittent operation of the betatron, counting taking place during the periods of no X-ray yield. The cross section for the reaction has a peak value of 2.72 mbarns at 22.2 Mev., a half-width of 4.7 Mev., and the integrated cross section to 26 Mev. is 0.013 Mev-barns.

## INTRODUCTION

The $Li^8$ nuclei, which are formed in the $(\gamma, p)$ process in $Be^9$, decay with a 0.88 sec., 13 Mev. $\beta^-$ activity to a broad excited state of $Be^8$. Almost instantaneously the $Be^8$ breaks down into two $\alpha$-particles with total kinetic energy of approximately 3 Mev. The reaction may thus be studied by detecting either the energetic $\beta$'s or the $\alpha$-pairs. Both methods have been used to confirm the production of the reaction by 23 Mev. betatron X-rays (2, 12). Titterton (14) has observed the reaction in beryllium-loaded photographic emulsions. Recently Tucker and Gregg (15) have measured the threshold for this reaction at 16.93 $\pm$ 0.15 Mev., in satisfactory agreement with the threshold calculated from mass values.

In the investigation described here, the cross section for the reaction has been determined for photon energies between the threshold and the maximum energy available, 26 Mev. A relative activation curve, giving the counting rate, in arbitrary units, per unit X-ray dose as a function of betatron energy, was first determined. Normalization of this curve was carried out by comparison with the activity induced in a copper sample at a fixed betatron energy. Finally the absolute activation curve was analyzed to yield the reaction cross section as a function of photon energy.

## EXPERIMENTAL

In order to detect and measure the short-lived $Li^8$ activity the beryllium sample is left in the same position in front of the betatron during irradiation and counting. An 'end-on' Geiger tube placed well below the collimated X-ray beam is used to count the energetic $\beta$-particles. The betatron is operated intermittently and counting takes place between irradiation periods, in a manner discussed below.

[1] *Manuscript received October 20, 1952.*
*Contribution from the Department of Physics, University of Saskatchewan, Saskatoon, Sask.*
[2] *Holder of a National Research Council of Canada Studentship, 1951–1952. Now with the Department of Health, Ottawa, Ontario.*
[3] *Holder of a National Research Council of Canada bursary, 1951–52. Now at the University of California, Berkeley, California.*
[4] *Holder of a National Research Council of Canada Fellowship, 1951–52. Now at the Iowa State College, Ames, Iowa.*

A typical irradiation set-up is shown in Fig. 1. The beryllium sample, in this case a cylinder $1\frac{1}{8}$ in. in height and $1\frac{1}{8}$ in. in diameter, is suspended in the beam by means of a holder of fine aluminum wire. In later experiments, to increase the counting rates, a slab of beryllium metal approximately 4 in. × 4 in. × 1 in. was used. The Geiger tube is placed within a castle, whose construction is shown in the diagram. It is designed to reduce background activities caused by X-rays or by neutron capture. The 2.3 min. beta activity due to neutron capture in the aluminum parts of the tube itself appears to form the most troublesome "background" activity, but this is reduced greatly by the castle. When the tube window is located about 1.5 in. below the open upper end of the castle a reasonable compromise is achieved between good counting geometry and efficient shielding.

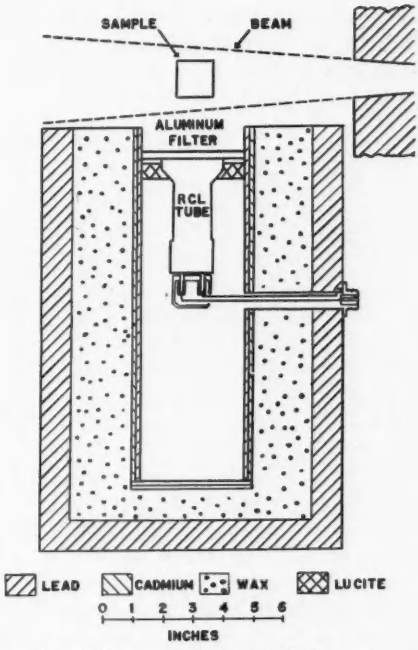


FIG. 1. Position of sample and Geiger tube during irradiation and counting. The construction of the shielding castle is shown.

A serious complication in this experiment is the fact that fast neutrons, unavoidably present in the X-ray beam, produce the reaction $Be^9(n, \alpha)He^6$. $He^6$ is also produced, but to a lesser extent, by the reaction $Be^9(\gamma, He^3)He^6$. The $He^6$ decays with a 0.82 sec., 3.5 Mev., $\beta^-$ activity (16). To eliminate this contaminant activity, which cannot be separated from the 0.88 sec. $Li^8$ activity because of the nearly equal half-lives, an aluminum filter is placed between the sample and the Geiger tube window. All $\beta$'s having energies up to 3.9 Mev. are absorbed by the

filter, whose thickness is 1.975 gm. per cm.$^2$ The $He^6$ activity is completely eliminated, but a large portion of the $Li^8$ spectrum also is absorbed, and this filtering has to be allowed for when the absolute counting rate from $Li^8$ is determined.

The short half-life of the activity to be measured makes special counting techniques necessary. As mentioned above, the sample is left in the same position during irradiation and counting. The betatron yield, and the scaling apparatus, is controlled by cam wheels mounted on a common shaft and driven at a constant speed of 3 r.p.m. by a synchronous motor with a suitable external gear ratio. Each of four microswitches is controlled by the cam wheel on which it rides. The first switch turns on the betatron yield (by turning on the electron injection pulse) for a period of 2.21 sec. Switches 2, 3, and 4 may be used to connect the Geiger tube, in succession, to one of three scalers. In practice most consistent results were obtained by using a common preamplifier whose output was fed in turn by the control mechanism to the three scalers, through these switches. The times and durations of the three counting periods were as follows:—

| Count period | Time after end of irradiation (sec.) | Duration (sec.) |
|---|---|---|
| 1 | 0.03 - 1.94 | 1.91 |
| 2 | 1.98 - 3.79 | 1.81 |
| 3 | 9.69 - 16.99 | 7.30 |

To determine a point on the relative activity curve, the betatron energy is fixed at a certain value by means of an 'integrator' circuit (7), and the cycling apparatus is set into operation for a sufficient number of cycles to ensure good statistics in the count registered by the three scalers. After the desired number of irradiation cycles the betatron is turned off, but the counting carries on automatically to the end of the cycle already begun. At the beginning of the third scaling interval the $Li^8$ activity has essentially disappeared and thus the count registered during this interval is due to 'background' activities. In effect, after each cycle, a new sample is presented to the beam in so far as the $Li^8$ activity is concerned. However, activities of longer period produced in the sample, in the aluminum filter, or in the walls of the counter tube may give rise to an increasing background count, which is of course in addition to the normal tube background. The assumption is made that the background is nearly constant over the counting period of any one cycle, and that the third scaler follows its variation over the set of cycles involved in the determination of the activation point. Thus the background to be subtracted for counting period 1 is 1.91/7.30 times the count registered in period 3.

In all cases the net number of counts registered during the first counting periods, that is to say by scaler 1, was used to measure the induced activity. From the ratio of the number of counts recorded by the first scaler to the number recorded by the second scaler (both corrected for background) the half-life of the activity may be measured. No attempt was made to carry out an accurate measurement of half-life, but in all cases the ratio was recorded to check the

correct functioning of the apparatus. For instance, if the Geiger counter had not reached its correct operating condition at the start of counting period 1, this fact would show up in an anomalous value of the ratio. In two typical runs the mean values of these ratios were 4.55 and 4.74 corresponding respectively to effective half-lives of 0.91 and 0.88 sec.

The X-ray dose given to the sample during an irradiation was measured by a modified Baldwin–Farmer radiation meter,* which integrates the dose received. Variations in dose from cycle to cycle are thus of no consequence, but erratic variations of yield during individual irradiation periods would introduce error.

The net number of counts recorded in the first counting period divided by the integrated X-ray dose yields one point on the relative activation curve shown in Fig. 2. The ordinate scale on the left-hand side is in arbitrary units. The initial portion of the curve has been replotted with the ordinate scale increased 10-fold. No attempt at an accurate threshold determination has been made, but the apparent threshold lies at about 16.9 Mev., in agreement with expectation.

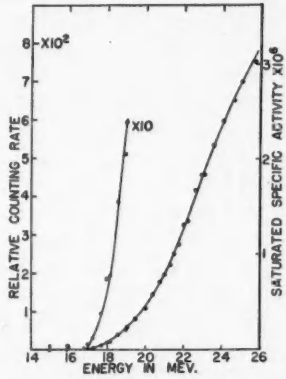


FIG. 2. Activation curve for the reaction $Be^9(\gamma, p)Li^8$. The ordinate scale to the right is in activations per minute per 100 r. per minute per gram-atom of $Be^9$. The initial portion of the curve is replotted with the ordinate scale increased 10-fold.

The absolute scale shown to the right of the activity curve, Fig. 2, is determined by calibrating one point on the activation curve, using the $Cu^{63}(\gamma, n)Cu^{62}$ activity as a standard. A beryllium disk of thickness 1440 mgm. per cm.$^2$ and diameter 4.8 cm. was irradiated at an energy of 24.0 Mev. and counted in the usual way by use of the cycling apparatus with the aluminum filter in place.The saturated activity per gram-atomic weight of $Be^9$ for unit dosage rate is then calculated. In effect the total dose is given in a period of 2.21 sec. and the total count recorded by the first scaler is registered in a 1.91 sec. interval starting 0.03 sec. after the end of irradiation. Thus the corrections to obtain saturated activity are applied in the usual way. The dosage rate is of course given by (recorded dose $\times$ 60/2.21) units per minute. Next a disk of copper of the same di-

*Product of the Baldwin Instrument Company, Dartford, Kent, England.

ameter and of thickness 125 mgm. per cm.$^2$ was irradiated for one minute with no filter in place and without the use of the cycling apparatus. The 10.1 min. $Cu^{62}$ copper activity was followed for several half-lives, and the saturated activity per gram-atom of $Cu^{63}$ per unit dosage rate was calculated. These observations were repeated six times for beryllium and five times for copper, and the mean values of saturated activity used in each case. Since the copper and beryllium samples were irradiated and counted in the same geometry the only corrections that need be applied are those for self-absorption and self-scatter. The assumption is made that the angular distribution of $\beta$'s emitted by the copper and beryllium disks is the same; and the effect of self-absorption was corrected for by dividing the observed counts in each case by the expression

$$\frac{1 - e^{-\mu x}}{\mu x}.$$

Here $x$ is the thickness of the sample in gm. per cm.$^2$ and $\mu$ is the mass absorption coefficient in cm.$^2$ per gm. The coefficient $\mu$ has been determined experimentally and is well represented by $15.5\ E^{-1.41}$ where $E$ is the end-point energy of the $\beta$-spectrum in Mev. (1). When this correction was applied, a value of $2.62 \times 10^{-3}$ was found for the ratio of the saturated activity per gram-atom of $Be^9$ per unit dosage rate (but measured through the aluminum filter) to the saturated specific activity per gram-atom of $Cu^{63}$ per unit dosage rate.

The effect of the aluminum filter used to cut out the 0.82 sec. $He^6$ activity must now be taken into account. The filter correction was calculated as follows. A momentum spectrum of $Li^8$ $\beta$-particles, as determined by Hornyak and Lauritsen (4), was converted to an energy spectrum. This spectrum is the upper curve of Fig. 3 (*b*). The vertical line at 3.9 Mev. marks the actual filter thickness. It is known that the absorption of monoenergetic electrons is linear when plotted on a 'fraction of range' scale (8). Then to determine the fraction of the $\beta$-spectrum transmitted, the ordinate at each energy has to be multiplied by the transmission factor for monoenergetic electrons of that energy for the given thickness of absorber. This is illustrated in Fig. 3 (*a*). The vertical line at 1.975 gm. per cm.$^2$ shows the filter thickness. The ranges corresponding to given energies were found from the range–energy relationship of Katz and Penfold (8). A straight line was drawn from a transmission factor of unity at zero thickness to zero at a thickness corresponding to the range of electrons of a certain energy. The intersection of this line with the vertical drawn at 1.975 gm. per cm.$^2$ shows the transmission factor for electrons of this energy. The ordinate of the upper curve of Fig. 3 (*b*) at that energy must then be multiplied by the transmission factor to yield the corresponding ordinate of the transmitted spectrum. This process was repeated at several energies to obtain the lower curve of Fig. 3 (*b*). The ratio of the area under the original curve to that under the transmitted curve gives the filter attenuation. It was found to be 3.33; that is, the true activity from beryllium is 3.33 times the observed activity.

An attempt was made to determine the filter attenuation experimentally. A series of runs at energies between 13.2 and 20.5 Mev. was taken with and without

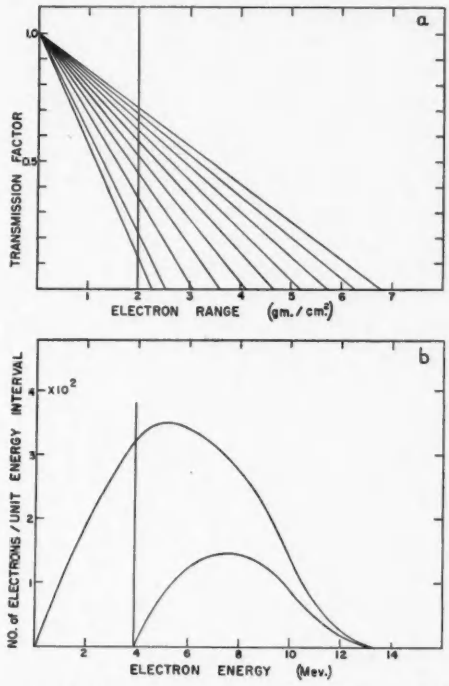


FIG. 3 (*a*) Diagram showing how the transmission of monoenergetic electrons through the aluminum filter is calculated.

(*b*) Diagram to show calculation of filter attenuation. The upper curve represents the incident electron spectrum, the lower curve shows the transmitted spectrum.

the aluminum filter in place. The beryllium sample used was relatively thick to give good counting statistics. When no filter was used, the net counting rate per unit dose was nearly constant between 13.2 Mev. and the threshold of the $(\gamma, p)$ reaction, 16.9 Mev. This counting rate is attributed to the production of $He^6$. If the (rather doubtful) assumption is made that the contribution of $He^6$ to the total activity remains nearly constant also between 16.9 and 20.5 Mev., the net counting rate per unit dose due to the $Li^8$ activity without the filter for this energy region may be plotted as a function of energy. Comparison with the curve obtained with the filter in place then makes possible a determination of the attenuation. An average value of $3.69 \pm 0.1$ was obtained in this way for the energy region in which statistics were sufficiently good, namely 18.5 to 20.5 Mev.

This value is thought to be an upper limit. If the $He^6$ activity in fact increases between 16.9 and 20.5 Mev., the ratio of the $Li^8$ activity measured without the filter to the activity measured with the filter at any particular energy is decreased. Further the effect of self-absorption in the rather thick beryllium sample itself is to decrease the average energy of the emitted $\beta$-particles in comparison

with the energy distribution from an 'infinitely' thin sample. Consequently, the filter will absorb a larger fraction of the total number of electrons, leading to an increased attenuation.

In view of these considerations, the theoretical value of filter attenuation, 3.33, has been used in the comparison of specific activities since a relatively thin beryllium sample was used in the standardization. The fact that the experimental value of 3.69 for the thick sample differs by only 10% and is expected to be too high gives added confidence in the theoretical value.

The application of the filter correction 3.33 thus yields a value of $2.62 \times 10^{-3} \times 3.33 = 8.72 \times 10^{-3}$ for the ratio of saturated activities produced in $Be^9$ and $Cu^{63}$ per gram-atom of isotope for equal dosage rates, by betatron bremsstrahlung of maximum energy 24.0 Mev. Using the value of $2.68 \times 10^8$ counts per min. per gram-atom of $Cu^{63}$ per 100 r. per minute determined in this laboratory, for the reaction $Cu^{63}(\gamma, n)Cu^{62}$ (3, 5), we obtain finally a value of $(8.72 \times 10^{-3} \times 2.68 \times 10^8)$ or $2.34 \times 10^6$ counts per min. per gram-atom of $Be^9$ per 100 r. per minute for the absolute activation value at 24.0 Mev.

The absolute activity curve is then analyzed by the photon difference method (6), to yield the cross-section curve reproduced in Fig. 4. The cross section rises from the threshold at 16.9 Mev. to a maximum value of 2.72 mbarns at 22.2 Mev. The width at half-maximum is 4.7 Mev., and the integrated cross section (to 26 Mev.) is 13 Mev-mbarns.

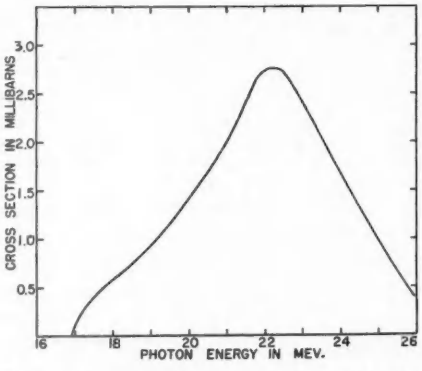


FIG. 4. Cross section vs. photon energy for the reaction $Be^9(\gamma, p)Li^8$.

## DISCUSSION OF RESULTS

Experimental errors are introduced mainly by three factors. Graphical evaluation of the filter attenuation may lead to an estimated maximum error of 10%. The assumption that the beryllium and copper comparison samples yield the same angular distribution of electrons may introduce an error of about 15%, and the $Cu^{62}$ activation value used as a standard may be in error by as much as 15%, though the recent work of Krohn and Shrader (9) indicates rather higher accuracy. An over-all probable error of about 30% is estimated, so that the saturated specific activity at 24.0 Mev. is $(2.34 \pm 0.7) \times 10^6$ counts per min.

per 100 r. per min. per gram-atom of $Be^9$. The ordinates of points on the cross-section curve may be in error by the same percentage; thus the peak cross section is $2.72 \pm 0.8$ mbarns per atom.

By detecting the emitted protons, Mann and Halpern (11) found the photoproton yield produced in $Be^9$ by 23.5 Mev. bremsstrahlung to be $(2.5 \pm 0.6) \times 10^4$ protons per gram-atom per r. This is in close agreement with our value at 23.5 Mev., namely $(2.1 \pm 0.6) \times 10^4$ activations per gram-atom per r.

Titterton (14) estimates the "mean" value of the cross section for the $(\gamma, p)$ reaction over the energy range from 18 to 24 Mev. to be $0.25 \pm 0.1$ mbarns per atom. This is considerably lower than our value, but it is based on the observation of only 21 $Be^9$ disintegrations in a beryllium-loaded emulsion.

A very rough estimate of 0.3 mbarns is reported by Tucker and Gregg (15) for the $(\gamma, p)$ cross section at 19 Mev. This is to be compared with our value of 0.9 mbarns.

The integrated cross section for the absorption of X-rays of all energies is calculated from the sum rule (10) to be 0.187 Mev-barns. The $(\gamma, p)$ and $(\gamma, n)$ reactions would be expected to account for the major part of this absorption, and in light nuclei the integrated cross section for the $(\gamma, p)$ reaction appears to be greater than that for the $(\gamma, n)$ reaction. The value of 0.013 Mev-barns for the integrated cross section to 26 Mev. of the $(\gamma, p)$ reaction, obtained in the present work, is thus surprisingly low. If the shape of the cross-section curve is correct it is obvious that little contribution is to be expected at photon energies higher than 26 Mev. Thus the $(\gamma, n)$ integrated cross section is presumed to be considerably larger than that for the $(\gamma, p)$ reaction. This is borne out by the fact that the yield of the $(\gamma, n)$ reaction, determined by Price and Kerst (13), at 22 Mev. is $3.0 \times 10^7$ neutrons per mole per 100 r., whereas the $(\gamma, p)$ yield at this same energy is about one twenty-fifth of this value. $Be^9$ might be expected to exhibit an exceptional behavior on account of the low $(\gamma, n)$ threshold (1.66 Mev.) in comparison with the $(\gamma, p)$ threshold. Determination of the $(\gamma, n)$ cross section in the energy range 0–26 Mev. would be of great interest.

The authors are indebted to the National Research Council of Canada for financial support.

## REFERENCES

1. Baker, R. G. and Katz, L. Nucleonics. In press.
2. Conklin, R. and Ogle, W. Phys. Rev. 73: 648 A. 1948.
3. Haslam, R. N. H., Johns, H. E., and Horsley, R. J. Phys. Rev. 82: 270. 1951.
4. Hornyak, W. F. and Lauritsen, T. Phys. Rev. 77: 160. 1950.
5. Johns, H. E., Katz, L., Douglas, R. A., and Haslam, R. N. H. Phys. Rev. 80: 1062. 1950.
6. Katz, L. and Cameron, A. G. W. Can. J. Phys. 29: 518. 1951.
7. Katz, L., McNamara, A. G., Forsyth, P. A., Haslam, R. N. H., and Johns, H. E. Can. J. Research, A, 28: 113. 1950.
8. Katz, L. and Penfold, A. S. Revs. Modern Phys. 24: 28. 1952.
9. Krohn, V. E. and Shrader, E. F. Phys. Rev. 87: 685. 1952.
10. Levinger, J. S. and Bethe, H. A. Phys. Rev. 85: 577. 1952.
11. Mann, A. K. and Halpern, J. Phys. Rev. 82: 733. 1951.
12. Ogle, W., Brown, L., and Conklin, R. Phys. Rev. 71: 378. 1947.
13. Price, G. A. and Kerst, D. W. Phys. Rev. 77: 806. 1950.
14. Titterton, E. W. Nature, 165: 721. 1950.
15. Tucker, B. L. and Gregg, E. C. Phys. Rev. 87: 907. 1952.
16. Wu, C. S., Rustad, B. M., Perez-Mendez, V., and Lidofsky, L. Phys. Rev. 87: 1140. 1952.

# THE ULTRAVIOLET ABSORPTION OF SILVER BROMIDE[1]

By J. R. Allen

ABSTRACT

The photoelectric absorption process in solid insulators is discussed and contrasted with that for free atoms and ions. It is suggested that in substances of high dielectric constant the resultant screening of the field of the remaining positive hole due to the polarization of the material results in a reduction of the absorption coefficient at the spectral edge, and produces a maximum at higher energies. This effect is illustrated by a calculation of the ultraviolet absorption coefficient of silver bromide using as a model a bromine ion in a hole in a uniform dielectric. The calculated absorption coefficient is found to rise from the edge to a maximum at a wave length of about 850Å.

## 1. INTRODUCTION

The photoelectric absorption coefficient for incident radiation of energy $E = h\nu$ and intensity $I$, falling upon an $n$-electron system with state functions normalized in the volume $V$, is given by

$$\tau = -\frac{1}{I}\frac{dI}{dx} = \frac{E}{VI}\sum_{if}\frac{w_{if}}{g_i} \qquad [1]$$

where $w_{if}$ is the transition probability per unit time of a transition from a state of the system $i$ to a state $f$ under the influence of the perturbing radiation, and $g_i$ is the statistical weight of the initial state (7, pp. 106, 108, 115). The transition probability, $w_{if}$, may be obtained in terms of the matrix elements of the radiation interaction part of the Hamiltonian, by means of the well-known time-dependent perturbation theory if the interaction Hamiltonian is sufficiently small. Now in photoelectric absorption problems the final state belongs to a continuous spectrum; that is, a very large number of states exist which have the same or nearly the same energy, momentum, etc. If we assume that in the neighborhood of the final state $f$ there are a large number of states with the same physical properties, and that the density of these states is $\rho_f(E)$, then the transition probability to any one of these states is given by

$$w_{if} = \frac{2\pi}{\hbar}\rho_f(E)\left|\int \Psi_f^* H_I \Psi_i \, d\tau\right|^2 \qquad [2]$$

in which $\Psi_i$ and $\Psi_f$ are the suitably normalized wave functions of the initial and final states; $H_I$, the interaction Hamiltonian, is taken to be

$$H_I = \frac{ie\hbar}{mc}\mathbf{A}\cdot\nabla,$$

$\mathbf{A}$ being the vector potential of the radiation field (7, p. 90). In considering the absorption of light in solids, where we may have a band structure, the initial state will also belong to a continuum; and in that case we must multiply the transition probability by the initial density of states $\rho_i$, as well as by $\rho_f$.

[1]*Manuscript received October 17, 1952.*
*Contribution from the H. H. Wills Physical Laboratory, Royal Fort, Bristol, England.*

Before discussing absorption in solids let us consider the absorption process in free atoms and ions. The photoelectric absorption by a single electron in the field of a bare nucleus has been treated by Stobbe (15), and in this case, since the wave functions of both the initial and final states are coulombic, the absorption coefficient can be calculated exactly. It is found that it has a finite value at the series limit and falls off approximately as the inverse cube of the frequency of the incident radiation. Stobbe has applied his results to X-ray absorption by actual atoms, by replacing the nuclear charge by a screened value taking into account in this way the effect of the other electrons. The values obtained for the $K$ and $L$ absorption are in reasonable agreement with experiment for many solid absorbers, except near the absorption edges. We should not expect this model to be valid, however, in the ultraviolet region. The ultraviolet absorption constant of free atoms and positive ions has generally a finite, nonzero value at the spectral head and either decreases, or at first rises slowly and then decreases away from the edge, except in the special cases in which we have almost complete cancellation of the matrix element near the edge; for instance, Bates (1) has shown this to occur in the case of potassium. On the other hand the absorption constant of negative ions normally tends to zero at the spectral edge. This behavior can be explained by the fact that for the bare nucleus, for positive ions, and for the free atom we always have an infinite number of bound states just below the continuum, while for negative ions the number of bound states will be finite and may be zero (13, p. 81). If a stationary state of very small binding energy does occur in the field of a negative ion, or if a virtual bound state exists just above the edge, we have so-called resonance conditions and the absorption constant has a nonzero value at the edge.

Let us consider now the energy levels associated with the absorption of X rays and ultraviolet light by solid insulators, e.g. ionic crystals. Before the absorption process when the crystal is in its ground state we have a series of full X-ray levels, more or less broadened by the lattice interaction, then the full band of the valence electrons, and above this the empty conduction band. In most insulating crystals we may use the Heitler–London treatment (i.e. the approximation of tight binding) for the unexcited states. After the absorption of a photon we have a vacancy in one of the full levels which behaves as a positive hole, and if the field of this hole is not too highly screened it may induce just below the conduction band a series of quantized exciton levels. Now in an insulating solid we might expect the effective potential in which the ejected electron moves to be at large distances of the form $e^2/\kappa_0 r$ owing to the polarization of the medium by the hole, $\kappa_0$ being the high frequency dielectric constant of the material (13, p. 99). A potential of this sort always gives an infinite series of bound states just below the continuum (13, p. 82). Thus we see that the absorption spectrum of an insulating crystal should be expected to consist of a series of lines leading up to a series limit, beyond which there will be continuous absorption. If $\kappa_0$ were sufficiently large, however, we might expect the absorption coefficient to be relatively reduced at the edge and to rise to a maximum at higher energies, the behavior of the negative ion providing the limiting

case for very large $\kappa_0$. The intensities of the exciton lines should also be reduced and they should be crowded more closely towards the series limit.

The silver halides have large high frequency dielectric constants and we might expect these considerations to apply in particular to them. The model used for the absorption by the $(4p)$ band of the silver bromide crystal consisted of a bromine atom in a hole in a uniform dielectric of dielectric constant $\kappa_0$. The potential in which the ejected electron was considered to move consisted of a scaled Hartree self-consistent field for the bromine atom inside the hole, and $e^2/\kappa_0 r$ outside, and the wave functions for the conduction band were taken to be the free electron wave functions in this potential.

## 2. THE ABSORPTION COEFFICIENT

The expression for the absorption coefficient may be reduced by using the usual electric dipole approximation for the matrix element $(f|H|i)$ and, after substituting the density of states of a free electron for $\rho_f$, and averaging over all directions of polarization of the incident radiation, it becomes

$$[3] \qquad \tau = \frac{2\alpha m}{3\hbar^2} Ek \sum_{if} \frac{\rho_i}{g_i} \left| \int \Psi_f^* \sum \mathbf{r}\, \Psi_i \, d\tau \right|^2$$

where $k$ is the wave vector of the ejected electron and $\alpha$ the fine structure constant. If we presume that the wave functions are separable in a spherically symmetric central field, we obtain for the individual bound state orbitals

$$[4] \qquad \psi_{nlm} = \left( \frac{2l+1}{2} \cdot \frac{(l-|m|)!}{(l+|m|)!} \right)^{\frac{1}{2}} \frac{e^{im\phi}}{\sqrt{2\pi}} P_l^m(\cos\theta)\, \frac{\chi_{nl}(r)}{r}$$

where the $\chi_{nl}$ satisfy the usual Hartree equations (5) and are normalized to unity. For the orbitals of the continuum we have expressions of the form

$$[5] \qquad \psi_{\epsilon l} = \frac{\epsilon^{-\frac{1}{4}}}{\sqrt{V}} (2l+1)\, i^l\, e^{i\eta_{\epsilon l}}\, P_l^0(\cos\theta)\, \frac{\chi_{\epsilon l}}{kr}$$

where $\epsilon$ is the energy of the ejected electron and the $\chi_{\epsilon l}$ are normalized so that the sum, $\sum_l \psi_{\epsilon l}$, becomes asymptotic in amplitude to the plane wave $e^{ikz}/\sqrt{V}$ at large distances. Then the asymptotic amplitude of $\chi_{\epsilon l}$ is $\epsilon^{-\frac{1}{4}}$.

If we consider absorption from the $(4p)$ shell the matrix elements of the $s$ and $d$ orbitals of the continuum are the only ones which do not vanish, and the expression for the absorption coefficient becomes, after integration over all angle coordinates and after performing the appropriate summations,

$$[6] \qquad \tau = \frac{8\pi N\alpha a_0^2}{3} \cdot \frac{E}{W} \left[ \left| \int_0^\infty \chi_{\epsilon s}\, r \chi_{4p}\, dr \right|^2 + 2 \left| \int_0^\infty \chi_{\epsilon d}\, r \chi_{4p}\, dr \right|^2 \right]$$

where $N$ is the number of ion pairs per unit volume of the material, $a_0$ is the Bohr radius, $W$ the Rydberg energy, and the expression in brackets is evaluated in atomic units. The change in the wave functions of the passive electrons due to the transitions has been neglected.

### 3. THE FIELD

The field for the bromine core and the $(4p)$ radial wave function in this field were obtained from the Hartree self-consistent fields for $Rb^+$ (4), As (6), and $Cs^+$ (3) by means of a method suggested by Manning and Millman (10).

The total charge lying inside a radius $r$ due to an electron occupying an $(nl)$ orbital is given by $Z_0(nl; r) = \int_0^r \chi^2_{nl}\, dr$. If $Z$ is the effective nuclear charge at radius $r$, then the field is $Z(r)/r^2$ and for an atom of total charge $Q$,

$$Z(r) = Q + \sum_{nl} q_{nl}(1 - Z_0(nl; r)),$$

where $q_{nl}$ is the number of occupied $(nl)$ orbitals. For an electron in an $(nl)$ orbital $C = 1 - Z_0(nl; r)$ is the charge lying outside a radius $r$ and is called the contribution to $Z$ at radius $r$ from that orbital. Now the basis of Manning and Millman's method is the fact that the $C$ vs. log $r$ curve for a particular orbital has almost the same shape for elements which do not differ too much in atomic number, and they point out that this can be related to the screening constant $S_{nl}$ for the $(nl)$ orbital by the equation

$$\log r_1 - \log r_2 = \log \frac{N_2 - S_{nl}}{N_1 - S_{nl}} \qquad [7]$$

where $N_1$ and $N_2$ are the atomic numbers of the two nuclei, and the radii are two for which $C$ is the same. Manning and Millman take $S_{nl}$ to be independent of $C$, but we may obtain a more accurate interpolation by computing $S_{nl}$ as a function of $C$ from the values of $r_1$, $r_2$ at constant $C$ as follows:

$$S_{nl}(C) = \frac{N_1\left(\frac{r_1}{r_2}\right)_C - N_2}{\left(\frac{r_1}{r_2}\right)_C - 1}. \qquad [8]$$

$S_{nl}(C)$ was computed from the self-consistent fields for $Rb^+$ (which has the same configuration as $Br^-$) and As (which has a half-filled $p$ shell). In the case of $S_{4p}(C)$ the data for $Cs^+$ were given some weight as well. When $S_{nl}$ had been obtained for all the shells, $C_{nl}$ as a function of $r$ for $Br^-$ was calculated from the data for $Rb^+$ by means of the relationship

$$[C_{nl}(r)]_{Br^-} = \left[ C_{nl}\left( r \cdot \frac{N_{Br} - S_{nl}(C)}{N_{Rb} - S_{nl}(C)} \right) \right]_{Rb^+}.$$

The effective field in which a $(4p)$ electron moves is then given by $Z(r)/r^2 = \sum_{nl} q_{nl} C_{nl}/r^2$ where $q_{4p} = 5$ and all other $q$'s are for closed shells. The potential $U(r)$ was obtained by numerical integration using the relation

$$U(r) = -\int_r^\infty \frac{N - Z(r)}{r^2}\, dr. \qquad [9]$$

The $(4p)$ radial wave function for $Br^-$ was obtained from that for $Rb^+$ by making use of the fact that the wave functions for an $(nl)$ orbital may be

written (5), $\chi_{nl}(r) = (N - S_{nl})^{\frac{1}{2}}\, G_{nl}[(N - S_{nl})r]$ where $G_{nl}(x)$ is a function that for fixed $x$ varies only slowly with $N$. Thus

$$[10] \qquad [\chi_{4p}(r)]_{Br^-} \simeq \beta\left[\chi_{4p}\left(r \cdot \frac{N_{Br} - S_{4p}}{N_{Rb} - S_{4p}}\right)\right]_{Rb^+}$$

where $\beta$ is a renormalization constant.

In considering the effective field in which the ejected electron moves we must take into account the polarization of the surrounding material produced by the positive hole. This polarization will set up at the lattice point an electric potential $\phi$, which may be regarded as the potential produced in a spherical hole of radius $R$ in a uniformly polarized medium of dielectric constant $\kappa_0$. The polarization energy $\frac{1}{2}e\phi$ and the value of the equivalent $R$ may be calculated by the method of Mott and Littleton (14). The values obtained for the $Br^-$ lattice site of silver bromide were $\frac{1}{2}e\phi = 2.50$ ev., $R = 4.25\ a_0$. The potential $U(r)$ was presumed to fall off as $e^2/\kappa_0 r$ at distances greater than $R$, the inner and outer values being joined smoothly at the boundary.

Knowing the value of $\frac{1}{2}e\phi$ Mott (11) has shown that the energy of the series limit may be estimated, and is given by

$$h\nu = W_L - \tfrac{1}{2}e\phi + E - \chi$$

where $W_L$ is the lattice energy, $E$ the electron affinity of the halogen atom, and $-\chi$ the lowest energy of the conduction band. Born and Göppert-Mayer give for the lattice energy of silver bromide 8.81 ev. (2, p. 727) and for the electron affinity of bromine approximately 3.55 ev. (2, p. 728). Mott and Gurney (13, p. 245) estimate $\chi$ from the Herschel effect to be of the order of 3.6 ev. We then obtain for the energy of the series limit approximately 6.25 ev.

## 4. THE ELECTRON WAVE FUNCTIONS

The individual orbital wave functions satisfy, in atomic units, the radial equations

$$[11] \qquad \frac{d^2\chi_l}{dr^2} + \left[\epsilon - U - \frac{l(l+1)}{r^2}\right]\chi_l = 0.$$

The bound state wave function is very sensitive to the form of the potential and rather than determining a true eigenfunction in the potential $U$ we have used the scaled $(4p)$ radial wave function for $Br^-$. As this wave function is small at distances greater than $R$ it is unlikely that it would be greatly altered by the addition of the polarization field.

The $s$ orbitals of the continuum were calculated by means of the W.K.B. approximation. The W.K.B. solution of equation [11] which has the asymptotic amplitude $\epsilon^{-\frac{1}{4}}$ is given by

$$\chi_\epsilon(r > R) = (\epsilon - U)^{-\frac{1}{4}} \sin\left[\int_\rho^r (\epsilon - U)^{\frac{1}{2}}\, dr\right].$$

This solution for distances $r > R$ was joined to the inner solution

$$\chi_\epsilon(r < R) = A(\epsilon - U)^{-\frac{1}{4}} \sin\left[\int_0^r (\epsilon - U)^{\frac{1}{2}} dr\right]$$

at $r = R$ and the normalization constant, $A$, and phase constant, $\rho$, thus determined. Mott (12) has pointed out that we may safely use the W.K.B. approximation in the atom core; for the charge drops slowly in the sense required by the approximation, each shell of screening electrons necessarily extending over a thickness somewhat larger than the wave length of an electron of positive energy.

The W.K.B. approximation was not used for the free $d$ orbitals, as here, owing to the shape of the effective radial potentials, at low energies five solutions would have had to be joined and their appropriate normalization and phase constants determined. Instead the equations were integrated numerically from the origin using the Gauss–Jackson method (9, p. 276) and normalized by putting the amplitudes of the solutions at large $r$ equal to $(\epsilon - U)^{-\frac{1}{4}}$.

## 5. RESULTS AND DISCUSSION

The wave functions described above were used to compute the dipole matrix elements as a function of $\epsilon$, the energy of the ejected electron. The absorption coefficient, $\tau$, was then obtained from equation [6] using the value 6.25 ev. for the energy at the spectral edge. The results are shown in Fig. 1, where $\tau$ in

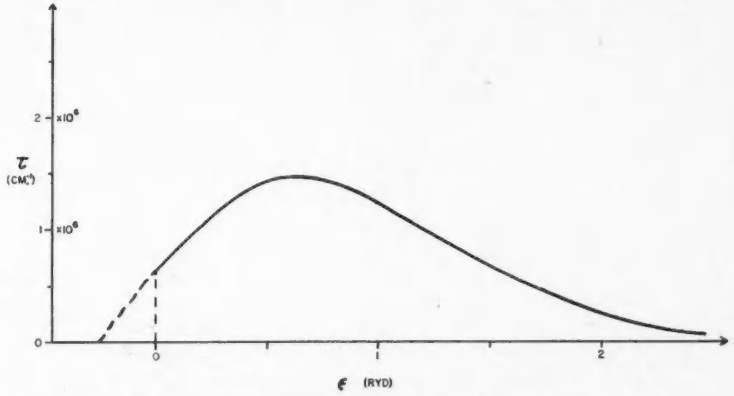


FIG. 1. Calculated absorption coefficient of silver bromide in cm.$^{-1}$ against energy of ejected electron in rydbergs. The dashed extension to the left of the edge represents the experimental longer wave length absorption fitted to the computed value at the edge.

cm.$^{-1}$ is plotted against $\epsilon$ in rydbergs. The dashed extension to the left of the edge represents the longer wave length absorption as measured by Hilsch and Pohl (8), fitted to the computed absorption coefficient at 6.25 ev. We interpret this extension as representing the broadened exciton lines, and the experimental curve does in fact show a structure with the separation of the spin doublet of the bromine atom. The value of $\tau$ rises from $0.6 \times 10^6$ cm.$^{-1}$ at the edge to a maximum value of $1.4 \times 10^6$ cm.$^{-1}$ at an energy corresponding to a wave length of approximately 850 Å, and then falls away again at shorter wave lengths. It was found that the $(4p\text{–}\epsilon d)$ transitions are considerably more

important than the $(4p–\epsilon s)$ transitions at all energies greater than about 1.5 ev. from the edge.

To obtain a check on the accuracy of the computed value for the absorption coefficient, the total oscillator strength $f$ for all $(4p)$ electron transitions was obtained by using the relation $f = 6.0 \times 10^{-6} \int \tau \, dE$ where $\tau$ is in cm.$^{-1}$ and $E$ in rydbergs. Its value was found to be 11.7. Now the well-known $f$-sum rule of Kuhn and Thomas states that $\sum_j f_{ij} = N$ where $f_{ij}$ is the oscillator strength of the transition $i$–$j$, $\sum_j$ represents a sum over the discrete spectrum and an integration over the continuum, and $N$ is the total number of electrons involved. For the $(4p)$ shell $N = 6$ but we might expect the total oscillator strength for absorption to exceed this value as the transitions to the inner levels, forbidden by the exclusion principle, will give negative contributions to the sum. For coulombic wave functions the total positive oscillator strength for $(4p)$ transitions is 1.223 per electron, and if the value should be of the same order of magnitude for our model then we would have a factor of about 1.6 to account for. Now the contributions to the dipole-length matrix elements come chiefly from relatively large values of $r$, where the bound state wave function is poorly determined, and this reduces the accuracy of the computation. A change of only about 25% in the value of the wave function at large distances would be sufficient to reduce the total oscillator strength to the coulombic value. Such a change in the bound state wave function, however, should not significantly alter the shape of the curve for $\tau$, though the value at the maximum would probably be reduced somewhat relative to the value at the edge, as the $(p–d)$ matrix elements are determined by contributions from larger values of $r$ than the $(p–s)$.

## 6. ACKNOWLEDGMENTS

The author wishes to thank Prof. N. F. Mott for suggesting the problem and for helpful discussions and guidance during the course of the work, Miss M. J. Littleton for her invaluable assistance with the computation of the wave functions, and the Royal Commissioners for the Exhibition of 1851, one of whose Science Research Scholarships he holds.

## REFERENCES

1. BATES, D. R. Proc. Roy. Soc. (London), A, 188: 350. 1947.
2. BORN, M. and GÖPPERT-MAYER, M. Handbuch der Physik. 24/2. Verlag von Julius Springer. 1933.
3. HARTREE, D. R. Proc. Roy. Soc. (London), A, 143: 506. 1934.
4. HARTREE, D. R. Proc. Roy. Soc. (London), A, 151: 96. 1935.
5. HARTREE, D. R. Repts. Progress Phys. Phys. Soc. (London), 11: 113. 1946–47.
6. HARTREE, D. R. and MANNING, M. F. Phys. Rev. 59: 299. 1941.
7. HEITLER, W. The quantum theory of radiation. 2nd. ed. Oxford University Press, London. 1944.
8. HILSCH, R. and POHL, R. W. Z. Physik, 64: 606. 1930.
9. JEFFREYS, H. and JEFFREYS, B. S. Methods of mathematical physics. Cambridge University Press, London. 1946.
10. MANNING, M. F. and MILLMAN, J. Phys. Rev. 49: 848. 1936.
11. MOTT, N. F. Trans. Faraday Soc. 34: 500. 1938.
12. MOTT, N. F. Private communication.
13. MOTT, N. F. and GURNEY, R. W. Electronic processes in ionic crystals. 2nd. ed. Oxford University Press, London. 1948.
14. MOTT, N. F. and LITTLETON, M. J. Trans. Faraday Soc. 34: 485. 1938.
15. STOBBE, M. Ann. Physik, 7(5): 661. 1930.

# A DESCRIPTION OF A LARGE DOUBLE-FOCUSING BETA SPECTROMETER AND ITS APPLICATION TO A STUDY OF THE DECAY OF $In^{114}$[1]

By M. W. Johns, H. Waterman,[2] D. MacAskill,[3] and C. D. Cox[4]

ABSTRACT

The design and performance of a Siegbahn type double-focusing beta spectrometer of radius of curvature 50 cm. are described. It has a resolution of 0.3% with a transmission of a few tenths of a per cent. A study of the decay of $In^{114}$ has revealed gamma rays in the $K$-capture branch of energies 0.556, 0.576, 0.722, 1.271, and 1.300 Mev. These define excited levels in $Cd^{114}$ of energies 0.556, 1.278, and 1.856 Mev. above the ground state. The end point of the $\beta^-$ spectrum is at 1.984 ± .004 Mev.

## INTRODUCTION

Since Siegbahn and Svartholm (14) first suggested the double-focusing magnetic-lens spectrometer, several instruments of this type have been described in the literature (1, 5, 12). The construction and performance of a Siegbahn-type double-focusing beta spectrometer of radius of curvature 50 cm. are described in this paper. The design was based on the theory given by Siegbahn and Svartholm and a similar treatment given by Shull and Dennison (13). The nomenclature of the latter authors will be used.

## THEORY OF THE SPECTROMETER

In principle the spectrometer is a modified semicircular instrument in which the field is made inhomogeneous in such a way as to provide both radial and axial focusing of electrons from the source. To achieve this the axial component of the magnetic field must be given by

$$H = H_0\left[1 - \frac{1}{2}\left(\frac{r-a}{a}\right) + \beta\left(\frac{r-a}{a}\right)^2 - \left(\frac{4\beta - 1}{4a^2}\right)z^2 + \ldots\right]$$

where $H_0$ refers to the axial field on the $r = a$, $z = 0$ circle. $\beta$ is a disposable parameter which affects the second order focusing properties of the field.

A few pertinent results from Shull and Dennison's paper (13) are given here. Using cylindrical coordinates $(r, \theta, z)$ consider the path of an electron leaving the point $(a + \delta r, 0, \delta z)$ of the source plane $(\theta = 0)$ in an initial direction making a small angle $\phi_r$ with the cylinder $r = a$ and a small angle $\phi_z$ with the plane $z = 0$. The image plane is defined by the equation $\theta = \pi\sqrt{2}$ and the trajectory of such an electron will pass through this plane at the point $(a + \delta r^*, \pi\sqrt{2}, \delta z^*)$. An analysis of the equations of motion shows that

[1] *Manuscript received October 17, 1952.*
*Contribution from the Department of Physics, Hamilton College, McMaster University, Hamilton, Ont.*
[2] *Recipient of a Research Council of Ontario Scholarship 1948–49. Present address: Department of Physics, University of British Columbia, Vancouver, B.C.*
[3] *Recipient of a National Research Council Bursary and Studentship, 1949–51. Present address: Royal Military College, Kingston, Ont.*
[4] *Recipient of a National Research Council Bursary, 1951–52. Present address: National Research Council, Ottawa.*

$$\delta r^* = -\delta r + \left(\frac{2-4\beta}{3a}\right)(\delta r^2 - \delta z^2) + \left(\frac{2-16\beta}{3}\right)a(\phi_r^2 - \phi_z^2) - \frac{1}{3a}\delta_z^2 - \frac{4a}{3}\phi_z^2,$$

$$\delta z^* = -\delta z + \frac{8\beta}{3a}\delta r\delta z + \frac{32\beta - 12}{3}a\phi_r\phi_z.$$

It is seen that the defects in the image are all of the second order in the small quantities $\delta r$, $\delta z$, $\phi_r$, and $\phi_z$ and that they may be minimized by an appropriate choice of the parameter $\beta$ in shaping the field. Rosenblum (11) has shown that $\beta = \frac{1}{4}$ gives the most perfect image and that good image formation may be expected for values of $\beta$ in the range $\frac{1}{8}$ to $\frac{3}{8}$.

For $a = 50$ cm. the terms involving $\delta r^2$ and $\delta z^2$ can be neglected if source or counter window dimensions are less than $2.5 \times 1.0$ cm. so that only the defocusing terms involving $\phi_r$ and $\phi_z$ need be considered. The fraction of the electrons transmitted by the instrument for a rectangular defining baffle is $\phi_{r\,\max.}\,\phi_{z\,\max.}/\pi$ and hence it is obvious that any attempt to reduce the size of the image by reducing $\phi_{r\,\max.}$ or $\phi_{z\,\max.}$ can only be made at the expense of transmission.

Since for $\beta = \frac{3}{8}$ the defocusing terms depend only on $\phi_r$, it was decided to shape the field to this choice of $\beta$ over a region defined by $\phi_{r\,\max.} = 0.10$ and $\phi_{z\,\max.} = 0.16$. With this choice the maximum possible transmission of the instrument would be 0.5% and the image formation would be defined by the equations:

$$\delta r^* \cong -\delta r - \frac{4a}{3}\phi_{r\,\max.}^2,$$

$$\delta z^* \cong -\delta z.$$

The shift in the image position for a fractional change $\delta H/H$ of the field is approximately given by

$$\delta r^* = 4a\delta H/H = 4a(\delta p/p).$$

Combining these results the expected resolution of the spectrometer will be

$$|(\delta p/p)| = \frac{\delta r}{4a} + \frac{1}{3}\phi_{r\,\max.}^2.$$

For $\phi_{r\,\max.} = 0.1$ this relation predicts a limiting resolution for very narrow source and detector of 0.3%.

## THE CONSTRUCTION OF THE SPECTROMETER

It is well known that it is possible to predict the properties of a large magnet from those of a small model by the use of simple scaling factors (16). In order to determine the correct profile for the pole faces of the large annular magnet to be used in the spectrometer, a mild steel model 1 ft. in diameter which could be machined in our research shop was constructed and tested. The gap in this model was made 6.55 cm. at $r = a = 11.54$ cm. and it was desired to shape the field from $r = 9.1$ to $r = 14$ cm.

The field exploration in the $z = 0$ plane was carried out by means of a search coil moved radially in known steps from infinity through the region of interest.

The cumulative deflection gave the value of $H_0$ while the differences could be used to obtain $H - H_0$ for any choice of $r$. This method made possible the measurement of $H/H_0$ to better than 0.2% over the range of interest, 0.9 to 1.1 $H_0$.

If edge effects are neglected and the pole faces are treated as equipotential surfaces, it can be shown that the desired field distribution will be obtained if the slope $\partial z/\partial r$ of each pole face is given by $g/4r$ where $g$ is the gap at radial distance $r$. This formula was used to compute the slope of each pole face at $r = a$ and adjustments in their contours to compensate for fringe effects were made at the inner and outer edges by cut and try methods. By this means, it was possible to obtain a good fit between the experimental curve and the desired theoretical one over the region desired.

The magnet used in the spectrometer was built from three forgings of Armco iron machined to the form shown in Fig. 1. The total mass is two tons. It has an over-all diameter of 52 in. and height of 17 in. The gap at the 50 cm. radius

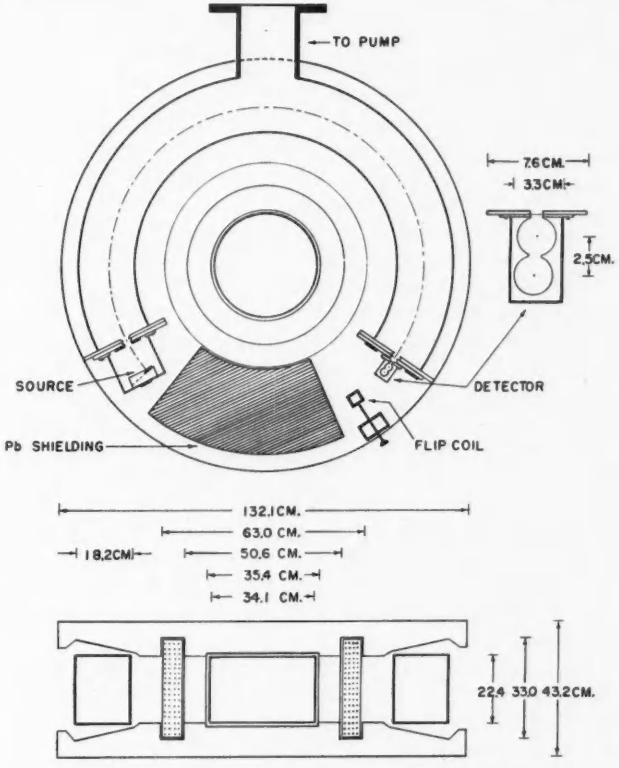


FIG. 1. Fifty centimeter double-focusing beta spectrometer.

is 28.4 cm. and the field in the $z = 0$ plane follows very closely the shape desired for good focusing from $r = 41$ to $r = 58$ cm.

The variation in the field in the vertical direction is quite sensitive to $\beta$ since

$$H_z(r, z) - H_z(r, 0) = -[(4\beta - 1)z^2/4a^2]\,H_0.$$

By exploring this field variation, it was found that $\beta$ appears to be nearer to $\frac{5}{8}$ than the value of $\frac{3}{8}$ desired. It was decided to test the focusing properties of the field as it was. Since these properties have proved satisfactory for our purpose, no attempt to improve the field has been made.

The vacuum chamber was constructed of $\frac{1}{4}$ in. aluminum sheet to form a tube of rectangular cross section 25 × 18 cm. extending through 237° of the electron path. The inner and outer radii of the chamber are 42 and 60 cm. respectively. The ends of the chamber are closed with sliding gates of brass which permit the source or detector assemblies to be changed easily and positioned accurately on the 50 cm. circle.

Baffles are provided at the 30°, 60°, 118°, 155°, 194°, and 224° positions. In addition, the exit slit from the source chamber acts as a source baffle. The transmission is determined by the choice of the 30° baffle which defines the electron beam.

A metal oil diffusion pump of capacity 100 liters per sec. and a Cenco Megavac fore-pump provide a vacuum of less than 1 micron. Fifty centimeters of lead shielding is provided between the source and detector. The magnet coils consist of 10,000 turns of No. 18 Formex wire wound in eight pi's.

An electronic stabilized power supply giving 850 ma. at 750 v. is used to supply and control the current. With this stabilizer (10) the current is kept constant to within 0.01% over long periods of time, while the short term variations are of the order of one part in a million. It is possible to focus 5 Mev. electrons with the spectrometer using this power supply.

Two types of detector have been used. The first is a cylindrical Geiger counter of diameter 4.12 cm. and length 14 cm., with a window 1.4 cm. by 7.6 cm. in the side wall. The thin window is supported by a brass grid which is transparent over 66% of its area. The counter has a normal background of about 40 counts per min.

The second detector shown in Fig. 1 consists of two Geiger counters in coincidence. Electrons entering the window must pass through both chambers to be detected. Combined with a coincidence circuit of resolving time 2 μsec., this counter has a natural background of 3.5 counts per min., with a 1 mc. $Co^{60}$ source placed in the source chamber. With betas from the chamber the coincidence counting rate is 0.7 of the counting rate in the front chamber. In order to reduce the photon crossfire between the two chambers, it was found necessary to use a filling of 2 cm. of alcohol with 8 cm. argon. With such fillings the coincidence plateau was of the order of 150 v. in length with a slope of 10% to 15% per 100 v. It has been possible to make useful measurements with this detector at counting rates of five particles per minute.

The magnetic field is measured by means of a flip coil and a Leeds and Northrup type $R$ galvanometer, with a lamp scale distance of 2 meters. The

galvanometer scale is linear within 0.6% over the entire range of deflections used and corrections for this lack of linearity are readily made. The magnet current as measured by the potential across a standard resistance is very nearly proportional to the field. If care in demagnetizing between runs is taken, it is possible to reproduce the field with a given current setting to within 0.2% at lower fields ($H\rho$ 1500) and to within 0.1% at higher ones ($H\rho$ 3000).

In operation it has been found useful to take potentiometer readings to evaluate the current and also flip coil readings to measure the field. Since the curve relating these is linear over the range of interest near any one peak, it is possible to use the potentiometer readings which are accurate to 0.05% to improve on the individual flip coil readings which are accurate to 0.3%. In this way the magnetic field readings for the position of a peak are reproducible to 0.1%.

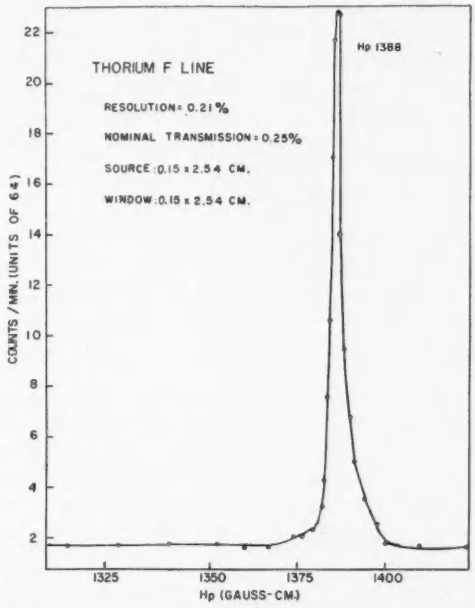


FIG. 2. Appearance of the thorium $F$ line under conditions of high resolution.

Because the source and detector are both small compared to the instrument dimensions, it is a very simple matter to exchange or relocate sources for the purposes of comparative measurements.

The focusing properties of the instrument have been examined with the $F$ line of Th B at $H\rho$ 1388 (8), the $Cs^{137}$ line at $H\rho$ 3381 (6), and the $X$ line of ThC″ at $H\rho$ 9988 (3) gauss-cm. The line shape is the same for all three. In addition, the line shape has been found to be independent of the direction of scanning. Fig. 2 shows a typical peak. The instrument has not yet been used for

very low momentum electrons ($H\rho \sim 500$) but it may be expected that in this region remanence in the iron may alter the focusing properties. The relation between the resolution, $\Delta p/p$, $\phi_{r\,\max.}$, and the source width $S$ for a narrow counter window seems to be quite well represented by the theoretical expression:

$$\Delta p/p = S/200 + \tfrac{1}{3}\phi_{r}{}^{2}{}_{\max.} \text{ applicable for } \beta = \tfrac{3}{8}.$$

TABLE I

| Source dimensions (cm.) | Window dimensions (cm.) | $\phi_{r\,\max}$ | Resolution (%) | Calculated transmission (%) | Effective transmission (%) |
|---|---|---|---|---|---|
| $2.5 \times 0.2$ | $3 \times 0.2$ | 0.05 | 0.25 | 0.15 | 0.05 |
| $2.5 \times 0.5$ | $3 \times 0.25$ | 0.10 | 0.5 | 0.3 | 0.1 |
| $2.5 \times 0.5$ | $3 \times 1.0$ | 0.10 | 0.7 | 0.3 | 0.2 |
| $2.5 \times 1.0$ | $3 \times 1.0$ | 0.10 | 1 | 0.3 | 0.3 |

Table I shows the performance of the instrument under various conditions of operation. The "calculated transmissions" are obtained from the formula $\phi_{r\,\max.}\ \phi_{z\,\max.}/\pi$ corrected for the 66% transmission of the window grid. The effective transmission, determined experimentally by using a $Cs^{137}$ source of known strength, is much more sensitive to window than source width and suffers seriously when very good resolution is required.

## THE GAMMA SPECTRUM OF $In^{114}$

The instrument described has proved useful in the study of radioactive decay processes. The experimental results given here will serve to illustrate its performance and support statements (4) which have emanated from this laboratory concerning the decay of $In^{114}$.

In the decay of $In^{114}$ a 50-day isomeric transition from the 0.192 level to the ground state is followed by a 72 sec. beta transition to the ground state of $Sn^{114}$. In addition to this dominant mode of decay, a $K$-capture process which occurs in a few per cent of the disintegrations was found by Boehm and Preiswerk (2) and Mei, Mitchell, and Zaffarano (9). This laboratory has studied this isotope both by energy measurements and coincidence experiments. The former are described below; the latter will be the subject of a subsequent publication.

The gamma spectrum of $In^{114}$ has been examined by external conversion using a lead radiator 2.5 cm. $\times$ 1 cm. and 19 mgm. per $cm.^2$ thick. The source consisted of 150 mgm. of indium metal which was given an activity of 150 mc. in the NRX pile at Chalk River. In order to avoid large corrections for radiator thickness, the 0.556 and 0.722 Mev. gamma rays were compared with the well known $Cs^{137}$ radiation of energy 0.6614 Mev. (6). The 1.3 Mev. radiation was compared to the $Co^{60}$ gamma rays at 1.1715 and 1.3316 Mev. (7). To do this, the gamma sources were interchanged with the radiator left in the same position. Since, in our case, the radiator thickness is such as to give an electron momentum spread considerably greater than the band admitted by the spectrometer (resolution 1%), the point of inflection on the high energy edge is a very reproducible position which should correspond closely to the electron momentum

with zero radiator thickness. In comparing peaks of nearly the same energies, corrections for radiator thickness may be neglected. In successive runs the flip coil reading of the position of this point of inflection on a peak of good intensity was reproducible to 0.1%.

The data are presented in Figs. 3 and 4 and the results tabulated in Table II.

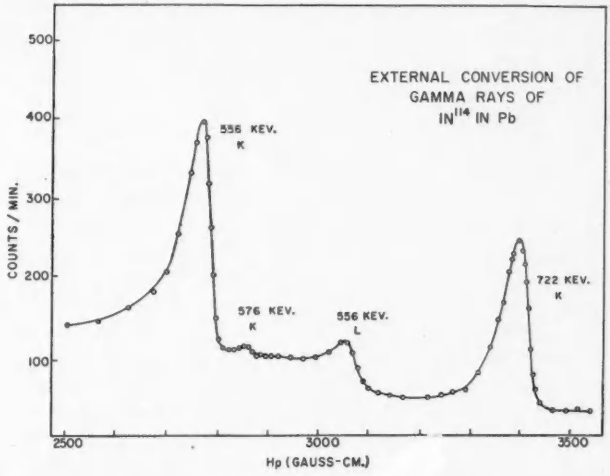


FIG. 3. External conversion lines of the 0.556, 0.576, and 0.722 Mev. gamma rays of $In^{114}$ in a 19 mgm. per cm.$^2$ lead radiator. The standard deviations of the individual measurements are shown by the size of the circles in the figure.

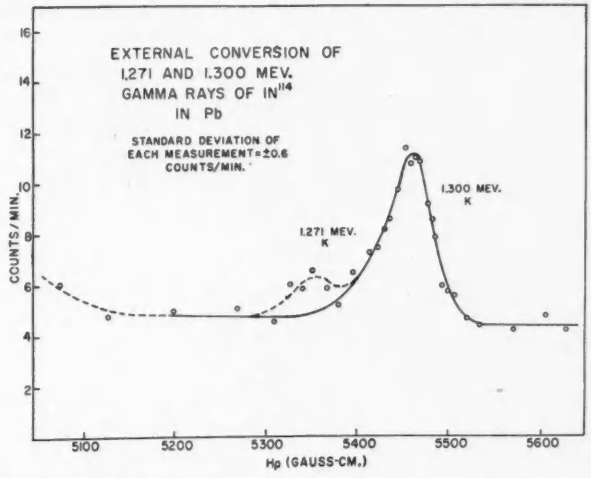


FIG. 4. External conversion of the 1.271 and 1.300 Mev. gamma rays of $In^{114}$ in a 19 mgm. per cm.$^2$ lead radiator.

TABLE II

ENERGIES AND INTENSITIES OF INDIUM$^{114}$ GAMMA RAYS

| Gamma energy (Mev.) | Intensity in quanta/disintegration | Comparison line |
|---|---|---|
| 0.5561 ± .001 | 0.036 | 0.6614 in $Cs^{137}$ |
| 0.5764 ± .003 | $1 \times 10^{-3}$ | 0.6614 in $Cs^{137}$ |
| 0.7225 ± .001 | 0.035 | 0.6614 in $Cs^{137}$ |
| 1.271 ± .006 | $3 \times 10^{-4}$ | 1.3316 in $Co^{60}$ |
| 1.300 ± .003 | $1.5 \times 10^{-3}$ | 1.3316 in $Co^{60}$ |

The energies and intensities of the two strong lines at 0.556 and 0.722 Mev. agree well with the values given in the literature.

The energy of the 1.3 Mev. gamma ray is too high for it to be the crossover transition which has been tacitly assumed by previous workers (9). The two weak gamma rays reported would have escaped detection by any of the low resolution instruments which have been used to study this spectrum, the 0.576 Mev. one because of the presence of the $L$ peak of the 0.556 and the 1.27 Mev. radiation because of the stronger 1.30 Mev. radiation. Even in this work, neither line is completely resolved. The heavy line drawn in Fig. 4 represents the shape of the 1.33 Mev. line of $Co^{60}$ with which the 1.30 Mev. line was compared, using the same radiator and source-radiator geometry, and it is obvious that the distortion on the low energy side is real. By the time its significance had been realized, the source had decayed to the point where we were unable to improve the statistical accuracy of the data in this region. The 1.300 and 0.576 Mev. radiations define an energy level at 1.85 Mev. A search for the 1.85 Mev. crossover to the ground state gave negative results. Its intensity is certainly less than $\frac{1}{4}$ of that of the 1.300 Mev. radiation. These gammas define excited states in $Cd^{114}$ of energies 0.556, 1.278, 1.856 Mev. This scheme is supported by coincidence experiments to be reported later.

The quantum yields were all based on a comparison of the 0.556 and 0.192 Mev. radiations, using an 8 mgm. per cm.$^2$ lead radiator and a thin-lens spectrometer. Since the internal conversion coefficient of the latter gamma is well known (15) and the 0.192 Mev. transition occurs in each disintegration, its yield of 19.3 quanta per disintegration could be computed. The yields of the others were determined from the photoelectric peak heights and the known dependence of the photoelectric cross section on the energy.

A thin beta source of strength about 1 mc. and area 2.5 cm. by 0.5 cm. was made by electroplating active indium metal (17) on copper foil. A search for the conversion lines of the 0.556, 0.722, and 1.3 Mev. gamma rays was unsuccessful because of the very large background of the $\beta^-$ continuum which extends to nearly 2 Mev.

A careful measurement of the $\beta$ end point was made, using this high specific activity source. The value obtained is 1.984 ± .004 Mev. and the data on which it is based are presented in Fig. 5.

This instrument has proved to be a powerful tool for the detailed examination of beta and gamma spectra and the accurate measurement of electron energies.

Because of its large dispersion, scanning must be done in steps of 0.5% in $H\rho$ or less to locate weak peaks. This is a serious disadvantage in the initial stages of an investigation. We have found that the low-dispersion thin-lens spectrometer also used in this laboratory is a very useful companion to this instrument for these preliminary measurements.

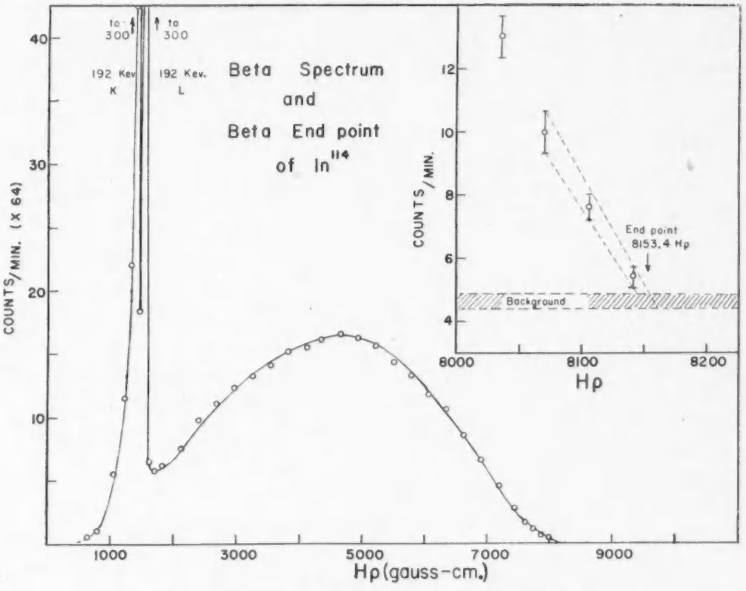


FIG. 5. Beta spectrum and beta end point of $In^{114}$.

## ACKNOWLEDGMENTS

We should like to acknowledge the assistance of Mr. T. H. Bryden, our instrument-maker, who helped greatly in the design of the instrument. Thanks are also due Dr. H. F. Dawes, emeritus professor of Physics, for his interest and advice, and to Dr. R. H. Tomlinson of the Chemistry Department for assistance in source preparation.

The financial assistance of the National Research Council of Canada in the form of grants is gratefully acknowledged. We are also indebted to both the National Research Council and the Research Council of Ontario for support in the form of scholarships to three of the authors.

## REFERENCES

1. BARTLETT, A. A. and BAINBRIDGE, K. T. Phys. Rev. 82: 316A. 1951.
2. BOEHM, F. and PREISWERK, P. Helv. Phys. Acta, 22: 331. 1949.
3. BROWN, W. L. Phys. Rev. 83: 271. 1951.
4. JOHNS, M. W., COX, C. D., DONNELLY, R. J., and MCMULLEN, C. C. Phys. Rev. 87: 1134L. 1952.

5. KURIE, F. D., OSABO, J. S., and SLACK, L. Rev. Sci. Instruments, 19: 771. 1948.
6. LANGER, L. M. and MOFFAT, R. D. Phys. Rev. 78: 74. 1950.
7. LIND, D. A., BROWN, J. R., and DU MOND, J. W. M. Phys. Rev. 76: 591A. 1949.
8. LINDSTROM, G. Phys. Rev. 83: 465L. 1951.
9. MEI, J. Y., MITCHELL, A. C. G., and ZAFFARANO, D. J. Phys. Rev. 76: 1883. 1949.
10. MILLER, S. E. Electronics, 14 (11): 27. 1942.
11. ROSENBLUM, E. S. Phys. Rev. 72: 731L. 1948.
12. SHULL, F. B. Phys. Rev. 74: 917. 1948.
13. SHULL, F. B. and DENNISON, D. M. Phys. Rev. 71: 681 and 72: 256. 1947.
14. SIEGBAHN, K. and SVARTHOLM, N. Arkiv. Mat. Astron. Fysik, A, 33: No. 21. 1947.
15. STEFFEN, R. M. Phys. Rev. 83: 166. 1951.
16. STONER, E. C. Magnetism. Methuen & Co. Ltd., London. 1930.
17. YATAWAGA, S. J. Soc. Chem. Ind. Japan, 44. 1941. Abstracted in "A bibliography of indium," 1941–2 supplement, p. 21, Indium Corporation of America.

# MEASUREMENT OF THE HALF-LIVES OF AcC″, $Cu^{66}$, $Mg^{27}$, $Ti^{51}$, $Tl^{206}$, AND $V^{52}$[1]

By B. W. Sargent,[2] L. Yaffe,[3] and A. P. Gray[4]


## ABSTRACT

With the exception of AcC″, which was collected by recoil, the radionuclides were produced by irradiating 'spec.-pure' metals or oxides with neutrons in the NRX reactor. The $\beta$-activities were measured by the rate of deflection of a quartz fiber in an electroscope of recent design. The residual activities were carefully analyzed and eliminated from the main activities by subtraction. Half-lives were determined by the method of least squares. In the case of copper, the effect of the positrons and negatrons from $Cu^{64}$ was suppressed with an aluminum absorber. The following values were found for the half-lives: AcC″, $4.79 \pm 0.02$; $Cu^{66}$, $5.10 \pm 0.02$; $Mg^{27}$, $9.45 \pm 0.04$; $Ti^{51}$, $5.79 \pm 0.03$; $Tl^{206}$, $4.19 \pm 0.02$; and $V^{52}$, $3.76 \pm 0.02$ min. The half-life found for $Cu^{66}$ from the measurements with the electroscope was confirmed in some measurements with a proportional counter and scale of 1000.


## INTRODUCTION

Discordant values for the half-life of $Cu^{66}$ in the literature in late 1950 induced us to undertake its measurement with an accuracy to better than 1%. We originally intended to use actinium C″($Tl^{207}$) as a test of the linearity of the activity-measuring equipment, as its half-life, 4.76 min., was considered known to $\frac{1}{2}$%. It was also rather convenient that 4.76 min. falls between 4.34 and (about) 5 min. reported for the half-life of $Cu^{66}$. After considerable effort had been expended on eliminating systematic errors and on improving consistencies, an absolute accuracy of 2 parts in 500 in the half-lives was thought to have been attained. It was therefore unnecessary to use the half-life 4.76 min. of AcC″ as standard. New values for the half-lives of AcC″, $Cu^{66}$, $Mg^{27}$, $Ti^{51}$, $Tl^{206}$, and $V^{52}$ are reported in this paper.

In the ideal experiment a perfectly pure radioactive nuclide would be prepared, and its activity followed over many decreasing powers of two with measuring equipment having perfect linearity of response and negligible background. The half-life would be obtained from a trustworthy analysis of the activity measurements such as by the method of least squares. In practice some unwanted radioactivities are present, and steps must be taken to reduce their intensities as far as possible. One must then correct the main decay curve for the irreducible minima of unwanted activities and analyze for the half-life. All, except AcC″, of the radioactive nuclides used in the experiments were produced by the radiative capture of slow neutrons in the NRX heavy water reactor. By using the purest materials that could be commercially obtained, radioactivities produced by radiative capture of neutrons in impurities were relatively small. Owing to the relatively high flux of slow neutrons in the reactor and to the naturally small cross

[1] *Manuscript received October 30, 1952.*
*Contribution from the Physics and Chemistry Branches, Atomic Energy of Canada, Limited, Chalk River, Ont. Issued as A.E.C.L. No. 30.*
[2] *Present address: Department of Physics, Queen's University, Kingston, Ont.*
[3] *Present address: Department of Chemistry, McGill University, Montreal, Que.*
[4] *Present address: Department of Chemistry, Massachusetts Institute of Technology, Cambridge, Mass.*

sections for the fast neutron $(n, p)$, $(n, \alpha)$, and $(n, 2n)$ reactions, the activities produced by them were also small. In the case of copper, where the stable isotopes $Cu^{63}$ and $Cu^{65}$ have similar abundances and capture cross sections, the unwanted $Cu^{64}$ activity as measured was reduced almost to a negligible proportion by the choice of short irradiation time and by differential absorption. Fortunately, the charged particles from $Cu^{66}$ are much more energetic than those from $Cu^{64}$. An aluminum absorber of thickness approximately equal to the ranges of the negatrons and positrons from $Cu^{64}$ was always used between the activated copper and the activity-measuring equipment.

In most of the work, the $\beta$-activities of the sources were measured by ionization in a quartz-fiber electroscope (known as Type TQQ at Chalk River). After the electroscope had been subjected to a test for loss of ions by recombination, it was modified to operate at a sufficiently high voltage that these small losses were completely eliminated. The very concordant results obtained with the TQQ electroscope show that it is an extremely reliable and accurate instrument. Some confirming measurements of the half-life of $Cu^{66}$ were made with a proportional counter and associated equipment. The counting losses at high rates were determined experimentally and taken into account. The TQQ electroscope and counting equipment will be described in detail in the next sections.

## TYPE TQQ ELECTROSCOPE

The Chalk River electroscope, Type TQQ, was designed in 1945 by Dr. H. Carmichael to meet the need for an instrument capable of measuring strong $\beta$-emitting sources. This electroscope is similar to the Faraday gold-leaf electroscope in that the voltage which deflects the index also serves to collect the ions. A simple instrument of this type is ideally suited for precision work because, given that the insulation is good, the position of the index apart from movement due to gravity can only be affected by the action of ionizing radiation. There are no auxiliary voltages which have to be adjusted and maintained constant.

A sectional perspective drawing of the TQQ electroscope in Fig. 1 shows a hemispherical collecting electrode $E$, 5 cm. in radius, mounted on an insulator within a thick-walled hemispherical chamber $C$. The source holder $S$ is on a simple mechanical slide, which can be withdrawn for loading and then pushed in so that the source is approximately at the center of the hemispherical electrode. This electrode is connected to the deflecting electrode $D$ through an insulator. The index of the electroscope is a quartz fiber, usually about 6 microns thick, bent in the form of a V. The ends of the V are fused to a thick T-shaped quartz support which is cemented into a hole in the flat face of a brass block $B$ in the shape of a segment of a sphere. The spherical surface of this block is mounted on the wall of the electroscope in such a way as to permit easy adjustment of the position of the index. The quartz index is made electrically conducting by means of a sputtered coating of gold; it is maintained at ground potential.

When the deflecting electrode $D$ is charged by means of a push-button (shown in inset drawing), the apex of the quartz V moves towards the deflecting electrode. The end of the V appears as a straight line across the field of view of the telemicroscope incorporating an eyepiece scale of 100 divisions. Illumination is by a

lamp and condensing lens, as shown. An open-ended brass cylinder with holes to allow passage of the light is fitted onto the deflecting electrode and is an important feature in that it makes the scale deflections of the index almost exactly linear. In a typical electroscope the fiber does not appear on the scale until some 100 v. have been applied to the charged electrode, and the index may reach the other end of the scale at about 120 v.

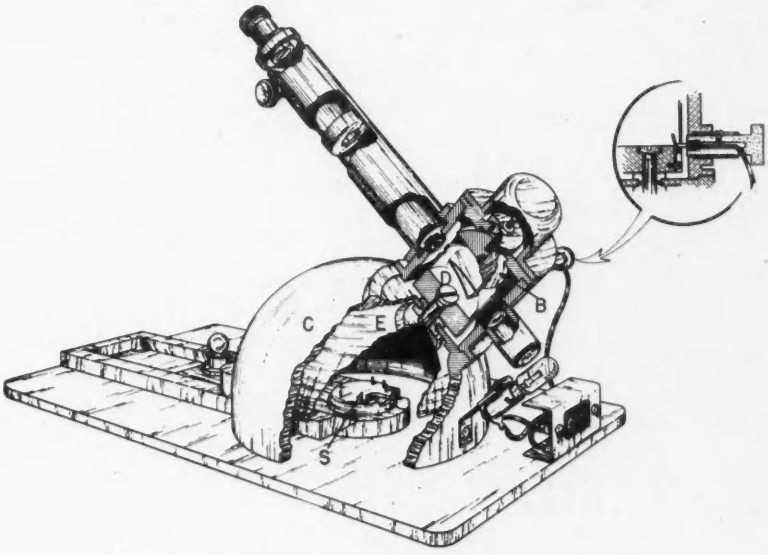


FIG. 1. A sectional perspective drawing of the TQQ electroscope.

We made some saturation tests on a TQQ electroscope modified by the addition of an insulated grid located just above the floor of the ionization chamber. This arrangement permitted the application of various voltages across the ionization chamber while the voltage between the quartz index and deflecting electrode was maintained at its normal value. Three sources of $P^{32}$ of graded strengths were placed in aluminum trays that would fit into the source holder. Rates of deflection were measured as a function of the potential difference between 35 and 250 v. across the ionization chamber. Saturation was obtained, even with the strongest $P^{32}$ source, at 200 v. As examples of the losses of ions by recombination, at 85 v. these were respectively 1.8, 1.2, and 0.8% for sources *A*, *B*, and *C*. Using a capacitance of 37 $\mu\mu$f. for the normal system, the saturation currents were estimated to be 81, 39, and 16 $\mu\mu$amp. for *A*, *B*, and *C* respectively.

For the measurements on half-lives, the quartz fiber in a TQQ electroscope with working range 75–95 v. was replaced by a thicker one in order to bring the working range between 230 and 280 v. (0–100 divisions) where saturation was assured. Associated with an increase in working voltage, the sensitivity of the

instrument decreases by a factor that is approximately the ratio of the applied voltages. Ratios of the intensities of the $P^{32}$ sources were carefully measured on the unmodified and modified electroscope. These agreed to 0.5% when the percentage losses for recombination listed above were applied. We are therefore confident that the activity measurements for the determination of half-lives do not contain systematic errors arising from recombination of ions.

Rates of deflection were measured over 60 scale divisions with a reliable stop watch. The times at the beginnings of the readings were noted and recorded from a watch with a seconds hand and known accuracy. Observations of the temperature of the outer hemispherical shell of the ionization chamber were occasionally made. The rates of deflection were normalized to correspond to a standard mass of air in the ionization chamber on the assumption that the ionization of the $\beta$ particles is directly proportional to the density. Relative corrections for density changes were always smaller than $\frac{1}{2}$%. Barograph records were sometimes noted, but the changes in atmospheric pressure over the hour or two of a run were so small that their effects on the density were completely negligible.

## COUNTING EQUIPMENT

The proportional counter and its associated equipment has been described by Yaffe and Stevens (39). The counter with thin glass window (30 mgm. per cm.$^2$) was filled with argon (67 cm.) and carbon dioxide (6 cm.). The counter assembly consisted of a preamplifier, linear amplifier, high voltage (3000 v.) supply, scale of 1000, and an Esterline–Angus recorder. The speed of the paper on the recorder was determined by counting line frequency (60 cycles per sec.). Each 0.75-in. division on the paper corresponded to 3.75 sec. In the measurements on the decay of $Cu^{66}$ the counting rates were usually determined in counts per quarter minute. During a run the scale was switched from 1000 to 100 and then to 10 at appropriate rates. The duration of a run was 90 min.

The counting losses of the equipment were measured by the addition of sources in a separate investigation. Eight sources of $P^{32}$ were prepared and deposited in aluminum trays. Their counting rates ranged from 1000 to 9000 per sec. The trays could be firmly mounted in two spring-loaded slots fastened to a lead block beneath the counter window. The procedure was as follows. One sample was counted with a blank tray in the second position to ensure identical $\beta$-scattering conditions. The blank tray was replaced with a second $P^{32}$ sample, and the two samples counted. The first sample was replaced with a blank tray, and the second sample counted. Let the observed counting rates (excluding background) be $N_1$, $N_3$, and $N_2$ respectively. The formula proposed by Kurbatov and Mann (19) was used to relate the observed rate $N$, the true rate $N_0$, and a dead time $\tau$:

$$N/N_0 = 1 - N\tau.$$

In our notation

$$\tau = \left\{1 - \left(1 - \frac{\Delta N_3}{N_1 N_2}\right)^{\frac{1}{2}}\right\} \Big/ N_3,$$

where $\Delta = N_1 + N_2 - N_3$. Two series of runs, each with five determinations, gave

$$\tau = 8.1 \pm 0.2\ \mu\text{sec}.$$

Since $\tau$ is constant within experimental error for the counting rates used, the correction formula above is adequate for our purpose. The counting rates observed with the $Cu^{66}$ sources were corrected accordingly for losses.

## METHOD OF ANALYSIS

Particular attention was given to the estimation of the unwanted activities with half-lives greater than that of the nuclide under investigation. The total activity varies with the time $t$ according to the formula:

$$A_1 e^{-\lambda_1 t} + A_2 e^{-\lambda_2 t} + A_3 e^{-\lambda_3 t} + A_4,$$

where the transformation constants $\lambda_1$, $\lambda_2$, and $\lambda_3$ are associated with the half-lives $T_1$, $T_2$, and $T_3$ in increasing order, and $A_1$, $A_2$, and $A_3$ are the initial values. $A_4$ is the constant background of the electroscope (0.005 div. per min.) or counter (30 counts per min.). $T_1$ is the half-life being measured. The analysis of the background must give $A_2$ and $A_3$ (if it is not negligible) and also $\lambda_2$ and $\lambda_3$ if these are not already known.

The activities are the observations in divisions per minute with the electroscope or counts per quarter minute with the proportional counter. (Corrections have already been applied for changes in air density or for counting losses.) First approximations for $A_1$ and $T_1$ are obtained from a semilogarithmic plot. For the later observations where the values of $A_1 e^{-\lambda_1 t}$ are less than half the observed, these are calculated and subtracted. From the resulting values of the residual activity, $A_2$, etc. are obtained by computation and graphs. The contribution of these longer period activities is calculated and subtracted from each observation to give a set of values for $A_1 e^{-\lambda_1 t}$. In practice this set is terminated before $A_1 e^{-\lambda_1 t}$ is less than half the observed. The method of least squares is applied to fit a straight line to the points in the semilogarithmic plot. Errors are assumed to be in the logarithms of the activities but not in the times, and the points are given equal weights. The values of $A_1$ and $T_1$ given later in the tables were obtained in this way. Since all of the analyses were done twice, the first approximations for $A_1$ and $T_1$ needed at the beginning of an analysis were quite accurate at the second computation.

The activity measurements were made over finite intervals of time, which increased during each run when the electroscope was used. Since the elapsed times were taken to the mid-points of the readings, corrections must be applied to some of the rates of deflection in divisions per minute. The ratio of the measured average rate over an interval $\Delta t$ to the instantaneous rate at the mid-point of the time interval is

$$(\sinh \tfrac{1}{2}\lambda_1 \Delta t)/\tfrac{1}{2}\lambda_1 \Delta t.$$

When $\Delta t/T_1$ is not large, the value of this ratio is

$$1 + 2{\cdot}00 \times 10^{-2}\left(\frac{\Delta t}{T_1}\right)^2.$$

In the analyses these expressions were used (where necessary) to convert observed rates of deflection to the instantaneous rates at the mid-points of the time intervals.

## ACTINIUM C″ ($Tl^{207}$)

*Survey of Other Work*

Actinium C″ was discovered in 1908 by Hahn and Meitner (14), who made six measurements of its half-life. Their result was 5.1 ± 0.1 min. Kovářik (17) used the results from 150 decay curves to plot a distribution resembling a probability curve. The most probable value was 4.71 min., while almost all the measurements fell between 4.60 and 4.85 min. Further measurements of the half-life of AcC″ were made by Albrecht (1) and Sargent (28). Albrecht reported that the individual values were almost always greater than 4.71 min. and lay in the interval 4.70 to 4.80 min. A set of nine best values were between 4.75 and 4.78 min. inclusive; from these the final result was 4.76 min. The duration of the runs seems to have been about 20 min., and in this time about seven activity measurements were made with an ionization chamber and electrometer. In Sargent's experiment some 20 measurements of ionization current by the rate of deflection of an electrometer needle were made in the course of each run of about 25 min. duration. Unfortunately, corrections of the order of 10% had to be applied to some of the observed rates of the needle owing to its peculiar motion (27). In spite of these limitations, individual measurements of the half-life were in close accord, and the final result was 4.76 ± 0.02 min.

*Results*

A very pure and rather active preparation of actinium was available for the production of actinon. Actinium (B + C) was collected by recoil and an electric field in moist air onto a platinum disk separated about 1 mm. from the actinium. The duration of collection was about two hours. Actinium C″ was in turn collected similarly by recoil onto a square sheet of silver. Maximum activity is obtained when the collection time is about 15 min. The silver sheet was quickly wrapped with aluminum foil (2 mgm. per cm.$^2$) and placed in the electroscope. Measurements were taken for about two hours.

TABLE I

MEASUREMENT OF THE HALF-LIFE OF AcC″

TQQ Electroscope. Activities $A$ in div. per min.

| Date 1951 | $A_1$ | $A_2$ | $A_3+A_4$ | $T_1$(min.) |
|---|---|---|---|---|
| Mar. 2* | 528.8 | 29.07 | 0.88 | 4.768 |
| Mar. 21 | 220.3 | 9.33 | 0.32 | 4.778 |
| Mar. 22 | 232.1 | 13.58 | 0.20 | 4.773 |
| May 2 | 117.2 | 7.60 | 0.70 | 4.832 |
| May 4 | 172.1 | 10.63 | 0.48 | 4.816 |
| | | | | Av. 4.793 |
| July 16 | 107.0 | 0.360 | 0.015 | 4.793 |
| July 17 | 146.7 | 0.880 | 0.090 | 4.780 |
| July 18 | 116.4 | 0.427 | 0.038 | 4.797 |
| July 19 | 168.4 | 0.340 | 0.040 | 4.780 |
| July 20 | 162.2 | 0.525 | 0.037 | 4.795 |
| | | | | Av. 4.789 |

**The run of March 2, 1951 was made with the TQQ electroscope before it was modified to have the working range 230–280 v. The sensitivity is approximately three times what it was after the modification. In this case it was necessary to correct the rates of deflection for losses of ions by recombination.*

Results are shown in Table I and Fig. 2. As expected, the residual activity consists of a 36.1-min. component, Ac(B + C), and a long period component, which result from aggregate recoil. In the first five runs (Table I) the source was covered with only one aluminum foil. As this was not sufficient to stop the $\alpha$ particles, the residual activity is comparatively high. In the last five runs the source was covered with four layers of aluminum foil, which stop the $\alpha$ particles. The values of the half-life of AcC″ are in particularly good agreement in the last five runs. The final result is 4.79 ± 0.02 min., where the error quoted contains some allowance for unknown systematic error. Fig. 2 shows some of the measurements, after corrections for residual activities, etc. have been made.

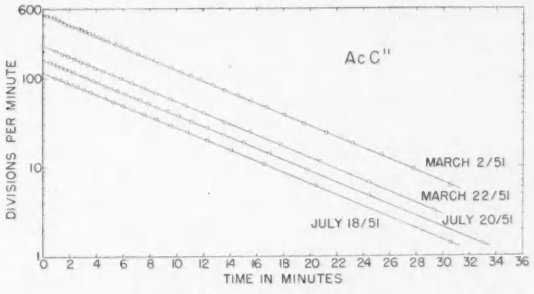


FIG. 2. Decay of AcC″ sources.

## COPPER[66]

*Survey of Other Work*

The 5-min. $\beta$-activity of copper was first produced by the bombardment of copper with slow neutrons and of zinc with fast neutrons in the classical investigations of Fermi *et al.* (3, 11). A radiochemical test indicated that the active nuclide was a copper isotope. The identification of the 12.8-hr. activity, produced in copper by neutrons and deuterons, as $Cu^{64}$ led Van Voorhis (35) to suggest that the 5-min. activity was due to $Cu^{66}$. Chang, Goldhaber, and Sagane (7) suggested that the 5-min. activity that they produced in gallium by bombardment with fast neutrons arose from the nuclear reaction $Ga^{69}(n,\alpha)\ Cu^{66}$.

Until recently, few authors have quoted more than one significant figure for the half-life of $Cu^{66}$. In the course of work on the energy spectrum of the $\beta$ particles in a cloud chamber, Sinma and Yamasaki (34) obtained 5.1 min. from a decay curve. In a study of the absorption of the $\gamma$ rays in lead, Meitner (21) found 5.05 ± 0.05 min. from several decay curves. Silver (32) obtained 4.34 min. for the half-life of $Cu^{66}$ with the aid of a differential ionization chamber and a vibrating reed electrometer. In consequence of new measurements (including the one in this paper), this value has been withdrawn (33).

Cameron and Katz (6) found 5.18 ± 0.10 min. for the half-life of $Cu^{66}$ from a decay curve taken with a Geiger counter. From an experiment with a flow proportional counter, the value 5.12 ± 0.05 min. was deduced by Schuman and Camilli (29). The decay scheme of $Cu^{66}$ was studied with spectrometers by Friedlander and Alburger (12), who reported a half-life of 5.2 ± 0.1 min. Using scintil-

lation detectors, Roderick, Meyerhof, and Mann (26) studied the radiations from $Cu^{66}$ and in the course of their work obtained 5.17 ± 0.07 min. for the half-life. The last three measurements have appeared since the work described in this paper was undertaken.

The end point of the $\beta$-spectrum has been given as 2.9 Mev. from cloud chamber measurements and a K.-U. plot (34) (which gives too high a value), 2.58 Mev. by absorption (13), and, finally and most accurately, 2.63 ± 0.02 Mev. with a lens type spectrometer (12).

*Results*

The copper and other materials for irradiation with neutrons in this work were obtained from Johnson, Matthey and Company. In the copper (Laboratory No. 2266) spectral lines* due to impurities were found only for silver, nickel, lead, iron, and manganese.

The experimental procedure was as follows. A small piece of copper foil weighing a few milligrams was enclosed in a 'spec.-pure' iron capsule and irradiated for about one second in the core of the NRX reactor. The pneumatic device, sometimes known as the 'rapid action rabbit', was used to return the capsule to a lead flask (39). The foil was cut down in size until its activity was suitable for the activity-measuring equipment. The lapse of time was 5 to 10 min. All measurements were made with an aluminum absorber of 0.216 gm. per cm.$^2$ over the source to stop the positrons and negatrons from $Cu^{64}$. The activity measurements were continued for about two hours with the electroscope or one and one-half hours with the proportional counter.

TABLE II

MEASUREMENT OF THE HALF-LIFE OF $Cu^{66}$

TQQ Electroscope. Copper activities $A$ in div. per min.

| Date 1951 | $A_1$ | $A_2$ | $T_1$(min.) |
|---|---|---|---|
| a.m. May 11 | 307.6 | 0.22 | 5.104 |
| p.m. May 11 | 610.4 | 0.38 | 5.100 |
| a.m. May 14 | 995.4 | 0.60 | 5.102 |
| p.m. May 14 | 601.1 | 0.38 | 5.109 |
| | | | Av. 5.104 |

TABLE III

MEASUREMENT OF THE HALF-LIFE OF $Cu^{66}$

Proportional counter. Copper activities $A$ in counts per quarter minute.

| Date 1951 | $A_1$ | $A_2$ | $A_4$ | $T_1$(min.) |
|---|---|---|---|---|
| Sept. 4 | 92,960 | 129.1 | 7.48 | 5.099 |
| Sept. 5 | 133,900 | 92.8 | 7.46 | 5.069 |
| Sept. 6 | 129,900 | 87.3 | 7.47 | 5.092 |
| | | | | Av. 5.087 |

**The results of spectrographic analysis given here and later in this paper were provided by Johnson, Matthey and Co., Ltd.*

Results of analysis of the measurements with the electroscope and counter are shown in Tables II and III respectively. The residual activity is 12.8-hr. $Cu^{64}$. Fig. 3 shows the corrected activities of $Cu^{66}$ in a semilogarithmic plot.

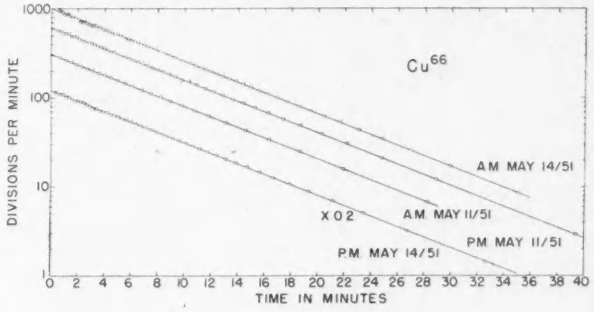


FIG. 3. Decay of $Cu^{66}$ sources.

The measurements with the counter were analyzed with the IBM machines at Chalk River. The half-life of $Cu^{64}$ was assumed, and first approximations to the other quantities including the natural background (about 30 counts per min.) were used in setting up for a least squares fit. The derived values are shown in Table III.

The final value for the half-life of $Cu^{66}$ is $5.10 \pm 0.02$ min.

## MAGNESIUM$^{27}$

### *Survey of Other Work*

Fermi and collaborators (3) found that a 10-min. $\beta$-activity was produced in magnesium by slow neutrons and in aluminum by fast neutrons. The radioactive nuclide was chemically identified as an isotope of magnesium. The mass assignment 27 followed from the only likely reactions—$Al^{27}(n,p)\ Mg^{27}$ and $Mg^{26}(n,\gamma)\ Mg^{27}$. Henderson (15) and Crittenden (8) reported a half-life of $10.25 \pm 0.25$ and $10.0 \pm 0.1$ min. respectively for the same nuclide produced in the Mg $(d,p)$ reaction. Eklund and Hole (9) obtained $9.58 \pm 0.10$ min. for the half-life from 24 runs with a Geiger counter and five runs with an ionization chamber and electrometer. The $\beta$-spectrum has been studied by the absorption (15, 38, 23), cloud chamber (8, 9), and spectrometer methods (4). Good agreement was obtained in locating the end point, which is at 1.80 Mev.

### *Results*

In the 'spec.-pure' magnesium oxide (Laboratory No. 2987) spectral lines due to impurities were found only for sodium, silicon, lithium, calcium, copper, silver, potassium, aluminum, iron, and boron. The irradiation procedure was the same as described for copper. The magnesium oxide sample weighed 5 mgm. The duration of irradiation in the reactor was 15 min. The sample was covered with aluminum foil (2 mgm. per $cm.^2$) during the activity measurements with the electroscope. The analysis of the residual activity showed weak activities of

TABLE IV

MEASUREMENT OF THE HALF-LIFE OF $Mg^{27}$

TQQ Electroscope. Activities $A$ in div. per min.

| Date 1951 | $A_1$ | $A_2$ | $A_3$ | $T_1$(min.) |
|---|---|---|---|---|
| June 20 | 379.1 | 0.40 | 1.10 | 9.456 |
| July 25 | 459.3 | 0.52 | 1.25 | 9.458 |
| Aug. 1 | 438.2 | 0.43 | 1.06 | 9.425 |
| Aug. 7 | 335.4 | 0.33 | 0.79 | 9.452 |
| Aug. 9 | 352.6 | 0.28 | 0.76 | 9.437 |
| | | | | Av. 9.446 |

half-lives 70 ± 20 min. and 14.9 hr. The latter is probably $Na^{24}$. Results are shown in Table IV and Fig. 4. The final result for the half-life of $Mg^{27}$ is 9.45 ± 0.04 min.

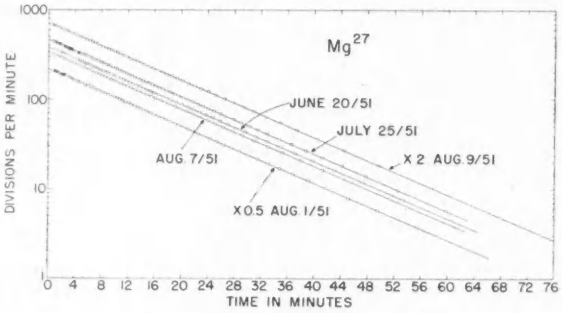


FIG. 4. Decay of $Mg^{27}$ sources.

## TITANIUM[51]

*Survey of Other Work*

The 6-min. nuclide $Ti^{51}$ escaped detection in the early experiments (3, 36) on the $(n,\gamma)$ and $(d,p)$ reactions in titanium. Using titanium metal and pile neutrons, Seren, Friedlander, and Turkel (31) obtained a half-life of 6 min. over three half-lives. Segrè (30) has reported a half-life of 6 min. and a maximum energy of 1.6 Mev. for the $\beta$ particles by an absorption method. The 72-day activity, found and attributed to $Ti^{51}$ by Walke, Williams, and Evans (37), has been traced to impurities such as 46-day $Hf^{181}$ and 60-day $Sb^{124}$ by Miskel, der Mateosian, and Goldhaber (22). Nuclear isomerism in $Ti^{51}$ does not occur.

*Results*

Spectral lines of impurities in the 'spec.-pure' titanium dioxide (Laboratory No. 2925) were found only for tin, magnesium, silver, calcium, and silicon. A sample of titanium dioxide, weighing 5 mgm., was irradiated for 20 min. in the reactor. It was then covered with 2 mgm. per $cm.^2$ aluminum, and its activity measured in the electroscope for about two hours. Subsequent measurements of the residual activity were made occasionally for several days. The analyses,

TABLE V

MEASUREMENT OF THE HALF-LIFE OF $Ti^{51}$

TQQ Electroscope. Activities $A$ in div. per min.

| Date 1951 | $A_1$ | $A_2$ | $A_3+A_4$ | $T_1$(min.) |
|---|---|---|---|---|
| June 28 | 523.8 | 13.7 | 0.35 | 5.778 |
| June 29 | 662.5 | 17.4 | 0.58 | 5.784 |
| July 4 | 510.4 | 20.5 | 0.50 | 5.792 |
| Aug. 3 | 339.5 | 5.5 | 0.15 | 5.796 |
| | | | | Av. 5.787 |

shown in Table V, reveal a moderately strong component of half-life about 40 min. and a very weak component of longer life. The decay of $Ti^{51}$ is shown in Fig. 5. The final value of the half-life is 5.79 ± 0.03 min.

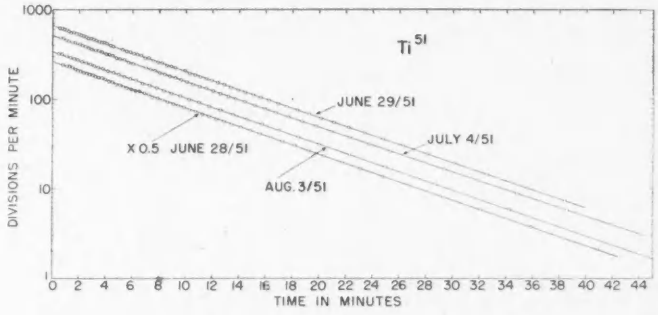


FIG. 5. Decay of $Ti^{51}$ sources.

## THALLIUM$^{206}$

*Survey of Other Work*

Preiswerk and von Halban (25) observed a 4 ± 0.5 min. $\beta$-activity in thallium after bombardment with neutrons. From the observation that the activity was enhanced when the neutrons were slowed down and from the negative results of attempted chemical separations, they concluded that the radioactive nuclide was either $Tl^{204}$ or $Tl^{206}$. Heyn (16) and Pool, Cork, and Thornton (24) reported respectively a 4.1 and 5 min. activity produced in thallium by bombardment with fast neutrons. Heyn favored the assignment $Tl^{204}$ from the supposed reactions $Tl^{203}$ $(n,\gamma)$ and $Tl^{205}$ $(n,2n)$; this is now known to be incorrect. The same radioactive nuclide was made by the $Tl(d,p)$ reaction by Fajans and Voigt (10) and by Krishnan and Nahum (18). Both groups chemically identified the nuclide as a thallium isotope. Krishnan and Nahum reported its half-life as 4.4 ± 0.1 min. Fajans and Voigt carefully compared the half-life with that of AcC″. They found that the activity obtained by short bombardment of thallium, with slow and fast neutrons and deuterons, had an average half-life of 4.23 ± 0.03 min. Under the same conditions of measurement with their Lauritsen electroscope, the half-life of AcC″ was 4.77 ± 0.05 min., in good agreement with the accepted value. The

correct mass assignment was shown to be 206 by Broda and Feather (5), who discovered an $\alpha$ particle branching from RaE ($Bi^{210}$) going to a 4.2-min. thallium isotope, which could only be $Tl^{206}$.

The maximum energy of the $\beta$ particles from $Tl^{206}$ was found to be about 1.7 Mev. by the absorption method (10, 18). Using a lens spectrometer and samples of thallium irradiated by pile neutrons, Alburger and Friedlander (2) obtained an apparently simple $\beta$-spectrum with an end point at $1.51 \pm 0.01$ Mev. The half-life observed was $4.3 \pm 0.1$ min.

*Results*

The impurities in the 'spec.-pure' thallium metal (Laboratory No. 2544) revealed by spectral lines were lead, magnesium, aluminum, copper, calcium, silicon, cadmium, iron, zinc, sodium, manganese, and silver. A few milligrams of

TABLE VI

MEASUREMENT OF THE HALF-LIFE OF $Tl^{206}$
TQQ Electroscope. Activities $A$ in div. per min.

| Date 1951 | $A_1$ | $A_2$ | $T_1$(min.) |
|---|---|---|---|
| a.m. Aug. 15 | 304.5 | 0.14 | 4.194 |
| a.m. Aug. 16 | 654.8 | 0.45 | 4.198 |
| p.m. Aug. 16 | 693.4 | 0.44 | 4.190 |
| a.m. Aug. 17 | 523.5 | 0.53 | 4.186 |
| p.m. Aug. 17* | 63.2 | 0.07 | 4.185** |
| | 63.1 | 0.07 | 4.195† |
| | | | Av. 4.192 |

**This sample was irradiated under cadmium.*
***All points shown in Fig. 6 were used in the least squares solution.*
*†The last point shown in Fig. 6 was omitted in the least squares solution. This run was omitted in finding the average half-life.*

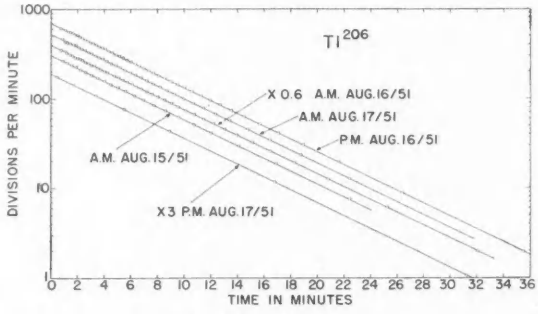


FIG. 6. Decay of $Tl^{206}$ sources.

the thallium metal were irradiated for one or two minutes in the reactor. The sample was covered with Scotch tape and its activity followed for a few hours. The main component of the weak residual activity had a half-life of the order of one hour. The results may be seen in Table VI and Fig. 6. The half-life of $Tl^{206}$ is $4.19 \pm 0.02$ min.

In one experiment (p.m. Aug. 17) the thallium sample was irradiated under cadmium to exclude thermal neutrons. If the reaction $Tl^{205}(n,p)$ $Hg^{205}$(5.5 min.) had been contributing to the activity, it would have been enhanced relative to $Tl^{205}(n,\gamma)$ $Tl^{206}$ in this experiment. As the half-life found did not differ from those obtained by irradiating in the normal manner, $Hg^{205}$(5.5 min.) could not have been present in a disturbing amount.

## VANADIUM[52]

### *Survey of Other Work*

The radioactive nuclide $V^{52}$ was discovered by Fermi and collaborators (3,11) who produced it by the slow neutron bombardment of vanadium and by the fast neutron bombardment of manganese and chromium and chemically identified it. Since stable vanadium and manganese consist of only one nuclide each, the mass assignment of the vanadium isotope followed from the only likely nuclear reactions—$V^{51}(n,\gamma)$ $V^{52}$ and $Mn^{55}(n,\alpha)V^{52}$. The possible reaction $Cr^{52}(n,p)V^{52}$ supports the assignment. The half-life was found to be 3.75 min. (3). Pool, Cork, and Thornton (24) chemically identified as vanadium a 4-min. activity produced by the bombardment of vanadium, chromium, and manganese by fast neutrons. Walke (36) produced $V^{52}$ by the $(d,p)$, $(n,\gamma)$, $(n,\alpha)$, and $(n,p)$ reactions, and found that the radioactivity in all cases decreased with a half-life of $3.9 \pm 0.1$ min. Ionization measurements were made with a Lauritsen quartz-fiber electroscope for (at most) 15 min.

More recently, Martelly (20) made a careful measurement of the half-life of $V^{52}$. An ionization chamber containing argon at a pressure of 3 kgm. per cm.$^2$ was used with an electrometer. Pure samples of vanadium pentoxide were activated for a few minutes with slow neutrons. The activity was followed for 50 min. Over the first 20 min. corrections had to be applied to the readings for losses of ions by recombination. Individual values of the half-life, found by a graphical method, in different runs ranged from 3.70 to 3.77 min. and had a weighted mean of 3.74 $\pm$ 0.01 min.

The maximum energy of the $\beta$ particles has been found to be 1.98 Mev. by the absorption method (13) and 2.65 Mev. by the cloud chamber method (40).

### *Results*

A spectrographic examination of the 'spec.-pure' vanadium pentoxide (Laboratory No. 2651) used in the experiment showed that small amounts of iron, lead,

TABLE VII

MEASUREMENT OF THE HALF-LIFE OF $V^{52}$
TQQ Electroscope. Activities $A$ in div. per min.

| Date 1951 | $A_1$ | $A_2$ | $T_1$(min.) |
|---|---|---|---|
| May 31 | 249.0 | 0.081 | 3.754 |
| June 1 | 657.9 | 0.008 | 3.773 |
| June 12 | 392.9 | 0.016 | 3.765 |
| June 13 | 429.9 | 0.018 | 3.766 |
| | | | Av. 3.765 |

copper, silicon, and sodium were present as impurities. A sample of a few milligrams was irradiated for about one second in the reactor. The source was covered with aluminum foil (2 mgm. per cm.$^2$) and its activity followed for about 30 min. Analysis showed that long period activities were extremely small. The experimental results may be seen in Table VII and Fig. 7. The final result for the half-life of $V^{52}$ is $3.76 \pm 0.02$ min.

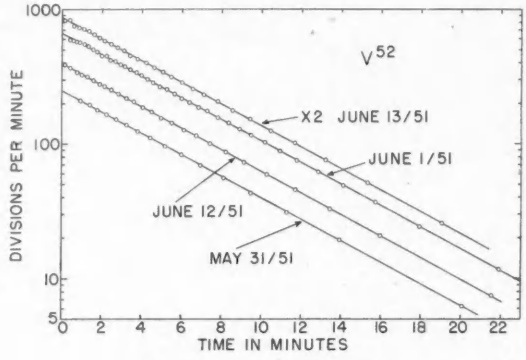


FIG. 7. Decay of $V^{52}$ sources.

## ACKNOWLEDGMENTS

We should like to express our thanks to several persons who have greatly assisted us. Dr. H. Carmichael has kindly given us permission to include a description of the TQQ electroscope in this paper and has provided the perspective drawing (Fig. 1) of the electroscope and a written account of it. Dr. A. J. Ferguson has assisted in setting up the least squares problem for the IBM machines. Miss A. R. Rutledge has greatly assisted by taking readings and making calculations. Miss G. E. Marshall has drawn Figs. 2–7.

The actinium used in the experiments was provided through the courtesy of the Atomic Energy Commission of the United States. This material was made available by Dr. F. Hagemann of the Argonne National Laboratory, to whom we are greatly indebted.

One of us (B.W.S.) is indebted to the National Research Council of Canada for a grant for a Marchant calculator, with which some of the calculations were done at Queen's University.

## REFERENCES

1. ALBRECHT, E. Sitzber. Akad. Wiss. Wien, Math. naturw. Klasse, Abt. IIa, 128: 925. 1919.
2. ALBURGER, D. E. and FRIEDLANDER, G. Phys. Rev. 82: 977. 1951.
3. AMALDI, E., D'AGOSTINO, O., FERMI, E., PONTECORVO, B., RASETTI, F., and SEGRÈ, E. Proc. Roy. Soc. (London), A, 149: 522. 1935.
4. BENEŠ, J., HEDGRAN, A., and HOLE, N. Arkiv. Mat. Astron. Fysik, A, 35: No. 12. 1948.
5. BRODA, E. and FEATHER, N. Proc. Roy. Soc. (London), A, 190: 20. 1947.
6. CAMERON, A. G. W. and KATZ, L. Phys. Rev. 80: 904. 1950.
7. CHANG, W. Y., GOLDHABER, M., and SAGANE, R. Nature, 139: 962. 1937.
8. CRITTENDEN, E. C., JR. Phys. Rev. 56: 709. 1939.
9. EKLUND, S. and HOLE, N. Arkiv. Mat. Astron. Fysik, A, 29: No. 26. 1943.

10. FAJANS, K. and VOIGT, A. F. Phys. Rev. 58: 177. 1940.
11. FERMI, E., AMALDI, E., D'AGOSTINO, O., RASETTI, F., and SEGRÈ, E. Proc. Roy. Soc. (London), A, 146: 483. 1934.
12. FRIEDLANDER, G. and ALBURGER, D. E. Phys. Rev. 84: 231. 1951.
13. GADSINSKI, N. N., GOLOTZWAN, I. A., and DANILENKO, A. I. J. Exptl. Theoret. Phys. (U.S.S.R.), 10: 1. 1940.
14. HAHN, O. and MEITNER, L. Physik. Z. 9: 649. 1908.
15. HENDERSON, M. C. Phys. Rev. 48: 855. 1935.
16. HEVN, F. A. Nature, 139: 842. 1937.
17. KOVÁŘIK, A. F. Physik. Z. 12: 83. 1911.
18. KRISHNAN, R. S. and NAHUM, E. A. Proc. Cambridge Phil. Soc. 36: 490. 1940.
19. KURBATOV, J. D. and MANN, H. B. Phys. Rev. 68: 40. 1945.
20. MARTELLY, J. Ann. phys. (12), 2: 555. 1947.
21. MEITNER, L. Arkiv. Mat. Astron. Fysik, A, 33: No. 3. 1946.
22. MISKEL, J. A., DER MATEOSIAN, E., and GOLDHABER, M. Phys. Rev. 79: 193. 1950.
23. MOORE, B. L. Phys. Rev. 57: 355. 1940.
24. POOL, M. L., CORK, J. M., and THORNTON, R. L. Phys. Rev. 52: 239. 1937.
25. PREISWERK, P. and VON HALBAN, H., JR. Compt. rend. 201: 722. 1935.
26. RODERICK, H., MEYERHOF, W. E., and MANN, L. G. Phys. Rev. 84: 887. 1951.
27. SARGENT, B. W. Can. J. Research, A, 17: 82. 1939.
28. SARGENT, B. W. Can. J. Research, A, 17: 103. 1939.
29. SCHUMAN, R. P. and CAMILLI, A. Phys. Rev. 84: 158. 1951.
30. SEGRÈ, E. and HELMHOLZ, A. C. Revs. Modern Phys. 21: 271. 1949.
31. SEREN, L., FRIEDLANDER, H. N., and TURKEL, S. H. Phys. Rev. 72: 888. 1947.
32. SILVER, L. M. Phys. Rev. 76: 589. 1949.
Can. J. Phys. 29: 59. 1951.
33. SILVER, L. M. Can. J. Phys. 29: 615. 1951.
34. SINMA, K. and YAMASAKI, F. Sci. Papers Inst. Phys. Chem. Research (Tokyo), 35: 16. 1938.
35. VAN VOORHIS, S. N. Phys. Rev. 50: 895. 1936.
36. WALKE, H. Phys. Rev. 52: 777. 1937.
37. WALKE, H., WILLIAMS, E. J., and EVANS, G. R. Proc. Roy. Soc. (London), A, 171: 360. 1939.
38. WIDDOWSON, E. E. and CHAMPION, F. C. Proc. Phys. Soc. (London), 50: 185. 1938.
39. YAFFE, L. and STEVENS, W. H. Can. J. Phys. 29: 186. 1951.
40. YUASA, T. Compt. rend. 215: 414. 1942.

# THE PHOTONEUTRON CROSS SECTIONS OF $Rb^{87}$, $Zr^{90}$, AND $Mo^{92}$[1]

By L. Katz, R. G. Baker, and R. Montalbetti


## ABSTRACT

The photoneutron cross sections of the 50-neutron isotopes $Rb^{87}$, $Zr^{90}$, and $Mo^{92}$ have been measured as a function of photon energy. These cross sections exhibit the peaked shape characteristic of photonuclear reactions. Peak values of 0.23, 0.27, and 0.14 barn at 17.5, 18.0, and 18.7 Mev. respectively were found for these nuclei. The widths of all the curves at half maximum were about 6 Mev. In the case of zirconium and molybdenum the cross sections to the isomeric and ground states of the residual nuclei have been determined separately. The ratio of the cross sections, $\sigma_{\text{ground}}/\sigma_{\text{isomeric}}$, has been examined as a function of photon energy and is discussed in the light of the elementary analysis previously presented.


## INTRODUCTION

In this paper we report on the $(\gamma,n)$ cross sections of $Rb^{87}$, $Zr^{90}$, and $Mo^{92}$, which have been measured as a continuation of our program on photonuclear reactions. The photoneutron cross sections of these isotopes are of particular interest, since the nucleus in each isotope contains a "magic" number of 50 neutrons.

Of added interest is the fact that each of the radioactive isotopes resulting from the above reactions contains an isomeric state. In the case of $Zr^{90}$ and $Mo^{92}$ the cross section leading to the ground and isomeric state of each has been determined separately. These measurements are similar to those reported for bromine in the paper (12) by Katz, Pease, and Moody. The isomeric state in $Rb^{86}$ was reported (6) after the completion of this work and was not examined by us, so that our $(\gamma,n)$ cross section for this isotope is indicative of its minimum value.

## MATHEMATICAL ANALYSIS

The number of nuclear reactions per unit time induced in a sample irradiated in the beam of a betatron has been given by equations (1) and (5) of Reference (12). These equations are for the general case where an isomeric state is present. The more frequent and less general case where the resultant radioactive nucleus decays with a single half-life is obtained by placing the cross section for the excited state $\sigma_i = 0$.

The activity detected by a Geiger-Mueller counter will depend on the decay scheme involved as well as the number of radioactive nuclei in the isomeric and ground states. A decay scheme which is general enough to include all the cases discussed in this paper is shown in Fig. 1. We define $p$ as the fraction of nuclei in the isomeric state which decay to the ground state by emission of $\gamma$ rays or conversion electrons; $f_g$ and $f_i$ as the fractions of radioactive nuclei in the ground and isomeric states respectively which proceed by $\beta$ (+ and −) emission;* and $\alpha$ as the internal conversion coefficient (number of converted gammas from state $i$ to the number of unconverted gammas).

[1] *Manuscript received October 21, 1952.*
*Contribution from the Department of Physics, University of Saskatchewan, Saskatoon, Sask.*

**The notation in this paper will be the same as in Reference (12) except the ground and isomeric states will be designated by subscripts g and i rather than 1 and 2.*

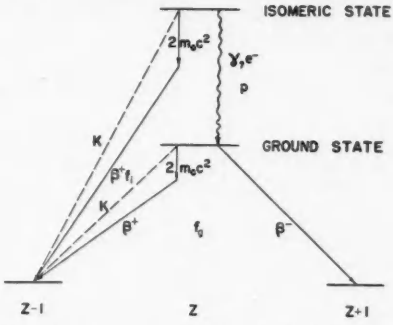


FIG. 1. A decay scheme which is general enough to include all cases discussed in this paper.

It has been shown in (12) (equations (6) and (7)) that the population in each state at a time $t$ after irradiation is

[1] $$N_i = N_{i0}\, e^{-\lambda_i t},$$

[2] $$N_g = N_{g0}\, e^{-\lambda_g t} + p\,\frac{\lambda_i N_{i0}}{\lambda_i - \lambda_g}\,(e^{-\lambda_g t} - e^{-\lambda_i t}).$$

The decay rates of these states are $\lambda_i N_i$ and $\lambda_g N_g$. However, the activities detected by a G.M. counter, which is primarily sensitive to beta particles, are given by:

[3] $$C_i = \left(g_i p\,\frac{\alpha}{\alpha+1} + g_i f_i\right)\lambda_i N_{i0}\, e^{-\lambda_i t},$$

[4] $$C_g = g_g f_g \lambda_g \left[\left(N_{g0} + p\,\frac{\lambda_i N_{i0}}{\lambda_i - \lambda_g}\right) e^{-\lambda_g t} - p\,\frac{\lambda_i N_{i0}}{\lambda_i - \lambda_g}\, e^{-\lambda_i t}\right]$$

where $g$ ($g_g$ and $g_i$) is a factor defined as the fraction of the beta particles emitted which are detected by the counter per unit time. The dependence of the counting rate on the beta energy, as well as geometry, self and external absorption, etc. is included in this factor. The evaluation of $g$ for thick samples will be treated in a paper by Baker and Katz to be published shortly.

We assume the Geiger-Mueller counter has such a low efficiency for the detection of $\gamma$ rays that their contribution to the counting rate may be entirely neglected. These general equations will be reduced to particular cases when they are discussed separately later. In any case, the counting rate measured by the counter may be written

[5] $$C = C_i + C_g = C_{g0}\, e^{-\lambda_g t} + C_{i0}\, e^{-\lambda_i t}.$$

Extrapolation of a decay curve to zero time gives $C_{g0}$ and $C_{i0}$. The initial populations in the two states $N_{i0}$ and $N_{g0}$ are then found from these values. $a_g(E_0)$ and $a_i(E_0)$, the activations induced per unit time by the photons in each of the states, are calculated through equations (4) and (5) of (12). A plot of each $a(E_0)$ vs. $E_0$ is termed an activation curve. This is then analyzed by the photon difference method of Katz and Cameron (11) to give the photo cross section $\sigma(E)$.

## EXPERIMENTAL PROCEDURE

*Rubidium*

The $(\gamma,n)$ reaction in this case involved the naturally radioactive isotope $Rb^{87}$. Samples of $RbNO_3$, shielded with cadmium against neutron capture, were irradiated in the betatron beam. After the short-lived activities had died out there remained a relatively high activity of 19.5 day half-life (22). Epicadmium neutrons in the betatron beam gave no observable 19.5 day activity from the reaction $Rb^{85}(n,\gamma)Rb^{86}$. Zaffarano, Kern, and Mitchell (23) have measured the disintegration scheme of the ground state of $Rb^{86}$ and found two beta rays of end point energies 0.716 Mev. (20%) and 1.822 Mev. (80%). Using this disintegration scheme, equations [3], [4], and [5] give $C_{g0} = g\lambda_g N_{g0}$. Combining this with equation (5) of (12) gives

$$[6] \qquad a(E_0) = \frac{\lambda_g N_{g0}}{1 - e^{-\lambda_g t_R}} = \frac{C_{g0}}{g\lambda_g t_R}$$

where we have taken the length of irradiation $t_R \ll 19.5$ days. The activation curve $a(E_0)$ vs. $E_0$ is shown in Fig. 2.

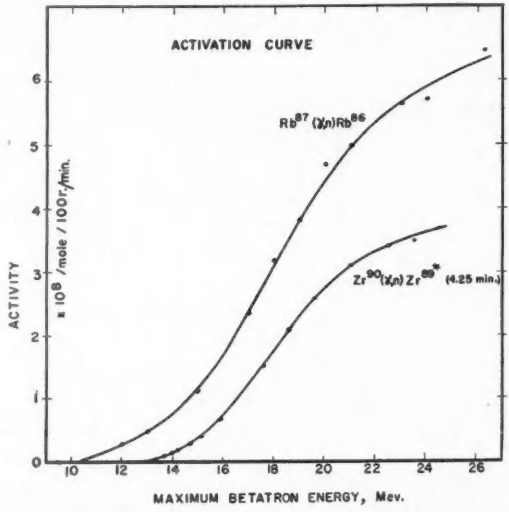


FIG. 2. Activation curves of the reactions $Rb^{87}(\gamma,n)Rb^{86}$ (19.5 day) and $Zr^{90}(\gamma,n)Zr^{89*}$ (4.25 min.) as obtained by irradiating samples in the betatron beam. Results are given in saturated activity per mole of parent isotope for an X-ray intensity of 100 roentgens per minute.

*Molybdenum*

Two half-lives are involved in this reaction: $Mo^{92}(\gamma,n)Mo^{91}$ with a half-life of 65.5 sec. and $Mo^{92}(\gamma,n)Mo^{91*}$ with a half-life of 15.5 min. Irradiation of cadmium shielded molybdenum behind a heavy lead plug, which effectively filtered the X-ray beam but gave a large neutron flux, gave a negligible 15 min. activity expected from the reaction $Mo^{100}(n,\gamma)Mo^{101}$. Because of the short half-life a

special apparatus was used to measure the activity induced in a cylindrical sample of molybdenum foil. Immediately after irradiation the sample was dropped by remote control into a lead castle where the counting rate was recorded automatically. The average of 15 decay curves followed out to background gave 15.5 ± 0.2 min. for the half-life of the excited state in good agreement with values found in the literature (3), but only 65.5 ± 2 sec. for the half-life of the ground state, a value considerably lower than that of 75 sec. reported by the workers at Illinois (3) and Zurich (22). The thresholds for these reactions were measured by us and found to be 13.1 ± 0.1 and 13.2 ± 0.1 Mev. The difference between the thresholds can of course be determined more accurately and was found to be 0.15 ± 0.05 Mev. Wäffler (21) has reported that betas from the ground state have an energy of 2.7 ± 0.2 Mev. He also finds a gamma ray of 0.140 ± 0.020 Mev. and some internal conversion electrons corresponding to this energy. According to Weisskopf's recent formula (16) the lifetime for a 0.14 Mev. $\gamma$-ray transition in this isotope involving a spin change of 4 is $\sim 10^7$ sec. Therefore, the low energy $\gamma$ rays observed probably come from the residual $Nb^{91}$ nucleus. Duffield and Knight (3) measured the end points of the two $\beta$ rays by the absorption method and found them to be 2.6 Mev. for the short-lived activity and 3.7 Mev. for the long-lived activity.

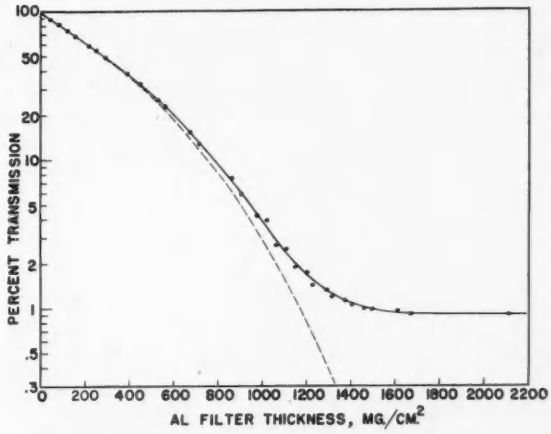


FIG. 3. Absorption curve for the 15.5 min. $Mo^{91}$ beta rays in aluminum filters. Dashed curve is obtained when the background activity (mainly annihilation radiation) is subtracted.

Measurements by us on the absorption of the 15.5 min. activity in aluminum gave the absorption curve shown in Fig. 3. This curve was analyzed by the method developed in this laboratory (13, 14) and gave an energy of 3.32 ± 0.05 Mev. We have also re-examined the absorption curve published by Duffield and Knight for this activity, using our method of analysis, and find an energy of 3.2 Mev.

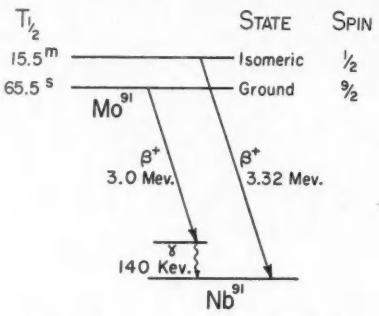


FIG. 4. Proposed decay scheme for $Mo^{91}$.

In view of the long lifetime for the $\gamma$-ray transitions from the isomeric to the ground states, it is reasonable to assume that they decay independently by $\beta^+$ emission to $Nb^{91}$. A proposed decay scheme is shown in Fig. 4. This requires that $f_i = 1$ and $p = 0$, and the $Mo^{91}$ activity, as detected by a counter, can be written:

$$C = g\lambda_g N_{g0}\, e^{-\lambda_g t} + g\lambda_i N_{i0}\, e^{-\lambda_i t}$$

$$= C_{g0}\, e^{-\lambda_g t} + C_{i0}\, e^{-\lambda_i t}. \qquad [7]$$

$K$ capture for this energy $\beta^+$ ray is about 5% (5) and the observed activity was corrected for it. The decays from the two levels are quite independent so that the values of $C_{g0}$ and $C_{i0}$ corrected to saturation and geometry give the number

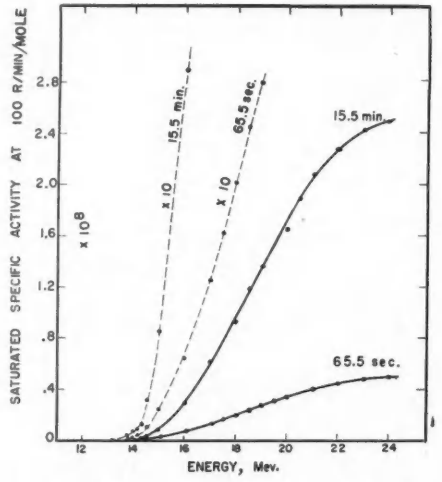


FIG. 5. Activation curves of the reaction $Mo^{92}(\gamma,n)Mo^{91*}$ (15.5 min.) and $Mo^{92}(\gamma,n)Mo^{91}$ (65.5 sec.) as obtained by irradiating samples of molybdenum foil in the betatron beam.

of activations per unit time induced in each of the states by the photons. This is shown clearly by combining equation [7] with (4) and (5) of Reference (12).

$$[8] \qquad a_g(E_0) = \frac{C_{g0}}{g(1 - e^{-\lambda_g t_R})} \qquad a_i(E_0) = \frac{C_{i0}}{g(1 - e^{-\lambda_i t_R})}$$

The activation curves shown in Fig. 5 were calculated by introducing the measured values of $C_{g0}$ and $C_{i0}$ into these equations.

*Zirconium*

Zirconium metal foils were irradiated in cadmium shielding and the activities resulting from the photonuclear reactions $Zr^{90}(\gamma,n)Zr^{89}$ (78 hr.) and $Zr^{90}(\gamma,n)Zr^{89*}$ (4.25 min.) were studied. The decay scheme of $Zr^{89}$ has recently been investigated by Shore, Bendel, and Becker (20) and by Goldhaber *et al.* (7) and is reproduced in Fig. 6. According to (20) the total conversion coefficient for the 588 kev.

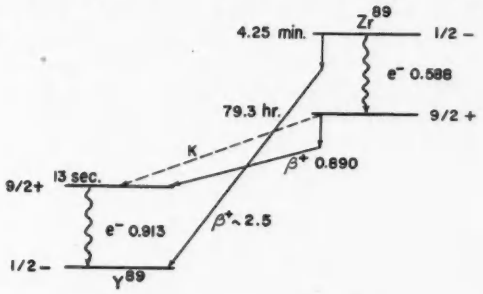


FIG. 6. The decay scheme of $Zr^{89}$.

gammas is 0.07 ± 0.02. They also found that the 2.5 Mev. positrons from the excited state are present to the extent of 6% of the conversion electrons; that is they correspond to about 0.4% of the transitions from this state and may be neglected. Conversion electrons and gamma rays from the isomeric state in $Y^{89}$ form about 2% (7) of our measured long-lived activity and a correction of this magnitude has been applied.

Transitions from the ground state go mainly by $K$ capture. Goldhaber finds the approximate ratio 3:1 for electron capture to positron emission. The graphs of Feenberg and Trigg (5) give a value of 3.5:1. We have used the theoretical value. The activity measured by a counter from a piece of activated zirconium is thus

$$[9] \qquad \begin{aligned} C = C_g + C_i &= g_g f_g \lambda_g (N_{g0} + N_{i0})\, e^{-\lambda_g t} + g_i \frac{\alpha}{\alpha + 1} \lambda_i N_{i0}\, e^{-\lambda_i t} \\ &= C_{g0}\, e^{-\lambda_g t} + C_{i0}\, e^{-\lambda_i t} \end{aligned}$$

where from the foregoing discussion of the disintegration scheme we have placed $f_i = 0$, $p = 1$, $\lambda_i/(\lambda_i - \lambda_g) \approx 1$ because $\lambda_g/\lambda_i = 0.94 \times 10^{-3}$. Here $f_g = 1/4.5$ and

$\alpha = 0.07 \pm 0.02$. The two values of $g$ ($g_g$ and $g_i$) are almost equal because they are for electrons of nearly equal energy, measured in the same sample and geometry.

Analysis of the decay curves of a large number of samples gave half-lives of 4.25 min. for the isomeric state and 78 hr. for the ground state, in good agreement with previously measured values.

The activities were normalized against the $Cu^{62}$ 10.1 min. activity at 19.6 Mev. A special case of self-absorption arises in the case of conversion electrons. These monoenergetic electrons follow a linear absorption law and it can be shown that the observed specific activity is related to the true specific activity by the equation $I = I_0\ (1 - kd/R)$ for $d < R$ where $d$ is the sample thickness. $R$ is the extrapolated range of the electrons (13) and $k$ is a constant equal to $\frac{1}{2}$ for a planar sample and small angle counting geometry. Samples thick enough to have a cosine distribution for the conversion electrons and the 78 hr. positron were used. $g_i$ was determined by comparison against $Cu^{62}$ at 19.6 Mev., then $g_g$ was determined from the equation

$$[10] \qquad g_g = g_i \frac{(1 - e^{-k_i d})/k_i d}{1 - d/2R}$$

where $k_i$ is the self-absorption coefficient of the beta rays from the isomeric state.

The values of $C_{i0}$ of equation [9] were obtained experimentally from the decay curves of samples irradiated at various betatron energies. The activation curve for the isomeric state was then obtained by combining equation [9] with (4) and (5) of Reference (12); this is shown in Fig. 2. Experimental values of $C_{g0}$ were difficult to determine accurately because of the very low activities obtainable and for this reason only the average value of $C_{g0}/C_{i0}$ in the region of 16 to 26 Mev. was measured. The ratio $R_a$ for this decay scheme was found by combining equation [9] with (4) and (5) of Reference (12) to give approximately:

$$[11] \qquad R_a = \frac{a_g(E_0)}{a_i(E_0)} = \left(\frac{g_i}{g_g f_g} \cdot \frac{\alpha}{\alpha + 1} \cdot \frac{C_{g0}}{C_{i0}} \cdot \frac{1 - e^{-\lambda_i t_R}}{1 - e^{-\lambda_g t_R}}\right) - 1.$$

Introducing the experimental value of $C_{g0}/C_{i0}$ into this equation gave $R_a = 0.8 \pm 0.1$ for $E_0 > 16$ Mev. This ratio is also very nearly the ratio for the $(\gamma,n)$ cross sections to the two states. Any 65 hr. $Y^{90}$ activity resulting from $(\gamma,d)$ and $(\gamma,p)$ reactions in zirconium could not be separated from the 78 hr. $Zr^{89}$ activity and the value for $R_a$ is thus a maximum.

## RESULTS

The activation curves shown in Figs. 2 and 5 were analyzed by the photon difference method of Katz and Cameron (11) and the cross section curves so obtained are shown in Figs. 7 and 8. In Table I we have summarized the pertinent results of this analysis. The threshold for the reaction in rubidium could not be measured accurately because of the high background from natural radioactivity in $Rb^{87}$ and the value given is calculated from masses kindly communicated to us by Dr. Duckworth. Values for the $Zr^{90}(\gamma,n)Zr^{89*}$ threshold found in the literature are $12.48 \pm 0.15$ Mev. (9) and $12.1 \pm 0.1$ Mev.(17). We have used the average of these values.

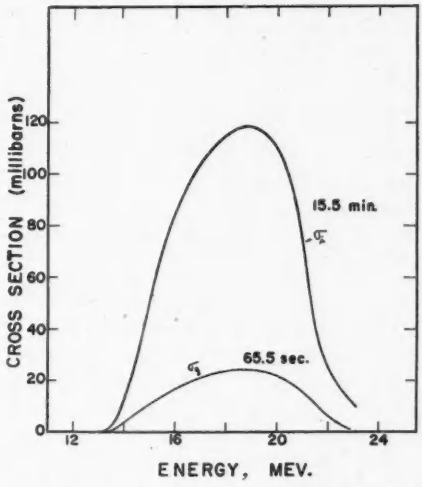


FIG. 7. The photoneutron cross sections for the reaction $Mo^{92}(\gamma,n)Mo^{91}$ leading to the ground and isomeric states, $\sigma_g$ and $\sigma_i$ respectively.

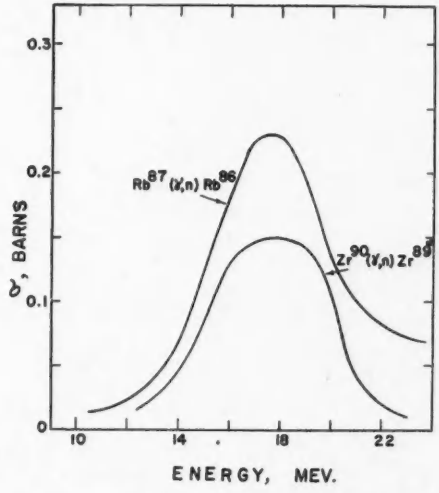


FIG. 8. The photoneutron cross sections for the reactions $Rb^{87}(\gamma,n)Rb^{86}$ leading to the 19.5 day state and $Zr^{90}(\gamma,n)Zr^{89*}$ leading to the 4.5 min. isomeric state.

TABLE I

PHOTONUCLEAR PROPERTIES OF THE ISOTOPES INVESTIGATED

| Reaction | Threshold | Energy at cross-section maximum, Mev. | Cross section at maximum, barns | Half width, Mev. | Integrated cross section, Mev-barn |
|---|---|---|---|---|---|
| $Rb^{87}(\gamma,n)Rb^{86}$ | $9.3 \pm 0.9$[a] | 17.5 | 0.23 | 6 | 1.68 |
| $Zr^{90}(\gamma,n)Zr^{89*}$ | $12.3 \pm 0.1$ | 18.0 | 0.15 | 5.7 | 0.93 |
| $Zr^{90}(\gamma,n)Zr^{89}$ | | 18.0 | $\sim 0.12$ | $\sim 5.7$ | $\sim 0.74$ |
| $Mo^{92}(\gamma,n)Mo^{91*}$ | $13.2 \pm 0.1$ | 18.7 | 0.12 | 6 | 0.71 |
| $Mo^{92}(\gamma,n)Mo^{91}$ | $13.1 \pm 0.1$ | 18.7 | 0.024 | 6 | 0.14 |

[a] *Calculated from masses assigned by Duckworth.*

It is possible to compare our results with measurements of Price and Kerst (18). These authors give the number of neutrons emitted per mole of natural element per roentgen of radiation when the irradiation is at betatron energies of 18 and 22 Mev. The number of neutrons from the $(\gamma,n)$ reactions for the isotopes involved in our work may be read off directly from the activation curves. Two points arise in such comparison. (i) The measurements of Price and Kerst snclude neutron contributions from all reactions, whereas in our work neutrons are from the $(\gamma,n)$ reaction only. However, the contribution from other reactions iuch as $(\gamma,np)$, $(\gamma,2n)$, etc. is small at these energies, particularly at 18 Mev. (2). (ii) The work of Price and Kerst is for the natural element whereas ours is only for the 50-neutron isotopes and any systematic difference in the measurements might then be attributed to this cause.

In Table II we have collected the values of Price and Kerst's work and those of the present experiments. No systematic difference between them is to be found and no definite conclusion regarding the cross section for the 50 neutron isotope as against the natural element may be drawn.

TABLE II

NEUTRONS PER MOLE PER ROENTGEN

| Parent isotope | 18 Mev. | | 22 Mev. | |
|---|---|---|---|---|
| | Present work | Price and Kerst | Present work | Price and Kerst |
| $Rb^{87}$ | $\geqslant 3.1 \times 10^6$ | $2.4 \times 10^6$* | $\geqslant 5.4 \times 10^6$ | $4.4 \times 10^6$* |
| $Zr^{90}$ | $\geqslant 1.7$ $\leqslant 3.2 \times 10^6$ | $2.7 \times 10^6$ | $\geqslant 3.3$ $\leqslant 5.9 \times 10^6$ | $4.7 \times 10^6$ |
| $Mo^{92}$ | $1.2 \times 10^6$ | $3.7 \times 10^6$ | $2.7 \times 10^6$ | $7.0 \times 10^6$ |

* *Values obtained by interpolation of the Price and Kerst results.*

## DISCUSSION

An analysis of the ratio between the cross sections leading to the ground and isomeric states in $Br^{80}$ has been presented in the paper by Katz, Pease, and Moody (12). A similar analysis may be adopted for the two isotopes $Zr^{89}$ and $Mo^{91}$, though in this case there are considerably fewer subsidiary experimental data to be found in the literature.

Both of the isotopes $Zr^{89}$ and $Mo^{91}$ have 49 neutrons and fall in the isomeric "island" which precedes the magic number 50 (4, 15). In this island the $g_{9/2}$ and $p_{1/2}$ levels should be adjacent, though other evidence is required to decide which is the ground state. Goldhaber and Sunyar (8) have listed the isotopes $Se^{83}$, $Kr^{85}$, $Sr^{87}$, and $Zr^{89}$ all with even number of protons and 49 neutrons as having a spin of 9/2 in the ground state and 1/2 in the isomeric state. We assume that this is also true for the 42 proton and 49 neutron isotope $Mo^{91}$.

The measured ratio between the $(\gamma,n)$ cross sections $(R_\sigma = \sigma_g/\sigma_i)$ in $Mo^{91}$, calculated on the basis of our assumed disintegration scheme, is shown in Fig. 9

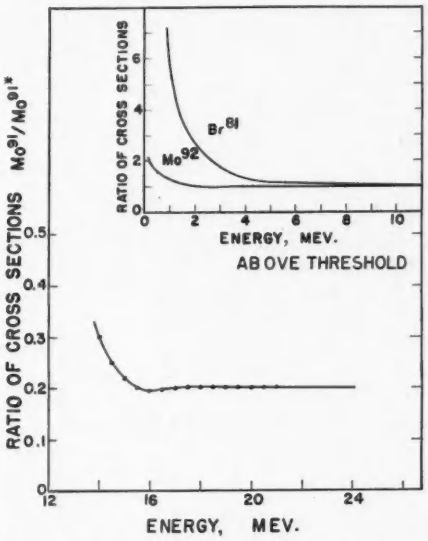


FIG. 9. Ratio of $\sigma_g/\sigma_i$ for $Mo^{92}$. Insert shows a comparison of the ratio $\sigma_g/\sigma_i$ for the isotopes $Mo^{92}$ and $Br^{81}$. These cross-section ratios are plotted against the energy measured from threshold of the isomeric state and each ratio has been normalized to unit value at high energy.

as a function of photon energy. Starting with spin 0 for $Mo^{92}$, electric dipole photon absorption ($l = 1$) and $s$ state neutron emission ($l = 0$, $s = 1/2$) excited $Mo^{91}$ nuclei will be obtained with levels of spin 1/2(0.333) and 3/2(0.667), where the weights of the levels according to their multiplicity, $(2l + 1)$, are shown in the parentheses. If $p$ state neutrons are emitted ($l = 1$, $s = 1/2$) the spins of the excited levels in $Mo^{91}$ are 1/2(0.222), 3/2(0.444), and 5/2(0.333). These data are summarized in Table III where the weight of each level corresponding to the different reactions is listed. Without attempting to decide what fraction of the levels of a given spin will cascade into the ground state and what fraction into the isomeric state, as we have done in bromine, it is immediately evident that after irradiation more isomeric states than ground states will be populated. This follows from the reasonable assumption that statistically, levels of small spin will

cascade predominantly into other levels of small spin. Our experimental ratio is less than 1 for this isotope and confirms the above conclusion. Similarly a ratio smaller than 1 is obtained for $Zr^{89}$. It should be pointed out that in the case of $Br^{80}$ the ground state has the smaller spin and a ratio greater than 1 is obtained.

TABLE III

THE SPINS AND THEIR STATISTICAL WEIGHTS FOR THE REACTIONS INDICATED

| Reaction \ Spin of level | 1/2 | 3/2 | 5/2 | 7/2 | Measured $R_\sigma = \frac{\sigma_g}{\sigma_i}$ |
|---|---|---|---|---|---|
| $Mo^{92}(\gamma,n)Mo^{91}$ neutron ($l = 0$, $s = 1/2$) | 0.333 | 0.667 | | | 0.2 |
| $Mo^{92}(\gamma,n)Mo^{91}$ neutron ($l = 1$, $s = 1/2$) | 0.222 | 0.444 | 0.333 | | |
| $Zr^{90}(\gamma,n)Zr^{89}$ neutron ($l = 0$, $s = 1/2$) | 0.333 | 0.667 | | | 0.8 |
| $Zr^{90}(\gamma,n)Zr^{89}$ neutron ($l = 1$, $s = 1/2$) | 0.222 | 0.444 | | | |

*Spins of $Zr^{89}$ and $Mo^{91}$; ground state 9/2, isomeric state 1/2.*

Cascade branching ratios for transitions from levels of any given spin to the ground and isomeric states can of course be chosen to match the calculated value of $R_\sigma = \sigma_g/\sigma_i$ to the measured value at a few Mev. above threshold. Considerable leeway is available in the choice of such branching ratios to give our single experimental measurement of $R_\sigma$. In spite of this wide choice it becomes immediately evident that the branching ratios used for bromine are quite unsatisfactory for molybdenum. Actually there is no reason why one should expect otherwise; the actual branching ratio in any nucleus should depend strongly on the properties of the low lying levels, particularly those immediately above the isomeric state, and there is thus no reason why one should expect a priori the same branching ratios in different nuclei. As an example of the strong dependence of the branching ratio on the nucleus involved we may compare the cross sections for thermal neutron capture by $Se^{82}$ and $Kr^{84}$ resulting in the ground and excited states of $Se^{83}$ and $Kr^{85}$. It is reasonable to assume that the initial spins of these even–even nuclides are 0 and that only $s$ state neutrons are captured in both cases, so that only levels of spin 1/2 are excited in the compound nuclides. Furthermore, each of these compound nuclides has a ground state spin of 9/2 and an isomeric state spin of 1/2. Neutron cross section measurements however give quite different ratios in the two cases; $\sigma_{gN}/\sigma_{iN} = 0.085$ for $Se^{82}$ and 0.65 for $Kr^{84}$ (1, 10). However, these ratios are less than 1 in each case, in agreement with our previous assumption regarding the preference for cascading between levels of nearly equal spin.

In the insert of Fig. 9 we have compared the ratio $R_\sigma$ for the bromine and molybdenum isotopes as a function of energy. For ease of comparison these ratios were normalized to unit value at high energy and are plotted against the energy measured from the threshold of the isomeric state. In each of the isotopes the isomeric state is only a fraction of a Mev. above the ground state and if the cross sections leading to these states were identical in shape, the ratio $R_\sigma$ should

rise very sharply only at energies very close to threshold. The fact that the bromine ratio rises very slowly, extending over a region of about 7 Mev., would suggest that the cross section leading to the isomeric state drops more rapidly than that leading to the ground state, as threshold is approached. The molybdenum curve, on the other hand, dips slightly to a shallow minimum then rises very sharply in approaching the threshold from the high energy side.

The behavior of these two ratios can be understood qualitatively if it is assumed that transitions to the small spin level are increasingly favored as the threshold is approached. In the case of bromine, since the ground state has the smaller spin, $\sigma_g/\sigma_i$ will increase in value as the threshold is approached. On the other hand since the isomeric state has the smaller spin in molybdenum the ratio will be depressed as threshold is approached, causing the curve to go through a minimum.

Sagane has shown (19) that the ratio of activities, $R_a$, for molybdenum remains constant up to betatron energies of 70 Mev. This result, which seems so surprising at first glance, may be explained as follows. Those $(\gamma,n)$ reactions in $Mo^{92}$ which leave the $Mo^{91}$ nucleus in a highly excited state will probably be followed by further particle emission; these do not contribute to the observed $Mo^{91}$ activities. Only those high energy $(\gamma,n)$ reactions which leave the residual nucleus below the threshold for further particle emission will contribute to the measured $Mo^{91}$ activities. We therefore conclude that even for high energy photon irradiation, the ratio $R_a = a_g/a_i$ comes from photon cascading in a region not too far above the threshold. There is no stable isotope of molybdenum from which $(\gamma,2n)$ reactions could contribute to the observed activities and the $(\gamma,3n)$ reaction has a small cross section in addition to originating in a low abundance isotope.

## REFERENCES


1. ARNOLD, J. R. and SUGARMAN, N. J. Chem. Phys. 15: 703. 1947.
2. CAMERON, A. G. W. Phys. Rev. 82: 272. 1951.
3. DUFFIELD, R. B. and KNIGHT, J. D. Phys. Rev. 76: 573. 1949.
4. FEENBERG, E. and HAMMACK, K. C. Phys. Rev. 75: 1877. 1949.
5. FEENBERG, E. and TRIGG, G. Revs. Modern Phys. 22: 399. 1950.
6. FLAMMERSFELD, A. Z. Naturforsch. A, 6: 559. 1951.
7. GOLDHABER, M., DER MATEOSIAN, E., SCHARFF-GOLDHABER, G., SUNYAR, A. W., DEUTSCH, M., and WALL, N. S. Phys. Rev. 83: 661. 1951.
8. GOLDHABER, M. and SUNYAR, A. W. Phys. Rev. 83: 906. 1951.
9. HANSON, A. O., DUFFIELD, R. B., KNIGHT, J. D., DIVEN, B. C., and PALEVSKY, H. Phys. Rev. 76: 578. 1949.
10. HOAGLAND, E. J. and SUGARMAN, N. National Nuclear Energy Series, Vol. 9. Book 2. McGraw-Hill Book Company, Inc., New York and London. 1951. p. 642.
11. KATZ, L. and CAMERON, A. G. W. Can. J. Phys. 29: 518. 1951.
12. KATZ, L., PEASE, L., and MOODY, H. Can. J. Phys. 30: 476. 1952.
13. KATZ, L. and PENFOLD, A. S. Revs. Modern Phys. 24: 28. 1952.
14. KATZ, L., PENFOLD, A. S., MOODY, H. J., HASLAM, R. N. H., and JOHNS, H. E. Phys. Rev. 77: 289. 1950.
15. MAYER, M. G. Phys. Rev. 74: 235. 1948.
16. MONTALBETTI, R. Can. J. Phys. 30: 660. 1952.
17. OGLE, W. E., BROWN, L. J., and CARSON, A. N. Phys. Rev. 78: 63. 1950.
18. PRICE, G. A. and KERST, D. W. Phys. Rev. 77: 806. 1950.
19. SAGANE, R. Phys. Rev. 85: 926. 1952.
20. SHORE, F. J., BENDEL, W. L., and BECKER, R. A. Phys. Rev. 83: 688. 1951.
21. WÄFFLER, H. "Conference on problems in nuclear physics" held at University of Birmingham in September 1948. See *University of Birmingham* Informal Report on Conference held 14–18 Sept. 1948. "Problems on nuclear physics" by M. L. Oliphant, R. E. Peierls, and P. B. Moon.
22. WÄFFLER, H. and HIRZEL, O. Helv. Phys. Acta, 21: 200. 1948.
23. ZAFFARANO, D. J., KERN, B. D., and MITCHELL, A. C. G. Phys. Rev. 74: 682. 1948.

# PHOTO-ALPHA PARTICLES FROM SILVER AND BROMINE IRRADIATED WITH 70 MEV. BREMSSTRAHLUNG[1]

By Chas. H. Millar

ABSTRACT

The energy spectrum of the $\alpha$ particles ejected from silver and bromine nuclei has been studied in a nuclear research emulsion irradiated with 70 Mev. bremsstrahlung from the Queen's University synchrotron. The main feature of the observed spectrum is a broad group with a peak at about 11 Mev. Evidence for particles of energies less than 6 Mev. is inconclusive.

Calculations have been made on the basis of the nuclear evaporation theory and give a predicted spectrum which is consistent in shape and peak position with the observed results.

## INTRODUCTION

Previous investigations (9, 4) of the energies of photo-alpha particles from silver and bromine irradiated with X rays of 27 Mev. or less have given results not entirely compatible with current theories of nuclear disintegration. In order to extend this experiment to higher energies we have carried out a similar investigation with 70 Mev. X rays and the results are described in this paper.

## EXPERIMENTAL METHOD

An Ilford type C2 nuclear research emulsion was enclosed in cadmium and exposed at the center of a 1-ft. cube of paraffin to 50 roentgens of X rays from the Queen's University synchrotron operating at approximately 70 Mev. The X-ray beam was filtered through 60 cm. of graphite in order to reduce preferentially the low energy X rays. The plate was developed by a "grain gradation" process (9) which enabled tracks of $\alpha$ particles of more than 30 Mev. in energy to be measured easily in the presence of the X-ray fogging. Protons of up to 10 Mev. in energy could also be seen, and were quite distinguishable from $\alpha$-particle tracks. Thus it is felt that under these conditions of development and observation, no high energy $\alpha$-particle tracks were missed, nor proton tracks falsely interpreted as $\alpha$-particle tracks.

A photo-alpha reaction in silver or bromine appeared as a single $\alpha$-particle track in the emulsion since the heavy residual nucleus had insufficient energy to recoil a measurable distance. Such events were distinguishable from photo-alpha reactions in carbon, nitrogen, and oxygen (8, 9), because the light residual nucleus in these latter events left a measurable, densely-ionized "recoil track" at the origin of the $\alpha$-particle track. The plate was searched for single $\alpha$-particle tracks and 500 of them were found in an area of 2.83 cm.$^2$

There was no difficulty in distinguishing or determining the direction of $\alpha$-particle tracks of energies greater than 5 or 6 Mev. Below this energy, however, the high grain density of an $\alpha$-particle track sometimes made it difficult to

[1] *Manuscript received October 20, 1952.*
*Contribution from the Physics Division, Atomic Energy of Canada Limited, Chalk River, Ontario, Canada. Issued as A.E.C.L. No. 19.*

distinguish its origin from its termination, and in cases of doubt as to the track direction, the track was not included in the survey. This procedure undoubtedly rejected some tracks of $\alpha$ particles ejected from middle-weight or heavy nuclei. However, it was hoped that this observational criterion would be sufficient to ensure that the tracks measured in this energy region were not those of photo-alpha events in light nuclei in which the observer had failed to detect the very short recoil tracks.

In order to estimate the background from $\alpha$ particles emitted by naturally radioactive contaminants in the emulsion, an equivalent area of an unirradiated plate from the same emulsion batch was similarly processed and surveyed, and the energies of *all* single $\alpha$-particle tracks recorded.

## EXPERIMENTAL RESULTS

In the irradiated plate 500 single $\alpha$-particle tracks were measured and the energy spectrum of these is shown in Fig. 1. This spectrum has been corrected for loss of particles which escape through the emulsion surfaces and for the variation with particle energy of the probability of observation, but no correction for background has been made.

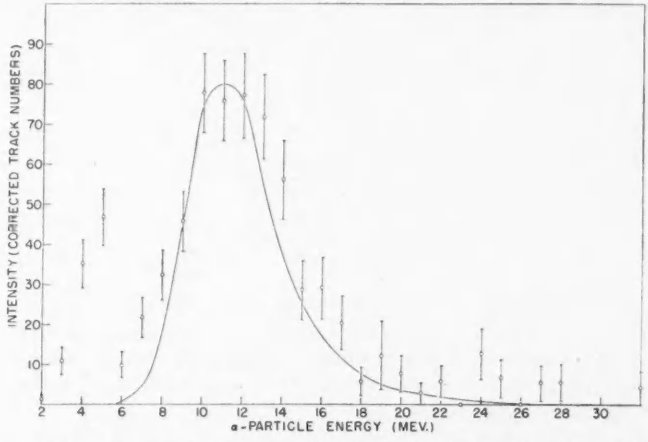


FIG. 1. Energy spectrum of single $\alpha$ particles observed in nuclear research emulsion irradiated with 70 Mev. bremsstrahlung. Observed points—shown with standard deviations—have been corrected for escape and observation probability, but not for background. Solid line shows predicted curve normalized to equal peak intensity with observed points.

Most of the tracks lie in a broad group with a peak at about 11 Mev. in energy. The intensity falls sharply on the low energy side of this peak, but extends in a long "tail" to about 30 Mev. on the high energy side.

The tracks in the 2 to 6 Mev. region must be studied in conjunction with the spectrum of the background plate, since it was in this region that all background tracks were found. Fig. 2 shows detailed histograms of these two spectra and

it will be noted that in the 4 to 5 Mev. region the background exceeds the number of tracks in the irradiated plate.

There is no essential disagreement here, since, as was mentioned previously, *all* tracks in the background plate were counted, while only "good" tracks were measured in the irradiated plate and thus some background tracks were probably rejected. Despite the rigid selection criterion there still appear to be some tracks with energies from 3 to 4 Mev. which are not due to the background from naturally radioactive contaminants. However, it is in this very low energy region that the distinguishing of photo-alpha events in middle-weight nuclei from those in light nuclei is most difficult, so that it is felt that the experiment is inconclusive as to whether or not there are any photo-alpha particles from silver or bromine below about 6 Mev. in energy.

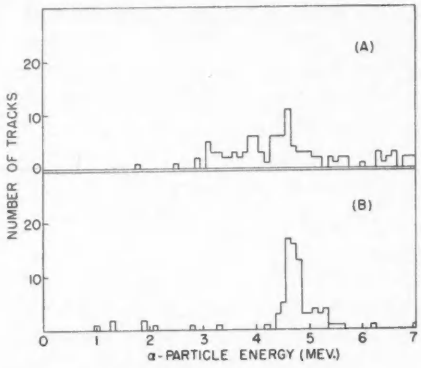


FIG. 2. Detailed histograms showing (*a*) low energy $\alpha$ particles in irradiated plate and (*b*) background $\alpha$-particle spectrum in unirradiated plate.

## DISCUSSION

The evaporation theory of nuclear disintegration developed by Blatt and Weisskopf (1) may be applied to the case of single $\alpha$ particles ejected from a middle-weight nuclide irradiated by bremsstrahlung. On the basis of this theory the relative number of $\alpha$ particles ejected with energies between $E_\alpha$ and $E_\alpha + dE_\alpha$ is given by the following expression:

$$G(E_\alpha)\,dE_\alpha = \int_0^{E_\gamma \max} \left[ E_\alpha \sigma(E_\alpha) \omega(E_{\alpha\,\max} - E_\alpha)\,dE_\alpha \right] \sigma(\gamma, n) f(E_\gamma) I(E_\gamma)\,dE_\gamma.$$

The definitions of the quantities in this equation and the values used in computing the numerical result are as follows.

"$I(E_\gamma)dE_\gamma$" is the number of photons of energy between $E_\gamma$ and $E_\gamma + dE_\gamma$. This was calculated according to Schiff's (10) formula for bremsstrahlung in the forward direction, making suitable modifications to take into account the absorption of the graphite filter.

"$\sigma(\gamma, n)$" is the cross section for photoneutron emission from the parent nucleus by $\gamma$ rays of energy $E_\gamma$. This cross section has been measured for silver

by Diven and Almy (2) up to about 18 Mev. Above this energy it was assumed that, analogous to the atomic case (5, p. 123), the cross section varies inversely as the 7/2ths power of the energy. For bromine the $(\gamma, n)$ cross sections determined by Katz *et al.* (6) were used with similar extrapolations to high energy.

"$f(E_\gamma)$" is the ratio of the number of excited nuclei which emit an $\alpha$ particle to the number which emit a neutron. Integrating the bracketed term in the above equation over all possible $\alpha$-particle energies gives a value proportional to the total number of $\alpha$ particles emitted. A value proportional to the total number of neutrons emitted may be obtained by the integration of an analogous expression. The ratio of the value so found for $\alpha$ particles to that for neutrons multiplied by the ratio of the $\alpha$-particle mass to the neutron mass gives the value for $f(E_\gamma)$.

At $\gamma$-ray energies below the photoneutron threshold, the product "$\sigma(\gamma,n)f(E_\gamma)$" becomes indeterminate but this does not materially affect the calculation since the Coulomb barrier prevents nuclei excited to these energies from making an appreciable contribution to the total spectrum.

"$E_{\alpha\,\max}$" is the energy of an $\alpha$ particle emitted from an excited nucleus in the case where the residual nucleus is left in the ground state. Thus $E_{\alpha\,\max} = (E_\gamma - B)$, where $B$ is the binding energy of an $\alpha$ particle in the parent nucleus. Values of this function were obtained using values of $B$ calculated from the atomic mass tables of Metropolis and Reitwiesner (7).

"$\sigma(E_\alpha)$" is the cross section of the residual nucleus excited to an energy of $(E_{\alpha\,\max} - E_\alpha)$ for the capture of an $\alpha$ particle of energy $E_\alpha$. Values for this function were obtained according to the method suggested by Blatt and Weisskopf (1) and are based on an assumed nuclear radius of $1.5 \times 10^{-13} A^{1/3}$ cm. and an $\alpha$-particle radius of $1.2 \times 10^{-13}$ cm.

"$\omega(E_{\alpha\,\max} - E_\alpha)$" is the level density of the residual nucleus at an excitation energy of $(E_{\alpha\,\max} - E_\alpha)$. These densities have been evaluated by means of the semiempirical formula of Blatt and Weisskopf (1),

$$\omega(E_{\alpha\,\max} - E_\alpha) = C \exp 2\sqrt{a(E_{\alpha\,\max} - E_\alpha)}$$

where "$C$" and "$a$" are functions of the atomic weight of the residual nucleus. The values used in the present calculations are given in Reference (3).

"$E_{\gamma\,\max}$", the upper limit of integration, is the maximum energy of the bremsstrahlung spectrum, in this case 70 Mev.

The numerical integration of the equation was carried out in detail for each of the two isotopes of silver and bromine present in the emulsion. These spectra, suitably weighted to take into account the different amounts of the various isotopes present, were summed to obtain the theoretical $\alpha$-particle spectrum shown in Fig. 1. This was normalized to have an intensity at 11 Mev. equal to that of the observed spectrum. It is of interest to note that though all of the four isotopes are present in roughly equal amounts, the theory predicts that only about one-tenth of the $\alpha$ particles come from silver, and that in each element the contribution of the lower atomic weight isotope is about three times that of the other.

It is also of interest that on the basis of this theory no photo-$\alpha$ particles from silver or bromine are to be expected with energies below about 6 Mev.

It will be seen that the computed curve agrees in both shape and peak position with the observed points. It is thus concluded that, in considering the spectrum of single $\alpha$ particles ejected from silver and bromine irradiated with 70 Mev. bremsstrahlung, the nuclear evaporation theory of Blatt and Weisskopf provides an interpretation which is consistent with the observed results.

ACKNOWLEDGMENT

The author wishes to thank Prof. J. A. Gray of Queen's University for his co-operation in carrying out the plate irradiation.

REFERENCES

1. BLATT, J. and WEISSKOPF, V. F. Theoretical nuclear physics. John Wiley & Sons, Inc., New York. 1952.
2. DIVEN, B. C. and ALMY, G. M. Phys. Rev. 80: 407. 1950.
3. FELD, B. T., FESHBACH, H., GOLDBERGER, M. L., GOLDSTEIN, H., and WEISSKOPF, V. F. U.S.A.E.C. Document NYO-636. 1951.
4. HASLAM, R. N. H., CAMERON, A. G. W., COOKE, J. A., and CROSBY, E. H. Can. J. Phys. 30: 349. 1952.
5. HEITLER, W. The quantum theory of radiation. Oxford University Press, London. 1944.
6. KATZ, L., PEASE, L., and MOODY, H. Can. J. Phys. 30: 476. 1952.
7. METROPOLIS, N. and REITWIESNER, G. U.S.A.E.C. Document NP-1980. 1950.
8. MILLAR, C. H. and CAMERON, A. G. W. Phys. Rev. 78: 78. 1950.
9. MILLAR, C. H. and CAMERON, A. G. W. (To be published.)
10. SCHIFF, L. I. *quoted by* ADAMS, G. D. Phys. Rev. 74: 1707. 1948.

# CROSS-SECTION MEASUREMENTS OF REACTIONS INDUCED BY NEUTRONS OF 14.5 MEV. ENERGY[1]

By E. B. Paul and R. L. Clarke


## ABSTRACT

The activation cross sections were measured for 57 elements bombarded with 14.5 Mev. neutrons from the $T^3(d, n)He^4$ reaction. Thirty-eight $(n, p)$, twenty-five $(n, \alpha)$, and thirty-four $(n, 2n)$ reactions resulting in known radioactive products with half-lives between a few seconds and a few days were observed. The counting arrangement was calibrated using samples containing standardized quantities of radioactive materials. The neutron monitor was calibrated by counting the $\alpha$-particles from the $T^3(d, n)He^4$ reaction. Calculations were made of the cross sections predicted by evaporation theory and compared with the observed values. For the charged particle reactions with mass number greater than 100 the theoretical cross sections were too small. Values of $\sigma_{obs}/\sigma_{cal}$ as high as 10,000 were obtained. However, the predicted cross sections for the $(n, 2n)$ reactions were in general agreement with the observed values. A possible interpretation of these results is discussed.


## INTRODUCTION

The activation cross sections for reactions induced by neutrons of energies 10–15 Mev. have been measured for a number of elements by Jelley and Paul (11), by Wäffler (16), and by Cohen (3) using neutrons from the $Be^9(d, n)B^{10}$, $B^{11}(d,n)C^{12}$, and $Li^7(d, n)Be^8$ reactions. Since these reactions give a complex spectrum of neutron energies extending down to a very low energy, an average cross section for the energy range down to that corresponding to the barrier height for the emitted particle is obtained. The neutrons from the reaction $T^3(d, n)He^4$ consist of a single group at an energy of 14.5 Mev. and hence are very suitable for cross section studies. In addition, the $\alpha$-particles associated with the neutrons provide a convenient method of determining the number of neutrons. The neutrons from this reaction have been used to measure the absolute yield curve for $Cu^{63}(n, 2n)Cu^{62}$, (7) as well as some activation cross sections for a number of elements (6).

In the experiments reported in this paper 57 elements have been bombarded with the 14.5 Mev. neutrons from this reaction and the activation cross sections have been measured. The activities studied were due to $(n, p)$, $(n, \alpha)$, and $(n, 2n)$ reactions. The experimental techniques used in this work restricted the activities measured to those with half-lives between about 10 sec. and about 20 days, and to those whose half-life could be clearly assigned without recourse to chemical identification of the nuclide. In all, thirty-eight $(n, p)$, twenty-five $(n, \alpha)$, and thirty-four $(n, 2n)$ cross sections were measured.

For a neutron bombarding energy of 14 Mev. the compound nucleus will have an excitation of about 22 Mev. and the maximum excitation energy available to the residual nucleus will in many cases be greater than 10 Mev. Hence, for all but the lightest nuclei the criteria for treating the nucleus thermodynamically should be satisfied. One would expect, moreover, that the

[1] *Manuscript received October 27, 1952.*
*Contribution from Physics Division, Atomic Energy of Canada Ltd., Chalk River, Ontario. Issued as A.E.C.L. No. 31.*

energy would not be high enough for those processes in which the energy of the neutron is not completely shared amongst the target nucleons and which are important at excitation energies greater than 50 Mev. (15) to play a large role. However, a comparison of the cross sections given by the statistical theory with the experimental results shows significant deviations.

## EXPERIMENTAL

The neutrons were produced by accelerating deuterons in a 100 kev. voltage doubler accelerator and allowing them to bombard targets of tritium absorbed in a titanium layer prepared by evaporation onto a molybdenum backing. A typical target and irradiation arrangement is shown in Fig. 1. The total neutron yields were of the order of $10^8$ neutrons per second.

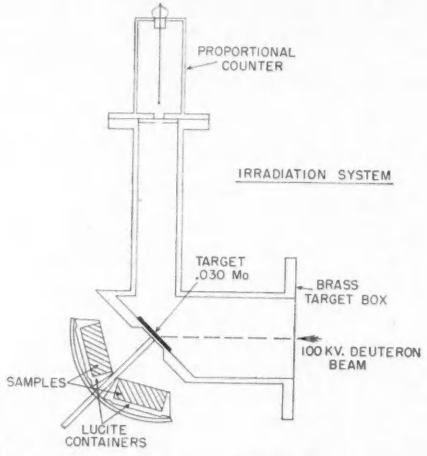


FIG. 1. Schematic diagram of the irradiation system.

Most of the samples were in the form of powders pressed into Lucite cups such that they had the form of cylinders 3.17 cm. in diameter and up to 1.27 cm. in thickness. A few of the samples were solid metal disks about 3 cm. in diameter and thicker than half the maximum $\beta$-ray range. The chemical form of the samples is listed in Column 2 in Tables II, III, and IV. The chemical impurity was generally less than 1%. The samples were irradiated at a position about 3 cm. from the target in order to produce a sufficient activity for accurate counting. Some of the samples which gave a very low yield were irradiated in contact with the back of the target chamber.

The cross section may be written (provided the sample is thick compared to the $\beta$-ray range)

$$\sigma = K\left(\frac{A}{\epsilon_s f}\right) \times \frac{1}{\phi}$$

where $A$ is the observed counting rate, $\epsilon_s$ is the fraction of saturation $(1 - e^{-\lambda T})$ where $T$ is the irradiation time and $\lambda$ is the decay constant of the activity, $f$ is the experimentally determined ratio of observed counting rate to specific

activity for the appropriate $\beta$-ray energy, $\phi$ is the neutron flux in neutrons per cm.$^2$ per sec. taken at the average depth in the sample from which countable $\beta$-particles come. $K$ is a constant equal to $M/naN_0$ where $M$ is the molecular weight of the sample material, $n$ is the number of atoms of the target element per molecule, $a$ is the isotopic abundance of the target nuclide, and $N_0$ is Avogadro's number.

The neutron yield was monitored by a long boron counter surrounded by paraffin (8). This neutron counter was calibrated at frequent intervals by counting the associated $\alpha$-particles emerging from the target at 90° to the deuteron beam into a carefully measured solid angle as shown in Fig. 1. The $\alpha$-particles were counted in a proportional counter, the pulses being amplified and recorded on a 30 channel pulse analyzer. The small correction for center of mass motion was made assuming that on the average the neutrons came from reactions with deuterons having an energy of 90 kev. (from the known yield curve and the fact that the target was thick).

The variation of the neutron flux $\phi$ with distance from the sample to the target was determined experimentally by irradiating thin copper disks 3.17 cm. in diameter at distances from the target varying from contact to the greatest distance used. The observed counting rates were compared with that for a disk irradiated at a distance such that the inverse square law held accurately. The variation was also checked in the region close to the target (contact position) with aluminum disks.

The angular distribution of the neutrons was measured using copper and aluminum detectors in order to confirm that the samples and neutron monitor were not in angular regions where the neutron distribution was being distorted by scattering in the target or target box.

The neutron flux was constant during any irradiation to better than 20% and the average flux was used in evaluating the cross sections. The small errors caused by this procedure are included in the quoted errors.

Since high accuracy in the $\beta$-ray counting was not being attempted in these experiments, the samples were in general made thicker than half the maximum range of the $\beta$-particles involved. The results of a subsidiary experiment showed that the half range thickness contributed more than 98% of all recorded $\beta$-ray counts. The ratio of observed counting rate to specific activity was determined directly by distributing known amounts of radioactive substances through inert samples and measuring the counting rates. The counters were end window counters with mica windows from 1.4 to 1.6 mgm. per cm.$^2$ and a diameter of 3.17 cm. They were surrounded by an aluminum lined lead castle which kept the background to about 20 c.p.m.

The radioactive substances used for calibration were obtained in the form of solutions with carrier added whose specific activities were known to better than 3%.* These substances are listed in Table I together with the energies of their radiations.

* *We are indebted to Mr. R. C. Hawkings and Mr. W. F. Merritt of the Radioisotopes Standardization Laboratory and Dr. L. Yaffe of the Chemistry Branch for the preparation and standardization of these solutions.*

TABLE I

| Radioactive substance | Half-life | Beta ray maximum energy, Mev. | Gamma-ray energy, Mev. |
|---|---|---|---|
| $Ca^{45}$ | 152 days | 0.255 | Nil |
| $Co^{60}$ | 5.2 years | 0.319 | 1.17 (100%) |
| | | | 1.33 (100%) |
| $Tl^{204}$ | 2.7 years | 0.783 | Nil |
| $Au^{198}$ | 2.69 days | 0.97 | 0.411 (100%) |
| $P^{32}$ | 14.3 days | 1.72 | Nil |
| $Ru^{106}$ | 1 year | 0.041 | Nil |
| $Rh^{106}$* | 30 sec. | 3.55 (82%) | 1.25 (1%) |
| | | 2.30 (18%) | 0.51 (17%) |
| | | | 0.73 (17%) |

* *The $Rh^{106}$ was at all times in equilibrium with its parent product, $Ru^{106}$. In the interpretation of the data of this experiment, the effect of the $Ru^{106}$ was neglected.*

The resulting calibration curve for the ratio, $f$, of the observed counting rate to the specific activity is presented in Fig. 2 as a function of maximum $\beta$-ray energy. Although a range of materials of differing atomic number was used with each radioactive substance, no dependence on $Z$ was observed to within 10% for the particular counting geometry used.

In a few cases the counts due to $\gamma$-rays could not be neglected. Their contribution was estimated in the following way. Thin sources of $Co^{60}$ and $Au^{198}$

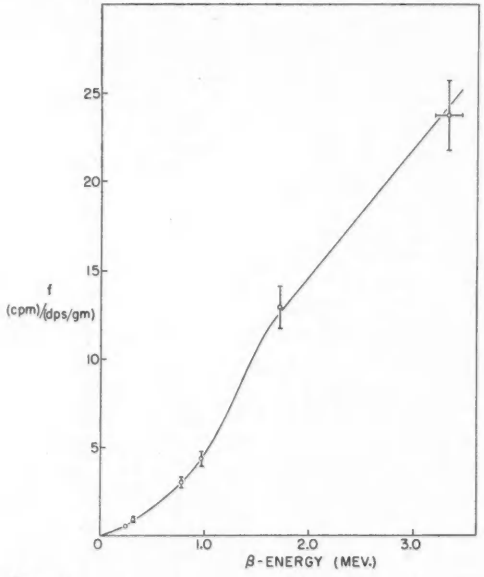


FIG. 2. Ratio of the observed counting rate to the specific activity plotted as a function of maximum $\beta$-ray energy. The standard deviations are shown. The smooth curve drawn through the points is used for interpolation.

covering the area of a sample were embedded at various depths in piles of inert lamina of aluminum, cadmium, and lead, the piles having the shape of a standard sample. The resulting curves of counting rate versus sample depth were then integrated (assuming that from the $\beta$-ray end point to zero absorber thickness, where $\beta$-ray counts predominated, the counting rate due to $\gamma$-rays was constant) to give the counting rate for a thick source. To calculate the counting efficiency for $\gamma$-rays of energies higher than those of $Co^{60}$, the efficiency curves of Bradt *et al.* (2) were used. At these energies the efficiency ratio does not depend very strongly on atomic number. Thus although second-

TABLE II

$(n, p)$ CROSS SECTIONS

| Target nuclide | Sample form | Half-life | Observed cross section, mbarns | Standard deviation, % | $Q$-value, Mev. | Calculated cross section, mbarns | Ratio $\sigma_{obs}/\sigma_{cal}$ |
|---|---|---|---|---|---|---|---|
| $O^{16}$ | Sugar | 7.3 sec. | 49.0 | 50 | − 9.35 | 72 | 0.68 |
| $F^{19}$ | $CaF_2$, NaF | 30 sec. | 135 | 35 | − 4.5 | 172 | 0.78 |
| $Na^{23}$ | NaCl | 40 sec. | 33.9 | 45 | − 4.3 | 265 | 0.128 |
| $Mg^{24}$ | Element | 15 hr. | 191 | 18 | − 4.7 | 11 | 17.3 |
| $Mg^{25}$ | Element | 60 sec. | 44.9 | 40 | − 2.9 | 186 | 0.24 |
| $Al^{27}$ | Element | 10 min. | 52.4 | 18 | − 1.8 | 146 | 0.36 |
| $Si^{28}$ | Element | 2.4 min. | 220 | 23 | − 4.0 | 70 | 3.1 |
| $Si^{29}$ | Element | 6.7 min. | 101 | 30 | − 2.9 | 133 | 0.76 |
| $P^{31}$ | Element | 2.7 hr. | 64.2 | 13 | − 1.0 | 205 | 0.31 |
| $S^{32}$ | Element | 14 days | 369 | 12 | − 0.95 | 220 | 1.68 |
| $S^{34}$ | Element | 12.4 sec. | 85.2 | 45 | − 4.3 | 50 | 1.70 |
| $Cl^{37}$ | $NH_4Cl$, NaCl, LiCl | 5 min. | 33.4 | 20 | − 3.5 | 85 | 0.393 |
| $K^{41}$ | $KNO_3$ | 110 min. | 81.2 | 40 | − 1.45 | 464 | 0.175 |
| $Ti^{48}$ | $TiH_x$ | 1.8 days | 92.7 | 35 | − 2.15 | 325 | 0.285 |
| $V^{51}$ | $V_2O$ | 6 min. | 27.0 | 15 | − 0.8 | 164 | 0.165 |
| $Cr^{52}$ | $Cr_2O_3$ | 3.9 min. | 77.7 | 14 | − 1.9 | 50 | 1.55 |
| $Fe^{56}$ | Element | 2.6 hr. | 96.7 | 12 | − 2.9 | 30 | 3.22 |
| $Ni^{61}$ | Element | 1.75 hr. | 181.5 | 14 | − 0.46 | 196 | 0.93 |
| $Zn^{64}$ | Element | 12 hr. | 386 | 15 | − 0.96 | 75 | 5.14 |
| $Zn^{66}$ | Element | 5 min. | 101 | 17 | − 2.2 | 37 | 2.72 |
| $Ga^{69}$ | Element | 14 hr. | 24.2[a] | 80 | − 0.06 | 123 | 0.197 |
| $Ge^{70}$ | Element | 20 min. | 129 | 50 | − 0.85 | 56 | 2.30 |
| $Ge^{72}$ | Element | 14 hr. | 65.2 | 40 | − 3.2 | 11.6 | 5.62 |
| $Ge^{73}$ | Element | 5 hr. | 136.6 | 50 | − 0.6 | 73 | 1.88 |
| $As^{75}$ | Element | 82 min. | 11.8 | 20 | − 0.4 | 64 | 0.184 |
| $Se^{77}$ | Element | 40 hr. | 45.2 | 50 | + 0.1 | 168 | 0.269 |
| $Sr^{88}$ | $SrCO_3$ | 17 min. | 17.7 | 20 | − 4.2 | 0.98 | 18.1 |
| $Zr^{90}$ | $Zr(NO_3)_2$, Element | 61 hr. | 247 | 40 | − 1.4 | 7.7 | 32.0 |
| $Zr^{94}$ | $Zr(NO_3)_2$, Element | 16.5 min. | 10.6 | 40 | − 4.6 | 0.17 | 62.4 |
| $Mo^{97}$ | Element | 76 min. | 108 | 50 | − 1.0 | 9.0 | 12.0 |
| $Ru^{101}$ | $RuO_2$ | 15 min. | 1.99 | 70 | − 0.5 | 10.0 | 19.9 |
| $Pd^{104}$ | Element | 44 sec.<br>4.3 min. | 132 | 50 | − 1.92 | 1.13 | 116 |
| $Pd^{105}$ | Element | 36.5 hr. | 743 | 70 | 0.0 | 11.5 | 64.6 |
| $I^{127}$ | $NH_4I$, LiI | 9.3 hr. | 231[a] | 60 | 0.0 | 3.9 | 59.2 |
| $Ba^{138}$ | $BaCO_3$ | 33 min. | 6.3 | 35 | − 1.8 | 0.24 | 26.3 |
| $La^{139}$ | $La(NO_3)_3$ | 85 min. | 5.7 | 42 | − 1.47 | 0.33 | 17.3 |
| $Tl^{205}$ | Element | 6 min. | 3.05 | 50 | − 0.80 | 0.016 | 190 |
| $Pb^{208}$ | Element | 3.1 min. | 0.96 | 100 | − 4.2 | 0.00006 | 16,000 |

[a] *Lower limit since only one isomer was observed.*

ary electrons were produced both in the sample and in the brass counter the error introduced was not large.

For samples which emitted conversion electrons, it was assumed that these were counted with the same efficiency as a $\beta$-ray spectrum having an end point of twice the energy. Measurements on the isomer of $Ba^{137}$ formed in the reaction $Ba^{138}(n, 2n)Ba^{137*}$, in which the counting efficiency for the conversion electrons relative to the $\gamma$-ray counting efficiency was determined, agreed with this assumption to within 10%.

In the case of positron emitters, where the $K$-capture branching is not known, the cross section has been corrected by using the curves published by Feenberg and Trigg (4) giving $K$-capture to positron ratios.

TABLE III

$(n, \alpha)$ CROSS SECTIONS

| Target nuclide | Sample form | Half-life | Observed cross section, mbarns | Standard deviation, % | $Q$-value, Mev. | Calculated cross section, mbarns | Ratio $\sigma_{obs}/\sigma_{cal}$ |
|---|---|---|---|---|---|---|---|
| $Al^{27}$ | Element | 15 hr. | 78.9 | 20 | + 2.3 | 273 | 0.29 |
| $Si^{30}$ | Element | 10 min. | 45.9 | 55 | − 4.2 | 13 | 3.53 |
| $P^{31}$ | Element | 2.4 min. | 146 | 20 | − 0.85 | 70 | 2.08 |
| $S^{34}$ | Element | 2.7 hr. | 138 | 25 | + 2.2 | 253 | 0.54 |
| $Cl^{35}$ | $NH_4Cl$, LiCl, NaCl | 14 days | 191 | 16 | + 0.63 | 267 | 0.71 |
| $Cl^{37}$ | $NH_4Cl$, LiCl, NaCl | 12.4 sec. | 52.4 | 50 | − 1.32 | 18.6 | 2.82 |
| $K^{41}$ | $KNO_3$ | 38 min. | 31.4 | 35 | − 0.83 | 14.6 | 2.15 |
| $V^{51}$ | $V_2O$ | 1.8 days | 28.6 | 42 | − 0.95 | 4.6 | 6.22 |
| $Mn^{55}$ | $MnO_2$ | 3.9 min. | 52.5 | 15 | + 0.04 | 4.5 | 11.7 |
| $Co^{59}$ | Element | 2.6 hr. | 39.1 | 20 | + 1.0 | 3.7 | 10.6 |
| $Ga^{69}$ | Element | 5 min. | 105 | 54 | + 1.42 | 12.3 | 8.53 |
| $Ge^{74}$ | Element | 2.2 min. | 14.9 | 40 | − 0.22 | 1.5 | 9.92 |
| $As^{75}$ | Element | 14 hr. | 12.3 | 18 | + 0.95 | 2.0 | 6.15 |
| $Se^{80}$ | Element | 59 sec., 12 hr. | 37.7 | 42 | − 1.4 | 0.17 | 222 |
| $Br^{81}$ | LiBr, NaBr | 90 min. | 103 | 20 | − 1.0 | 0.18 | 572 |
| $Rb^{87}$ | $Rb_2CO_3$ | 33 min. | 38.9 | 42 | + 0.42 | 0.14 | 278 |
| $Sr^{88}$ | $SrCO_3$ | 4.5 hr. | 64[a] | 30 | + 1.57 | 0.14 | 173 |
| $Y^{89}$ | $Y_2O_3$ | 19 days | 69.7 | 60 | + 2.6 | 1.2 | 58.0 |
| $Zr^{90}$ | Element | 2.75 hr. | 194[a] | 55 | + 3.66 | 2.15 | 90.2 |
| $Rh^{103}$ | $Rh_2O_3$ | 80 sec. | 63.0 | 40 | + 4.2 | 0.8 | 78.8 |
| $Pd^{110}$ | Element | 4 min. | 13.8 | 45 | + 2.13 | 0.29 | 47.6 |
| $I^{127}$ | $NH_4I$, LiI | 20 min. | 18.4[a] | 15 | + 3.85 | 0.02 | 920 |
| $Ce^{140}$ | $Ce(NO_3)_3$ | 2.6 min. | 12.1[a] | 50 | + 3.9 | 0.0015 | 8050 |
| $Sm^{152}$ | $Sm_2O_3$ | 1.7 hr. | 8.9 | 55 | + 4.98 | 0.0064 | 1390 |
| $Bi^{209}$ | $Bi_2O_3$, Element | 4 min. | 1.2 | 85 | + 7.5 | 0.00005 | 24,000 |

[a] *Lower limit since only one isomer was observed.*

## RESULTS

The measured $(n, p)$, $(n, \alpha)$, and $(n, 2n)$ cross sections are listed in Tables II, III, and IV. The half lives used for identification have been taken from N.B.S. Circular 499 (17) and are listed in Column 3.

TABLE IV

($n$, $2n$) CROSS SECTIONS

| Target nuclide | Sample | Half-life | Observed cross section, mbarns | Standard deviation, % | $Q$-value, Mev. | Calculated cross section, mbarns | Ratio $\sigma_{obs}/\sigma_{cal}$ |
|---|---|---|---|---|---|---|---|
| $N^{14}$ | Melamine ($C_3N_6H_6$) | 9.9 min. | 5.67 | 15 | −10.9 | 31.2 | 0.182 |
| $F^{19}$ | $CaF_2$, NaF | 1.8 hr. | 60.6 | 30 | −10.3 | 69 | 0.88 |
| $Cl^{35}$ | $NH_4Cl$, LiCl, NaCl | 33 min. | 3.47 | 45 | −13.2 | 4.5 | 0.77 |
| $K^{39}$ | $KNO_3$ | 7.7 min. | 10.0 | 55 | −13.2 | 7.2 | 1.39 |
| $Ni^{58}$ | Element | 36 hr. | 40.6 | 30 | −11.7 | 265 | 0.153 |
| $Cu^{63}$ | Element | 10 min. | 482 | 15 | −10.9 | 507 | 0.950 |
| $Cu^{65}$ | Element | 12 hr. | 1085 | 16 | −10.2 | 690 | 1.57 |
| $Zn^{64}$ | Element | 38 min. | 224 | 20 | −11.8 | 329 | 0.68 |
| $Ga^{69}$ | Element | 68 min. | 552 | 30 | −10.2 | 691 | 0.80 |
| $Ga^{71}$ | Element | 20 min. | 700 | 15 | −10.2 | 725 | 0.965 |
| $Ge^{70}$ | Element | 40 hr. | 666 | 35 | − 9.2 | 950 | 0.70 |
| $Ge^{76}$ | Element | 82 min. | 1820 | 30 | − 9.5 | 1025 | 1.77 |
| $As^{75}$ | Element | 17 days | 545 | 29 | −10.3 | 875 | 0.623 |
| $Se^{82}$ | Element | 59 min. | 1500[a] | 33 | − 9.8 | 1430 | 1.05 |
| $Br^{79}$ | LiBr, NaBr | 6.4 min. | 1141 | 25 | −10.7 | 815 | 1.40 |
| $Br^{81}$ | LiBr, NaBr | 4.4 hr. | 828[a] | 20 | −10.1 | 1000 | 0.83 |
| $Zr^{90}$ | $Zr(NO_3)_2$, element | 4.5 min. | 79.8[a] | 50 | −12.0 | 478 | 0.167 |
| $Mo^{92}$ | Element | 75 sec., 15 min. | 190 | 15 | −13.3 | 112 | 1.70 |
| $Mo^{100}$ | Element | 68 hr. | 3790 | 50 | − 9.0 | 1420 | 2.67 |
| $Ru^{96}$ | $RuO_2$ | 1.6 hr. | 478 | 19 | − 8.7 | 1440 | 0.332 |
| $Pd^{110}$ | Element | 13 hr. | 1948 | 50 | − 9.1 | 1530 | 1.27 |
| $Ag^{107}$ | Element | 25 min. | 519[a] | 50 | − 9.5 | 1460 | 0.355 |
| $Ag^{109}$ | Element | 2.3 min. | 311 | 50 | − 9.3 | 1500 | 0.207 |
| $Sb^{121}$ | Element | 15 min. | 750[a] | 25 | − 9.3 | 1640 | 0.457 |
| $Sb^{123}$ | Element | 2.8 days | 1245 | 25 | − 9.1 | 1680 | 0.74 |
| $Te^{128}$ | Element | 9.3 hr. | 779[a] | 30 | − 8.3 | 1825 | 0.426 |
| $Te^{130}$ | Element | 70 min., 32 days | 599 | 20 | − 8.3 | 1865 | 0.322 |
| $I^{127}$ | $NH_4I$, LiI | 13 days | 1120 | 35 | − 9.4 | 1225 | 0.913 |
| $Pr^{141}$ | $PrO_2$ | 3.4 min. | 2060 | 35 | − 9.5 | 1750 | 1.18 |
| $Sm^{154}$ | $Sm_2O_3$ | 47 hr. | 225[a] | 40 | − 7.5 | 2100 | 1.07 |
| $Gd^{160}$ | $Gd_2O_3$ | 18 hr. | 1470 | 55 | − 7.5 | 2150 | 0.683 |
| $Ta^{181}$ | Element | 8 hr. | 867 | 25 | − 7.7 | 2280 | 0.38 |
| $Pt^{198}$ | Element | 18 hr. | 2770 | 55 | − 8.0 | 2375 | 1.17 |
| $Au^{197}$ | Element | 5.5 days | 1722 | 27 | − 8.0 | 2400 | 0.72 |

[a] *Lower limit since only one isomer was observed.*

## DISCUSSION OF RESULTS

It is of interest to compare the observed cross section values with the values predicted from existing nuclear theory. The most fully developed nuclear model is the thermodynamic one described by Blatt and Weisskopf (1). This model yields a density of levels for the nucleus at excitation $E$

[1] $$\omega = C \exp (aE)^{\frac{1}{2}}$$

where $C$ and $a$ are slowly varying functions of mass number derived from experimental data.

The general expression for the cross section leading to emission of particle $x$ is given by

$$[2] \qquad \sigma_{(nx)} = \sigma_c \frac{F_x}{\sum_i F_i}$$

where $\sigma_c$ is the cross section for the formation of a compound nucleus, $F_x$ is proportional to the sum of the partial widths for emission of particle $x$, summed over all possible final states of the residual nucleus, and $\sum_i F_i$ is summed over all modes of disintegration of the compound nucleus. $F_x$, from the reciprocity theorem (1), is given by

$$[3] \qquad F_x = \int_0^{E\max} E\sigma_{IN}(E)\ \omega(E_{\max} - E)\, dE$$

where $E_{\max}$ is the maximum energy of excitation available for the residual nucleus, $\sigma_{IN}(E)$ is the cross section for capture of particle $x$ of energy $E$ by the residual nucleus at an excitation of $(E_{\max} - E)$, and $\omega(E_{\max} - E)$ is the level density in the residual nucleus at an excitation of $(E_{\max} - E)$ and is given by equation [1].

We have computed the cross section values expected on this model for the observed $(n, p)$ and $(n, \alpha)$ reactions. The values of the $F$ functions were taken from the Fast Neutron Data Project Report (5) and from the work of Heidmann and Bethe (10). The $(n, p)$ reaction $Q$-values used in the computation were derived from the known total $\beta$-ray disintegration energy of the residual nucleus and neutron–proton mass difference and the $(n, \alpha)$ reaction $Q$-values were calculated from semiempirical mass values (13). The values of $\sigma_c$ used were obtained by interpolation of the results of Phillips (14) for 14 Mev. neutrons.

The $(n, 2n)$ cross section will depend on the fraction of primary neutrons emitted from the compound nucleus with low enough energy such that the residual nucleus is left with an energy of excitation sufficient to boil off a second neutron. If the emission of $\gamma$-radiation is neglected at excitations greater than the neutron separation energy, then according to Blatt and Weisskopf (1)

$$[4] \qquad \sigma_{(n,\,2n)} = \xi\sigma_c[1 - (1 + \Delta E/T)\exp(-\Delta E/T)]$$

where $\Delta E$ is the difference between the incident neutron energy and the neutron separation energy in the target nucleus, $\sigma_c$ is defined above, $T$ is defined as $(E/a)^{\frac{1}{2}}$ (the function $a$ occurring in equation [1]) and represents a nuclear temperature of the intermediate nucleus remaining after the first neutron has evaporated. We have computed the $(n, 2n)$ cross sections using the neutron separation energies given in the compilation of Harvey (9) and again the values of $\sigma_c$ obtained from the work of Phillips (14).

The $Q$-values used in the calculations, the computed cross sections, and the ratios of the observed cross sections to the computed ones, $\sigma_{obs}/\sigma_{cal}$, are given in Tables II, III, and IV in Columns 6, 7, and 8 respectively. The ratios

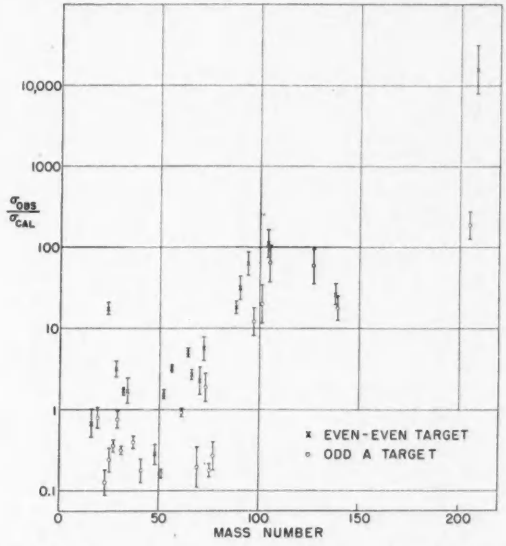


FIG. 3. Ratio of the observed to the calculated cross sections for $(n, p)$ reactions as a function of the mass number of the target nucleus. The experimental standard deviations are shown.

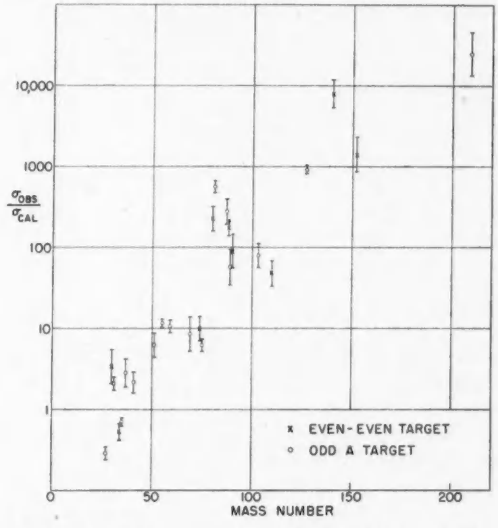


FIG. 4. Ratio of the observed to the calculated cross sections for $(n, \alpha)$ reactions as a function of the mass number of the target nucleus. The experimental standard deviations are shown.

$\sigma_{obs}/\sigma_{cal}$ are plotted against the mass number, $A$, of the target nucleus in Figs. 3, 4, and 5.

In the case of the charged particle reactions the ratio $\sigma_{obs}/\sigma_{cal}$ is seen to increase in general with $A$. In the case of the $(n, 2n)$ results, however, the ratio remains in general slightly less than one over the whole range of $A$. A number of upper limits for the ratio $\sigma_{obs}/\sigma_{cal}$ were obtained for some $(n, p)$ and $(n, \alpha)$ reactions which were not detected. In no case did the upper limit lie significantly below the general trend of Figs. 3 and 4.

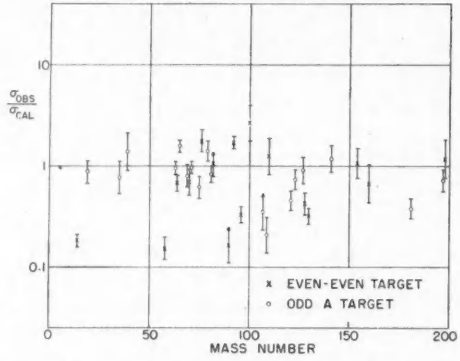


FIG. 5. Ratio of the observed to the calculated cross sections for $(n, 2n)$ reactions as a function of the mass number of the target nucleus. The experimental standard deviations are shown.

The values of the ratio $\sigma_{obs}/\sigma_{cal}$ for the $(n, p)$ reaction in even–even target nuclei cluster about a line roughly a factor of 6 higher than those for odd $A$ target nuclei. This suggests that level densities in odd–odd nuclei are about six times greater than level densities in comparable even–even nuclei. The ratios $\sigma_{obs}/\sigma_{cal}$ for $(n, \alpha)$ reactions in even–even nuclei cluster about a line at most a factor of 1.5 higher than those for odd–even nuclei. Combining this information with the $(n, p)$ result above would indicate that odd $A$ nuclei have level densities at most three times that in comparable even–even nuclei. No other data are at present available with which these estimates may be compared.

In speculating on the reasons for the deviations of the $(n, p)$ and $(n, \alpha)$ results from the evaporation theory, one may either try to change the assumptions in the theory to improve the fit or postulate a separate process. The values of $C$ and $a$ in the level density formula [1] have been derived from a variety of other experimental evidence. The small changes which could be made in these values are not sufficient to give agreement with our results. Some expansion of the nucleus or distortion of its shape which would make the potential barrier (involved in $\sigma_{IN}$ in formula [3]) smaller for highly excited nuclei might be postulated. Preliminary calculations indicate that the dis-

tortions required would be much larger than would be reasonably expected at these energies.

One may, however, assume that in those cases in which a compound nucleus is formed (that is, the energy of the incident neutron is completely shared amongst the nucleons) the evaporation theory is approximately correct. Then the observed deviation may be interpreted as another process in which the neutron interacts strongly with only one proton or $\alpha$-particle which escapes before much energy sharing takes place. Calculations which have been made in this laboratory by Drs. H. McManus and W. T. Sharp (12) for the $(n, p)$ case indicate that this model offers a possible explanation of the observed results.

## ACKNOWLEDGMENTS

It is a pleasure to acknowledge the help of Mr. R. A. Fraser in taking the data. We are indebted to Dr. L. G. Elliott and Prof. V. Weisskopf for helpful discussions.

## REFERENCES

1. BLATT, J. M. and WEISSKOPF, V. F. Theoretical nuclear physics. Chap. VIII. John Wiley & Sons, Inc., New York. 1952.
2. BRADT, H., GUGELOT, P. C., HUBER, O., MEDICUS, H., PREISWERK, P., and SCHERRER, P. Helv. Phys. Acta, 19: 77. 1946.
3. COHEN, B. L. Phys. Rev. 81: 184. 1951.
4. FEENBERG, E. and TRIGG, G. L. Revs. Modern Phys. 22: 399. 1950.
5. FELD, B. Final report of fast neutron data project, NYO-636, A.E.C., Oak Ridge. 1951.
6. FORBES, S. G. Report AECU-1883. Los Alamos Laboratory. 1952.
7. FOWLER, J. L. and SLYE, J. M. Phys. Rev. 77: 787. 1950.
8. HANSON, A. O. and MCKIBBEN, J. C. Phys. Rev. 72: 673. 1947.
9. HARVEY, J. A. Phys. Rev. 81: 353. 1951.
10. HEIDMANN, J. and BETHE, H. A. Phys. Rev. 84: 274. 1951.
11. JELLEY, J. V. and PAUL, E. B. Proc. Phys. Soc. (London), A, 63: 112. 1949.
12. MCMANUS, H. and SHARP, W. T. Phys. Rev. 87: 188. 1952.
13. METROPOLIS, N. and REITWIESNER, G. Table of atomic masses NP-1980, A.E.C., Oak Ridge. 1950.
14. PHILLIPS, G. C. Report AECU-404. Los Alamos Laboratory. 1949.
15. SERBER, R. Phys. Rev. 72: 1114. 1947.
16. WÄFFLER, H. Helv. Phys. Acta, 23: 239. 1951.
17. WAY, K., FULLER, G., WOOD, M., THEW, K., and JURGENS, A. Nuclear Data, Natl. Bur. Standards (U.S.), Circ. 499. 1952.

# ENERGY LEVELS IN LEAD AND BISMUTH AND NUCLEAR SHELL STRUCTURE[1]

By John A. Harvey[2]

ABSTRACT

A bismuth target and lead targets enriched in $Pb^{206}$, $Pb^{207}$, and $Pb^{208}$ have been bombarded with 14-Mev. deuterons from the M.I.T. cyclotron. Proton and triton spectra were measured with aluminum absorbers and a triple proportional counter. The spectra have been carefully analyzed and resolved into a relatively small number of groups. The proton spectra from all four targets are very similar, except for the long range state groups from the $Pb^{206}$ and $Pb^{207}$ targets. A striking similarity also occurs among the triton spectra from the four targets. The simplicity in the spectra probably arises because we are dealing with residual nuclei with closed or nearly closed shells of 82 protons and 126 neutrons. The fact that a $(d,p)$ reaction proceeds mainly by means of a stripping process, in which only the neutron enters the nucleus, suggests the possibility that the similarities can be explained by a single particle model of the nucleus. Moreover, the $(d,t)$ reaction is principally a pickup process and thus the single-particle model is suggested again. Observed energy levels are compared with the known levels measured from radiative transitions. Aided by the angular momentum and parity assignments of some of these known levels, tentative assignments of angular momentum and parity are made to many of the new levels from a strong spin-orbit coupling shell model.

## I. INTRODUCTION

Many nuclear properties such as the natural abundances of the stable isotopes, quadrupole moments, $\alpha$-decay energies, nuclear fission, neutron binding energies, fast neutron capture cross section strongly suggest the existence of "magic numbers" and a shell model for nuclear structure. From considerations of spins and magnetic moments (22, 29), orbital angular momenta have been assigned to the ground states of odd-$A$ nuclei (mainly stable nuclei). These assignments agree with one of the few possible choices allowed by the strong spin-orbit coupling shell model proposed by Mayer (25, 26) and Haxel, Jensen, and Suess (16). The positions of the initial and final odd nucleon groups in the nuclear shell scheme have been determined from comprehensive analyses of the allowed or forbidden character of $\beta$-decay data of odd-$A$ nuclei (27). A similar consideration (30) has been extended to even-$A$ nuclei and assignments of "orbitals" have been made to the neutron and proton groups in the odd–odd nuclei. The $\beta$-decay studies include not only ground state transitions but also transitions to isomeric and other excited states of the residual nuclei. Thus, assignments of "orbitals" to excited and ground states of final nuclei are made together with assignments to the initial nuclei. The spin and parity of low lying isomeric levels, deduced from a classification of nuclear isomers (10) and a review of isomerism and shell structure

[1] *Manuscript received October 16, 1952.*
*Contribution from Laboratory for Nuclear Science, Massachusetts Institute of Technology, Cambridge, Mass.*
*Part of a thesis submitted in partial fulfillment of the requirements for the degree of Doctor of Philosophy in Physics in the Graduate School of the Massachusetts Institute of Technology. This work was supported by the joint program of the ONR and the AEC. The experimental results were reported at the Washington Meeting (April, 1950) of the American Physical Society and in a Mass. Institute of Technology Progress Report April 1, 1950.*
[2] *Now at Brookhaven National Laboratory, Upton, New York.*

(9), are consistent with the possible choices (restricted to one or a few) of the strong spin-orbit coupling model. However, at present, the shell model is not capable of giving the order of the levels and their separation from one another.

The angular distribution of $(d,p)$ and $(d,n)$ nuclear reactions, which proceed mainly by a stripping process, often yields the orbital angular momentum of the final state (5, 20, 31) and serves as a test for the single particle model (3). While measuring neutron binding energies from a bismuth target and targets of the separated lead isotopes, complete proton spectra were measured. The proton spectra could be resolved into a relatively small number of groups, indicating a wide level spacing, in contrast to the spectrum from gold. Also, a surprising similarity in the proton spectra from all targets was noted (except for the closing of the 126 neutron shell). Triton spectra were measured from the same targets and a similarity of triton spectra from the $(d,t)$ reaction was obvious. This similarity in the nuclear energy level diagrams can be interpreted by means of a single particle model of the nucleus. The observed energy levels agree in many cases with levels measured from radiative transitions. Tentative assignments of spin and parity are suggested for many of the new levels.

## II. DESCRIPTION OF APPARATUS

The equipment is the same as that described by Boyer *et al.* (4) and only a brief account will be given here. The 15.5-Mev. deuteron beam from the M.I.T. cyclotron was focused at the center of a target chamber about 12 ft. from the cyclotron. Targets were held in small aluminum frames 1 in. square and mounted at the center of the chamber. The targets could be retracted into the target holder and inserted into the deuteron beam by compressed air. A side port of the chamber contained another target holder which held a second target. Alternate runs could be taken on the two targets and one target was used as a reference. The lead targets were about 20 mgm./cm.$^2$ thick, the bismuth target 10 mgm./cm.$^2$ thick, and the aluminum reference target 1.9 mgm./cm.$^2$ thick. The deuteron beam was uniformly spread over a $\frac{1}{2}$ in. square at the center of the target.

The protons and tritons were detected by a triple coincidence proportional counter. The proton and triton ranges were measured in aluminum absorbers by the principle of "peaking"; only protons or tritons ending their range in the third counter were counted. In order to discriminate against protons in favor of tritons the voltage gates on the first two counters were raised since the tritons have a higher specific ionization. The triple proportional counter could be rotated in angle about the target and the spectra could be measured for angles from 30°-150°. The solid angle of the counter was defined by a rectangular slit $\frac{3}{4}$ in. high and 0.4 in. wide, located 4 in. from the target. A parallel plate ionization chamber was located at the entrance of the target chamber in order to monitor the beam. This reduced the deuteron energy to 14 Mev.

## III. EXPERIMENTAL PROCEDURE AND RESULTS

### *A. Proton Spectra*

In order to set the pulse heights on the three counters for protons, sufficient aluminum absorbers were added so that the long range group from an aluminum

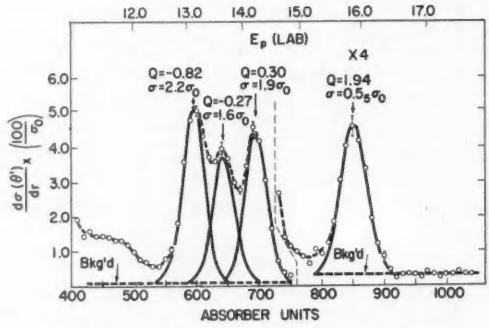


FIG. 1. Proton spectrum at $\theta = 50°$ from a 10 mgm./cm.$^2$ bismuth target bombarded with 14-Mev. deuterons from the reaction $Bi^{209}$ $(d,p)$ $Bi^{210}$. The ordinate is the differential cross section in the center-of-mass system per absorber unit in terms of the ground state proton peak from aluminum, $\sigma_0$. ($\sigma_0 = 2.5 \pm 1.0$ mb./steradian.) $\theta'$ is the angle measured in the center-of-mass system. The abscissa is in units of 0.416 mgm./cm.$^2$ of aluminum. The proton energy in the laboratory system is also given. The vertical bar represents the square root of the number of counts.

target ended its range in the third counter. The amplifier gain was then adjusted to give a reasonable voltage pulse and a fairly wide voltage gate (40%) was set on the discriminator, in order to detect also those protons of slightly shorter or longer range. Fairly narrow voltage gates were set on the pulses from counters 2 and 1 and their levels were determined by maximizing the double and the triple coincidence rates. For the proton spectra we do not have to discriminate against deuterons since, for 14-Mev. deuterons, all proton groups leading to bound states of the residual nucleus have ranges greater than the range of the elastically scattered deuterons. Differential spectra were obtained from the triple coincidence rate as a function of the aluminum absorber thickness.

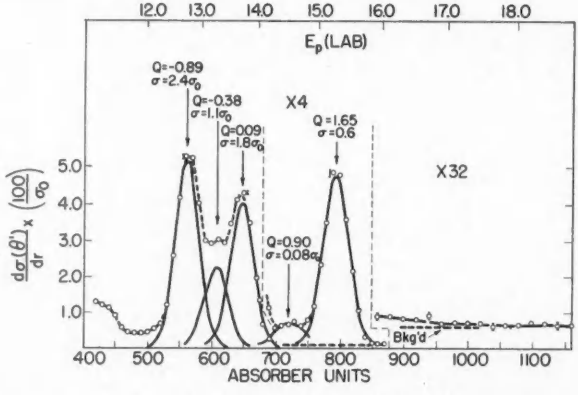


FIG. 2. Proton spectrum at $\theta = 50°$ from a 20.5 mgm./cm.$^2$ $Pb^{208}$ target after correcting for the contributions due to the other isotopes. The ordinate and abscissa scales are the same as for Fig. 1.

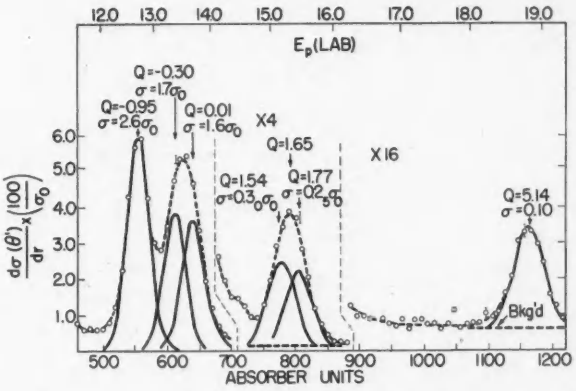


FIG. 3. Proton spectrum at $\theta = 50°$ from a 23.0 mgm./cm.$^2$ $Pb^{207}$ target after correcting for the contributions due to the other isotopes. The ordinate and abscissa scales are the same as for Fig. 1.

The aluminum absorber thickness was varied in steps of about 4 mgm./cm.$^2$ For the more intense proton groups the peak counting rate was several hundred counts per second. Thus, a region several million electron volts wide could be run in 10-15 min. with almost a 1% statistical accuracy at the peak. For the low intensity long range groups somewhat longer runs had to be taken. In order to compensate for the slight drifts in the equipment, the ground state peak from the thin aluminum target, mounted in the side target holder, was run as a monitor peak before and after every run. Any run in which the aluminum ground state peak drifted by more than 30 kev. in energy or 10% in intensity was discarded. The proton spectra from bismuth and $Pb^{208}$ were divided into two sections and the spectra from $Pb^{207}$ and $Pb^{206}$ into three sections as shown in Figs. 1-4. Several alternate runs were taken on each section of the spectrum from the center target

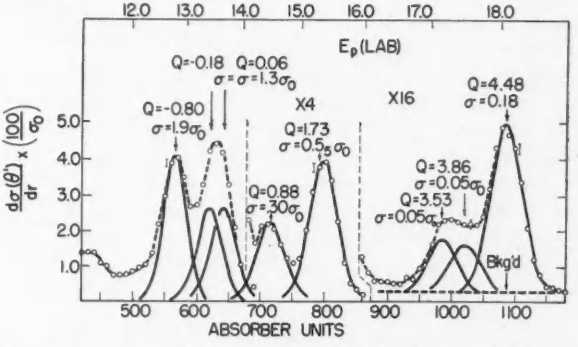


FIG. 4. Proton spectrum at $\theta = 50°$ from a 24.5 mgm./cm.$^2$ $Pb^{206}$ target after correcting for the contributions due to the other isotopes. The ordinate and abscissa scales are the same as for Fig. 1.

and the ground state group from the aluminum side target. The spectra were averaged. Although the spectra were measured at an angle of 50° from the direction of the deuteron beam, the target was set perpendicular to the beam in order to eliminate most of the spread of the proton groups due to the target thickness. All factors contributing to the spread of the proton groups have been carefully analyzed (15) and the spectra have been resolved into a small number of groups.

This simplicity in the proton spectra is attributed to the fact that we are considering nuclei which have closed, or nearly closed, shells of 82 protons and 126 neutrons. This simplicity is to be contrasted with the proton spectrum from a gold target, which cannot be resolved into a few levels (13, 23). $Q$-values and differential cross sections of the groups have been calculated relative to the aluminum ground state group ($Q$ = 5.50 Mev.) as previously discussed (15). The $Q$-values are accurate to 50 kev. when the groups are well resolved experimentally, and to 100 kev. when resolved graphically. The relative differential cross sections are accurate to 20%. The differential cross section ($\sigma_0$) of the aluminum ground state group at 50° has been measured to be 2.5 ± 1.0 millibarns/steradian (13).

Fig. 1 shows the differential range spectrum from a 10 mgm./cm.$^2$ evaporated bismuth target. The spectrum has been measured at several angles from 30°–90° and the peaks shift as expected. Also, the angular distribution is in agreement with that expected for a heavy element from a stripping process (12).

TABLE I
PERCENTAGE ISOTOPIC ABUNDANCE OF ENRICHED LEAD TARGETS

| | Target | | |
|---|---|---|---|
| Isotope | $Pb^{206}$ | $Pb^{207}$ | $Pb^{208}$ |
| $Pb^{204}$ | 0.5 | 0.2 | Less than 0.1 |
| $Pb^{206}$ | 71.3 | 6.2 | 1.6 |
| $Pb^{207}$ | 5.1 | 66.8 | 2.6 |
| $Pb^{208}$ | 23.1 | 26.8 | 95.8 |

Lead targets enriched in $Pb^{206}$, $Pb^{207}$, and $Pb^{208}$ were obtained from Oak Ridge* with the enrichments shown in Table I. The lead chromates and sulphates were reduced to the metal by Mrs. E. Backofen and the lead pellets were rolled into thin metallic foils. The differential spectra have been measured from these targets and the data carefully analyzed. For each target the contributions due to the other isotopes were subtracted. The final data are shown in Figs. 2-4. The $Q$-values and their differential cross sections are listed in Table II. Neutron binding energies computed from the ground state $Q$-values are in good agreement with the gamma ray energies of 4.17 Mev. from bismuth, 7.38 Mev. from $Pb^{207}$, and 6.73 Mev. from $Pb^{206}$ measured by Kinsey *et al.* (21). Although protons were observed at lower energies than the $Q$-values listed in Table II, no distinct group was observed down to a $Q$-value of − 2.23 Mev. The number of protons in this region was considerably less than that from a gold or tantalum target (13, 23).

**Supplied by Carbide and Carbon Chemical Division, Oak Ridge National Laboratory, Oak Ridge, Tenn.*

TABLE II

Q-VALUES AND DIFFERENTIAL CROSS SECTIONS OF PROTON GROUPS FROM $(d,p)$ REACTIONS
$Q$-Values in Mev.; $\sigma$ (50°) in units of $\sigma_0 \approx 2.5$ mb./steradian

| $Pb^{206}(d,p)$ | | $Pb^{207}(d,p)$ | | $Pb^{208}(d,p)$ | | $Bi^{209}(d,p)$ | |
|---|---|---|---|---|---|---|---|
| $Q$ | $\sigma/\sigma_0$ | $Q$ | $\sigma/\sigma_0$ | $Q$ | $\sigma/\sigma_0$ | $Q$ | $\sigma/\sigma_0$ |
| − 0.80 | (1.9) | − 0.95 | (2.6) | − 0.89 | (2.4) | − 0.82 | (2.2) |
| − 0.18 | (1.3) | − 0.30 | (1.7) | − 0.38 | (1.1) | − 0.27 | (1.6) |
| 0.06 | (1.3) | 0.01 | (1.6) | 0.09 | (1.8) | 0.30 | (1.9) |
| 0.88 | (0.3) | | | 0.90 | (0.1) | | |
| | | 1.54 | (0.3) | | | | |
| 1.73 | (0.6) | | | 1.65 | (0.6) | 1.94 | (0.6) |
| | | 1.77 | (0.3) | | | | |
| 3.53 | (0.05) | | | | | | |
| 3.86 | (0.05) | | | | | | |
| 4.48 | (0.2) | | | | | | |
| | | 5.14 | (0.1) | | | | |

The surprising similarity of the curves suggested the possibility that a contaminant was present in all the targets. From the energy shift of the groups as a function of angle, we could conclude that the protons came from a nucleus with an atomic weight of 200 ± 20. This eliminated common contaminants such as carbon, oxygen, etc. The angular distributions of the groups were in agreement with those expected for a heavy element. A bismuth target was spectrochemically analyzed and it contained less than a few parts per million of lead and tungsten. The lead targets were freshly prepared by melting them in carbon crucibles in order to reduce any oxide and were rolled with clean rollers. An enriched $Pb^{206}$ target was also obtained from Columbia University* and the spectrum agreed with that of Fig. 4. Thus, these proton spectra must definitely be assigned to bismuth and the lead isotopes.

It was suggested** that the low energy proton groups may be caused by a "tunnelling" effect since these protons have an energy of about 13 Mev., which is just the height of the Coulomb barrier for these nuclei. To eliminate this possibility the low energy section of the spectrum from $Pb^{208}$ was taken at deuteron energies of 12 Mev. and 10 Mev. With 12-Mev. deuterons, the low energy protons had an energy of about 11 Mev. The $Q$-values for the two outer peaks were − 0.87 Mev. and 0.07 Mev., in good agreement with the values obtained with 14-Mev. deuterons. With 10-Mev. deuterons, the low energy protons had an energy of about 9 Mev. The $Q$-values obtained were − 0.88 and 0.00 Mev., with an accuracy of 0.1 Mev. Since the $Q$-values are independent of deuteron energy, the groups must arise from nuclear properties and not a Coulomb barrier effect.

The low energy proton spectrum from a gold target was also run at a 12-Mev. deuteron energy to determine whether the broad peak with a $Q$-value of − 0.1 Mev. which occurred with 14-Mev. deuterons would split into two peaks at the lower bombarding energy. This might be expected if the Coulomb barrier had caused the splitting in the $Pb^{208}$ spectrum. Since the barrier is less in gold, one

*The author wishes to thank I. Ruderman for the loan of a sample of radiogenic lead.
**M. Deutsch.

might expect that a splitting would occur if the proton energy were reduced below the barrier height. However, the single broad proton peak with a $Q$-value of $-0.2$ Mev. was observed with 12-Mev. deuterons. Thus, we conclude that the proton groups observed do correspond to levels in the residual nucleus.

The proton spectrum from a thallium target also has a shape quite similar to that from the $Pb^{206}$ target. However, since natural thallium has two isotopes, no attempt was made to resolve the spectrum into groups. Preliminary runs were made on thallium oxide samples enriched in $Tl^{205}$ and $Tl^{203}$, but further data are needed.

*B. Triton Spectra*

Tritons from the $(d,t)$ reactions have a shorter range than that of the elastically scattered deuterons. The voltage gates on the discriminators must be raised in order to utilize the higher specific ionization of a triton and thus discriminate against protons and deuterons (4). When the gates are set for tritons, the triton

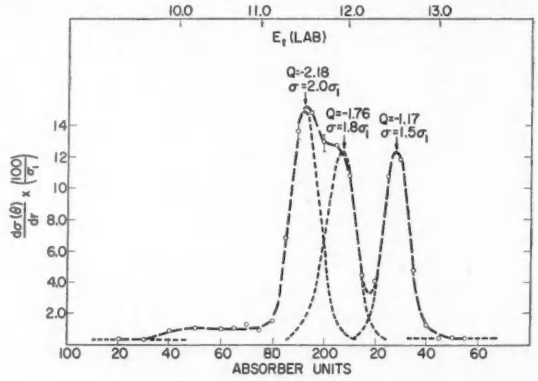


FIG. 5. Triton spectrum at $\theta = 90°$ from the same 10 mgm./cm.$^2$ bismuth target bombarded with 14-Mev. deuterons from the reaction $Bi^{209}(d,t)Bi^{208}$. The ordinate is the differential cross section in the center-of-mass system of coordinates in terms of $\sigma_1$. ($\sigma_1 \simeq 2.5$ mb./steradian.) $\theta'$ is the angle measured in the center-of-mass system. The abscissa is in units of 0.416 mgm./cm.$^2$ of aluminum. The triton energy in the laboratory system is also given. The vertical bar represents the square root of the number of counts. [On the ordinate $\theta$ should read $\theta'$.]

groups from a $Pb^{208}$ target at 90° have a counting rate 200 times that of the proton groups. However, when the gates are set for protons, the triton groups have the same counting rate as that of the proton groups. Range spectra were taken of the tritons from the same four targets with the long range triton groups from the $Pb^{208}$ target, mounted in the side target holder, as a monitor since no tritons were observed from the aluminum target. The spectra were taken in 2 mgm./cm.$^2$ range steps. The final data for the same targets, corrected for the contributions of the other isotopes in the case of the lead targets, are shown in Figs. 5-8. Each curve represents the average of four runs.

$Q$-Values were calculated relative to the $-1.10$ Mev. $Q$-value for the $Pb^{208}$ $(d,t)$ ground state group. The $Q$-values are accurate to 50 kev. for experimentally

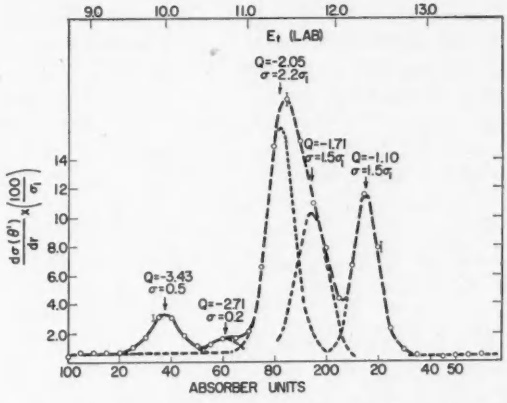


FIG. 6. Triton spectrum at 90° from the 20.5 mgm./cm.$^2$ $Pb^{208}$ target after correcting for the contributions due to the other isotopes. The ordinate and abscissa scales are the same as for Fig. 5.

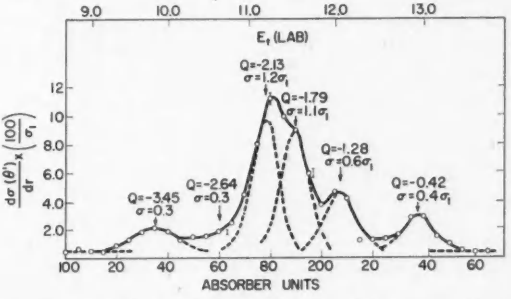


FIG. 7. Triton spectrum at 90° from the 23.0 mgm./cm.$^2$ $Pb^{207}$ target after correcting for the contributions due to the other isotopes. The ordinate and abscissa scales are the same as for Fig. 5.

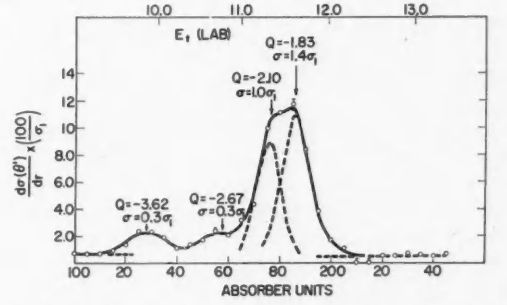


FIG. 8. Triton spectrum at 90° from the 24.5 mgm./cm.$^2$ $Pb^{206}$ target after correcting for the contributions due to the other isotopes. The ordinate and abscissa scales are the same as for Fig. 5.

resolved peaks and 100 kev. for the graphically resolved peaks. The differential cross sections have been measured relative to the differential cross section of the highest energy triton group of bismuth, which was taken to be 1.5 $\sigma_1$ mb./steradian. From an integral spectrum from a bismuth target, $\sigma_1$ was estimated to be about 2.5 mb./steradian but may be as much as a factor of two lower. The spectra were measured at different angles around 90° and from the energy shift the groups can be assigned to a heavy element. It is assumed that a triton does not have any excited levels and that the observed triton groups indicate excited levels in the residual nucleus. Table III summarizes the $Q$-values and the differential cross sections of the groups observed from the $(d,t)$ reaction.

TABLE III

$Q$-VALUES AND DIFFERENTIAL CROSS SECTIONS OF TRITON GROUPS FROM $(d,t)$ REACTIONS
$Q$-Values in Mev.; $\sigma$ (90°) in units of $\sigma_1 \approx 2.5$ mb./steradian

| $Pb^{206}(d,t)$ | | $Pb^{207}(d,t)$ | | $Pb^{208}(d,t)$ | | $Bi^{209}(d,t)$ | |
|---|---|---|---|---|---|---|---|
| $Q$ | $\sigma/\sigma_1$ | $Q$ | $\sigma/\sigma_1$ | $Q$ | $\sigma/\sigma_1$ | $Q$ | $\sigma/\sigma_1$ |
| − 3.62 | (0.3) | − 3.45 | (0.3) | − 3.43 | (0.5) | | |
| − 2.67 | (0.3) | − 2.64 (?) | (0.3) | − 2.71 | (0.2) | | |
| − 2.10 | (1.0) | − 2.13 | (1.2) | − 2.05 | (2.2) | − 2.18 | (2.0) |
| − 1.83 | (1.4) | − 1.79 | (1.1) | − 1.71 | (1.5) | − 1.76 | (1.8) |
| | | − 1.28 | (0.6) | − 1.10 | (1.5) | − 1.17 | (1.5) |
| | | − 0.42 | (0.4) | | | | |

The alpha particle spectrum was measured from a bismuth target bombarded with 14-Mev. deuterons. Owing to poor resolution only a broad group (3 Mev. wide) of alphas was observed, corresponding to an excitation energy in $Pb^{207}$ of about 4 Mev.

## IV. DISCUSSION OF RESULTS

The surprising agreement among the observed groups from the several targets, both in $Q$-value and in intensity, from the $(d,p)$ and $(d,t)$ reactions can be explained by a single particle model for the nucleus. Since a $(d,p)$ reaction for both light and heavy nuclei (5, 12) proceeds mainly by means of a stripping process, in which only the neutron enters the nucleus, we might expect that this single neutron would possess all the excitation energy. Thus, the excited levels observed would be just those levels which agree with a single particle model. Similarly, the $(d,t)$ reaction probably occurs by means of a pickup process (6, 11), in which a single neutron is pulled out of the target nucleus and a "hole" is left in the shell. This "hole" in a shell is equivalent to saying that the unpaired neutron remaining in the shell becomes the neutron possessing the excitation energy. The levels from the $(d,p)$ reaction require a shell picture in which single neutrons outside of a central core possess the excitation energy. On the other hand, the levels from the $(d,t)$ reaction suggest that neutrons inside a central core exist in shells and that the "hole" or the unpaired neutron possesses the excitation energy.

In order to discuss the agreement among the energy levels let us first select a nuclear shell scheme from which we can also make some tentative assignments

to the excited levels. We have selected the strong spin-orbit coupling model and have accepted the arrangement of the subshells from 82-126 neutrons quoted by Klinkenberg (22), which gives agreement with the ground states of nuclei. Fig. 9 shows this level scheme for proton and neutron shells greater than 50.

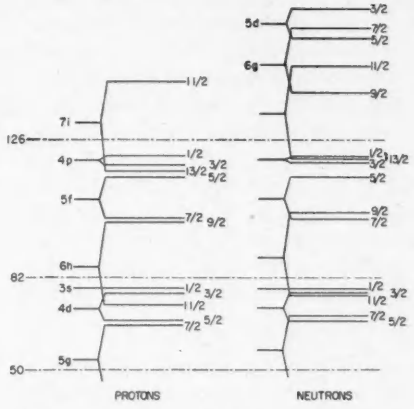


FIG. 9. Nuclear shell scheme for the neutron and proton shells greater than 50 determined by Klinkenberg (22) from the *jj*-coupling model, in order to account for the ground states of odd-mass nuclei.

We see that for $Pb^{208}$, which has 126 neutrons, the $4p_{1/2}$, $4p_{3/2}$, $7i_{13/2}$, $5f_{5/2}$, etc. states are all filled. Thus, for the $Pb^{209}$ nucleus the 127th neutron would have to go into one of the higher shells. Fig. 9 would predict that the 127th neutron would be in a $g_{9/2}$ state for the ground state of $Pb^{209}$. Excited states would be explained as $i_{11/2}$, $d_{5/2}$, $g_{7/2}$, $d_{3/2}$, etc. neutrons. The order should not be taken too literally. Similarly, for the $Pb^{207}$ nucleus we might expect excited levels to occur when the odd 125th neutron was in a $g_{9/2}$, $i_{11/2}$, $d_{5/2}$, etc. state.

However, we would also expect lower excited levels for the $Pb^{207}$ nucleus from "holes" in the subshells in the 126 neutron core. The ground state of $Pb^{207}$ arises when the 125th neutron is in the $p_{1/2}$ state. Excited states would correspond to "holes" in $i_{13/2}$, $p_{3/2}$, $f_{5/2}$, etc. shells. Again the sequence may not be in order of increasing energy. Since nuclear isomers occur just before the completion of a closed shell, the angular momentum and parity assignments of the excited levels determined from isomeric transitions enable one to arrange these single-particle levels in order of excitation. For example, in $Pb^{207}$ the first excited level at 0.565 Mev. is an $f_{5/2}$ level, the $i_{13/2}$ level is at 1.63 Mev., and the $p_{3/2}$ and $f_{7/2}$ assignments are made tentatively to the 0.870 Mev. and 1.1 Mev. levels respectively (9).

The energy levels observed can be explained with the aid of the two following assumptions. (1). Neutron shells are largely independent of proton shells (30). Thus, for $Bi^{210}$ we assume that the 83rd proton is in the same state as the 83rd proton in $Bi^{209}$ and the 127th neutron is in the same state as the 127th

neutron in $Pb^{209}$. Excited states in $Bi^{210}$ arise from excited neutron levels and the 83rd proton is always an $h_{9/2}$ proton. However, in order to explain the occurrence of the two proton groups corresponding to the $f_{5/2}$ and $p_{3/2}$ levels in $Pb^{207}$, we must assume that there is a weak coupling between neutron shells. This is discussed later. (2). The interaction energy between two unpaired nucleons for an even-$A$ nucleus is small ($< 0.5$ Mev.) and depends on the resultant spin.* Thus, the excited levels observed for $Bi^{210}$ would be expected to agree with those of $Pb^{209}$ (except for a slight lowering due to the small interaction between the odd neutron and odd proton). The probability of combining a $g_{9/2}$ neutron with the $h_{9/2}$ proton to produce a state of spin 0 is small compared to the probability of producing a state of higher spin. This accounts for the absence (or low intensity) of the ground state group in $Bi^{210}$. There is also a small interaction energy between two unpaired neutrons. Thus, the excited states of $Pb^{206}$ from the $(d,t)$ reaction result from an interaction between the $p_{1/2}$ neutron and $f_{5/2}$, $p_{3/2}$, etc. neutrons. Also, the first excited state observed for $Pb^{208}$ is a doublet because of the interaction between the $g_{9/2}$ neutron and the $p_{1/2}$ neutron.

*A. Energy Levels from (d,p) Reactions*

Energy level diagrams obtained from $(d,p)$ reactions have been plotted in Fig. 10 in such a way that levels of equal $Q$-value correspond. This is equivalent to matching the boundary between virtual and real levels. The excitation energies computed from the $Q$-values are given on the diagrams and have an accuracy of 50 kev. for the experimentally resolved peaks and 100 kev. for the graphically resolved peaks. Within the limit of error, the $Q$-values of most of the levels agree. The binding energy for a neutron in any level is simply the distance from the dotted line, which represents the boundary between virtual and bound levels, to the particular level in question. The neutron binding energy for the ground state and excited states is simply the $Q$-value plus 2.23 Mev. (the deuteron binding energy). The decrease in neutron binding energy upon completion of the 126 neutron shell is evident from the binding energies of the ground states. It has been pointed out by several observers (15, 17, 21, 35) that an error of 450 kev. exists in a closed cycle including the four ground state $Q$-values, the $\beta$-decay energies of Ra E and $Pb^{209}$, and the $\alpha$-energy of $Po^{210}$. Analyses of binding energies in this region indicate that the neutron binding energy for $Bi^{210}$ is in error (17, 21, 34, 35). It is also possible that both the $Pb^{208}$ and $Bi^{209}$ $Q$-values are in error or that the observed groups are transitions to excited states. However, the neutron binding energy calculated from the $Bi^{209}$ $Q$-value agrees with the energy of the gamma ray found by Kinsey *et al.* We have assumed that the $Bi^{209}$ $Q$-value is not the ground state $Q$-value and the ground state of $Bi^{210}$ is shown dotted in Fig. 10, 450 kev. below the lowest observed level. Excitation energies of the higher levels have been computed from this assumed ground state.

*[*Note added in proof*]: *M. H. L. Pryce, Proc. Phys. Soc. (London), A, 65: 773. 1952. This paper discusses the interaction between an odd neutron and odd proton in great detail. A very complete discussion is devoted to the energy levels of* $Pb^{206}$ *and* $Pb^{208}$ *which arise from the interaction of two odd neutrons. Energy levels which arise from the excitation of two nucleons also are considered.*

First let us consider the energy level diagram for the $Pb^{209}$ nucleus which contains 127 neutrons. From a consideration of the $\beta$-decay selection rules (27) it is concluded that the 127th neutron is a $g_{9/2}$ neutron which transforms into an $h_{9/2}$ proton in the $\beta$-decay of $Pb^{209}$. The ground state of $Bi^{209}$ is known to have a nuclear spin of 9/2 and an $l$-value of 5. The assignments of orbitals to the excited states are made with the aid of Fig. 9 and from the observed intensities of the groups. The 0.75 Mev. level is thought to be an $i_{11/2}$ level because of the low intensity of the proton group. To form this state the neutron must carry in six units of orbital angular momentum. A 14-Mev. deuteron, which has a

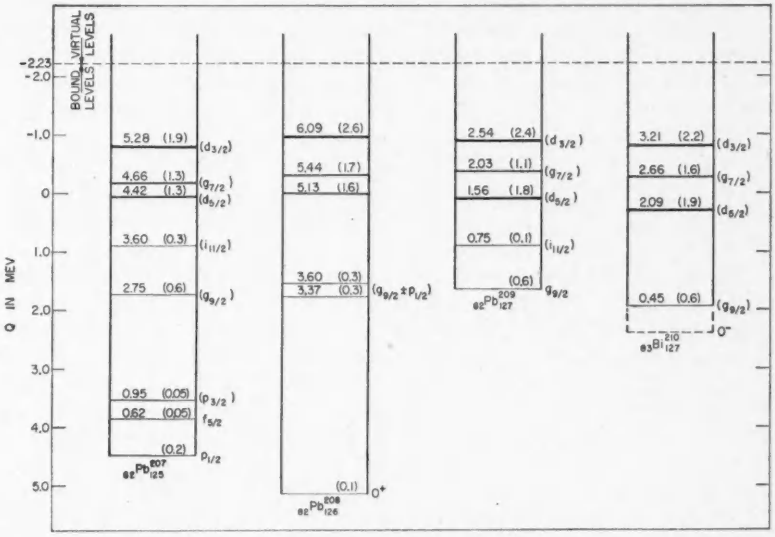


FIG. 10. Energy level diagrams of $Pb^{207}$, $Pb^{208}$, $Pb^{209}$, and $Bi^{210}$ measured from $(d,p)$ reactions. The level diagrams are plotted so that levels with similar $Q$-values agree. The excitation energy in Mev. is given for each level and also its differential cross section at 50° is given in parentheses in units of $\sigma_0$ ($\sigma_0 = 2.5$ mb./steradian). Tentative assignments of orbital angular momentum quantum numbers to some of the levels are given in parentheses. The ground state of $Bi^{210}$ is shown 0.45 Mev. below the lowest observed level as explained in the text. It is assumed that the odd proton in $Bi^{210}$ is always in an $h_{9/2}$ state and the assignments refer to the odd neutron.

$\lambda/2\pi = 0.85 \times 10^{-13}$ cm., would possess relative $l$-values up to 10 or 11 for a nucleus the size of lead, $R = 9 \times 10^{-13}$ cm. However, since the $(d,p)$ reaction is a stripping process, the proton carries away considerable momentum and even allowing for the size of the deuteron, the probability of a large $l$-value transfer to the nucleus is small. Thus, the low intensity of the proton group corresponding to the first excited level is attributed to the six units of angular momentum required to form the state. The 2.03 Mev. level is tentatively thought to be a $g_{7/2}$ level on a similar intensity consideration argument. The intensity of the proton group corresponding to this level is only 50% that of the two neighboring

groups, which are designated as $d_{5/2}$ and $d_{3/2}$ levels. Strong spin-orbit coupling requires that the $d_{5/2}$ state be lower than the $d_{3/2}$ state. It should be pointed out that the splitting of the two $g$-levels is 2 Mev. and that of the two $d$-levels is 1 Mev. This ratio of 2 is in fair agreement with that predicted from strong spin-orbit coupling theory (26), which predicts a splitting proportional to $(2l + 1)$ and hence a ratio of 9/5.

The agreement between the levels observed in $Bi^{210}$ and those in $Pb^{209}$ leads one to the conclusion that these levels are again neutron levels, i.e., the 127th neutron in $Bi^{210}$ possesses the excitation energy. This assumes that the neutron shell is independent of the proton shell and that the neutron–proton interaction energy is small. From the persistence of islands of isomerism, Nordheim (30) also suggests that proton and neutron configurations are largely independent of each other. Thus, using arguments identical to those used for the levels in $Pb^{209}$, the three upper levels arise from $d_{3/2}$, $g_{7/2}$, and $d_{5/2}$ neutrons. It will be noted that the $i_{11/2}$ level does not appear. A search was made for a proton group in this energy region but it was not found. However, owing to the background and the low resolution only an upper limit for its intensity of $\sigma/\sigma_0 = 0.05$ could be measured. This is only a factor of two less than the intensity of the group corresponding to the $i_{11/2}$ level in $Pb^{209}$.

Although angular distributions were taken from 30°–90°, they do not show any structure other than that found by Gove (12) which might enable us to determine the $l$-values of the levels from Butler's stripping theory. However, the effect of the Coulomb field certainly could not be ignored in the stripping theory. The data were taken early in 1950 before it was known that angular distributions could be useful in determining the $l$-values of the residual nucleus. It is now felt that a careful study of this problem might prove valuable in assigning $l$-values to the levels.

The ground state of $Bi^{210}$ probably has zero spin and odd parity (33). The ground state from the $Bi^{209}(d,p)$ reaction could arise from an interaction of the $g_{9/2}$ neutron and the $h_{9/2}$ proton to produce a state of spin zero. The probability of a $g_{9/2}$ neutron's combining with an $h_{9/2}$ proton to produce a zero spin state is small compared to that of higher spin states. The level (or center of several levels) observed at 0.45 Mev. is assigned to a $g_{9/2}$ neutron which has combined with the $h_{9/2}$ proton to produce a state of high spin. An energy of $\frac{1}{2}$ Mev. is reasonable for the interaction in order to produce the state of spin zero (Pryce). From the $\beta$-decay of $Pb^{210}$ (2, 18, 19) an excited state at 47 kev., probably odd parity and spin 1 (9), could arise from an interaction between the odd neutron and proton. Also five other possible levels have been detected at lower energies (2, 19).

From the agreement of the upper levels in $Pb^{207}$ with those in $Pb^{209}$ and similar intensity arguments, we conclude that these levels are $g_{9/2}$, $i_{11/2}$, $d_{5/2}$, $g_{7/2}$, and $d_{3/2}$ levels. Possibly the $d_{5/2}$ and the $g_{7/2}$ assignments could be interchanged. In order to explain the two low-lying excited levels we must postulate that a coupling exists between $p_{1/2}$, $f_{5/2}$, and $p_{3/2}$ neutron shells. Otherwise, only the proton group to the ground state of $Pb^{207}$ would occur since all subshells except the $p_{1/2}$ shell

are filled in the $Pb^{206}$ target nucleus. Two excited levels are observed at 0.62 $\pm$ 0.1 Mev. and 0.95 $\pm$ 0.1 Mev. which agree with the $f_{5/2}$ level at 0.565 Mev. (7, 14) and the level at 0.870 Mev., possibly a $p_{3/2}$ level. The absence of the $i_{13/2}$ level at 1.63 Mev. agrees with the requirement of high angular momentum to produce this state. Goldhaber and Hill (9) also list a level at 1.10 Mev. (28), possibly an $f_{7/2}$ level. Owing to the low resolution, the proton group corresponding to an excitation of 0.95 Mev. might be a double group consisting of the 0.870 and 1.10 Mev. levels. However, if we fit the first excited group at 0.565 Mev. excitation, the second excited group has an excitation energy of 0.89 Mev. The differential cross section of the first excited group (the $f_{5/2}$ level) is then 0.03 $\sigma_0$ and that of the second group (the $p_{3/2}$ level) is 0.07 $\sigma_0$. From the $(d,t)$ reaction we also observe only two levels in this region. If the group corresponding to the 1.10 Mev. level is present it must be of low intensity.

For the $Pb^{208}$ nucleus we might expect the first excited state to occur when a $g_{9/2}$ neutron enters the $Pb^{207}$ nucleus. However, there is an interaction energy between this $g_{9/2}$ neutron and the $p_{1/2}$ neutron in $Pb^{207}$. This results in two levels with spins 4 and 5. The proton group observed at this energy is somewhat wider than expected and has been resolved into two groups with a separation of 0.2 Mev. Protons are present in the energy region corresponding to a level (or a doublet) corresponding to the $i_{11/2}$ level in $Pb^{209}$, but no definite peak could be resolved (see Fig. 2). The absence of the 2.62 Mev. and the 3.20 Mev. levels with spins of 2 and 4 respectively (24, 32) is explained by assuming that these two levels are excited proton levels since they are produced in the $\beta$-decay of $Tl^{208}$. The three higher levels (probably doublets) arise from $d_{5/2}$, $g_{7/2}$, and $d_{3/2}$ neutrons interacting with the unpaired $p_{1/2}$ neutron.

*B. Energy Levels from $(d,t)$ Reactions*

Fig. 11 is a plot of energy level diagrams obtained from $(d,t)$ reactions and lined up so that levels with similar $Q$-values agree. The energy necessary to pull a neutron out of the target nucleus is given by the distance from a line at a $Q$-value

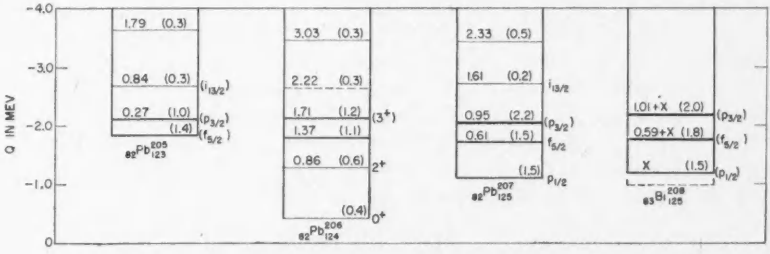


FIG. 11. Energy level diagrams of $Pb^{205}$, $Pb^{206}$, $Pb^{207}$, and $Bi^{208}$ measured from $(d,t)$ reactions. The level diagrams are plotted so that levels with similar $Q$-values agree. The excitation energy in Mev. is given for each level and also its differential cross section at 90° is given in parentheses in units of $\sigma_1$ ($\sigma_1 \simeq$ 2.5 mb./steradian). Tentative assignments of orbitals to some of the levels are given in parentheses. The level at 3.03 Mev. in $Pb^{206}$ is probably a doublet. The ground state of $Bi^{208}$ is shown $x$ Mev. ($\sim$ 0.05 Mev.) below the lowest observed level as explained in the text. It is assumed that the odd proton in $Bi^{208}$ is always in an $h_{9/2}$ state in $Bi^{208}$ and the assignments refer to the odd neutron.

of 6.27 Mev. (the triton binding energy) and the level in question. The excitation energies are given for the various levels with the differential cross sections at 90°, in units of $\sigma_1$, following in parentheses. Again the agreement among the levels suggests a single particle model. We shall make tentative assignments to the levels from the level scheme of Fig. 9 and from assignments made from isomeric transitions.

The excited levels in $Pb^{207}$ from the $(d,t)$ reaction agree very well with the diagram given by Goldhaber and Hill. The first excited level arises when an $f_{5/2}$ neutron is pulled out of the closed shell of 126 neutrons and leaves a "hole" in the $f_{5/2}$ shell, which is equivalent to an unpaired neutron in an $f_{5/2}$ state. The excitation energy of 0.61 ± 0.1 Mev. agrees with the gamma ray energy of 0.565 Mev. The level at 0.95 ± 0.1 Mev. is in agreement with the 0.870 Mev. level, possibly a $p_{3/2}$ level. If the group corresponding to the first excited level is fitted at 0.565 Mev., the excitation energy of the second excited level drops to 0.90 Mev. If there is a group corresponding to a level at 1.1 Mev. it must be of low intensity. The level at 1.61 Mev. agrees with the $i_{13/2}$ level at 1.63 Mev. from isomeric transitions. The low intensity of this triton group is due to the large angular momentum ($l = 6$) necessary to excite this level. Since the $(d,t)$ reaction probably occurs by means of a pickup process, less than half of the original deuteron angular momentum is available in the pickup process. The level at 2.33 Mev. agrees with a gamma ray energy of 2.33 Mev. found in the decay of $Bi^{207}$ (28). It is suggested that this level might be the $f_{7/2}$ level. Assuming the splitting to be proportional to $(2l + 1)$, the splitting of the two $f$-levels would be 7/3 times the splitting of the two $p$-levels (0.87 Mev.). This expected value of 2.0 Mev. is in good agreement with the observed energy difference of 1.8 Mev. and supports the $f_{7/2}$ assignment to the 2.33 Mev. level.

The three levels observed in $Bi^{208}$ arise from $p_{1/2}$, $f_{5/2}$, and $p_{3/2}$ neutrons interacting with the odd $h_{9/2}$ proton. It is assumed that the long range group is a doublet arising from the combination of the $p_{1/2}$ neutron and the $h_{9/2}$ proton to produce states of spin 4 and 5. We estimate the doublet to have $\sim 0.1$ Mev. separation. This estimate is based on the 0.2 Mev. doublet in $Pb^{208}$ (resulting from a $p_{1/2}$ neutron and a $g_{9/2}$ neutron), the 0.040 Mev. doublet in $Tl^{208}$ (probably resulting from a $g_{9/2}$ neutron and an $s_{1/2}$ proton), and the observed width of the triton group. The ground state for $Bi^{208}$ is shown in Fig. 11, a distance of $x$ Mev. below the average of the doublet ($x$ is about half the doublet spacing). The two higher levels arise from $f_{5/2}$ and $p_{3/2}$ neutrons and each group probably consists of several levels. From Fig. 5 we can see that tritons are present above background in the region corresponding to an excitation of from 1.5 to 2.5 Mev.

The energy levels in $Pb^{205}$ are assigned from a comparison to the levels in $Pb^{207}$. The ground state of $Pb^{205}$ is predicted to be an $f_{5/2}$ state. The ground state of $Hg^{203}$, which also has 123 neutrons, is classified as an $f_{5/2}$ state (27). From systematics given by Goldhaber and Hill the energy difference between the $i_{13/2}$ and $f_{5/2}$ levels in $Pb^{205}$ is predicted to be 0.82 Mev. This is in good agreement with the value of 0.84 Mev. for the second excited level. The level at 1.79 Mev. excitation may be the $f_{7/2}$ level.

The energy levels in $Pb^{206}$ cannot be compared directly to those of $Pb^{207}$ since we have postulated that there is an interaction between two unpaired neutrons. The ground state of $Pb^{206}$ is formed when the odd $p_{1/2}$ neutron in the $Pb^{207}$ nucleus is pulled out of the target nucleus and leaves the $Pb^{206}$ nucleus with all subshells except the $p_{1/2}$ shell filled. We should expect the first excited state for the $Pb^{206}$ nucleus to occur when an $f_{5/2}$ neutron is extracted from the $Pb^{207}$ nucleus and the unpaired $f_{5/2}$ neutron interacts with the unpaired $p_{1/2}$ neutron. This would produce two excited states with spins 2 and 3 with even parity. The excited state at 803 kev. is known to have spin 2 and even parity (8). The level observed at 0.86 Mev. is believed to arise from unpaired $f_{5/2}$ and $p_{1/2}$ neutrons to form a $2^+$ state. The $3^+$ state arising from the combination of these two unpaired neutrons is possibly the level at 1.71 Mev. A 1.71 Mev. gamma ray has been detected (1) from the decay of $Bi^{206}$. The level at 1.37 Mev. could arise from a combination of the unpaired $p_{3/2}$ neutron with the unpaired $p_{1/2}$ neutron to form a $1^+$ state. Although a dotted level is shown at 2.22 Mev. no definite peak corresponding to this level was observed in the triton spectrum (Fig. 7). It is very likely that this region consists of two or three groups which we are not able to resolve. The triton peak corresponding to an excitation of 3.03 Mev. is somewhat broader than the corresponding peak from the $Pb^{208}$ target, suggesting that this level may be a doublet with a few hundred kev. separation. A doublet structure would be predicted from the interaction of the unpaired $f_{7/2}$ and $p_{1/2}$ neutrons. Other levels arising from two $p_{3/2}$ or two $f_{5/2}$ neutrons are eliminated because of the assumption of weak interaction between neutron shells.*

## V. CONCLUSIONS

A bismuth target and lead targets of the separated isotopes of $Pb^{206}$, $Pb^{207}$, and $Pb^{208}$ have been bombarded with 14-Mev. deuterons. The proton and triton spectra have been resolved into a few groups. However, owing to the poor resolution and the optimistic graphical resolution, it is possible that some of these groups represent several levels, particularly in the case of bismuth. Since the reactions occur by means of a stripping or a pickup process, a single neutron carries the excitation energy. The similarities among the energy levels can be accounted for by two assumptions. (1) There is no coupling between neutron and proton shells and only weak coupling between neutron shells. Thus the incoming neutron possesses all the excitation energy. (2) There is a small interaction energy between two unpaired nucleons which depends on the spins of the two nucleons and their resultant spin. The absence of the ground state group from $Bi^{209}(d,p)$ is explained from these two assumptions. It should be emphasized that the assignments to the levels are very tentative. If the spectra were measured with high resolution, obtainable with magnetic analysis, the results would provide a valuable test of the assumptions postulated in this discussion.

Although all the discussion has been based on a single-particle model for the nucleus it does not mean that this model is completely valid. For example, as pointed out by Goldhaber and Hill, a "$g_{9/2}$ assignment need not imply that all

* [*Note added in proof*]: *See paper by Pryce for a discussion of the energy levels in* $Pb^{206}$.

the angular momentum is carried by a single particle with four units of angular momentum and its spin parallel to its orbit. However, it is probable that a good portion of its wave function can be represented by a $g_{9/2}$ component of a single particle in the 'field' of an even-even core."

## VI. ACKNOWLEDGMENTS

The experimental work for this research was carried out under the direction of Professors M. Deutsch and M. S. Livingston. The author has had many valuable discussions with K. Boyer and H. E. Gove. The cooperation of all the personnel of the Cyclotron Laboratory is gratefully acknowledged. The author also wishes to thank M. Deutsch, M. Goldhaber, and A. W. Sunyar for helpful suggestions and criticisms of this paper.

## REFERENCES

1. Alburger, D. E. and Friedlander, G. Phys. Rev. 81: 523. 1951.
2. Bannerman, R. C. and Curran, S. C. Phys. Rev. 85: 134. 1952.
3. Bethe, H. A. and Butler, S. T. Phys. Rev. 85: 1045. 1952.
4. Boyer, K., Gove, H. E., Harvey, J. A., Deutsch, M., and Livingston, M. S. Rev. Sci. Instruments, 22: 310. 1951.
5. Butler, S. T. Proc. Roy. Soc. (London), A, 208: 559. 1951.
6. Butler, S. T. and Salpeter, E. E. Phys. Rev. 88: 133. 1952.
7. Campbell, E. C. and Goodrich, M. Phys. Rev. 78: 640. 1950.
8. De Benedetti, S. and Minton, G. H. Phys. Rev. 85: 944. 1952.
9. Goldhaber, M. and Hill, R. D. Revs. Modern Phys. To be published.
10. Goldhaber, M. and Sunyar, A. W. Phys. Rev. 83: 906. 1951.
11. Gove, H. E. Mass. Inst. Technol. Progress Rept. July 1, 1950.
12. Gove, H. E. Phys. Rev. 81: 364. 1951.
13. Gove, H. E. and Boyer, K. Phys. Rev. 79: 241. 1951.
14. Grace, M. A. and Prescott, J. R. Phys. Rev. 84: 1059. 1951.
15. Harvey, J. A. Phys. Rev. 81: 353. 1951.
16. Haxel, O., Jensen, J. H. D., and Suess. H. E. Phys. Rev. 75: 1766. 1949.
17. Huizenga, J. R., Magnusson, L. D., Simpson, O. C., and Winslow, G. H. Phys. Rev. 79: 908. 1950.
18. Insch, G. M., Balfour, J. G., and Curran, S. C. Phys. Rev. 85: 805. 1952.
19. Jaffe, A. A. and Cohen, S. G. Phys. Rev. 86: 1041. 1952.
20. King, J. S. and Parkinson, W. C. Phys. Rev. 88: 141. 1952.
21. Kinsey, B. B., Bartholomew, G. A., and Walker, W. H. Phys. Rev. 82: 380. 1951
22. Klinkenberg, P. F. A. Revs. Modern Phys. 24: 63. 1952.
23. Livingston, M. S., Boyer, K., Gove, H. E., and Harvey, J. A. Mass. Inst. Technol. Progress Rept. July 1, 1949.
24. Martin, D. G. E. and Richardson, H. O. W. Proc. Phys. Soc. (London), A, 63: 233. 1950.
25. Mayer, M. G. Phys. Rev. 75: 1969. 1949.
26. Mayer, M. G. Phys. Rev. 78: 16, 22. 1950.
27. Mayer, M. G., Moszkowski, S. A., and Nordheim, L. W. Revs. Modern Phys. 23: 315. 1951.
28. Neumann, H. M. and Perlman, I. Phys. Rev. 81: 958. 1951.
29. Nordheim, L. W. Phys. Rev. 75: 1894. 1949.
30. Nordheim, L. W. Revs. Modern Phys. 23: 322. 1951.
31. Parkinson, W. C., Beach, E. H., and King, J. S. Phys. Rev. 87: 387. 1952
32. Petch, H. E. and Johns, M. W. Phys. Rev. 80: 478. 1950.
33. Petschek, A. G. and Marshak, R. E. Phys. Rev. 85: 698. 1952.
34. Wapstra, A. H. Physica, 16: 33. 1950.
35. Way, K. and Wood, M. Phys. Rev. 86: 608. 1952.

# LA REGRESSION DE L'IMAGE LATENTE DUE AUX PARTICULES CHARGEES[1]

PAR PIERRE DEMERS, JACQUES LAPALME,[2] ET JACQUES THOUVENIN[3]

SOMMAIRE

Nous décrivons des expériences comparatives sur la régression dans plusieurs types d'émulsion, des mesures précises sur des traces de protons, deux procédés nouveaux s'appliquant aux rayons $\alpha$, l'un utilisant un mécanisme et l'autre l'analyse des étoiles du thorium, et des expériences sur l'action de l'air, de l'humidité et de la température. Ces expériences montrent les relations entre la densité granulaire $D$ des traces observables, l'ionisation $I$ et le temps $t$. La nature de l'émulsion n'influe guère, sauf par la sensibilité et la dimension des grains. L'oxygène est presque *sans effet*, l'humidité est un facteur prépondérant, et les températures très basses arrêtent toute régression. Quatre lois expérimentales générales sont dégagées. (1) La densité $D$ est une fonction exponentielle de la puissance $n$ du temps: $D_0 \exp -(t/\tau)^n$; $n$ varie entre 0.5 et 2. (2) $D$ est une fonction linéaire de la densité initiale et de coefficients dépendant du temps: $D_0(1-b)-a$. (3) Aux régressions extrêmes, $D$ ne dépend pas de $I$. (4) La fluctuation de $D$ augmente avec le temps. De ces lois on tire divers caractères de l'image latente. On propose un mécanisme de la régression, analogue de l'effet Herschel. (1) Emission thermique d'un électron $\epsilon^-$ et d'ion $Ag^+$, par le centre $A$. (2) Fixation d'$\epsilon^-$ et $Ag^+$ sur des centres de type $B$, dont les propriétés sont analysées. (3) Ou encore capture d'$\epsilon^-$ par un accepteur extérieur. (4) Production de centres $B$ par évolution du cristal bromure d'argent, très rapide en présence de beaucoup d'eau.

## I. INTRODUCTION

*Effet collectif dû à la lumière*

L'image latente due à l'action de la lumière sur une émulsion photographique n'est pas parfaitement stable. On cite des cas particuliers où on réussit à la conserver plusieurs années. Ainsi les astronomes étudient les changements lents dans la carte du ciel, en prenant des photographies de la même région deux fois sur une même plaque après 15 ou 20 ans d'intervalle; et quand on retrouve les films d'une expédition polaire perdue depuis 20 ou 40 ans, on peut souvent en tirer une image développée. Dans ces cas la conservation de l'image latente a été favorisée par le froid du climat ou d'une glacière. Cependant il semble bien que dans tous les cas l'impression s'affaiblisse après un temps très long, surtout à la chaleur et à l'humidité. L'accroissement simultané du voile concourt à rendre les impressions affaiblies difficiles à reconnaître.

La diminution ou régression éventuelle est souvent précédée d'un accroissement. Brush (11) en 1910 observa un tel accroissement, pour une durée d'attente de quelques minutes, au cours de mesures photométriques. Le phénomène a été étudié depuis par Jausseran (23, 24), et par Barabascheff et Semejkin (5). Il est très variable, dépendant de nombreux facteurs tels que la nature de l'émulsion, les conditions d'irradiation, de conservation et de développement. Il importe en photométrie photographique, où par suite il est recommandé, si les poses sont faites successivement sur une même plaque, de recourir à une

[1] *Manuscrit reçu le 3 octobre 1952.*
*Contribution de l'Institut de Physique, Université de Montréal.*
[2] *Adresse actuelle, Laboratoire de l'Hôpital du Sacré Coeur de Rosemont, Montréal.*
[3] *Adresse actuelle, Laboratoire de Physique de l'Ecole Normale Supérieure, Paris V, France.*

durée d'attente beaucoup plus longue que l'intervalle de temps qui les a séparées. En effet l'évolution de l'image latente est rapide au début, elle augmente parfois immédiatement puis diminue rapidement, mais la diminution devient généralement graduellement plus lente. En l'absence de toute précaution, la régression peut modifier la densité optique de 50%. Elle importe aussi dans la photographie en couleurs, si elle n'est pas la même pour toutes les couches sensibles. La question, vu son importance, a été sans doute l'objet d'études poussées dans les laboratoires des grandes industries photographiques.

Berg (9) a étudié la régression accompagnant ou suivant des irradiations par de faibles éclairements agissant longtemps, correspondant à une extrémité de la courbe de régression. Dans ce cas, l'image latente se forme très lentement, et avant de posséder sa taille définitive, reste longtemps à l'état de "sous centre" de développement, défini comme possédant une certaine stabilité. Un éclairement trop faible ne forme jamais d'image latente, ce que Berg explique par l'hypothèse des "précentres" de développement, très peu stables. Les précentres disparaissent assez facilement, de sorte que s'ils ne passent pas en un temps suffisamment court à la taille plus considérable de sous centre, l'effet lumineux qui les a formés est perdu pour le résultat final. Précentres, sous centres et centres de développement ou images latentes disparaissent par l'effet du brome formé par l'action de la lumière, ou par agitation thermique. Winand et Falla (45) ont observé que les impressions plus faibles disparaissent plus rapidement. Loening (30) a étudié la régression rapide de l'image latente pour des sols de bromure d'argent, déjà observée par Urbach (42). Elle est réduite mais non supprimée par l'absence d'oxygène, par les alcalis, par le nitrite de sodium qui est un accepteur d'halogène, par le nitrate d'argent et fortement réduite par la gélatine. Elle est très lente pour l'image latente interne.

Jenny a étudié l'effet de la lumière sur des émulsions pour la physique nucléaire de sa préparation (21, 25), et sur l'émulsion Ilford $C_2$. L'effet d'un éclair lumineux disparaît plus vite que celui d'une irradiation prolongée, à dépense d'énergie égale. Dans un diagramme où le logarithme de la densité optique est en ordonnées et la durée d'attente est en abscisses, il obtient une ligne brisée, montrant l'existence de deux composantes, décroissant exponentiellement avec des périodes de 3 jours et de 140 jours. Il n'a pas observé d'accroissement initial.

*Effet collectif des rayonnements ionisants*

Blau (10) étudia le noircissement dû aux rayons X, et aux rayons $\alpha$; comme celui dû à la lumière, il augmente légèrement, diminue rapidement puis devient à peu près stationnaire. Voir aussi Heisenberg (22).

*Image latente des grains individuels*

Blau (10) fit la première étude de la régression le long des traces individuelles de rayons $\alpha$ et de protons examinées sous le microscope. De la sorte on peut étudier diverses quantités, outre le noircissement global mesuré par la densité optique $D_{opt}$. On peut déterminer le long des traces encore visibles le nombre de grains par unité de longueur de la trace, densité granulaire ou densité linéaire

des grains $D$, en nombre par microns par exemple; on peut compter le nombre total de grains encore visibles $G$ causés par une irradiation $\alpha$ par exemple, par unité de surface. Ce nombre n'est pas simplement proportionnel au précédent parce que des traces deviennent invisibles. On peut finalement compter le nombre de traces encore visibles $N$ qui doit être égal à $G/D$. On dispose donc ainsi de plusieurs quantités mesurables, pour l'étude de la régression.

Lauda (29) fit dans le laboratoire de Blau une étude d'ensemble dont les résultats principaux ont depuis été retrouvés indépendemment par plusieurs auteurs. (1) Il y a parfois un accroissement initial pour une durée d'attente d'une dizaine d'heures, puis la densité linéaire des grains $D$ décroît rapidement et devient à peu près fixe après plusieurs semaines. En même temps le nombre de traces encore visibles $N$ diminue et s'annule finalement. (2) L'humidité, la chaleur, un développement peu énergique, et l'oxygène de l'air surtout si l'émulsion renferme un désensibilisateur, favorisent la régression. (3) Les traces laissées par les particules les plus énergiques s'effacent plus vite, évidemment parce qu'elles perdent moins d'énergie par unité de longueur, et les traces des protons sont moins persistantes que celles des rayons $\alpha$, aussi parce que l'ionisation $I$, exprimée en Mev. par micron d'émulsion, est plus faible. Ces résultats concernent les émulsions de 1937 contenant 40% de bromure d'argent, de 60% gélatine. Les résultats plus récents concernent surtout les émulsions concentrées, qui existent depuis 1945 (15), contenant 82% de bromure d'argent environ.

Lapalme et Demers (28) firent une étude comparative de plusieurs types d'émulsions, et proposèrent une théorie de l'évaporation: les atomes d'argent de l'image latente la quittent par agitation thermique et retournent au cristal de bromure d'argent d'où ils proviennent. L'image latente due aux particules ionisantes—comme celle due à la lumière—peut être détruite par l'action de solutions d'oxydants tels que l'acide chromique, plus facilement que les centres de sensibilité selon Demers (15, 16). Voir aussi Cüer et Winand (14). Perfilov a aussi pu supprimer ainsi l'image latente, il a étudié l'action des oxydants, surtout en vue d'une diminution de la sensibilité. Occhialini et Powell (35), et Perfilov (36) ont observé la régression des traces des rayons $\alpha$ et des protons dans les émulsions Ilford $B_1$, $C_2$, etc.

Yagoda (46, 47, 48) et Yagoda et Kaplan (49) ont trouvé que la régression est plus faible dans les émulsions concentrées. Ils ont trouvé que la vapeur saturante de l'eau oxygénée à 3% efface toute trace en quatre heures, et ils ont suggéré que la régression naturelle est due à la même réaction. L'hypothèse est plausible en effet puisque les rayonnements ionisants forment de l'eau oxygénée en agissant sur l'eau, comme l'a montré Krenz par exemple (26), et la gélatine renferme de l'eau ou du moins ses éléments. Mais il parait peu probable qu'il s'en forme suffisamment.

Albouy et Faraggi (1, 2, 3, 4) ont trouvé que l'humidité saturante jointe à l'oxygène de l'air suffit à enlever en 72 heures à 50°C., toute trace d'électron dans Ilford $G_5$ sans réduire la sensibilité, et sans causer de voile, les autres émulsions étant voilées par un tel traitement. Elles supposent que les centres de sensibilité doivent être également détruits et par conséquent régénérés par maturation

pendant ce temps. L'hypothèse ne s'impose peut-être pas, puisque Demers (16) a trouvé des solutions oxydantes enlevant toute image latente à froid sans réduction de la sensibilité. A humidité constante, la régression est deux fois plus rapide dans l'oxygène que dans l'air, et cinq fois plus rapide dans l'air que dans l'azote. La régression est plus rapide près de la surface, d'accord avec la pénétration d'un agent extérieur. Elles ont suggéré que la régression se fait par l'oxydation en présence d'eau, de l'argent de l'image latente suivant l'équation $2Ag + O + H_2O \rightarrow 2Ag^+ + 2OH^-$. On peut supposer que les ions résultants passent dans la gélatine, l'hydroxyde d'argent étant assez soluble, ou que l'ion $Ag^+$ reste dans le cristal de bromure d'argent. Mather (31) a montré que la régression, mesurée par la densité $D$ des traces encore visibles, est à peu près dix fois plus lente dans le vide absolu et sec que dans les conditions ordinaires. Beiser (7), à sa suite, a expliqué cette régression par l'évaporation thermique d'un électron de l'image latente, avec transformation d'un atome Ag en ion $Ag^+$. Selon lui, l'énergie requise est 0.77 ev., tandis que l'agitation thermique peut fournir 0.7 ev.

Wäffler et Junis (43) ont expérimenté avec des émulsions mouillées. Celles-ci perdent complètement en quatre heures l'impression des rayons $\alpha$, même en l'absence d'oxygène. Coppens (13) a constaté que l'addition de borax à l'émulsion réduit la régression, ce qu'il a interprété dans la théorie d'Albouy et Faraggi, par l'action de masse des ions $OH^-$ du borax alcalin. Picciotto (37, 38) a proposé que l'action du borax s'exerce peut être seulement au développement, en élevant le pH de l'émulsion jusqu'à une valeur plus voisine de celui du révélateur.

Schopper, Magun et Braun (40) ont étudié l'effet Herschel positif qui consiste à accroître une sous-image latente par l'action de la lumière rouge. Ils ont constaté que les traces accrues par effet Herschel régressent plus facilement, même dans une atmosphère d'azote sans oxygène.

Hälg et Jenny (21) ont étudié la régression des traces des rayons $\alpha$ et des protons et ils ont établi pour les protons que la variation de la densité $D$ avec le temps présente deux composantes exponentielles, de périodes 3 et 140 jours, comme pour la lumière. Pour les rayons $\alpha$, il n'y a que la période longue. La période courte est plus sensible aux oxydants. Selon eux, les émulsions à gros grains et à l'ammoniaque conservent mieux l'image latente. Lapalme et Demers (28) ont trouvé pour la variation avec le temps une loi exponentielle du type $\exp - (t/\tau)^n$, l'exposant $n$ valant $1/2$. Coppens (13) a trouvé pour le nombre des traces encore visibles une loi intégrale de celle de Gauss $\exp - (t - t_0)^2/\sigma^2$. Selon Albouy et Faraggi (4) les variables $D$, $N$ et $G$ ne suivent aucune loi simple.

Thouvenin et Demers (41) ont expérimenté sur l'action de l'oxygène, de l'humidité et du pouvoir ionisant. Le présent article rassemble et utilise des travaux précédents du laboratoire (27, 28, 41) et leur ajoute des résultats expérimentaux et théoriques.

*Applications*

La régression modifie le nombre, la densité granulaire, l'opacité et l'aspect des traces. Sa connaissance est donc essentielle dans la détermination de l'inten-

sité des sources, et de la nature et de l'énergie des particules, si on se base pour les identifier sur la densité granulaire ou sur leur opacité, chaque fois que la durée d'attente n'est pas négligeable. C'est en particulier souvent le cas dans les irradiations cosmiques, soit qu'on prolonge les séjours en haute montagne, soit parce que la récupération n'est pas immédiate après les ascensions de ballons. C'est aussi le cas de certaines irradiations prolongées avec des sources faibles au laboratoire. Le parcours des traces faibles peut aussi être réduit par la disparition des grains.

Une régression controlée peut effacer complètement les impressions précédentes, en particulier supprimer les traces d'électrons parasites, comme l'ont montré Yagoda et Kaplan (49), et Albouy et Faraggi (4). Une émulsion perdant rapidement l'impression des protons et des rayons $\alpha$ dans les conditions ordinaires peut être utile dans les irradiations cosmiques de brève durée à haute altitude, parce qu'elle contient peu de traces parasites enregistrées au sol.

Une régression modérée permet parfois une meilleure discrimination. C'est ainsi qu'un jour d'attente environ permet de reconnaître l'origine des désintégrations $Li_6(n, H_3)\alpha$, $B_{10}(n, \alpha)Li_7$, $N_{14}(n, p)C_{14}$, comme l'ont montré Faraggi (20), et d'autres, par exemple Dilworth, Occhialini et Vermaesen (19, Figs. 8 et 10), et Mortier et Vermaesen (34). La discrimination obtenue par Demers (16, Figs. 14, 15, 16), dépendait probablement en partie de cette cause.

## II. COMPARAISON EXPERIMENTALE DE PLUSIEURS TYPES D'EMULSIONS

Une série d'expériences a porté sur neuf types d'émulsions: Eastman $\alpha$, V-O et 548, Ilford $B_1$, $C_1$, $C_2$, et $D_1$, une émulsion à grain fin formule 2 préparée au laboratoire (15, 16), $F_{II}$ sensibilisée au trempé dans la triéthanolamine 1%, et $F_{II}$ non sensibilisée. Toutes les irradiations ont été faites en un jour, le 21 décembre 1946. Une source de dépot actif Th(B + C + C') a été approchée pendant quelques secondes de façon à inscrire des rayons $\alpha$ longs sous incidence rasante, commençant tous à la surface. Puis les plaques enveloppées de papier noir ont été approchées pendant une heure et demie d'une source de 2 curies de polonium mélangé à du béryllium. Les neutrons rapides ont projeté à l'intérieur de l'émulsion des protons de la gélatine, avec une énergie atteignant 10 Mev. Les traces des protons commençaient dans l'épaisseur même des plaques. Ces irradiations relativement intenses montraient environ 12 rayons $\alpha$ et 6 protons par champ de 180 $\mu$ de diamètre, l'épaisseur étant environ 50 $\mu$.

Les plaques ont été développées après des durées d'attente de 0, 1, 3, 10, 30 et 120 jours. On a vérifié dans le cas de $F_{II}$, qu'il n'y avait aucune différence perceptible entre des durées de 30 min., 5 et 10 heures; dans aucun cas on n'a observé d'accroissement initial. La conservation s'est faite dans les conditions ordinaires, soit 20–25°C., et 20–45% d'humidité relative. Le développement s'est fait dans la formule Eastman D19 pendant environ 10 min., sauf $F_{II}$ et Eastman 548, qui ont été développées 5 min. dans la formule D8 diluée 1: 1. Ces conditions n'assurent pas le développement maximum sauf peut être dans le cas de D8 de sorte qu'elles peuvent exagérer légèrement l'importance de la régression dans l'ensemble.

Dans les conditions optiques déjà décrites (16) on a repéré des traces $\alpha$ et $P$ et on a dénombré les grains de traces suffisamment horizontales, dans des segments successifs $\alpha_I$, $\alpha_{II}$, $\alpha_{III}$, $P_I$, $P_{II}$, $P_{III}$, $P_{IV}$, mesurés à partir de la fin de la trajectoire, et on y a déterminé la densité linéaire en grains par micron $D$.

| Segment | Position, microns | $I$, kev./micron |
|---|---|---|
| $\alpha$I | 0 à 11.4 | 300 |
| $\alpha$II | 11.4 à 22.8 | 190 |
| $\alpha$III | 22.8 à 34.2 | 143 |
| $P$I | 0 à 5.7 | 100 |
| $P$II | 5.7 à 11.4 | 77 |
| $P$III | 11.4 à 22.8 | 50 |
| $P$IV | 22.8 à 79.8 | 29 |

Dans ces segments, le pouvoir ionisant $I$ varie d'un facteur 10 environ. Il a été déterminé pour le parcours moyen du segment, au moyen d'une courbe $I$ vs. $R$ tirée des résultats de Rotblat (39).

Les mesures sont des moyennes portant sur 10 trajectoires dans chaque cas, sauf pour les traces les plus faibles, au maximum de régression permettant encore une mesure. Le comptage des grains est difficile dans les trajectoires les plus denses, et dans certains cas seule une indication approchée de la densité saturante peut être donnée: 3.58 pour $F_{II}$ et 2.5 pour $C_2$. Dans Eastman 548, les traces étaient faibles et le voile élevé, dès le temps zéro, aucune mesure n'a été faite. Sauf $C_2$ et $B_1$, les mesures étaient impossibles au temps 120 jours, par suite de l'écaillement de la plaque causé par la sécheresse, à cause d'un voile excessif ou faute de traces visibles. Le nombre des traces encore visibles diminue avec le temps en même temps que leur densité, et la relation $D$ vs. $t$ devient indéfinie sans que $D$ devienne nulle, au moment où l'on ne peut plus repérer de traces. Le Tableau I rassemble ces mesures (27).

TABLEAU I

DENSITÉ LINÉAIRE EN NOMBRE DE GRAINS PAR MICRON (27)

| Durée d'attente $t$ en jours | $\alpha$I | $\alpha$II | $\alpha$III | $P$I | $P$II | $P$III | $P$IV |
|---|---|---|---|---|---|---|---|
| *$F_{II}$ sensibilisée* | | | | | | | |
| 0 | 3.58 | 3.58 | 3.58 | 2.92 | 2.50 | 2.37 | 2.13 |
| 1 | 3.58 | 3.58 | 3.58 | 2.40 | 2.09 | 2.02 | 1.95 |
| 3 | 3.58 | 3.58 | 3.58 | 2.12 | 1.90 | 1.90 | 1.78 |
| 10 | 2.66 | 2.43 | 2.31 | 1.92 | 1.72 | 1.70 | 1.48 |
| 30 | 2.21 | 2.12 | 2.06 | 1.67 | 1.40 | 1.40 | 1.12 |
| *$F_{II}$ non sensibilisée* | | | | | | | |
| 0 | 2.23 | 2.14 | 2.09 | Visible nets | | | |
| 1 | 1.98 | 1.83 | 1.59 | Faibles | | | |
| 3 | 1.73 | 1.53 | 1.53 | Rares | | | |
| 10 | 1.52 | 1.45 | 1.15 | | | | |
| 30 | 1.44 | 1.12 | — | | | | |

| | | | | | | | |
|---|---|---|---|---|---|---|---|
| $B_1$ | | | | | | | |
| 0 | 2.01 | 1.74 | 1.74 | 1.56 | 1.42 | 1.29 | 0.81 |
| 1 | 1.77 | 1.58 | 1.54 | 1.52 | 1.23 | 0.91 | 0.76 |
| 3 | 1.49 | 1.42 | 1.25 | 1.17 | 0.72 | 0.69 | 0.53 |
| 10 | 1.14 | 1.11 | 0.97 | 0.95 | 0.64 | 0.54 | 0.47 |
| 30 | 0.80 | 0.69 | 0.67 | 0.70 | 0.56 | 0.41 | 0.25 |
| 120 | 0.35 | — | — | — | — | — | — |
| $C_1$ | | | | | | | |
| 0 | 2.12 | 1.90 | 1.83 | 1.60 | 1.28 | 0.98 | 0.81 |
| 1 | 1.69 | 1.53 | 1.49 | 1.34 | 1.10 | 0.85 | 0.75 |
| 3 | 1.55 | 1.35 | 1.21 | 1.08 | 0.84 | 0.74 | 0.53 |
| 10 | 1.21 | 0.97 | 0.93 | 0.94 | 0.78 | 0.60 | 0.43 |
| 30 | 0.99 | 0.88 | 0.78 | 0.80 | 0.53 | — | — |
| $C_2$ | | | | | | | |
| 0 | 2.50 | 2.50 | 2.50 | 1.68 | 1.59 | 1.29 | 1.07 |
| 1 | 2.50 | 2.50 | 2.50 | 1.59 | 1.42 | 1.24 | 0.99 |
| 3 | 2.37 | 2.23 | 2.18 | 1.58 | 1.43 | 1.21 | 0.97 |
| 10 | 1.90 | 1.73 | 1.73 | 1.34 | 1.11 | 1.07 | 0.85 |
| 30 | 1.81 | 1.66 | 1.45 | 1.17 | 1.02 | 0.83 | 0.77 |
| 120 | 0.96 | 0.40 | — | 0.9 | 0.64 | 0.47 | 0.34 |
| $D_1$ | | | | | | | |
| 0 | 1.25 | 1.14 | 1.13 | 0.63 | 0.45 | 0.22 | — |
| 1 | 1.06 | 0.87 | 0.81 | 0.56 | 0.25 | 0.11 | — |
| 3 | 0.77 | 0.57 | 0.54 | — | — | — | — |
| 10 | 0.56 | 0.45 | 0.34 | — | — | — | — |
| 30 | 0.47 | 0.34 | — | — | — | — | — |
| *Eastman* $\alpha$ | | | | | | | |
| 0 | 0.97 | 0.68 | 0.67 | 0.7 | 0.45 | 0.43 | 0.13 |
| 1 | 0.69 | 0.56 | 0.42 | 0.52 | 0.30 | 0.26 | 0.08 |
| 3 | 0.64 | 0.46 | 0.39 | 0.50 | 0.25 | 0.20 | 0.07 |
| 10 | 0.54 | 0.32 | 0.16 | 0.45 | 0.21 | 0.16 | — |
| 30 | 0.43 | 0.15 | — | — | — | — | — |
| *V-O* | | | | | | | |
| 0 | 0.80 | 0.55 | 0.47 | 0.68 | 0.50 | 0.29 | 0.18 |
| 1 | 0.74 | 0.52 | 0.45 | 0.54 | 0.32 | 0.20 | 0.14 |
| 3 | 0.65 | 0.48 | 0.43 | — | — | — | — |
| 10 | 0.60 | 0.41 | 0.35 | — | — | — | — |
| 30 | 0.55 | 0.39 | 0.25 | — | — | — | — |

*Influence du pouvoir ionisant et de la nature de la particule*

La Fig. 1 représente pour chaque émulsion et chaque durée d'attente, la densité en fonction du pouvoir ionisant. On devrait obtenir une courbe unique pour les deux sortes de particules puisqu'on ne voit pas bien en quoi les différences dans la structure des trajectoires $\alpha$ et $P$ pourraient modifier la densité pour une

même valeur de $I$ et de $t$. De plus Barkas (6) a montré sur des protons et des rayons $\alpha$ de grande énergie, qu'il n'y a qu'une courbe $D$ vs. $I$ pour les deux particules. Ici les diagrammes s'accordent, quoiqu'imparfaitement, avec cette loi. Les divergences se manifestent surtout après une forte régression, et paraissent résulter d'une disparition comparativement plus rapide des grains dans les traces $\alpha$. Comme celles-ci sont en moyenne plus proches de la surface que les protons, cet effet provient peut être d'une régression plus faible en profondeur, d'accord avec une observation déjà rapportée, d'Albouy et Faraggi.

*Période de réduction à demi densité*

Sur la Fig. 1, on peut reconnaître pour chaque pouvoir ionisant, l'influence du temps qui sert de paramètre, et aussi sur la Fig. 2. Dans celle-ci, les résultats

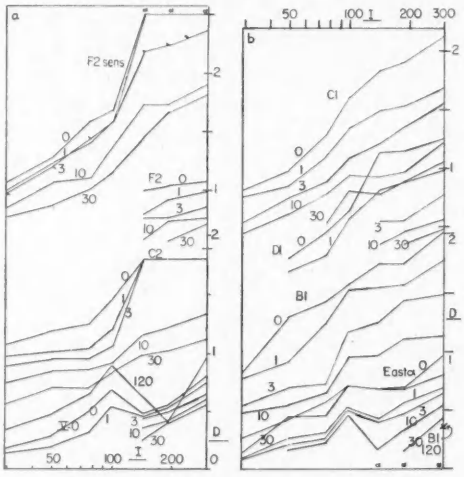


FIG. 1. Variation de la densité linéaire des traces observables $D$ en grains par microns, avec le pouvoir ionisant $I$ en kev./$\mu$ d'émulsion, pour des protons $P$ et des rayons $\alpha$, enregistrés dans huit types d'émulsions, pour des temps de conservation $t$ = 0, 1, 3, 10, 30 et 120 jours.

disponibles sont condensés en prenant pour chaque émulsion la densité moyenne observée pour $\alpha$ et $P$ respectivement, et non la densité séparée de chacun des sept segments. L'ordonnée est log $D$, et l'abscisse est $t^{\frac{1}{3}}$. Dans ce système de représentation, on voit que les mesures disponibles s'accordent assez bien avec une droite pour chacune des quinze séries de points, c'est à dire que la densité est sensiblement une fonction exponentielle du temps élevé à la puissance $n = 0.5$. La Fig. 3 représente dans le système log $D$ vs. $t$, les fonctions $2^{-(t/T)^n}$, avec $n = 0.5$, $n = 1$ et $n = 2$. Avec $n = 0.5$, la régression devient plus lente aux grands temps, et au contraire elle devient plus rapide avec $n = 2$. L'accord avec l'expérience serait légèrement amélioré en prenant une valeur inférieure à 0.5 dans neuf cas où la courbe expérimentale de la Fig. 2 paraît tournée vers le haut, et supérieure à 0.5 dans un cas où la courbe est tournée vers le bas.

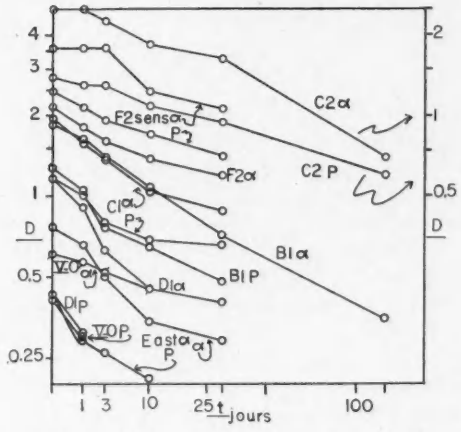


FIG. 2. Variation de la densité $D$ avec $t$ pour $P$ et $\alpha$, pour huit types d'émulsions. En abscisses $t^n$, $n = 0.5$.

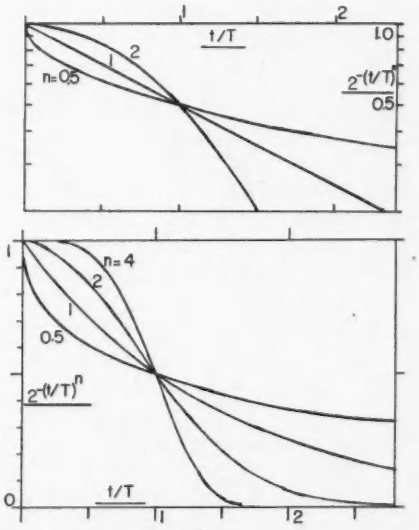


FIG. 3. Diagrammes des fonctions $2-(t/T)^n$ avec $n = 0.5$, 1 et 2, $t$ en abscisses.

La période a été déterminée pour des droites convenant aux points de la Fig. 2, selon l'équation

$$D = D_0\, 2^{-(t/T)^n},\quad n = 0.5$$

avec les résultats approximatifs suivants:

| | | | | |
|---|---|---|---|---|
| $F_{II}$ sens. | $\alpha$: 29 jours, | $P$: 45 jours | $B_1$ | $\alpha$: 19, $P$: 18 |
| $F_{II}$ non-sens. | $\alpha$: 32, | $P$: – | $D_1$ | $\alpha$: 10, $P$: (3.6) |
| $C_2$ | $\alpha$: 37, | $P$: 79 | V-O | $\alpha$: 48, $P$: (3) |
| $C_1$ | $\alpha$: 23, | $P$: 28 | Eastman $\alpha$ | $\alpha$: 12, $P$: 10 |

Les périodes $\alpha$ sont fréquemment plus courtes que les périodes $P$, bien que les rayons $\alpha$ en général restent visibles plus longtemps. Les périodes sont en général plus longues dans les émulsions où la densité initiale est plus élevée. La période ainsi déterminée n'a pas une signification très précise lorsque la courbure est évidente, puisqu'alors il faudrait d'abord modifier $n$. D'autre part il est à remarquer que la valeur de la période n'est pas unique si on change l'origine des temps puisque la fonction $e^{-x^n}$ n'est pas multiplicative, i.e., $e^{-x_1^n} \cdot e^{-x_2^n} \neq e^{-(x_1+x_2)^n}$ sauf si $n = 1$. Si l'origine est déplacée vers les temps positifs, les mêmes données expérimentales seraient représentées par une période plus longue avec $n < 1$, et plus courte avec $n > 1$.

L'extrémité de la courbe aux grands temps est difficile à déterminer avec précision, parce qu'on se base alors sur des trajectoires rares et faibles; puisqu'il y en a d'invisibles il y en a toujours de plus faibles que celles qu'on a déjà trouvées, de sorte que la densité trouvée alors dépend dans une certaine mesure de l'abondance initiale des traces et des conditions d'exploration. Si les traces sont nombreuses, on peut supposer que les plus denses attireront d'abord l'attention à l'exclusion des plus faibles.

*Relation entre les densités*

Les mesures faites à des temps successifs sur une émulsion et sur les divers segments d'une même particule soit $\alpha$, soit $P$, s'accordent approximativement avec la règle suivante: "La diminution de la densité granulaire est la même, dans un temps donné, pour tous les pouvoirs ionisants." Cette règle signifie que si l'on connaît le diagramme $D$ vs. $R$ ou $D$ vs. $I$ au temps zéro, ceux aux temps ultérieurs s'en déduisent par une simple translation verticale vers le bas. La Fig. 2 montre un accord approximatif avec cette règle pour les points $\alpha$ et $P$ pris séparément pour autant, semble-t-il, que les erreurs de mesure permettant de définir une courbe.

La vérification est la meilleure pour les séries de mesures les plus étendues, dans les émulsions montrant le mieux les trajectoires soit $F_{II}$ sensibilisée, $F_{II}$ non sensibilisée, $B_1$, $C_2$ et $C_1$. Elle est plus loin de se vérifier pour la série combinée des mesures $\alpha$ et $P$.

La Fig. 4 permet une vérification plus précise. La densité au temps zéro est portée en abscisses et celle au temps $t$, en ordonnées, les points correspondants au même temps de conservation sont joints par une ligne brisée, pour chaque émulsion. On devrait trouver des familles de droites parallèles, et de pente unité. En fait, pour les émulsions les mieux étudiées $F_{II}$, $B_1$, $C_2$ et $C_1$, c'est sensiblement ce qu'on observe, mieux si on considère les points $\alpha$ et $P$ séparément.

Dans certains cas cependant, comme V-O et Eastman $\alpha$, c'est plutôt la variation relative de la densité qui est constante, de sorte que la variation absolue de la densité est proportionnelle à $D_0$. Dans l'ensemble, même si on considère

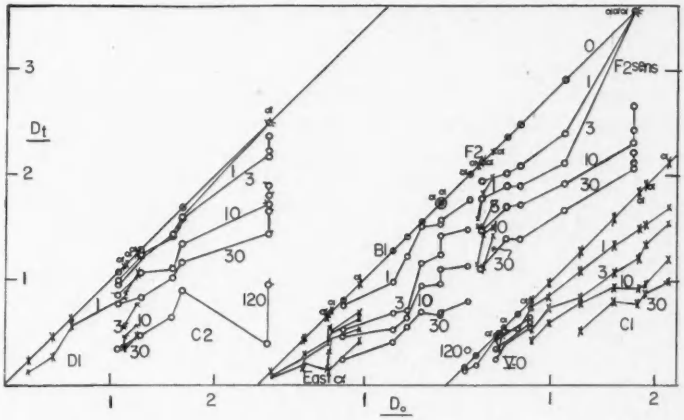


FIG. 4. Variation de la densité $D$ au temps $t$ avec $D_0$ pour $P$ et $\alpha$, huit types d'émulsion.

tous les points expérimentaux $\alpha$ et $P$ à la fois la variation de la densité est comprise entre les deux lois que voici: (1) la densité absolue varie de la même quantité dans des temps égaux; (2) la densité relative varie de la même quantité dans des temps égaux. Nous proposons finalement une combinaison linéaire de ces deux règles:

$$D = D_0 - a(t) - D_0 b(t) = D_0[1 - b(t)] - a(t).$$

"La densité est une fonction linéaire de la densité initiale". Les paramètres $a$ et $b$ sont des fonctions dépendant du temps mais non de la densité. La variation relative est constante si $a = 0$.

On peut remarquer dès lors que des grains également impressionnés devraient disparaître en proportions égales dans des temps égaux. Le cas $b = 0$, variation absolue constante, qui représente mieux les séries de nos résultats les plus étendus, indique des grains plus faiblement impressionnés lorsque la densité est plus faible.

Des mesures précises que nous allons maintenant décrire confirment l'équation ci-dessus.

## III. MESURES PRECISES SUR DES PROTONS (41)

Des feuilles d'émulsion à grain fin sans support préparées par la méthode à deux jets déjà décrite (18) ont été irradiées par des neutrons d'énergie comprise entre 0 et 42 Mev., dûs au bombardement d'une cible de béryllium par des protons du cyclotron de l'Université McGill. On a ainsi enregistré des protons de choc élastique, et des étoiles de désintégration, en particulier $n + C \rightarrow 3\alpha$. La conservation s'est faite en vase clos à 25°C., en présence d'une solution de potasse assurant une humidité relative de 80%, ou de 90%, pendant 0, 1 et 3 jours. Le développement s'est fait à 0°C. en 30 min. dans la formule D8 diluée 1: 2. Les feuilles montées sur une lame de verre après lavage, montraient peu de distorsion et étaient allongées dans leur plan uniformément d'environ 5%.

Le pouvoir d'arrêt a été déterminé par la mesure des rayons $\alpha$ du ThC', voir section V, dans la même émulsion fixée sur une plaque de verre. Le parcours moyen de cent traces était $47.95 \pm 0.18$ $\mu$ avec un écart normal $\sigma = 2.5\%$, le pouvoir d'arrêt est donc $1797 \pm 5$, égal à celui des émulsions concentrées Ilford et Eastman.

Des traces longues de protons ont été repérées et examinées avec un micromètre dont chaque division valait 0.555 $\mu$. Cette longueur de l'objet examiné, vu l'allongement de 5%, représente 0.527 $\mu$ de la trajectoire au moment de son

TABLEAU II

PROTONS ÉNERGIQUES DANS UNE ÉMULSION À GRAIN FIN, DENSITÉS EN GRAINS PAR MICRON

| Parcours $R$ en divisions | $\bar{R}$, $\mu$ | $\bar{E}$, Mev. | $I(\bar{R})$, kev./$\mu$ | 0 jour | 1 jour 90% 25°C. | 3 jours 90% 25°C. | 1 jour 80% 25°C. | 3 jours 80% 25°C. |
|---|---|---|---|---|---|---|---|---|
| 0– 20 | 5.27 | 0.5 | 93 | | | 1.08 | | |
| 20– 40 | 15.81 | 1.1 | 52 | | | 0.90 | | |
| 40– 60 | 26.35 | 1.5 | 41 | | | 0.78 | | |
| 60– 80 | 37.89 | 1.9 | 35 | | | 0.81 | | |
| 80– 100 | 47.43 | 2.2 | 32 | | | 0.75 | | |
| 0– 100 | 26.35 | 1.5 | 41 | 2.16 | 1.84 | 0.93* | 1.94 | 0.97 |
| 100– 200 | 79.05 | 3.1 | 25 | 1.88 | 1.64 | 0.82 | 1.79 | 0.80 |
| 200– 300 | 132 | 4.1 | 20 | 1.78 | 1.58 | 0.70 | 1.48 | 0.66 |
| 300– 400 | 184 | 5.2 | 18 | 1.71 | 1.55 | 0.69 | 1.35 | 0.61 |
| 400– 500 | 237 | 6.1 | 15.3 | 1.65 | 1.45 | 0.66 | 1.22 | 0.66 |
| 500– 1000 | 395 | 8.2 | 12.0 | 1.47 | 1.295 | 0.49 | 1.24 | 0.53 |
| 1100– 1500 | 685 | 11.2 | 9.5 | 1.28 | 1.09 | 0.27 | 1.06 | 0.49 |
| 1600– 2000 | 949 | 13.8 | 8.2 | 1.22 | 0.99 | 0.32 | 0.94 | 0.44 |
| 2100– 2500 | 1212 | 15.8 | 7.1 | 1.08 | 0.91 | 0.24 | 0.89 | 0.41 |
| 2600– 3000 | 1476 | 17.7 | 6.7 | 1.08 | 0.89 | 0.26* | 0.84* | 0.36 |
| 3100– 3500 | 1739 | 19.4 | 6.2 | 1.00 | 0.80 | 0.184 | 0.81 | 0.26* |
| 3600– 4000 | 2004 | 20.7 | 5.9 | 0.89 | 0.74 | — | 0.72 | 0.22 |
| 4100– 5000 | 2398 | 23.3 | 5.6 | 0.87* | 0.67 | — | 0.72 | 0.21 |
| 5100– 6000 | 2925 | 26.1 | 5.1 | 0.78 | 0.58 | — | 0.65 | 0.21 |
| 6100– 7000 | 3452 | 28.2 | 4.8 | 0.74 | 0.51 | — | 0.56 | — |
| 7100– 8000 | 3979 | 30.0 | 4.5 | 0.66 | — | — | 0.48 | — |
| 8100– 9000 | 4506 | 32.6 | 4.2 | 0.63 | — | — | 0.48 | — |
| 9100–10000 | 5133 | 35 | 4.1 | 0.60 | — | — | 0.43 | — |
| 10100–11000 | 5560 | 36.8 | 3.9 | 0.60 | — | — | — | — |
| Nombre de traces | | | | 6 | 2 | 10 | 3 | 4 |
| . . . à partir de l'astérisque | | | | 3 | | 7 | 2 | 2 |
| . . . du second astérisque | | | | | | 3 | | |

TABLEAU III

RAYONS $\alpha$ ÉNERGIQUES DANS UNE ÉMULSION À GRAIN FIN, DENSITÉS EN GRAINS PAR MICRON

| $R$, divisions | $\bar{R}$, $\mu$ | $\bar{E}$, Mev. | $I(\bar{R})$, kev./$\mu$ | 0 jour Extrapolé Fig. 5 | 1 jour 90% 25°C. | 3 jours 90% 25°C. |
|---|---|---|---|---|---|---|
| 0–100 | 26.35 | 5.9 | 158 | (2.87) | 2.58 | 1.1 |
| 100–200 | 79.05 | 12.3 | 97 | (2.69) | 2.41 | — |

inscription. Les grains ont été comptés dans des segments de 20, de 100, de 400 et de 900 divisions. Les valeurs, rapportées au Tableau II, sont des moyennes basées sur la mesure de 2 à 10 traces. Les parcours moyens $\bar{R}$ concernent les trajectoires au moment de leur inscription. Le Tableau III montre quelques mesures sur les rayons $\alpha$ longs, la densité au temps zéro était saturante et ne

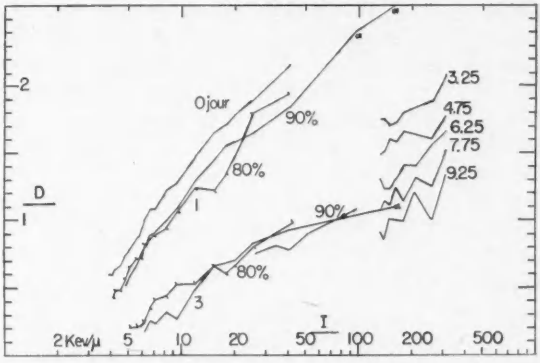


FIG. 5. Variation de la densité $D$ avec le pouvoir ionisant $I$ pour des protons énergiques dans une émulsion à grain fin, pour 0, 1 et 3 jours de conservation à 25°C. et à une humidité de 80% ou de 90%. Dans une autre émulsion à grain fin, variation de la densité des rayons $\alpha$ ThC′ avec $I$, à divers temps $t$, 25°C., 70% déterminée par l'analyse intégrale des étoiles du thorium.

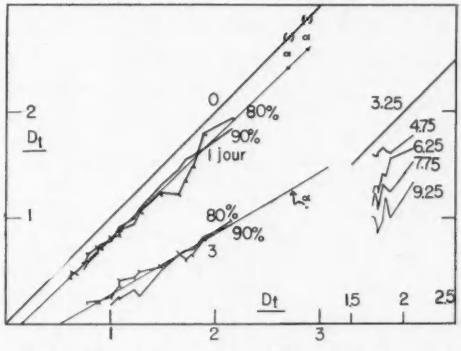


FIG. 6. Comme Fig. 5, mais variation de la densité $D$ avec $D_0$. En abscisses lire $D_0$ et non $D_t$.

pouvait être mesurée directement, on l'a estimée par l'utilisation de la Fig. 6. La Fig. 5 montre l'ensemble des résultats avec log $I$ en abscisses, les mesures sur les rayons $\alpha$ s'accordent à peu près avec l'hypothèse d'une courbe $D$ vs. $I$, unique pour toutes les sortes de particules.

Dans l'ensemble la régression est plus rapide que pour l'émulsion comparable $F_{II}$ sensibilisée de la Fig. 2, ce qui résulte d'une humidité plus forte, les traces étant peu faciles à observer après trois jours. Une courbe unique paraît repré-

senter assez bien les résultats à 80% et à 90% d'humidité relative. Les résultats au temps zéro suivent mieux une courbe continue que ceux aux temps ultérieurs, ce qui dépend d'une fluctuation plus grande de la densité dans les traces régressées.

La loi de la régression proposée plus haut se vérifie assez bien dans la Fig. 5 et surtout dans la Fig. 6. Dans celle-ci, nous avons tracé une seule droite pour les séries de mesures aux deux humidités. De ce diagramme on a tiré les densités $\alpha$ au temps zéro, en traçant la droite pour un jour d'après les points $P$ seulement. L'ordonnée étant connue, on tire l'abscisse qui est $D_0$. Alors la densité $\alpha$ au temps trois jours tombe nettement sous la droite tracée pour les protons. Ici la difficulté d'accorder les points $\alpha$ et $P$ avec une courbe unique ne peut être attribuée à une position différente dans l'émulsion, puisque tous les phénomènes analysés étaient en profondeur. Le désaccord peut provenir d'erreurs de mesure, mais il reste une possibilité que la densité ne soit pas une fonction du pouvoir ionisant seulement et dépende dans une petite mesure, de la nature de la particule, surtout après régression.

Les droites tracées Fig. 5 ont pour équation

$$D = D_0 - a(t) - b(t)D_0,$$

$a = 0.13, 0.30$ $\qquad b = 0.06, 0.42$ $\qquad t = 1, 3$ jours.

On voit que $b$ augmente avec le temps beaucoup plus rapidement que $a$.

On peut chercher à représenter la densité en fonction du temps, Fig. 7, comme dans la Fig. 2. Ici on ne dispose que de trois valeurs du temps, mais par contre de nombreux pouvoirs ionisants, et de deux humidités. On trouve un

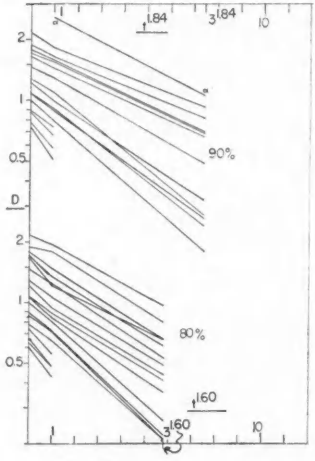


FIG. 7. Comme les protons de la Fig. 6, mais variation de $D$ avec $t$, pour plusieurs pouvoirs ionisants. En abscisses $t^n$, $n = 1.84$ (90%) et $n = 1.6$ (80%).

accord satisfaisant à condition de prendre une valeur de $n$ très différente de 0.5. Nous avons trouvé: $n = 1.60$ à 80%, $n = 1.84$ à 90%, $T \backsim 2.35$ pour les deux humidités:

$$D/D_0 = 2^{-(t/T)^n}.$$

Au contraire de la loi avec $n = 0.5$, celle-ci loin d'indiquer un palier aux grands temps, indique une variation accélérée de la dérivée logarithmique de la densité $(dD/dt)/D$. L'accord est satisfaisant, et il n'y a pas de variations systématiques de $n$ avec le pouvoir ionisant. La période $T$ au contraire diminue légèrement quand le pouvoir ionisant diminue.

Des mesures à des temps différents seraient nécessaires pour établir cette loi définitivement; cependant cette formule prédit une densité très faible après 4 jours, et imperceptible après 5 jours, ce qui s'accorde avec les observations, toute apparence de trace étant disparue après 5 jours.

Les mesures d'Albouy et Faraggi, relevées au Tableau IV peuvent aussi être représentées par la même équation, avec $n$ peu différent de 2, et $T$ voisin

TABLEAU IV

DENSITÉ DES RAYONS $\alpha$ DU POLONIUM

Appareil chronométrique à 25°C., 40–65%, émulsion à grains fins non sensibilisée

| $D$, grains/micron<br>$t$, heures | 2.09<br>0 | 1.80<br>10 | 1.55<br>20 | 1.44<br>30 | 1.39<br>40 | 1.30<br>50 | |
|---|---|---|---|---|---|---|---|
| $D$<br>$t$ | 1.21<br>60 | 1.30<br>70 | 1.14<br>80 | 1.17<br>90 | 1.19<br>100 | 1.08<br>110 | 1.08<br>120 |

Mesures d'Albouy et Faraggi, température et humidité non spécifiées. Fig. 1, courbe II, Ref. (4)

| $D$ valeurs relatives<br>$t$, heures | 1<br>0 | 0.94<br>0.08 | 0.88<br>1.9 | 0.81<br>2.8 | 0.70<br>4.2 | 0.70<br>5.2 |
|---|---|---|---|---|---|---|
| $D$<br>$t$ | 0.64<br>6.1 | 0.61<br>6.9 | 0.48<br>8.3 | 0.43<br>9.2 | 0.38<br>9.8 | 0.32<br>10.4 |

de 6 heures. Ces mesures ont dû être exécutées à grande humidité étant donné la période très courte et la valeur de $n$.

Tous les résultats s'accordent bien avec la loi exponentielle proposée; l'exposant $n$ augmente avec l'humidité et passe de 0.5 pour 30% à des valeurs comprises entre 1.6 et 2 pour des humidités comprises entre 80% et 100%. La période diminue par contre avec l'humidité, passant de 30 jours à 0.25 jours. Les mesures section IV s'accordent aussi avec cette loi.

D'autres formules peuvent sans doute représenter les résultats aussi bien dans certains cas, ainsi Albouy et Faraggi ont adopté une fonction linéaire, qui à la précision des mesures possibles près, et dans le domaine des valeurs de $D$ mesurables, s'accorde également bien avec leurs résultats. Cependant il n'est peut être pas légitime de prolonger la courbe d'Albouy et Faraggi

jusqu'à $D = 0$; en effet la densité des traces encore visibles cesse d'être définie quand on ne voit plus de traces, elle ne peut atteindre 0, la courbe cesse au moment où les traces sont invisibles.

## IV. DISPOSITIF CHRONOMETRIQUE D'IRRADIATION $\alpha$

Un appareil a été réalisé, qui permet de déplacer d'un mouvement uniforme, une plaque sensible devant une source de polonium munie d'un collimateur à fente. Le mouvement est assuré par un moteur synchrone Hayden faisant un tour en 10 heures, avec une vis de pas 1 mm. Celle-ci est engagée par un trou fileté dans une petite plaque d'aluminium portant la plaque sensible. Cette plaque de métal glisse à plat sur une tablette entre deux coulisses. Le collimateur, formé de deux lames de laiton de 1 mm., espacées de 0.5 mm. surmonte la plaque. L'irradiation s'est faite à 25°C., 40 à 65% d'humidité relative, sur une émulsion, à grain fin comparable à celle de la section III, sensibilisée sur une moitié de sa surface. De la sorte l'échelle des temps est connue avec précision, et le procédé se prête bien à des mesures comparatives.

Un premier résultat concerne le noircissement visible à l'oeil nu: il diminue dès le début, et il n'y a aucune indication d'un accroissement initial. S'il a lieu il doit être faible et se situer à un temps inférieur à 1 heure. Les grains ont été comptés dans les 11.4 premiers microns des traces dans la partie non sensibilisée seulement, la densité étant saturante dans l'autre partie. (Tableau IV et Fig. 8 et Fig. 9). Ces mesures s'accordent bien avec la formule exponentielle proposée, avec $n = 0.5$ et $T = 113$ heures ou 4.7 jours. L'exposant s'accorde avec les mesures faites à faible humidité.

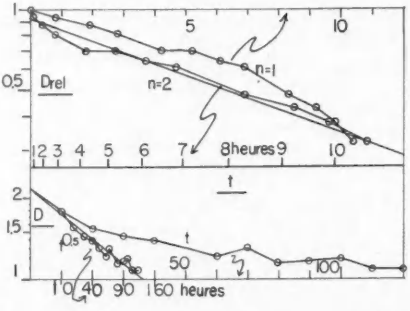


FIG. 8. Variation de $D$ avec $t$ pour les rayons $\alpha$ Po. I. En bas. Mécanisme chronométrique, émulsion à grain fin du 27 septembre 1951 non sensibilisée, 25°C., 40–70%, en abscisses $t^n$, $n = 1$ et $n = 0.5$. II. En haut. Mesures d'Albouy et Faraggi (4), $n = 1$ et $n = 2$, $n$ compris entre 1 et 2 donnerait un meilleur accord.

## V. ANALYSE INTEGRALE DES ETOILES DU THORIUM

Une émulsion à grain fin a été mélangée à l'état liquide avant d'être coulée, avec le sensibilisateur, et avec une petite quantité de $Th(NO_3)_4$, assurant une teneur en thorium d'environ 0.1% de l'émulsion sèche. Mieux que l'imprégnation, ce procédé de mélange à l'état liquide assure une composition définie et uniforme,

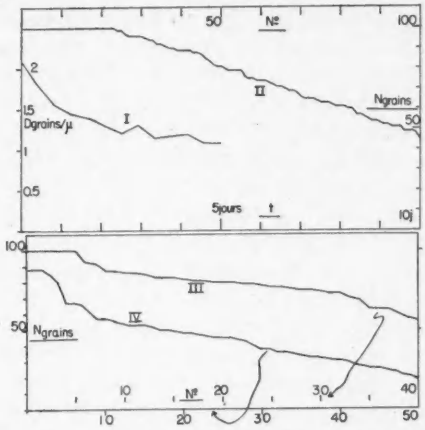


FIG. 9. I. Comme Fig. 8. I, mais $t$ en abscisses et échelle cartésienne en ordonnées. II. Analyse intégrale $\alpha$ ThC′ émulsion à grain fin du 14 décembre 1951 sensibilisée, 25°C., 40–70%, en ordonnées le nombre total de grains par trace, en abscisses le numéro de classement donnant une échelle du temps. Conservation 10 jours. III. Comme II, mais émulsion du 22 janvier 1952 sensibilisée, 25°C., 40–70%. Conservation environ 10 jours. IV. Comme III, mais non sensibilisée.

et une pénétration égale de tous les constituants radioactifs. Les plaques ont séché en deux heures et ont été conservées, soit 1 jour soit 10 jours, à 25°C., 40%–65% d'humidité relative avant de les développer.

Les plaques conservées un jour se prêtent à une recherche de l'accroissement initial de la densité. Les étoiles à quatre branches renfermant un $\alpha$ ThC ou ThC′, se sont formées par l'inscription successive des $\alpha$ de ThX, Tn, ThA, précédant celui de ThC ou ThC′. Les intervalles qui ont séparé l'inscription des quatre traces sont de l'ordre des périodes interposées, pratiquement ThC 60.5 min., et ThB 10.6 heures. La quatrième et plus longue trace (ThC ou ThC′), s'est donc inscrite en moyenne environ 10 heures plus récemment que les trois autres. La densité granulaire était trop forte pour permettre le comptage, mais si on pouvait comparer la densité du groupe ancien ThX, Tn, ThA, et celle du groupe récent ThC ou ThC′, dans des segments égaux, on trouverait la différence de densité correspondant à $t \backsim 10$ heures, dans d'excellentes conditions de comparaison et cette différence montrerait peut être l'accroissement initial.

D'autre part dans une étoile observée dans une plaque conservée un temps quelconque, un rayon $\alpha$ ThC′ est plus récent que les rayons $\alpha$ associés, la difference d'âge la plus probable étant zéro, et la différence moyenne, pour une plaque âgée, environ $T/0.693 = 15.3$ heures. S'il existait un *accroissement* initial, on devrait observer au moins dans certains cas, une densité ou une opacité plus grande dans une trajectoire associée que dans la trajectoire ThC′. Nous avons observé plusieurs étoiles dans ce but, sans voir de différence systématique. Les différences d'opacité étaient de $\pm$ 10% environ dans les cas individuels. Toutes nos expériences s'accordent donc avec une diminution se manifestant dès le début.

L'étude de la plaque conservée 10 jours a suggéré une méthode d'analyse intégrale pour déterminer la variation de la densité avec le temps. Considérons 100 traces $\alpha$ ThC′ observées au hasard. Elles se sont inscrites à toutes les époques et ont avec une égale probabilité, tous les âges possibles entre 0 et 10 jours, pourvu que les traces les plus âgées soient encore toutes visibles. Négligeant les fluctuations de la régression, qui font parfois que de deux traces la plus dense n'est pas la plus récente, nous admettons que dans une liste des traces classées dans l'ordre de leur densité, l'âge est proportionnel au numéro de classement.

On a d'abord trouvé que 23% des traces étaient saturées, par l'observation de 100 traces. Puis sur 77 traces prises au hasard, non saturées, le nombre des grains a été déterminé. Il était compris entre 45 et 99. La Fig. 9 représente en abscisses le nombre intégral de traces ayant un nombre de grains au moins égal à celui porté en ordonnées. Puisque le numéro d'ordre d'une trace est une mesure de son âge, l'âge relatif se trouve porté en abscisses, et la densité étant en ordonnées, cette courbe représente aussi la variation de la densité avec le temps.

La courbe ainsi obtenue pour l'émulsion sensibilisée présente une période d'environ 8.5 jours. Elle ne se distingue pas d'une droite; il semble qu'elle devrait être courbée vers le haut, de même que celle obtenue par le procédé chronométrique pour une émulsion semblable non sensibilisée, qui se trouve sur la même figure. La raison tient peut être à des différences entre les émulsions et surtout entre les conditions d'humidité au cours de la conservation, qui n'a pas été surveillée très exactement. Cependant la considération de cette courbe fait ressortir une cause possible d'erreur. Dans une plaque suffisamment vieille, l'une des hypothèses cesse d'être vraie, les traces très vieilles ne sont plus toutes visibles. Cela fausse non l'échelle des densités mais l'échelle des temps pour toutes les trajectoires sauf la première et la dernière, puisqu'on aurait dû trouver une plus grande proportion de numéros d'ordre supérieur avec une densité faible. Cette cause d'erreur tend à imprimer une courbure vers le bas, et pourrait expliquer dans le cas actuel, que la courbure vers le haut est annulée. Cependant il serait curieux qu'une proportion notable de traces soit invisible quand la plus faible observée comptait encore 45 grains.

La même cause d'erreur, si les plaques sont tellement vieilles que les premières traces inscrites sont totalement effacées, aura pour effet de donner des courbes toutes semblables, quel que soit l'âge de la plaque. En effet on ne trouvera aucune densité granulaire inférieure à une densité minimum correspondant à l'âge maximum laissant encore une trace perceptible. D'autre part l'échelle des temps est affectée puisque le numéro d'ordre maximum correspond invariablement à l'âge maximum, et comme précédemment l'échelle relative des temps est faussée pas l'abondance excessive des traces récentes. La courbe doit présenter une chute brusque au voisinage du numéro d'ordre maximum.

Une autre hypothèse est inexacte, il y a des fluctuations de densité, dont l'effet est difficile à prévoir exactement, mais doit être dans l'ensemble de rendre moins nettes les caractéristiques prévues, et de transformer en droites toutes les

courbes. Un caractère commun à toutes ces courbes, imposé par hypothèse, est que la densité ne peut augmenter vers les numéros d'ordre supérieur.

La Fig. 9 montre l'analyse intégrale portant sur une autre émulsion à grain fin conservée plusieurs jours avant d'être développée, sensibilisée et non sensibilisée. On voit au moins l'indication d'une chute brusque aux grands temps. Les conditions étaient 25°C., 40–65% d'humidité relative.

Le procédé permet de distinguer dans une seule plaque des traces appartenant à des groupes d'âge différents, et connus avec une précision relative. On a ainsi reconnu dans la plaque conservée 10 jours cinq groupes égaux définis par le nombre total de grains, parmi 100 traces $\alpha$ ThC′ mesurables. La densité a été mesurée pour des segments de 10 divisions, les traces mesuraient de 81 à 90 divisions. Les résultats sont rapportés au Tableau V. L'âge moyen le plus récent est 3.25

TABLEAU V

ANALYSE INTÉGRALE DES RAYONS $\alpha$ DU ThC′. DENSITÉ EN GRAINS PAR MICRON, PARCOURS ET ÂGE

| Parcours $R$ en divisions | $\bar{R}$, $\mu$ | $I(\bar{R})$, kev./$\mu$ | 2.5 à 4 jours $t = 3.25$ | 4–5.5 4.75 | 5.5–7 6.25 | 7–8.5 7.75 | 8.5–10 9.25 |
|---|---|---|---|---|---|---|---|
| 0–10 | 2.78 | 310 | 2.09 | 1.78 | 1.65 | 1.53 | 1.34 |
| 10–20 | 8.33 | 260 | 1.87 | 1.61 | 1.56 | 1.25 | 1.00 |
| 20–30 | 13.89 | 210 | 1.83 | 1.63 | 1.40 | 1.31 | 1.19 |
| 30–40 | 19.44 | 180 | 1.80 | 1.66 | 1.41 | 1.14 | 0.99 |
| 40–50 | 25.00 | 162 | 1.72 | 1.58 | 1.30 | 1.24 | 1.00 |
| 50–60 | 30.56 | 150 | 1.70 | 1.60 | 1.23 | 1.12 | 1.01 |
| 60–70 | 36.11 | 140 | 1.75 | 1.51 | 1.23 | 1.14 | 0.86 |
| 70–80 | 41.67 | 134 | 1.75 | 1.49 | 1.30 | 1.08 | 0.91 |

jours, et le plus élevé, 9.25 jours. Ces résultats sont représentés Fig. 5 où ils montrent la variation de la densité avec le pouvoir ionisant, et le déplacement graduel des courbes vers le bas aux temps croissants. Ces courbes ne sont pas précisément comparables à celles pour les protons et pour les rayons $\alpha$ de la section III, vu la différence d'humidité. La Fig. 4 représente aussi ces résultats. Au lieu de $D_0$, on a porté en abscisses la densité au temps 3.25. On trouve une vérification grossière de la loi de la régression modifiée, selon laquelle la densité au temps $t$ est une fonction linéaire de la densité au temps $t_0$

$$D = D_{t_0} - a - b\,D_{t_0}$$

l'accord est passable avec $b = 0$.

On voit que la méthode d'analyse intégrale peut donner des résultats précis à condition de mesures nombreuses et d'une interprétation appropriée.

## VI. EFFET DE L'HUMIDITE, DE LA TEMPERATURE ET DE L'OXYGENE

L'influence de l'humidité apparaît dans les mesures des sections précédentes, les périodes étant en général plus courtes aux grandes humidités pour les émulsions à grain fin étudiées. Des expériences comparatives plus précises ont été effectuées sur les rayons $\alpha$. L'irradiation a été faite en approchant soit une source de polonium, soit une source de ThB + . . . obtenue par le procédé suivant.

On électrolyse avec un courant d'environ 10 ma. 200 cm.$^3$ d'une solution à 20% $Th(NO_3)_4$ contenue dans un verre conique sur pied, sur des électrodes de platine ou de palladium d'environ 3 cm.$^2$ chacune. Le plomb présent se dépose surtout sur l'anode à l'état de $PbO_2$. Ce plomb est surtout du plomb inactif, mais il contient aussi une partie du ThB présent. On laisse l'électrolyse se poursuivre sans arrêt et on enlève le dépôt, abondant au début qui dilue le produit actif. Ce dépôt au début est peu solide et tombe au fond où on peut le recueillir. Après une semaine de fonctionnement, le dépôt qui se forme renferme une moindre proportion de plomb inerte et forme une couche plus mince d'où les rayons $\alpha$ peuvent sortir avec un plus grand parcours. Selon des mesures rapides au compteur de Geiger-Müller, on recueille une fraction de l'ordre de 10% du ThB théoriquement présent. Le dépôt sur l'électrode est lavé et chauffé légèrement pour le faire mieux adhérer. L'activité se concentre sur une face si l'autre est vernie de glyptal par exemple. Cette source posée sur une plaque deux minutes y laisse de nombreuses traces.

TABLEAU VI

INFLUENCE DE LA TEMPÉRATURE, DE L'HUMIDITÉ ET DE L'OXYGÈNE DE L'AIR SUR LA DENSITÉ EN GRAINS PAR MICRON. EMULSIONS À GRAIN FIN SENSIBILISÉES OU NON. RAYONS $\alpha$ Po SAUF INDICATION CONTRAIRE, PARCOURS MOYEN 5.56 $\mu$ DANS LES PLAQUES, 5.27 DANS LES FEUILLES

| Conditions | | 0 jour | 0.75 | 1 | 1.75 | 2 | 3 | Réduction du tiers |
|---|---|---|---|---|---|---|---|---|
| (1) *Plaques* 27 *décembre* 1951 | | | | | | | | |
| Non sens. $\alpha$ ThC′ | $\bar{R} = 5.56$ | 2.14 | | | | 1.73* | 1.77 | |
| 48°C., 10–15% | 16.67 | 2.07 | | | | 1.55 | 1.76 | |
| (air de la pièce) | | | | | | | | 90 heures |
| | 27.78 | 1.85 | | | | 1.48 | 1.64 | |
| | 38.89 | 1.5 | | | | 1.44 | — | |
| Non sens. 48°C., 10–15% | | 2.09 | | | | 1.73 | 1.42 | |
| Non sens. 25°C., 70% | | | | | | | | 45 |
| Non sens. 25°C., 40–65% | | | | | | | | 120 de moitié |
| Sens. 25°C., 80% | | (3.0 ∼) | | 2.98† | | | 2.52 | |
| Non sens. 25°C., 80% | | | | 2.61† | | | 1.77 | 48 |
| Sens. 25°C., 90% | | | | 2.98† | | | 1.70 | |
| Non sens. 25°C., 90% | | | | 2.44† | | | 1.01 | 43 |
| (2) *Plaque sensibilisée* | | | | | | | | |
| 35°C., 80% pyrogallol | | (3.0 ∼) | | 1.5 | | 1.08 | | |
| 25°C., 80% pyrogallol | | | | | | | 1.93 | |
| (3) *Feuille sans support sensibilisée* 25°C. | | | | | | | | |
| 95% air | | (3.0 ∼) | 1.94 | | 1.00 | | | |
| 95% pyrogallol argon | | | | | | | 1.03 | |
| 70% air | | | | 2.26 | | 1.60 | | |
| 70% pyrogallol argon | | | | | | 2.04 | | |
| 100% hydrogène | | | | | | | 1.02 | |
| Argon sec | | | | | | | 2.84 | |

**Développement insuffisant?*

*†Evaluée indirectement en comptant le nombre i d'intervalles par unité de longueur, et en admettant D = 2.98 − i.*

Les résultats sont décrits dans le Tableau VI. La régression à 48°C. 10–15% est plus lente qu'à 25°C. 70%, ce qui illustre l'importance de l'humidité. La conservation peut être meilleure à une température plus élevée si l'humidité est plus faible. Cependant une température très basse ralentit la régression. Une plaque $F_{II}$ sensibilisée et non sensibilisée (voir Tableau I) montrait après trois mois de conservation à la température de la glace sèche − 85°C., des traces $\alpha$ et $P$ exactement aussi denses qu'au temps zéro (28), il n'y avait même pas une régression atteignant celle observable en un jour dans les conditions ordinaires.

D'autre part les résultats à 70, 80 et 90% montrent des régressions peu différentes, d'accord avec une remarque d'Albouy et Faraggi. La gélatine selon une courbe de Mees (32, p. 78) absorbe une proportion d'eau croissant avec l'humidité si celle-ci augmente de 0 à 70%, l'accroissement devenant très rapide entre 70 et 100%. Il semble donc que la proportion d'eau retenue par la gélatine joue un rôle essentiel.

Des plaques enfermées dans une bouteille avec une solution de potasse et de pyrogallol ont montré une régression presqu'aussi forte qu'en l'absence du pyrogallol qui absorbe l'oxygène (Tableau VI, (2)). Ce résultat publié par Thouvenin et Demers (41) a été précisé par les expériences du Tableau VI, (3). En fait l'oxygène de l'air contribue un peu à la régression mais beaucoup moins qu'indiqué par Albouy et Faraggi (4). A humidité constante tandis que celles-ci trouvent une régression cinq fois plus lente dans l'azote que dans l'air, nous trouvons dans l'argon privé d'oxygène, environ 60 à 80% de la régression observable dans l'air. Cette observation s'accorde avec celles de Wäffler et Junis, qui ont trouvé que la suppression de l'oxygène ne ralentit pas la régression des traces $\alpha$ dans les émulsions Ilford mouillées d'eau légère ou d'eau lourde $D_2O$.

Ces expériences ont été faites avec une boîte cubique de parois de Lucite épaisse de 8 mm. Cinq parois sur six sont soudées au chlorure de méthylène. La dernière est appliquée fortement par une vis, avec une feuille de caoutchouc graissé interposée. Au fond on place la solution concentrée de potasse, puis la feuille d'émulsion dans un papier noir, soutenue par un treillage en fil de fer, et le pyrogallol en poudre sur un papier. Par deux soupapes de pneu de bicyclette, le couvercle étant en place, on fait circuler de l'argon pur pendant quelques minutes. Puis on en laisse une surpression pour éviter les rentrées de gaz, on sépare de la bouteille d'argon, et on agite assez pour que le pyrogallol tombe et se dissolve.

Dans nos conditions, il apparaît bien établi que la partie principale de la régression en milieu humide est insensible à la présence d'oxygène et n'est donc pas une oxydation selon l'équation proposée par Albouy et Faraggi.

## VII. CONDITIONS DE PREPARATION DE L'EMULSION

Plusieurs essais plutôt qualitatifs ont permis, à diverses époques, de constater la régression des rayons $\alpha$ dans un grand nombre d'émulsions préparées au laboratoire, après conservation dans les conditions ordinaires. Ces émulsions

peuvent se diviser en deux types, grains fins comme $F_{II}$, ou la formule à deux jets (15, 16, 17, 18), et grains moyens selon la formule à trois jets (18). Des mesures au microscope électronique faites par M. A. Nantel à l'Institut de Microbiologie de l'Université de Montréal ont montré que le diamètre des grains est légèrement inférieur à 0.1 $\mu$ pour les grains fins, et voisin de 0.3 $\mu$ pour les grains moyens.

De l'ensemble de ces observations on peut déduire que le détail des procédés de fabrication a peu d'influence sauf par la taille du grain et la sensibilité qu'ils confèrent. La régression, évaluée par la durée nécessaire pour la disparition des traces, par la période à demi réduction de la densité ou par le temps minimum nécessaire pour réduire de façon perceptible l'opacité des traces $\alpha$ ou $P$, est deux ou trois fois plus rapide avec un grain fin qu'avec un grain moyen. L'absence de triéthanolamine comme sensibilisateur rend la régression plus rapide, de 50 à 100% environ. Autrement, nous n'avons trouvé aucune modification des procédés, changeant de façon perceptible la régression. Hälg et Jenny (21) ont observé une régression plus faible dans des émulsions à l'ammoniaque que dans celles sans ammoniaque. La différence tient peut être simplement à l'accroissement de la sensibilité.

## VIII. THEORIE DE LA REGRESSION

*Lois expérimentales*

Les mesures précédentes s'accordent avec les deux lois qui suivent et suggèrent la troisième, qui concernent toutes la densité linéaire des grains $D$ dans les traces encore visibles après le temps $t$.

1ère *loi. La densité varie suivant une fonction exponentielle modifiée,*

$$D = D_0\, 2^{-(t/T)^n} = D_0 \exp -(t/\tau)^n, \quad T = 0.693^{1/n}\tau,$$

l'exposant $n$ et l'inverse de la période $1/T$ augmentent avec l'humidité, l'exposant est voisin de 0.5 à sec, et paraît augmenter rapidement vers 70%, pour atteindre 1.84 à 90%, dans les cas observés par nous. L'exposant ne paraît pas dépendre du pouvoir ionisant ni de la densité initiale.

Cette loi peut représenter de façon satisfaisante les observations de Hälg et Jenny, la somme de deux fonctions exponentielles qu'ils observent dans un cas avec $n = 1$, et deux périodes de 3 et de 140 jours, pouvant être remplacée par la fonction ci-dessus avec $n = 0.5$ et une période intermédiaire. Dans un autre cas, ils représentent leurs résultats par une exponentielle avec $n = 1$. Les diagrammes de Lauda ont aussi l'aspect approximatif de nos courbes Fig. 3 avec $n = 0.5$. Les résultats d'Albouy et Faraggi, représentés par une droite dans le système de coordonnées $D$ vs. $t$, s'accordent également bien avec la formule ci-dessus si $n \backsim 2$. Les mesures de Loening sur l'effet de la lumière s'accordent bien avec la formule ci-dessus, si $n$ est voisin de 0.5. En particulier on représente bien ainsi la portion initiale de la courbe où la dérivée $dD/dt$ observée est extrêmement grande.

Cette loi ne s'applique pas précisément au nombre total de grains visibles $G$ ni au nombre de traces encore visibles $N$. Cependant les courbes d'Albouy et

Faraggi pour $N$ et pour $G$, et les résultats de Coppens concernant $N$ sont représentables assez exactement par la formule ci-dessus avec des exposants voisins de 2 à 4 pour $N$, et voisins de 1 à 1.5 pour $G$.

$2^{\text{ème}}$ *loi. La densité est une fonction linéaire de la densité initiale,*

$$D = D_0\,[1 - b(t)] - a(t),$$

les coefficients $a$ et $b$ dépendant du temps mais non de la densité initiale.

Ces deux lois sont incompatibles si on suppose la période indépendante de la densité initiale, puisqu'il faudrait alors supposer $a = 0$ dans la seconde. Cependant elles s'accordent si la période varie avec $D_0$ suivant l'équation:

$$\tau = t[\log_e 1/(1 - b - a/D_0)]^{-1/n}$$

qui indique une période plus courte aux densités plus faibles. L'examen de la Fig. 6, où la densité $D_0$ varie d'un facteur 3 environ, montre en effet que la pente des courbes augmente en valeur absolue, c'est à dire que la période diminue, lorsque $D_0$ diminue.

Faute de résultats publiés par d'autres auteurs, nous ne pouvons vérifier à leur aide cette $2^{\text{ème}}$ loi, qui est basée sur l'analyse de nos propres mesures. Cependant elle indique, si $a$ est notable et si $b$ est petit, que la diminution relative $(D - D_0)/D$ de la densité est plus grande aux faibles densités, ce qui s'accorde avec les observations de Lauda, que les protons disparaissent plus vite que les rayons $\alpha$ plus denses.

On a constaté sur la Fig. 4 que $b$ augmente avec le temps plus vite que $a$, ou encore, que la courbe tend à devenir une droite horizontale, de telle sorte qu'aux grands temps la densité est à peu près indifférente à la densité initiale. Cette extrapolation s'accorde avec l'observation occasionnelle que nous avons faite de traces longues et très vieilles, qui montrent une densité faible présentant des fluctuations le long du parcours, mais ne variant presque pas de façon systématique d'une extrémité à l'autre, à tel point qu'on a peine à reconnaître la début et la fin, et à discerner un rayon $\alpha$ d'un proton. Une troisième loi peut donc s'énoncer ainsi:

$3^{\text{ème}}$ *loi. Aux âges extrêmes, toutes les traces encore visibles ont la même densité très faible.*

Enfin il est une autre observation qui paraît assez générale et importante pour caractériser le phénomène. La régression est irrégulière et des traces de densité égale au début deviennent inégales, ou encore, la relation densité vs. parcours pour un proton long montre des variations irrégulières plus considérables après régression. Ces fluctuations de la densité nuisent à l'identification des traces vieillies. Puisque des traces deviennent invisibles avec le temps, il faut admettre que la distribution des densités observables dans des traces semblables initialement, suffisamment régressées, n'est qu'une partie de la distribution des densités idéales, qui sont pour un certain nombre des traces, nulles ou trop faibles pour être observables. D'après la Fig. 1 d'Albouy et Faraggi et d'après

nos propres mesures, nous présentons dans la Fig. 10 un diagramme suggérant qualitativement comment la distribution de la densité varie avec le temps.

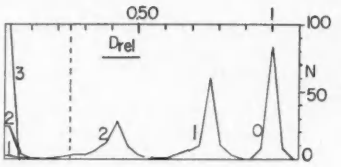


FIG. 10. Diagramme qualitatif suggérant comment la fluctuation des densités observables $D$, et inobservables (à gauche du pointillé), varie avec le temps. Toutes les courbes sont normalisées. Trois temps $t_0 = 0$; $t_1$, régression à $D = 2/3\ D_0$; $t_2$, régression à $D = 0.4\ D_0$; $t_3$, plus de traces visibles. En abscisses densités relatives, en ordonnées, fréquences $N$ de ces densités.

$4^{\text{ème}}$ *loi. La fluctuation de la densité est une fonction croissante du temps.*

*Conséquences des lois expérimentales*

I. De la *diversité des exposants* trouvés dans la première loi, nous pouvons conclure immédiatement que les images latentes subsistant après régression ne sont pas semblables à celles qui existaient initialement. En effet la vitesse relative de réduction de la densité varie avec le temps, quand $n \neq 1$:

$$(dD/dt)/D = -n(t/\tau)^{n-1}.$$

Dans le cas de Jenny, où $n = 1$, la vitesse relative est constante et par conséquent la régression fait alors disparaître les images latentes ou les laisse semblables à elles-mêmes.

Supposons des images latentes formées d'un seul élément atomique toujours identique, et placé dans un grain de bromure d'argent toujours identique; ou encore, des images latentes complexes, mais toutes identiques et identiquement entourées, chacune subsistant intacte ou bien disparaissant brusquement sans résidu si elle commence d'être attaquée. Dans ces cas les images latentes subsistantes seraient semblables à celles existant au début, et il n'y aurait aucune raison pour qu'il n'en disparaisse pas, du début à la fin, des proportions égales dans des temps égaux, i.e., on aurait $n = 1$.

Le fait que l'exposant $n$ est le plus souvent différent de l'unité montre la complexité des images latentes. Elles ne sont certainement pas formées d'un seul élément atomique puisqu'il réagirait plus ou moins vite suivant les conditions extérieures mais toujours avec $n = 1$. Il est probable que les images latentes sont formées de plusieurs atomes, que leur entourage est variable, et que lorsqu'elles commencent de disparaître, elles subsistent encore un temps mesurable avant de disparaître complètement.

II. La complexité des images latentes apparaît encore si on compare la vitesse de disparition d'une *densité égale* dans une trace initialement faible, et dans une trace régressée plus forte initialement après régression. Ces deux vitesses sont inégales en général comme il ressort de l'analyse des courbes pour les protons Figs. 5 et 6. Pour qu'elles fussent égales il faudrait que la densité

fût une fonction linéaire du temps, c'est à dire dans la 2ème loi, $b = 0$ et $a = kt$ en désaccord avec l'expérience. Dans le cas des rayons $\alpha$ analysés par la méthode intégrale Fig. 5 et Fig. 6, on trouve au contraire que la densité est simplement une fonction linéaire du temps, puisqu'on peut admettre que les points expérimentaux Fig. 6 s'accordent avec des droites parallèles équidistantes; cependant l'échelle des temps n'est pas absolument certaine.

On peut conclure qu'en général, les images latentes présentes le long de traces de densités égales mais d'âges différents, ne sont pas exactement comparables, leurs propriétés dépendent non seulement de la densité actuelle mais aussi de leur histoire. En cela les images latentes ressemblent à beaucoup de systèmes tels que les colloïdes dont les propriétés dépendent du traitement préalable et pas seulement de l'état actuel (caoutchouc, gélatine, etc.).

III. La complexité des images latentes apparaît encore comme une conséquence du *processus de leur formation*. En effet, comme Demers (15, p. 246) l'a signalé les images latentes formées par le passage d'une particule de pouvoir ionisant $I$ ne peuvent être toutes égales. Supposons des grains sphériques, ce qui n'est pas loin de la réalité, de diamètre $d$. Le parcours de la particule dans un grain qu'elle touche n'est pas toujours le même. Il varie entre 0 et $d$. Supposons l'ionisation due à la particule distribuée dans un cylindre de diamètre petit par rapport à $d$, ce qui est légitime pour la plus grande partie de l'ionisation, même si des rayons delta sont formés le long de la trajectoire. La perte d'énergie $E$ dans un grain vaut $Il$. Un calcul géométrique simple montre que la probabilité $dP$ d'un parcours compris entre $l$ et $l + dl$, ou d'une perte d'énergie comprise entre $E$ et $E + dE$, suit les relations

$$dP/dl = 2l/d^2, \qquad 0 < l < d,$$
$$dP/dE = 2E/E^2_{\max}, \quad 0 < E < E_{\max},$$

ces fonctions convenablement normalisées varient entre 0 et 2, Fig. 11.

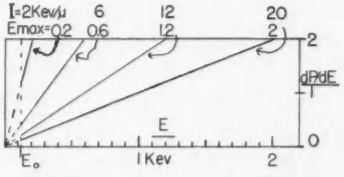


FIG. 11. Variation de la probabilité $dP/dE$ avec l'énergie dépensée $E$, $E_{\max}$ = énergie maximum que la particule peut dépenser dans le grain dont le seuil de développement est $E_0$. Les ordres de grandeur de l'échelle conviennent aux grains les plus sensibles dans les émulsions à grain fin sensibilisées, avec $d = 0.1\ \mu$, $E_0 = 0.120$ kev. On a $E_{\max} = I.\ d$.

Pour continuer une théorie de la formation des images latentes, on pourrait supposer que les grains bromure d'argent tous semblables requièrent tous une même dépense minimum $E_0$, pour acquérir une image latente. Une meilleure approximation exigerait de tenir compte d'une distribution des seuils de sensibilité $E_0$; $E_0$ est plus petit pour un grain très sensible, et plus grand pour un grain moins sensible.

Sans poursuivre davantage ici l'élaboration d'une telle théorie générale, dont celle de Demers (loc. cit.) est un cas particulier, on voit que le passage de la particule ionisante dans un grain bromure d'argent y fait apparaître une image latente si $E - E_0 > 0$, et que la taille de l'image latente étant une fonction croissante de la différence $E - E_0$ pour le grain particulier, est variable le long d'une trajectoire donnée, à cause de la double variation d'un grain à l'autre de l'énergie dépensée $E$, et du seuil de sensibilité $E_0$. Sauf pour les densités granulaires les plus faibles, pour lesquelles toutes les images latentes doivent être comparables et très faibles.

IV. Les *fluctuations* notables de la densité qui apparaissent après régression obligent d'autre part à penser que les images latentes sont toutes de taille assez réduite, i.e. que les plus petites doivent contenir un nombre restreint d'atomes.

En effet, de deux traces voisines, que le développement immédiat aurait fait paraître semblables, l'une est visible et l'autre peut être disparue; la différence n'est pas attribuable au milieu qui est le même, elle doit provenir d'inégalités notables entre le mode de disparition des images latentes respectivement comparables dans les deux traces. Il est naturel d'attribuer ces inégalités à des fluctuations statistiques dans la désintégration atome après atome, des images latentes individuelles. On peut difficilement supposer que des fluctuations notables apparaîtraient pour des amas de 1000 ou de 10000 atomes, tandis qu'une taille de 10 à 100 atomes, comparable à celle admise pour les images latentes les plus faibles dûes à l'action de la lumière, semble d'accord avec les fluctuations remarquées.

Une analyse statistique précise des fluctuations observables fournirait un procédé nouveau pour estimer le nombre d'atomes par image latente.

*Ordre de la réaction par rapport à l'argent*

Désignons par $x$ la quantité d'argent présente. Cette quantité est probablement mesurée assez exactement aux faibles régressions par la densité $D$. Aux fortes régressions, le nombre total de grains $G$ en serait probablement une mesure plus exacte, vu la réduction du nombre $N$ des trajectoires encore visibles. Il semble légitime pour nos fins actuelles d'admettre que $x$ varie selon une loi exponentielle avec un exposant voisin de $n$ et compris entre $n$ et $2\,n$.

Dans le langage de la chimie physique, l'ordre de la réaction qui fait disparaître l'argent est le nombre $m$ d'atomes d'argent qui interviennent dans l'écriture de la réaction qui le fait disparaître. Quels que soient les autres réactifs qui interviennent dans cette réaction, on peut supposer que leur concentration est constante au cours de la diminution de $x$. Si $1/\tau$ désigne un paramètre constant dont dépend la vitesse de réaction, pour $m = 1$:

$$\mathrm{Ag} + \ldots \rightarrow \ldots \quad dx/dt = -x/\tau, \quad x = x_0 \exp - t/\tau.$$

Pour $m$ quelconque

$$m\,\mathrm{Ag} + \ldots \rightarrow \ldots \quad dx/dt = -x^m/\tau, \quad x = x_0(1 + t/\tau)^{-1/(m-1)}$$

la réaction du premier ordre procède à une vitesse relative constante, les autres, à des vitesses relatives décroissantes, qui décroissent d'autant plus vite que $m$ est plus élevé.

Ce raisonnement vaut pour une réaction en phase homogène, i.e., où l'argent est dispersé atomiquement. Si on suppose qu'il forme un grain compact dont la surface détermine la vitesse de réaction, il faut appliquer la théorie des réactions hétérogènes. La vitesse serait alors proportionnelle à $x^{2/3}$ si on suppose le grain constamment sphérique par exemple, et à une puissance supérieure de $x$ si on suppose qu'il devient poreux; la loi est donc voisine de celle du premier ordre. La variation expérimentale de $x$ s'accorde donc approximativement avec une réaction homogène du 1$^{er}$ ordre ou d'un ordre légèrement supérieur pour la régression à sec lorsque $n = 0.5$ ou $n = 1$, sans qu'on ait besoin de supposer une variation du paramètre $1/\tau$ avec la valeur de $x$.

D'autre part la régression humide avec $n = 1.5$–2 ne peut s'accorder avec l'un quelconque des types de réactions proposées. Il faut admettre que le paramètre $1/\tau$ augmente à mesure que la réaction procède. Cette hypothèse s'accorde bien avec ce qu'on sait des niveaux d'énergie des électrons dans les centres de développement de taille variable: plus ils sont petits, plus ils sont instables, à la façon de microgouttelettes ou de microcristaux de taille suffisante, dont la tension de vapeur ou la solubilité sont invariablement plus élevées que leur diamètre est plus faible.

Mais la même raison devrait aussi rendre plus instables les centres de développement régressés à sec et accélérer de la même manière leur disparition, au contraire de ce qu'on observe. La conclusion la plus plausible paraît être qu'il existe deux mécanismes qui agissent l'un à sec et l'autre aux grandes humidités. Dans la régression à sec puisque la vitesse diminue ou tout au moins reste constante, il faut supposer qu'un autre facteur compense énergiquement l'accroissement de vitesse que devrait causer la diminution de la taille des images latentes.

*Température, humidité et oxygène*

L'abaissement de la température, comme nous l'avons noté, réduit ou annule la régression, ce qui indique l'effet de l'agitation thermique, commun à la plupart des réactions entre atomes ou ions. L'effet de l'eau en première analyse s'explique parce qu'elle facilite toutes les réactions ioniques. La suppression de l'image latente, au moins dans certains cas est une oxydation certaine; ce fait nous conduit à admettre que la régression doit être fondamentalement une oxydation, même dans les cas où elle est moins rapide.

La réaction en présence d'air humide, pour la part due à la présence d'oxygène, par que nous trouvons très faible d'accord avec Wäffler et Junis (43), peut s'écrire de deux façons, l'oxygène étant diatomique, et la vitesse doit dépendre de la pression partielle de l'oxygène et de l'eau de façons différentes suivant le cas:

$$2Ag + O + H_2O \rightarrow 2Ag^+ + 2\,OH^-,\ dx/dt \propto P_o \cdot P_{H_2O} \propto P_{O_2}^{\frac{1}{2}} \cdot P_{H_2O},$$

$$4Ag + O_2 + 2H_2O \rightarrow 4Ag^+ + 4\,OH^-,\ dx/dt \propto P_{O_2} \cdot P_{H_2O}^2.$$

Ces formules prêtent à des vérifications expérimentales.

Remarquons ici que la régression suit un processus bien différent de celui de la formation de l'image latente, laquelle se forme à peu près de la même façon quelle que soit l'humidité. On peut en effet enregistrer des traces dans le

vide absolu, ou encore, dans des émulsions gonflées d'eau et dans ces deux cas extrêmes, la sensibilité des grains ne paraît pas être très différente. Cependant selon des informations privées, des résultats inédits de M. John Spence, d'Eastman Kodak, semblent montrer une influence de l'humidité au-dessus de 70%.

*Mécanisme de la régression à sec*

Nous admettrons que la réaction fondamentale dans tous les cas est une oxydation ionique:

$$[1] \qquad Ag \rightarrow Ag^+ + \epsilon^- \qquad \text{(1)}$$

un atome d'argent perd un électron et donne un ion argent. Dans la *régression à sec*, nous admettrons que l'électron est émis par le centre de développement *A* dans le cristal bromure d'argent. Il faut pour cela qu'il acquière une énergie potentielle d'une fraction de volt. Cette énergie d'activation est fournie, quoique rarement, par l'agitation thermique, qui vaut 0.013 ev. à 300°K. par degré de liberté. Le froid ralentit la réaction en réduisant cette énergie. L'électron circule ensuite dans la bande de conduction du cristal.

On peut lui reconnaître quatre sorts possibles.

(1) Il peut retomber sur le *centre de développement* qu'il vient de quitter, attirer là et neutraliser un ion $Ag^+$, et le restituer à son état initial. Comme le centre de développement, même après diminution d'un atome d'argent, est encore relativement gros, il constitue un trou de potentiel particulièrement profond où l'électron a de grandes chances de retourner, dans ce cas il n'y a pas de régression.

(2) L'électron peut réussir à tomber dans un autre trou de potentiel dans le cristal, que nous appellerons un "*centre accepteur*". Ce centre accepteur d'électrons peut être un autre centre de développement puisqu'il s'en trouve parfois plus d'un dans un même cristal, ou encore, il peut être un centre auquel il ne manque qu'un atome d'argent pour être un centre de développement. Dans ces deux cas il n'y a pas de régressions.

(3*a*) Le centre accepteur peut aussi être un trou de potentiel moins profond, un centre actif ou un défaut du cristal, qu'il charge et où il attire puis neutralise un ion $Ag^+$. Pour qu'il joue un rôle dans la régression, il faut qu'une fois accrû, il ne constitue pas un centre de développement. Nous appellerons un centre accepteur satisfaisant à cette condition, un "*centre accepteur de type B*".

Une fois accrû, le centre *B* pourrait être plus stable, présenter pour un autre électron, libéré par le centre *A*, un trou plus profond. L'ionisation d'un autre atome *A* étant plus facile, et sa capture par *B* étant plus probable, la réaction devrait se précipiter. Comme la régression à sec tend plutôt à être de plus en plus lente, il faut supposer que le centre *B* est incapable de s'accroître beaucoup, c'est à dire, qu'après fixation d'un petit nombre d'atomes d'argent, ou même d'un seul, il cesse d'être un trou de potentiel notable pour un autre électron.

(3*b*) Cette situation est contraire à celle considérée le plus souvent, d'un centre actif ou d'un centre de développement d'autant plus stables qu'ils sont plus gros.

Utilisons les lettres $A'$ et $B$ pour désigner des centres tendant à s'accroître sans limite, ou au contraire, s'accroissant jusqu'à une faible limite. Dans la mesure où on peut assimiler un cristal ionique à une vapeur plus ou moins sursaturée, l'existence des types de centres $A'$ et $B$ peut se comprendre par analogie avec la théorie des petites gouttes. Par suite de phénomènes capillaires, la tension de vapeur $p$ d'une petite goutte est une fonction de son rayon $r$, qui tend vers une valeur constante lorsque $r \to \infty$. Lorsque $r$ croît à partir de zéro, $p$ diminue sans cesse pour une goutte neutre, ce qui permet d'expliquer le cas $A'$; dans une atmosphère sursaturée, la goutte ne peut que s'évaporer et disparaître si son rayon est inférieur à une certaine limite $r_2$, et au contraire tend à s'accroître si $r > r_2$. Cependant pour une goutte chargée, la pression augmente d'abord à partir de zéro, passe par une valeur maximum à $r = r_0$, puis diminue, et cette propriété permet d'expliquer les cas $A'$ et $B$: en effet supposons $0 < r_1 < r_0 < r_2$, dans une atmosphère sursaturée, la goutte de rayon zéro tend à s'accroître jusqu'à un certain rayon $r_1$, et si une goutte possède un rayon compris entre $r_1$ et $r_2$, elle tend à diminuer et à prendre le rayon $r_1$, ce qui correspond au cas $B$; si $r > r_2$, le rayon tend à augmenter indéfiniment, ce qui correspond au cas $A'$.

L'analogie avec un grain d'argent entouré des ions du cristal n'est pas parfaite. En particulier le grain résultant tel qu'on se le figure habituellement dans la théorie de la formation de l'image latente, n'est pas chargé, et d'après la théorie de la goutte neutre, on ne peut expliquer le cas $B$ qui nous intéresse. Cependant le milieu entourant le grain est formé d'ions, et on peut supposer qu'une étude plus précise tenant compte de leur action justifierait l'existence du cas $B$. On peut faire l'hypothèse qu'un ion $Ag^+$ est lié faiblement au centre, lui assurant une faible charge moyenne. On ne peut naturellement supposer que l'ion $Ag^+$ est lié en permanence, à moins d'abandonner le processus électrostatique d'attraction d'un ion $Ag^+$ par le centre qui vient de se charger d'un électron.

Tenons compte maintenant des échanges possibles avec le milieu. La goutte liquide échange avec la vapeur des molécules mais garde sa charge. Le grain n'échange pas directement des atomes mais il peut gagner ou perdre un électron, avec acquisition ou départ d'un ion $Ag^+$. C'est l'énergie potentielle de l'électron $V$ sur le centre chargé qu'il faut considérer plutôt que la tension de vapeur de l'argent. Les grandes énergies $V$ correspondent à une grande facilité de départ: l'électron quitte le centre neutre et un ion $Ag^+$ le suit; les faibles énergies correspondent à une probabilité de capture d'un électron et d'un ion $Ag^+$. Nous avons tracé Fig. 12 un diagramme suggérant une disposition plausible des niveaux d'énergie $V$, aux diverses tailles du centre, mesurées par $n$, qui peut être le nombre d'atomes d'argent. Pour le tracer nous avons admis que $V$ dépend de $n$, de la même façon générale que la pression de vapeur d'une goutte chargée dépend de son rayon.

(3c) Le premier centre $B$ qui a été occupé est le plus probablement celui qui offrait à l'électron, le trou de potentiel le plus profond. Parmi les centres $B$ encore libres, aucun n'est donc aussi facile à remplir. La rareté croissante, jointe

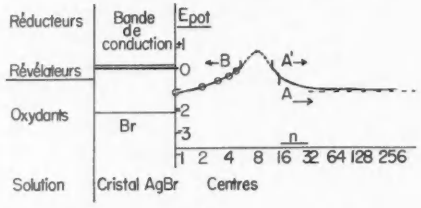


FIG. 12. Niveaux de l'énergie potentielle de l'électron $E_{pot}$ en ev., origine arbitraire; $n$ est le nombre d'atomes, par exemple Ag dans le centre. Ce diagramme fait apparaître la possibilité de centres $B$, capables de s'accroître jusqu'à une taille maximum de cinq atomes à partir de la bande de conduction. La région $A'$ comprend les centres de sensibilité et les centres de développement $A$.

à l'efficacité décroissante des centres $B$, permet d'expliquer le ralentissement de la régression.

Ces centres accepteurs de type $B$ ont donc un rôle comparable à celui des pièges d'électrons qu'il faut imaginer dans les irradiations aux basses températures. A ces températures, seule la première étape de la formation de l'image latente peut se produire, soit la libération d'électrons. La conductivité ionique étant supprimée par le froid, la migration des ions $Ag^+$ pour former des images latentes n'a lieu que pendant le réchauffement de la plaque. On admet que les électrons, tant que la plaque est froide, sont retenus par des centres actifs et par des pièges, qui sont des défauts du cristal. Les centres $B$ sont évidemment comparables à ces pièges et jouent le même rôle, mais naturellement ils ne peuvent rester longtemps chargés d'un électron sans attirer un ion $Ag^+$.

On peut faire à ces hypothèses les critiques suivantes. Le centre $B$, même après son accroissement, doit être plus instable que le centre $A$ même décrû. S'il existe un processus permettant le transfert d'un atome d'argent de $A$ sur $B$, le transfert en sens inverse doit être encore plus probable. D'autre part, si le centre accepteur était présent au moment de l'irradiation, il a eu l'occasion de se charger d'électrons et de s'accroître. A ce moment $B$ ne s'est pas accrû et n'a pas empêché $A$ de s'accroître aux dépens de $A$.

(*3d*) Cette dernière difficulté, sinon la précédente, disparaît si on suppose que des centres accepteurs $B$ se forment par une évolution constante des cristaux. En effet la sensibilité de nos émulsions (16), comme celle d'émulsions au bromure d'argent pur contenant peu de bromures solubles, selon Carroll (12), augmente avec le temps. Toutes les émulsions se voilent avec le temps. Il paraît donc que les cristaux de bromure d'argent se modifient avec le temps, même au sec, et plus vite au chaud et à l'humidité. Il est donc tout à fait plausible que des déformations et des modifications apparaissent avec le temps dans le cristal, prêtes à jouer le rôle de centres accepteurs $B$. On peut aussi admettre que des déformations peuvent disparaître.

La formation d'argent très dispersé sur les centres $B$ est l'équivalent de la formation d'argent colloïdal complexe dans la théorie d'Urbach (42) décrite par Loening, les atomes d'argent étant liés par des valences covalentes avec les ions

$Ag^+$ et $Br^-$ et avec les impuretés du cristal et peut être avec la gélatine environnante.

(4) Enfin l'électron peut réagir sur un *accepteur d'électrons* extérieur au cristal. Dans l'émulsion tout à fait sèche, la gélatine est un mauvais conducteur, elle n'est pas ionisée et ne s'ionise pas facilement, nous admettrons donc que la réaction (3) ci-dessus est plus probable. Cependant on peut imaginer que l'électron disparaisse par une réaction schématisée ainsi, G représentant la molécule de gélatine, $G^-$ un anion, et R un reste neutre:

[2] $$\epsilon^- + G \rightarrow R + G^-.$$

L'eau retenue en atmosphère humide gonfle la gélatine adsorbée au cristal et forme avec la gélatine une structure complexe. Les expériences de Loening ont montré que l'eau seule est un excellent accepteur d'électrons au contraire de la gélatine puisque celle-ci ajoutée à l'eau retarde la régression. Dans l'émulsion humide, il paraît donc raisonnable d'attribuer à l'eau plutôt qu'à la gélatine le rôle d'accepteur d'électrons selon la réaction:

[3] $$\epsilon^- + H_2O \rightarrow H + OH^-.$$

L'influence de l'oxygène se comprend bien lorsqu'elle existe, puisqu'il s'unit à l'hydrogène formé dans la réaction [3],

[4] $$2H + O \rightarrow H_2O.$$

Lorsque du brome est présent dans la gélatine il réagit facilement par la réaction

[5] $$\epsilon^- + Br \rightarrow Br^-.$$

L'action des bromures solubles contenant $Br^-$ est double; au moment de la formation de l'image latente, ils empêchent le brome libéré de disparaître par une réaction sur la gélatine. D'autre part ils gênent la réaction [5].

Dans les réactions [2], [3] ou [5], une charge négative quitte le cristal, son électroneutralité requiert le départ d'un ion $Ag^+$, de sorte que la somme des réactions [1] + [2], [1] + [3], [1] + [3] + [4], ou [1] + [5], équivaut à la formation de gélatinate, d'hydroxyde ou de bromure d'argent à l'extérieur du cristal.

Il n'est pas exclu que des centres *B* après leur accroissement puissent à leur tour, être détruits dans certains cas par les présentes réactions.

*Mécanisme de la régression humide*

La disparition des traces des particules ionisantes aux grandes humidités est rapide et s'accélère avec le temps, ce qui suggère que le mécanisme doit être différent. Aux grandes humidités la gélatine est fortement gonflée, et la protection colloïdale qu'elle assure est réduite. Cette protection assurait la stabilité du cristal et de l'image latente. Peut-être y a-t-il alors réaction directe de l'eau sur l'image latente, pourvu que celle-ci soit superficielle.

Mais il semble que la remarque (3*d*) ci-haut apporte l'explication. En présence de beaucoup d'eau, le cristal évolue rapidement, ce qui permet la formation d'un nombre croissant de centres *B*. L'existence d'une évolution s'accorde avec

les vues d'Albouy et Faraggi; dans certaines conditions elles estiment que la régression observée s'accompagne de la disparition et de la régénération de centres de sensibilité. En l'absence de gélatine protectrice, l'évolution est plus rapide, selon Loening, le voile et la dimension des grains augmentent. Enfin on sait que dans les émulsions mouillées ou liquides le voile et la sensibilité évoluent plus rapidement qu'à sec.

Les mécanismes proposés sont basés sur la théorie de Gurney-Mott, et accordent une importance spéciale aux défauts du cristal qu'étudie Mitchell (33).

*Régression et effet Herschel négatif*

Il est naturel de rapprocher les deux phénomènes, comme l'a proposé Beiser (7). L'un et l'autre conduisent à la disparition de l'image latente, et sont aidés par le brome résiduel, par les oxydants faibles et par les accepteurs d'électrons. L'effet Herschel négatif sur les traces $\alpha$ a été observé par Winand (44) en présence d'oxygène et d'un désensibilisateur tel que la rhodamine et le jaune de pinakryptol, et ces mêmes agents favorisent la régression selon Lauda.

Dans certains cas au moins, l'effet Herschel négatif s'observe sans l'aide d'un accepteur d'électrons, et doit alors consister dans la dispersion du centre de développement $A$ ou centre $F$ par l'émission d'un électron et d'un ion $Ag^+$ qui vont se neutraliser sur un centre comparable à nos centres $B$.

Dans l'effet Herschel, l'émission de l'électron par le centre $A$ ou $F$ a lieu par l'effet photoélectrique d'un quantum de lumière rouge. Dans la régression, l'émission de l'électron est attribuée à l'agitation thermique.

*Accroissement initial de l'image latente et effet Herschel positif*

Le mécanisme (2) discuté plus haut peut expliquer un accroissement de l'image latente. S'il existe dans un cristal deux centres qui ne sont pas de type $B$, trop petits l'un et l'autre pour amorcer le développement, la désintégration thermique de l'un avec émission d'électrons et d'ions $Ag^+$ peut accroître l'autre et l'amener à la taille d'un centre de développement.

Le phénomène est entièrement parallèle à l'effet Herschel positif, qui se manifeste de façon particulièrement satisfaisante dans les expériences de Schopper, Magun et Braun (40), où des traces augmentent de densité par l'effet de la lumière rouge. Voir aussi la discussion par Berg (8) des travaux sur l'effet Herschel faits par Debot, Hautot, et Falla.

## IX. REMERCIEMENTS

Nous remercions l'Office des Recherches du Ministère de l'Industrie et du Commerce de la province de Québec, pour une bourse accordée à Jacques Lapalme; le Conseil Canadien pour la Reconstruction par l'UNESCO, et le Service des Oeuvres du Ministère de l'Education Nationale (France), pour des bourses accordées à Jacques Thouvenin; et enfin le Conseil National des Recherches, pour un octroi qui a permis ce travail. Nous remercions aussi Mlle Hanne Lauda boursière de l'UNESCO, pour des échanges de vues sur le sujet pendant son séjour dans ce laboratoire en 1950. Nous remercions M. D. I. Wanklyn et le Prof. J. S. Foster pour des irradiations avec le cyclotron de l'Université

McGill. Enfin les premières irradiations section II ont été faites au laboratoire de Chalk River.

SUMMARY

We describe comparative tests on regression in several types of emulsions, accurate measurements on proton tracks, two new procedures concerning $\alpha$ rays, using either a mechanism or the analysis of thorium stars, and experiments on the action of air, of humidity, and of temperature. These all show relations between linear density of grains $D$, of the observable tracks, ionizing power $I$, and time $t$. The nature of the emulsion matters little, except through the size and the sensitivity of the grains. Oxygen is almost *without effect*, humidity is a foremost factor, and very low temperatures stop all regression. Four experimental laws are derived. (1) Density $D$ is an exponential function of the $n$th power of time: $D_0 \exp - (t/\tau)^n$, $n$ varies from 0.5 to 2. (2) $D$ is a linear function of initial density and of time dependent coefficients: $D_0(1 - b) - a$. (3) At extreme regressions, $D$ does not depend upon $I$. (4) Straggling of $D$ increases with time. From these several characters of the latent image are drawn. A mechanism of regression, analogous to Herschel effect, is proposed: (1) thermal emission of an electron $\epsilon^-$ and of an ion $Ag^+$, by the center $A$; (2) $\epsilon^-$ and $Ag^+$ fall on a *type B center*, the properties of which are discussed; (3) or $\epsilon^-$ is captured by an external acceptor; (4) production of centers by the evolution of the silver bromide crystal, which is very fast in the presence of water.

BIBLIOGRAPHIE

1. ALBOUY, G. et FARAGGI, H. Compt. rend. 226: 117. 1948.
2. ALBOUY, G. et FARAGGI, H. Compt. rend. 228: 68. 1949.
3. ALBOUY, G. et FARAGGI, H. J. phys. radium, 10: 105. 1949.
4. ALBOUY, G. et FARAGGI, H. Photographic sensitivity. J. W. Mitchell, *rédacteur*. Butterworth Scientific Publications, London. 1951. p. 290.
5. BARABASCHEFF, N. et SEMEJKIN, B. Z. wiss. Phot. 28: 333. 1931.
6. BARKAS, W. H. Colloque internationale de Photo. Scient. Paris. 1951.
7. BEISER, A. Phys. Rev. 80: 112. 1950.
8. BERG, W. F. Phot. J. B, 87: 112. 1947.
9. BERG, W. F. Trans. Faraday Soc. 44: 783. 1948.
10. BLAU, M. Sitzber. Akad. Wiss. Wien, Math. naturw. Klasse. Abt. IIa, 140: 623. 1931.
11. BRUSH, C. F. Phys. Rev. 31 II: 241. 1910.
12. CARROLL, B. J. Chem. Education, 8: 2341. 1931.
13. COPPENS, R. Compt. rend. 227: 61. 1948.
14. CÜER, P. et WINAND, L. Science et inds. phot. 12: 445. 1948.
15. DEMERS, P. Phys. Rev. 70: 86. 1946.
16. DEMERS, P. Can. J. Research, A, 24: 223. 1947.
17. DEMERS, P. Science, 100: 380. 1950.
18. DEMERS, P. Science et inds. phot. 23: 1. 1952.
19. DILWORTH, C. C., OCCHIALINI, G. P. S. et VERMAESEN, L. Photographic sensitivity. J. W. Mitchell, *rédacteur*, Butterworth Scientific Publications, London. 1951. p. 297.
20. FARAGGI, H. Thèse. Univ. de Paris Faculté des Sciences. 1951.
21. HÄLG, W. et JENNY, L. Helv. Phys. Acta, 24: 508. 1951.
22. HEISENBERG, H. Veröffentl. wiss. Zentral-Lab. phot. Abt. I. G. Farbenind. Akt.-Ges. AGFA. 3: 47. 1933.
23. JAUSSERAN, G. Compt. rend. 188: 783. 1929.
24. JAUSSERAN, G. Rev. optique, 8: 119. 1929.
25. JENNY, L. Photographic sensitivity. J. W. Mitchell, *rédacteur*. Butterworth Scientific Publications, London. 1951. p. 259.
26. KRENZ, F. H. Can. J. Research, B, 26: 647. 1948.
27. LAPALME, J. Thèse de maitrise, Univ. de Montréal. Faculté des Sciences. 1948.
28. LAPALME, J. et DEMERS, P. Phys. Rev. 72: 536. 1947.
29. LAUDA, J. Sitzber Akad. Wiss. Wien, Math. naturw. Klasse Abt. IIa, 145: 107. 1936.

30. LOENING, E. E. Photographic sensitivity. J. W. Mitchell, *rédacteur*. Butterworth Scientific Publications, London. 1951. p. 149.
31. MATHER, K. B. Phys. Rev. 78: 486. 1949.
32. MEES, C. E. K. The theory of the photographic process. The MacMillan Company, New York. 1945.
33. MITCHELL, J. W. Photographic sensitivity. J. W. Mitchell, *rédacteur*. Butterworth Scientific Publications, London. 1951. p. 242.
34. MORTIER, M. et VERMAESEN, L. Bull. Centre de Physique Nuclaire U. L. Bruxelles N° 5. 1948.
35. OCCHIALINI, G. P. S. et POWELL, C. F. Nature, 159: 186. 1947.
36. PERFILOV, N. A. J. Phys. U.R.S.S. 17: 376. 1947.
37. PICCIOTTO, E. Compt. rend. 228: 173. 1949.
38. PICCIOTTO, E. Compt. rend. 228: 247. 1949.
39. ROTBLAT, J. Nature, 167: 550. 1951.
40. SCHOPPER, E., MAGUN, S. et BRAUN, W. Z. Naturforsch. A, 6: 338. 1951.
41. THOUVENIN, J. et DEMERS, P. Compt. rend. 234: 1968. 1952.
42. URBACH, F. Compt. rend. 4ème Congrès Intern. Phot.: 432. 1935.
43. WÄFFLER, H. et JUNIS, S. Helv. Phys. Acta, 22: 414. 1949.
44. WINAND, L. Communication privée.
45. WINAND, L. et FALLA, L. Bull. soc. roy Sci. Liège, 18: 184. 1949.
46. YAGODA, H. Am. Mineral. 31: 87. 1946.
47. YAGODA, H. Phys. Rev. 71: 910. 1947.
48. YAGODA, H. Nucleonics, 2: 2. 1948.
49. YAGODA, H. et KAPLAN, N. Phys. Rev. 72: 634. 1948.

# THERMODYNAMICS OF SOME SPECIAL FIELDS[1]

By R. V. Krotkov[2] and A. E. Scheidegger[3]

ABSTRACT

The free energy, internal energy, and entropy of two quantized fields are calculated, using the method introduced by Scheidegger and McKay. The two fields examined are those representing (*a*) an ensemble of mesons bound by an interaction with their source (a nucleon), and (*b*) an ensemble of electrons perturbed by an external electromagnetic field. The presence of a source in the first case is found to have no effect on the thermodynamic functions of the mesons, while an external electromagnetic field does affect the thermodynamic functions of the electrons. Explicit formulas in the latter case are given.

## 1. INTRODUCTION

It is well known that a quantized field represents an ensemble of particles, the wave equation of each particle being the differential equation satisfied by the nonquantized field variables. Scheidegger and McKay (2) have found the thermodynamic functions of such an ensemble by applying the quantum statistics of von Neumann (4) and Klein (1) to the quantized field. Among the fields so treated were the Schrödinger–Gordon and Dirac vacuum fields, corresponding to ensembles of free, uncharged mesons and of free electrons respectively.

It is the purpose of this paper to extend the results of Scheidegger and McKay (2) for the above mentioned fields by calculating the thermodynamic functions of an ensemble of mesons which are bound by an interaction with the source of the meson field (a nucleon) and of electrons in a uniform, external electromagnetic field.

The method employed will be the same one used by Scheidegger and McKay (2), and consists of the straightforward application, to an appropriate quantized field, of the prescription laid down by von Neumann (4) and Klein (1) for finding the thermodynamic functions of any quantum mechanical system. Application of this prescription involves a knowledge of the energy eigenvalues for the system in question. These will be found by perturbation theory.

To anticipate the final results, it will turn out that, up to the second order, the switching on of the interaction between a meson field and its source does not essentially alter the thermodynamic functions of the field. This is because the first order perturbation in the energy eigenvalues is zero, while the second order perturbation is the same for all energy levels. However, for the vacuum Dirac field, it will turn out that, to a first order approximation, switching on a uniform external electromagnetic field does change the thermodynamic functions in a nontrivial way. The final formulas in this case are quite complicated.

Before describing the actual calculations, we may briefly recall that according to the prescription of von Neumann (4) and Klein (1) referred to above, the

[1] *Manuscript received October 31, 1952.*
*Contribution from the Department of Physics, Queen's University, Kingston, Ont.*
[2] *Holder of Shell Oil Fellowship, Queen's University, 1951–52. Now at Palmer Physical Laboratory, Princeton University, Princeton, N.J., U.S.A.*
[3] *Now with Imperial Oil Ltd., Calgary, Alta.*

first step in finding the thermodynamic functions of a system is to calculate the partition function $Z$ = trace $\exp(-\theta\mathbf{H})$. In this definition, $\mathbf{H}$ (operators are denoted by **bold-faced** type or underlined letters) is the Hamiltonian of the system considered, and $\theta$ is $1/kT$, where $k$ is Boltzmann's constant and $T$ the absolute temperature. $Z$ may be computed by summing over the eigenvalues of $\mathbf{H}$. The free energy $F$, internal energy $E$, and entropy $S$ of the ensemble are then found from simple formulas involving log $Z$. These formulas are given by Scheidegger and McKay (2).

## 2. THE REAL MESON FIELD WITH A SOURCE

In order to describe an ensemble of mesons interacting with their source, one quantizes the real field described by the differential equation (Wentzel (6), page 37)

$$[2.1] \qquad (\Box - \mu^2)\psi = \frac{1}{c}\eta\,(x, t), \quad \mu = \frac{mc}{\hbar},$$

where $\eta$ is a density function. Using box normalization, and taking $\eta$ to be $(g/c)\,e(x)$, where $g$ is a coupling constant and $e(x)$ the extension function of the source, an analysis very similar to Wentzel's ((6)§7) shows that the interaction Hamiltonian $\mathbf{H}'$ representing the effect of the source on the quantized field is

$$[2.2] \qquad \mathbf{H}' = g\sqrt{\frac{\hbar}{2V}}\sum_k \frac{v_k}{\sqrt{\omega_k}}(\mathbf{a}_k + \mathbf{a}^*_{-k}).$$

In equation [2.2], $\omega_k$ and $v_k$ are defined to be

$$[2.3] \qquad \omega_k = c\sqrt{\mu^2 + k^2},$$

$$[2.4] \qquad v_k = \int e(x)\exp(ikx)\,d^3x,$$

and $V$ is the volume of the enclosing box. The summation is over lattice points in $k$ space; $\mathbf{a}_k$ and $\mathbf{a}^*_k$ are the usual destruction and creation operators.

Taking $g$ to be small, $\mathbf{H}'$ may be considered as a small perturbation. The interpretation of $\mathbf{a}_k$ and $\mathbf{a}^*_k$ in equation [2.2] as destruction and creation operators then shows that the diagonal elements in the matrix for $\mathbf{H}'$, and hence the first order perturbations, are zero.

To find the second order perturbation $\lambda'_i$ in the $i$'th energy eigenvalue $\lambda^0_i$, the matrix element $H'_{ij}$, taken between two ensemble state vectors $\psi_i$ and $\psi_j$, may be written as the inner product:

$$[2.5] \qquad H'_{ij} = (\mathbf{H}'\psi_j, \psi_i) = g\sqrt{\frac{\hbar}{2V}}\sum_k \frac{v_k}{\sqrt{\omega_k}}\Big[(\mathbf{a}_k\psi_j, \psi_i) + (\mathbf{a}^*_{-k}\psi_j, \psi_i)\Big].$$

Then, once more using the fact that the $\mathbf{a}$'s are destruction and creation operators, it follows that $H'_{ij}$ will vanish unless one or other of the following two cases holds:

(1) The indices $i$ and $j$ stand for two sets of occupation numbers, $i \equiv N_1, N_2, N_3, \ldots$ and $j \equiv N'_1, N'_2, N'_3, \ldots$ such that $N'_l = N_l + 1$ for some $l$, but $N'_k = N_k$ for all the other $k$'s.

(2) $i$ and $j$ are such that $N_l' = N_l - 1$ for some $l$, but $N_k' = N_k$ for all the other $k$'s.

Clearly, cases (1) and (2) cannot hold simultaneously. If (1) holds, it follows from equation [2.5] that $H_{ij}'$ is given by

$$H_{ij}' = g\sqrt{\frac{\hbar}{2V}}\sqrt{N_l + 1}\,\frac{v_l}{\sqrt{\omega_l}}, \tag{2.6}$$

where the factor $\sqrt{N_l + 1}$ comes from the properties of $\mathbf{a}_k$. Similarly, if (2) holds, [2.5] reduces to

$$H_{ij}' = g\sqrt{\frac{\hbar}{2V}}\sqrt{N_l}\,\frac{v_{-l}}{\sqrt{\omega_{-l}}}. \tag{2.7}$$

Furthermore, it is clear that $\lambda_i^0 - \lambda_j^0 = \mp\,\hbar\omega_l$, ($\hbar\omega_l$ being the energy of one meson with momentum $\hbar l$), where the minus sign holds for $i$ and $j$ satisfying case (1), the plus sign for case (2).

The standard formula (Schiff (3), page 151) for the second order perturbation $\lambda_i''$ then leads to the result

$$\lambda_i'' = \frac{g^2\hbar}{2V}\sum_l \frac{N_l + 1}{-\hbar\omega_l}\frac{|v_l|^2}{\omega_l} + \frac{g^2\hbar}{2V}\sum_l \frac{N_l}{\hbar\omega_l}\frac{|v_{-l}|^2}{\omega_{-l}}, \tag{2.8}$$

where the first term arises from the sum over $j$'s satisfying case (1), and the second term is generated by $j$'s satisfying case (2). All other $j$'s give $H_{ij}' = 0$.

Noting further that $\omega_{-k} = \omega_k = c\sqrt{\mu^2 + k^2}$ and $|v_{-k}| = |v_k|$, the second order perturbation finally becomes

$$\lambda_i'' = -\frac{g^2}{2V}\sum_k \frac{|v_k|^2}{\omega_k^2}. \tag{2.9}$$

As the volume $V$ of the enclosing box increases to infinity, the lattice points in $k$ space crowd together, and the sum in [2.9] goes over in the usual way (see (2)) into the integral, taken over all $k$ space,

$$\lambda_i'' = -\frac{g^2}{16\pi^3 c^2}\int \frac{|v_k|^2}{\mu^2 + k^2}\,d^3k. \tag{2.10}$$

*Discussion*

The striking fact about equation [2.10] is that $\lambda_i''$ is independent of $i$; i.e. the interaction of the meson field with its source merely depresses all the energy eigenvalues uniformly, at least to a second order approximation. Thus log $Z$, and with it all the thermodynamic functions, changes only by the addition of a constant. This change is meaningless, since an infinite constant has to be subtracted from the internal energy anyway (see (2)) owing to the zero point energy of the unperturbed Hamiltonian.

One may note that if the extension function $e(x)$ is taken to be a delta function (i.e. if a point source is assumed), the second order perturbation will become infinite. Cutoff methods must be used if this is to be avoided. However, the

essential point is that, infinite or not, $\lambda_i''$ is just a constant, and as such does not affect the thermodynamic functions.

## 3. ELECTRONS IN AN ELECTROMAGNETIC FIELD

This case can be treated in exactly the same way as the preceding one.

In order to describe an ensemble of electrons interacting with a uniform external electromagnetic field, one quantizes the Dirac equation with forces:

$$\left(\frac{\hbar}{i}\frac{\partial}{\partial t} + \underline{\epsilon}^0 + \underline{\epsilon}'\right)\psi = 0. \tag{3.1}$$

In equation [3.1], $\underline{\epsilon}^0$ is the Dirac operator $(c\hbar/i)\ (\vec{\underline{\alpha}}\cdot\vec{\underline{\nabla}}) + mc^2\underline{\beta}$, where the $\underline{\alpha}$'s and $\underline{\beta}$ are Dirac matrices. $\underline{\epsilon}'$ is the operator $e\vec{\underline{\alpha}}\vec{\underline{\phi}} - e\underline{\phi}_0$, $e$ being the charge on a positron, $\vec{\underline{\phi}}$ the magnetic vector, and $\underline{\phi}_0$ the scalar operator-potential. Also, $\psi$ is a four-component spinor.

*Calculation of the Energy Eigenvalues*

The total Hamiltonian $\mathbf{H}$ of the quantized field [3.1] may, as in the meson case, be written in the form (Wentzel, (6) p. 193)

$$\mathbf{H} = \mathbf{H}^0 + \mathbf{H}', \tag{3.2}$$

$$\mathbf{H}^0 = \sum_m E_m^0 \mathbf{N}_m, \tag{3.3}$$

$$\mathbf{H}' = \sum_{mn} E'_{mn} \mathbf{a}_m^* \mathbf{a}_n, \tag{3.4}$$

$$E'_{mn} = e\int_V u_m^*(\vec{\underline{\alpha}}\ \vec{\underline{\phi}} - \underline{\phi}_0)\, u_n\, d^3x. \tag{3.5}$$

In these equations, the electrons are considered to be confined to a box of volume $V$. The $u_m$ and $E_m^0$ are eigenspinors and eigenvalues respectively of the Dirac operator $\underline{\epsilon}^0$. The subscript $m$ stands for two indices, $k$ and $s$, $k$ as usual labelling lattice points in $k$ space, and $s$ distinguishing between the two spin orientations for positive ($s = 1, 2$) and negative ($s = 3, 4$) energies. The $\mathbf{a}_m$ and $\mathbf{a}_m^*$ are again destruction and creation operators respectively, while the eigenvalues of $\mathbf{N}_m$ are occupation numbers (0 or 1 only).

Utilizing once more the properties of destruction and creation operators, it is easily seen that the first order perturbation $H'_{ii}$ in the $i$'th energy level is given by the expression

$$H'_{ii} = \sum_m E'_{mm} N_m. \tag{3.6}$$

Assuming that the axes of coordinates are oriented so that $\phi_1 = \phi_2 = 0$, substitution of explicit expressions for $u_m$, $\vec{\underline{\alpha}}$, and $\underline{\beta}$ into [3.5] yields the formula

$$E'_{mm} = \frac{ec\hbar k_3}{E_m^0 V}\int \phi_3\, d^3x - \frac{e}{V}\int \phi_0\, d^3x, \tag{3.7}$$

$k_3$ being the third component of the lattice vector $\vec{k}$ associated with the index $m$.

The eigenvalues $H_{ii}$ of **H** are thus, to a first order approximation, given by

$$[3.8] \qquad H_{ii} = \sum_m E_m N_m, \qquad E_m = E_m^0 + E'_{mm}.$$

These eigenvalues, [3.8], must, however, be renormalized in the usual way so as to make **H** positive definite. Thus, one subtracts from the right-hand side of [3.8] the quantity $\sum_m E_m$ ($E_m < 0$). This leads, after substitution of explicit expressions for $E_m^0$, to the result

$$[3.9] \qquad H_{ii} = \sum_{ks}^{s=1,2} E_k^+ N_{ks} + \sum_{ks}^{s=3,4} E_k^- N'_{ks}$$

where

$$[3.10] \qquad E_k^{\pm} = mc^2\sqrt{1 + (k^2/\mu^2)} \pm v\frac{k_3/\mu}{\sqrt{1 + (k^2/\mu^2)}} - w,$$

$$[3.11] \qquad v = \frac{e}{V}\int \phi_3 \, d^3x,$$

$$[3.12] \qquad w = \frac{e}{V}\int \phi_0 \, d^3x,$$

$$[3.13] \qquad N'_{ks} = 1 - N_{ks} \; (s = 3, 4).$$

We have taken into account the fact that the particles of our ensemble are electrons in positive energy states (charge minus) and positrons in negative energy states (charge plus).

*Calculation of Thermodynamic Functions*

In order to calculate the partition function $Z$, as required by the general prescription of von Neumann (4) and Klein (1), one substitutes equation [3.9] for the eigenvalues of **H** into the expression

$$[3.14] \quad Z = \sum_i \exp(-\theta H_{ii}) = \sum_i \exp\left[-\theta\left(\sum_{ks}^{s=1,2} E_k^+ N_{ks} + \sum_{ks}^{s=3,4} E_k^- N'_{ks}\right)\right].$$

Writing each term of the sum on $i$ in [3.14] as the product of exponentials, it may be seen that $Z$ can be put into the form

$$[3.15] \qquad Z = \prod_k (1 + \exp(-\theta E_k^+))^2 \, (1 + \exp(-\theta E_k^-))^2.$$

In this way, $\log Z$ becomes a sum over $k$; the sum may be evaluated by letting $V$ go to infinity, in which case the sum as before may be replaced by the integral

$$[3.16] \quad \frac{\log Z}{V} = \frac{2}{(2\pi)^3}\int \log\,(1 + \exp\,(-\theta E_k^+))\, d^3k + \frac{2}{(2\pi)^3}\int \log\,(1 + \exp\,(-\theta E_k^-))\, d^3k.$$

To evaluate the integrals in [3.16], one may replace the logarithmic factors by their Taylor series expansions; using also equation [3.10] for $E_k^{\pm}$, one is led to the relation

$$[3.17] \qquad \frac{\log Z}{V} = \frac{2}{(2\pi)^3}\sum_1^\infty \frac{(-1)^{n+1}}{n} \exp(n\theta w)\, I_n,$$

where $I_n$ is the integral

$$[3.18] I_n = 2\int \exp\left(-n\theta mc^2\sqrt{1+(k^2/\mu^2)}\right)\sinh\left(-n\theta v \frac{k_3/\mu}{\sqrt{1+(k^2/\mu^2)}}\right) d^3k.$$

$I_n$ may be manipulated so as to assume the form

$$[3.19] \qquad I_n = 2\pi\mu^3(K_3 - K_1) + \frac{2\pi\mu^3}{3!} n^2\theta^2 v^2 (K_3 - 5K_1 + 4K_0),$$

where the $K_\nu(\nu = 0, 1, 3)$ are modified Hankel functions with argument $nmc^2/kT$. The manipulations referred to above involve expressing [3.18] in polar coordinates, integrating over the angles, making the substitution $r = \sinh\varphi$, retaining only the first two terms of a power series expansion for $\sinh x$, and finally using the formula (Watson (5) page 181)

$$[3.20] \qquad K_\nu(z) = \int_0^\infty \exp(-z\cosh\varphi)\cosh\nu\varphi\, d\varphi.$$

The integral

$$[3.21] \qquad \int_0^\infty \exp(-z\cosh\varphi)\frac{d\varphi}{\cosh\varphi},$$

which also appears in the derivation of [3.19], is to be replaced by $K_0$. It may be shown that this substitution is equivalent to discarding a term of order $10^{-7}$ times the term retained.

Since $p = mc^2/kT$ is very large (for $T = 300°$ K., $p = 2 \times 10^7$), the Hankel functions in [3.19] may be replaced by their asymptotic expansions. By substituting these expansions into [3.19], and [3.19] in turn into [3.17], we finally arrive at an expression for $(\log Z)/V$. Using this expression in the standard formulas for the free energy $F$, internal energy $E$, and entropy $S$, these quantities become as shown below:

Free Energy

$$\frac{F}{V} = -4\frac{(2\pi m)^{3/2}(kT)^{5/2}}{h^3}\left\{\sum_1^\infty \frac{(-1)^{n+1}}{n^{5/2}}\exp\left(\frac{nw}{kT}\right)\exp\left(-\frac{nmc^2}{kT}\right)\left[1+\frac{15}{8n}\frac{kT}{mc^2}+\ldots\right]\right.$$
$$\left. + \frac{v^2}{12(kT)^2}\sum_1^\infty \frac{(-1)^{n+1}}{n^1}\exp\left(\frac{nw}{kT}\right)\exp\left(-\frac{nmc^2}{kT}\right)\left[1+\frac{33}{8n}\frac{kT}{mc^2}+\ldots\right]\right\}$$

Internal Energy

$$\frac{E}{V} = 4\frac{(2\pi mkT)^{3/2}}{h^3}mc^2\left\{\sum_1^\infty \frac{(-1)^{n+1}}{n^{3/2}}\exp\left(\frac{nw}{kT}\right)\exp\left(-\frac{nmc^2}{kT}\right)\left[1+\frac{27}{8n}\frac{kT}{mc^2}+\ldots\right]\right.$$
$$\left. - \frac{w}{mc^2}\sum_1^\infty \frac{(-1)^{n+1}}{n^{3/2}}\exp\left(\frac{nw}{kT}\right)\exp\left(-\frac{nmc^2}{kT}\right)\left[1+\frac{15}{8n}\frac{kT}{mc^2}+\ldots\right]\right.$$

$$+\frac{v^2}{3mc^2kT}\sum_1^\infty \frac{(-1)^{n+1}}{n^{\frac{1}{2}}}\exp\left(\frac{nw}{kT}\right)\exp\left(-\frac{nmc^2}{kT}\right)\left[1-\frac{483}{16n}\frac{kT}{mc^2}+\dots\right]$$

$$-\frac{v^2w}{12mc^2(kT)^2}\sum_1^\infty(-1)^{n+1}n^{\frac{1}{2}}\exp\left(\frac{nw}{kT}\right)\exp\left(-\frac{nmc^2}{kT}\right)\left[1+\frac{33}{8n}\frac{kT}{mc^2}+\dots\right]\Bigg\}$$

Entropy

$$\frac{S}{V}=\frac{4}{T}\frac{(2\pi mkT)^{3/2}}{h^3}mc^2\Bigg\{\sum_1^\infty\frac{(-1)^{n+1}}{n^{3/2}}\exp\left(\frac{nw}{kT}\right)\exp\left(-\frac{nmc^2}{kT}\right)\left[1+\frac{35}{8n}\frac{kT}{mc^2}+\dots\right]$$

$$-\frac{w}{mc^2}\sum_1^\infty\frac{(-1)^{n+1}}{n^{3/2}}\exp\left(\frac{nw}{kT}\right)\exp\left(-\frac{nmc^2}{kT}\right)\left[1+\frac{15}{8n}\frac{kT}{mc^2}+\dots\right]$$

$$+\frac{5}{12}\frac{v^2}{mc^2kT}\sum_1^\infty\frac{(-1)^{n+1}}{n^{\frac{1}{2}}}\exp\left(\frac{nw}{kT}\right)\exp\left(-\frac{nmc^2}{kT}\right)\left[1+\frac{57}{40n}\frac{kT}{mc^2}+\dots\right]$$

$$-\frac{v^2w}{12(kT)^2mc^2}\sum_1^\infty(-1)^{n+1}n^{\frac{1}{2}}\exp\left(\frac{nw}{kT}\right)\exp\left(-\frac{nmc^2}{kT}\right)\left[1+\frac{33}{8n}\frac{kT}{mc^2}+\dots\right]\Bigg\}$$

*Discussion*

The above formulas are valid under the following restrictions, imposed in the course of the derivation:

(1) $v$, $w$, and $kT$ must all be much less than $mc^2$, the rest energy of an electron.

(2) $v^2$ must be much less than $kT$.

(3) The $x$ and $y$ components of the magnetic vector potential must vanish.

The formulas are admittedly complicated. However, one may note, on comparison with the corresponding formulas given in (2), that in each of the present expressions, the first term on the right-hand side is, apart from a factor $\exp(nw/kT)$, the unperturbed function.

Taking, for simplicity, $n$ to be one, it is seen that the electric field multiplies all three functions by the factor $\exp(w/kT)$, and in addition subtracts from $E/V$ and $S/V$ a term of order $w/mc^2$ times the unperturbed function.

The magnetic field, on the other hand, subtracts from $F/V$ a term of order $v^2/(kT)^2$ times the unperturbed function, while it adds to $E/V$ and $S/V$ a term of order $v^2/(mc^2\,kT)$ times the unperturbed energy and entropy.

There are in addition "cross terms" involved in the expressions for $E/V$ and $S/V$. These are of the order $v^2w/[mc^2(kT)^2]$ times the unperturbed function.

## 4. ACKNOWLEDGMENTS

The authors would like to express their appreciation of the interest taken in this work by colleagues and students in the Department of Physics, Queen's University. In addition, one of us (R.V.K.) is greatly indebted to the Shell Oil Company for the generous award of a fellowship, without which the present work could not have been done.

## REFERENCES

1. KLEIN, O. Z. Physik, 72: 767. 1931.
2. SCHEIDEGGER, A. E. and MCKAY, C. D. Phys. Rev. 83: 125. 1951.
3. SCHIFF, L. I. Quantum mechanics. McGraw-Hill Book Co. Inc., New York and London. 1949.
4. VON NEUMANN, J. Mathematische Grundlagen der Quantenmechanik. Dover Publications, New York. 1943. Chapt. V.
5. WATSON, G. N. Theory of Bessel functions. Cambridge University Press, Cambridge. 1922.
6. WENTZEL, G. Quantum theory of fields. Interscience Publishers, Inc., New York. 1949.

## LETTERS TO THE EDITOR

*Under this heading brief reports of important discoveries in physics may be published. These reports should not exceed 600 words and, for any issue, should be submitted not later than six weeks previous to the first day of the month of issue. No proof will be sent to the authors.*

### Angular Separation of Electron Pairs

In a recent paper (1) the scattering method has been used to determine the energies of a number of electron pairs produced by 0–70 Mev. X-rays in G-5 emulsions. The purpose of this note is to give the mean projected angle between members of a pair and the distribution of these angles as a function of the pair energy. It has been shown in Reference 1 that the pairs used for the angle measurements are approximately representative of pair production, i.e. that the method of selection does not discriminate against pairs with any particular energy division between members. This is done in Fig. 3 of Reference 1 where the measured energy distributions between members of a pair are compared with the known distributions and the agreement is seen to be fair, the measured distributions being slightly low for the case of extreme asymmetric energy division.

A simple protractor eyepiece reading to $\frac{1}{4}$ of a degree was used to measure the projected directions of the two tracks. The accuracy with which an individual reading of direction could be taken was limited by the coulomb scattering of the electron and to a much smaller extent by the lateral distribution of the grains in the track. Since the scattering increases with distance along the track and is greater for the lower energy electrons, only the first $20\mu$ of track was used for electrons of energy less than 20 Mev. while the first $50\mu$ was used for electrons of higher energy. In the case of a 5-Mev. electron the average error in an individual reading of direction due to scattering would be expected to be of the order of 1 degree. Since these errors are as likely to increase as decrease the measured angles, they should affect the measured distributions only slightly and the mean values of these angles even less.

The general trend of the distributions can be seen from Fig. 1 in which the pairs are grouped into 10-Mev. energy intervals and four distributions are plotted. The large angle tails of these

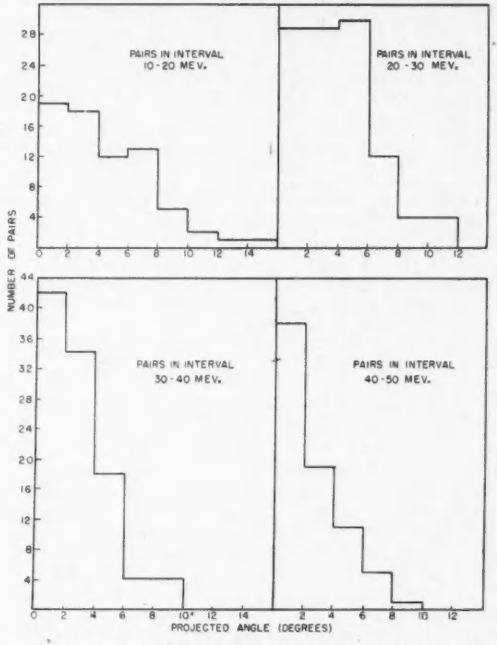


FIG. 1. Distributions of the projected angle between members of a pair for pairs of different total energy.

distributions should probably be slightly more pronounced if, as indicated by Fig. 3 of Reference 1, some of the pairs in which the energy division is extremely asymmetric were not measured.

In Fig. 2 the data are grouped into 5-Mev. intervals and the mean projected angle between members of a pair is plotted against total pair energy. The solid vertical lines indicate the

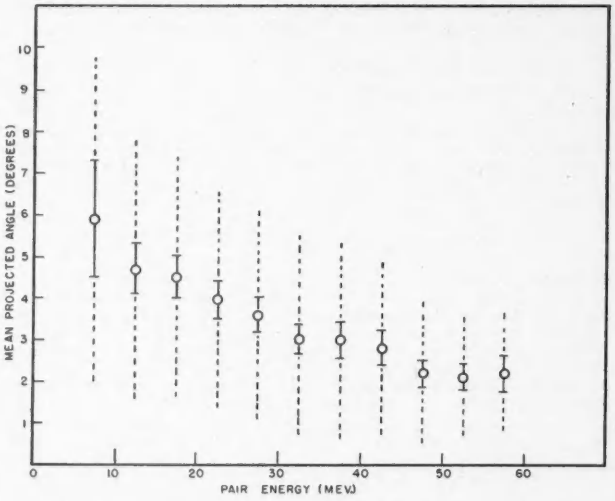


FIG. 2. Mean projected angle as a function of pair energy. The solid vertical lines are the standard errors of the mean and the dashed lines are the root mean square deviations of a single angle from the mean angle.

statistical accuracy of the mean, i.e. the standard error of the mean, and the dashed vertical lines indicate the width of the distributions, i.e. the root mean square deviation of a single angle from the mean angle.

The theoretical problem of calculating the distribution between members of a pair is complicated by the fact that the local nucleus can take up an unspecified amount of momentum, and to the writer's knowledge no such calculations have been made. However, the present results are in good agreement with measurements made by Voyvodic and Pickup (2) using pairs produced by the 17-Mev. $\gamma$-rays from $Be^8$. These authors find a mean angle of $5.0 \pm 0.3$ degrees and a nearly constant distribution in angle up to 8 degrees falling off rapidly at larger angles.

It is a pleasure to thank Prof. J. A. Gray for the interest he has taken in this problem. I am also indebted to the National Research Council of Canada for financial assistance.

1. McDIARMID, I. B. Can. J. Phys. 30: 670. 1952.
2. VOYVODIC, L. and PICKUP, E. Phys. Rev. 85: 91. 1952.

RECEIVED DECEMBER 22, 1952.
I. B. McDIARMID
SYNCHROTRON LABORATORY,
QUEEN'S UNIVERSITY,
KINGSTON, ONT.

# CANADIAN JOURNAL OF PHYSICS

## Notice to Contributors

GENERAL: Manuscripts should be typewritten, double spaced, and the **original and one extra copy** submitted. Style, arrangement, spelling, and abbreviations should conform to the usage of this Journal. Names of all simple compounds, rather than their formulas, should be used in the text. Greek letters or unusual signs should be written plainly or explained by marginal notes. Superscripts and subscripts must be legible and carefully placed. Manuscripts should be carefully checked before being submitted, to reduce the need for changes after the type has been set. If authors require changes to be made after the type is set, they will be charged for changes that are considered to be excessive. **All pages, whether text, figures, or tables, should be numbered.**

ABSTRACT: **An abstract of not more than about 200 words, indicating the scope of the work and the principal findings, is required.**

ILLUSTRATIONS:

(i) *Line Drawings:* All lines should be of sufficient thickness to reproduce well. Drawings should be carefully made with India ink on white drawing paper, blue tracing linen, or co-ordinate paper **ruled in blue only;** any co-ordinate lines that are to appear in the reproduction should be ruled in black ink. Paper ruled in **green, yellow, or red should not be used** unless it is desired to have all the co-ordinate lines show. Lettering and numerals should be neatly done in India ink preferably with a stencil (**do not use typewriting**) and be of such size that they will be legible and not less than one millimeter in height when reproduced in a cut three inches wide. All experimental points should be carefully drawn with instruments. Illustrations need not be more than two or three times the size of the desired reproduction, but the ratio of height to width should conform with that of the type page. **The original drawings and one set of small but clear photographic copies are to be submitted.**

(ii) *Photographs:* Prints should be made on glossy paper, with strong contrasts; they should be trimmed to remove all extraneous material so that essential features only are shown. Photographs should be submitted **in duplicate;** if they are to be reproduced in groups, one set should be so arranged and mounted on cardboard with rubber cement; the duplicate set should be unmounted.

(iii) *General:* **The author's name, title of paper, and figure number should be written in the lower left hand corner (outside the illustration proper) of the sheets on which the illustrations appear.** Captions should not be written on the illustrations, but typed together at the end of the manuscript. All figures (including each figure of the plates) should be numbered consecutively from 1 up (arabic numerals). **Each figure should be referred to in the text.** If authors desire to alter a cut, they will be charged for the new cut.

TABLES: Each table should be typed on a separate sheet. Titles should be given for all tables, which should be numbered in roman numerals. Column heads should be brief and textual matter in tables confined to a minimum. **Each table should be referred to in the text.**

REFERENCES: **These should be listed alphabetically by authors' names, numbered in that order, and placed at the end of the paper.** The form of literature citation should be that used in this Journal. **Titles of papers should not be given.** The first page only of the references cited should be given. **All citations should be checked with the original articles.** Each citation should be referred to in the text by means of the key number.

REPRINTS: A total of 50 reprints of each paper, without covers, are supplied free to the authors. Additional reprints will be supplied according to a prescribed schedule of charges. On request, covers can be supplied at cost.

Approximate charges for reprints may be calculated from the number of printed pages, obtained by multiplying by 0.6 the number of manuscript pages (double-spaced typewritten sheets, 8½ in. by 11 in.) and making allowance for space occupied by line drawings and half-tones (not inserts). The cost per page is tabulated at the back of the reprint request form sent with the galley.

## *Contents*



*Printed* in Canada *by* University of Toronto Press